Development of microindentation robot for hardness and stiffness measurement with vision based navigation system

Montree PAKKRATOKE

Department of Mechanical Engineering and Intelligent systems

The University of Electro-Communications

A Thesis submitted for the degree of

Doctoral of Engineering

2013 March

Development of microindentation robot for hardness and stiffness measurement with vision based navigation system

Approved by Supervisory Committee:

Chair Person: Prof. Dr. Hisayuki AOYAMA
Member: Assoc. Prof. Dr. Chisato KANAMORI
Member: Assoc. Prof. Dr. Aiguo MING
Member: Assoc. Prof. Dr. Koichi MORISHIGE
Member: Assoc. Prof. Dr.Takuji KOIKE

概要

　本論文ではマイクロロボットを用いた精密微小硬さ計測システムの開発を目的に、2段平行ばね、VCA、圧子およびLVDTなどから構成される微小力発生検知機構とこれを搭載する超小形精密自走機械および画像計測に基づく経路誘導方法について論じている。本論文では生体材料などの柔らかい材料表面を環境を制御されたチャンバー内で精密に検査することや従来サイズの機構では到達が困難な狭所での検査作業を目標とし、システムの提案、設計試作および基本性能評価を行った。この装置では最大17mNの発生力で50μNの分解能を有すること確認し、さらにシステムに実装し、応用実験を行った。その結果、±3μmの分解能で検査対象に精密誘導し、表面特性を自動連続取得が可能であることを示した。

Abstract

A microsurface measurement system that is composed of a microrobot with an indenter, and a vision-based navigation system is proposed for investigating the hardness and stiffness of microparts. The microindentation mechanism is composed of the small force generator mechanism, which is simply combination between a voice coil actuator (VCA) and the tandem leaf spring mechanism. The generated force can be controlled by electrical current, which is supplied to coil and positioned precisely at the balance point with the parallel leaf spring without mechanical friction. And the full bridge strain gauges on both sides of double leaf spring can be detected the small force which is applied to the sample with a microindenter. This handmade small mechanism can produce and verify a small force up to 17 mN with good linearity and 50 μN resolutions. The displacement of the indenter head is measured by a linear variable differential transformer (LVDT) which is included in machine. Thus, this mechanism generates small force and monitors the depth behavior of the indenter during the indentation test.

Since the overall mechanism is very small, then it is implemented on the microrobot. The piezo-driven microrobot is capable of moving step by step precisely with 1 μm per step, so the sample surface can be penetrated anywhere by the microindenter. With the benefits of the image processing technique, a vision-based coordination system with a local close-up view and an overall global view has been developed to identify the locations of the robot and the indenter precisely within ±3 μm of accuracy over the working range.

The experiment results present the performance of this machine by the surface stiffness investigation of several materials including metal and bio materials. The surface stiffness/hardness was successfully checked, and the indentation load-depth characteristics were precisely acquired. With the surface characteristic results of the certified hardness blocks (30HV and 100HV), the degree of stiffness and hardness can be compared. Finally, the performance of a vision-based navigation system is present on the surface characteristics of the unhealthy human tooth that are precisely acquired at the specified measurement point.

Contents

List of Figures

xiv

List of Tables

CHAPTER 1. INTRODUCTION

Material selection in engineering applications is crucial. Engineers have to confirm that material properties are appropriate for the operational condition. There are many kinds of material properties, and ultimate tensile strength is one of the most useful for predicting the strength of a material. The tensile test is a fundamental materials science test in which a sample is subjected to uniaxial tension until failure. It can be predicted the strength of materials, which the maximum stress on the stress-strain curve (UTS) is the point that the material under test can be withstood before damage.
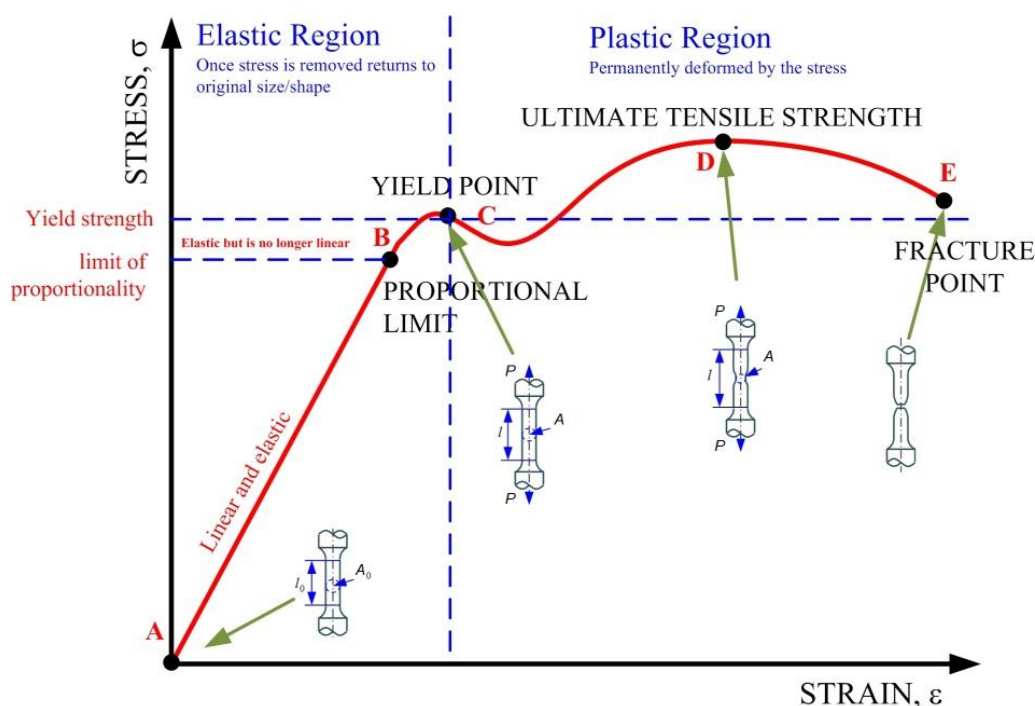
Figure 1.1 The relationship between the stress and strain of a material under tension force applied

The relationship between the stress and strain of a material under tension force applied is shown in Fig. 1.1 most of the material display linear elastic behavior from the pulling point A up to a proportional limit point B. At this region the deformations are completely recoverable upon removal of the load. That is a specimen loaded elastically in tension will elongate, but after unloaded it will return to the original shape and size. Pass this linear region, the deformation of metal materials still elastic but no longer linear. The deformed specimen will not return to its original size and shape when unloaded. For many applications, when a material passed a proportional limit deformation, it is unacceptable and cannot be used. At this point is used as the safety design

limitation. After the yield point C, the deformation of ductile materials is plastic. It is gone over a period of strain hardening. That is a stress increases again with increasing strain, and they begin to a neck shape. When necking becomes substantial, it causes a reversal of the stress-strain curve, i.e., it is calculated assuming the original cross-sectional area before necking. The reversal point is the maximum stress on the stress-strain curve, and the stress coordinate of this point is the ultimate tensile strength (UTS), given by point D. The UTS is used for quality control, because of the ease of testing. It is also used to roughly determine material types for unknown samples. However, in tensile testing method, the test material is destroyed, which means that such testing is not appropriate in some situations. In addition, there is another way to predict the strength of a material without greatly damaging a test sample that is the hardness test. In Fig. 1.2 has shown the relationship between hardness and ultimate tensile strength, it is nearly proportional each other.
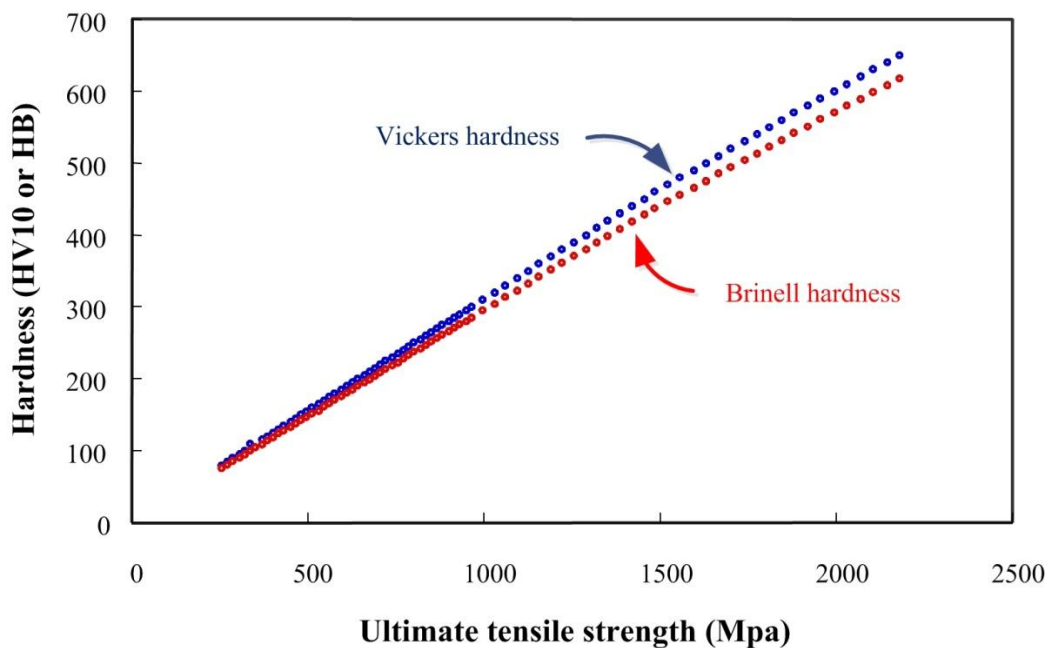
Figure 1.2 The relationship between hardness and UTS. From the conversion of hardness to hardness or hardness to tensile strength values for unalloyed and low-alloy steels and cast iron [1-1]

1.1 Hardness measurement

The hardness test has been widely used for nearly 100years because indentations are very small and the surface quality of the material is not destroyed. This technique is therefore considered as nondestructive test method.

Hardness is not the physical parameter like length, time, mass, electric current; it is the industrial parameter or the comparative value same as other mechanical characteristics. The Metals Handbook defines hardness as "Resistance of metal to local plastic deformation", usually by indentation. However, the term may also refer to stiffness or temper or to resistance, to scratching, abrasion, or cutting. It is the property of a metal, which gives it the ability to resist being permanently, deformed (bent, broken, or have its shape changed), when a load is applied [1-2]. This is the usual type of hardness test, in which rounded indenter is pressed into a surface under a substantially static load. There are three general types of hardness measurements as follows.

1.1.1 Scratch hardness

Scratch hardness test (Fig. 1.3) is the resistance of solid surfaces to permanent deformation under the action of a single point (diamond stylus tip) [1-3]. It is a companion method to quasi-static hardness tests in which a stylus is pressed into a surface under a certain normal load and the resultant depth or impression size is used to compute a hardness number. Scratch hardness numbers involve a different combination of properties of the surface because the indenter (diamond stylus) moves tangentially along the surface. Therefore, the stress state under the scratching stylus differs from that produced under a quasi-static indenter. Scratch hardness numbers are in principle a more appropriate measure of the damage resistance of a material to surface damage processes like two-body abrasion than are quasi-static hardness numbers.

| (A) | (B) |
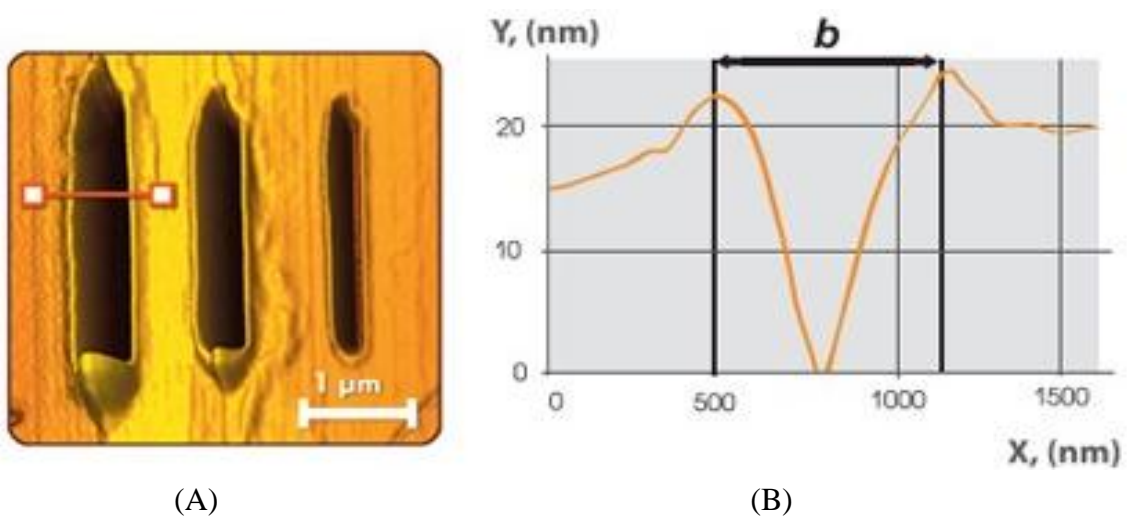
Figure 1.3 (A) Scratches on the material with different loads. (B) Defining the average of the scratch width [1-4]

Before the measurements, the indenter shape is calibrated on a reference sample using the series of scratches at several defined loads. The material hardness value is calculated in comparison to the reference hardness as a proportion between the loads and widths of scratches on both the tested and reference materials. The scratch hardness value is expressed as the load in kilograms divided by the square of the width of the scratch in millimeters as follows Eq. (1.2) [1-4].

$$H_{ref} = k\frac{P_{ref}}{b_{ref}^2} \dots\dots\dots\dots\dots\dots\dots\dots\dots\dots\dots\dots (1.1)$$

$$H = k(b)\frac{P}{b^2} \dots\dots\dots\dots\dots\dots\dots\dots\dots\dots\dots (1.2)$$

Where;

H is hardness.

b is scratch width (mm).

P is normal load (kgf).

k(b) is the calibration function.

This test method is applicable to a wide range of materials. These include metals, alloys, and some polymers. The main criteria are that the scratching process produces a measurable scratch in the surface being tested without causing catastrophic fracture, spallation, or extensive delamination of surface material. Severe damage to the test surface, such that the scratch width is not clearly identifiable or that the edges of the scratch are chipped or distorted, invalidates the use of this test method to determine a scratch hardness number. Since the degree and type of surface damage in a material may vary with applied load, the applicability of this test to certain classes of materials may be limited by the maximum load at which valid scratch width measurements can be made.

Figure 1.4 (A) File hardness set 40HRC to 55HRC model TTC HTF-6S. [1-5] (B) Pencil hardness set model FMH-5 [1-6]

Other methods for scratch hardness determination include the use of hardness standards for scratching plastics such as hardness-graded pencils (kohinoor value), minerals of known hardness (mohs value) falling carborundum particles (Fig. 1.4).

1.1.2 Rebound hardness test

Rebound hardness test [1-7] or Leeb rebound hardness test is a dynamic hardness testing. It is determined by the action when making an object collides with the test surface and the rebound height is measured. This type of hardness is related to elasticity. The device used to take this measurement is known as scleroscope and Shore hardness. The rebound hardness test method was developed in 1975 by Leeb and Brandestini at Proceq SA (the Switzerland company who is a developer, manufacturer and distributor of portable instruments for nondestructive testing of material properties) to provide a portable hardness test for metals. It was developed as an alternative to the unwieldy and sometimes intricate traditional hardness measuring equipment. The first rebound product on the market was named "Equotip" as shown in Fig. 1.5 a dynamic hardness test method and instrument. The traditional hardness measurements likes Rockwell or Vickers are set up in segregated testing areas or laboratories of plants. Samples are cut off from selected parts and measured in the laboratory. It was required to test a very large piece or pieces that are unwieldy to be tested in the usual types of testing machines no alternative was

<div align="center">(A)   (B)</div>

Figure 1.5 (A) First two models of EQUOTIP hardness testers. 1975 series, and (B) series of red hexagonal EQUOTIP, produced between 1978 and 1990 [1-7]

available. Testing parts of fixed structures, or testing under any conditions which require that the indentation force be applied in a direction other than vertical, made the search for portable solutions indispensable. Such hardness testers were initially limited to field tests where the test piece could not be brought to the testing instrument. Meanwhile the portable Leeb rebound hardness mainly used as a portable hardness tester.

An impact device shown in Fig. 1.6(A) containing a permanent magnet and the very hard sphere shape indenter facing towards the surface of the test material. The velocity of the impact body is recorded in three main test phases; First, the pre-impact phase, where the impact body is accelerated by spring force towards the surface of the test piece. Second, the impact phase, where the impact body and the test piece are in contact. The hard indenter tip deforms the test material elastically and plastically and is deformed itself elastically. After the impact body is fully stopped, elastic recovery of the test material and the impact body takes place and causes the rebound of the impact body. Finally, the rebound phase, where the impact body leaves the test piece with residual energy, not consumed during the impact phase. The Leeb method idea was to measure the velocity of the impact body contact-free via the induction voltage generated by the moving magnet trough a defined induction coil mounted on the guide tube of the device.

(A)	(B)
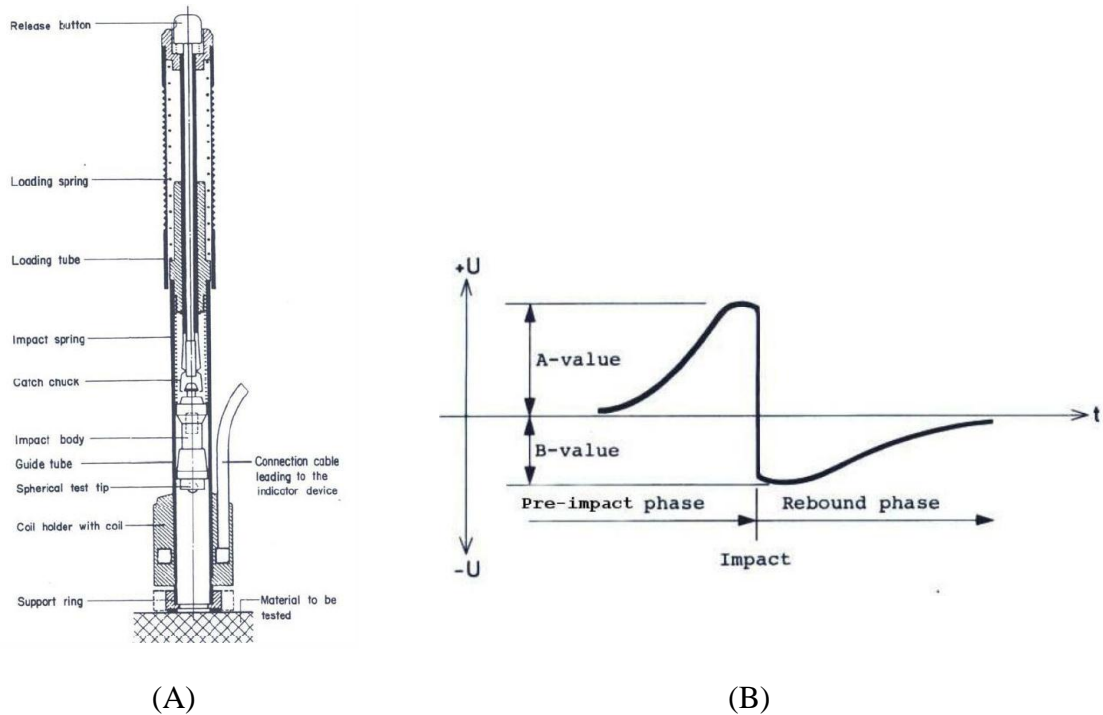
Figure 1.6 (A) Schematic view of the EQUOIP impact device. (B) Typical induction voltage signal generated by the permanent magnet inside the impact body during the main three test phases of an EQUOTIP hardness test [1-7]

The induced voltage is directly proportional to the velocity of the magnet, thus, the impact body containing the magnet. The induced induction signal shown in Fig. 1.6(B) is recorded in an electronic indicator device and the peak induction voltages are further processed to give Leeb.s hardness number, the L-value. The shape of the induction signal is unique for each device type. The L-value, also known as Leeb-number or Leeb hardness(HL), is simply described as equal to the ratio of the rebound velocity v_r to the impact velocity v_i of the impact body, multiplied by 1000 as shown in Eq.1.3.

$$L = \frac{A}{B} \times 1000 \propto \frac{V_r}{V_i} \times 1000 \dots\dots\dots\dots\dots\dots\dots\dots\dots\dots\dots(1.3)$$

The specified impact body represents by impact velocity, impact body mass and overall elasticity the penetration stressing and in form of the rebound velocity v_r the materials response to this penetration. Thus, all information on hardness is available and the L-value is a suitable and direct measure for materials hardness. However, the Leeb hardness test is a superficial determination only measuring the condition of the surface contacted. The results generated at that location do not represent the part at any other surface location and yield no information about the material at subsurface locations [1-8].

7

1.1.3 Indentation hardness test

The Indentation hardness test is determined from the dimension of permanent deformation on the test surface and testing force that makes the deformation. By one of the most common methods of hardness testing (Rockwell), hardness is determined by the depth of the indentation in the test material resulting from application of a given force on a specific indenter. In the Brinell and Vickers hardness test, hardness is determined by the impression created by forcing a specific indenter into the test material under a specific force for a given length of time. It depends on the time of loading, the temperature and other operating conditions. The indentation hardness tests can be divided from testing force into three classes as shown in Fig. 1.7 the macroindentation, microindentation and the nanoindentation test.
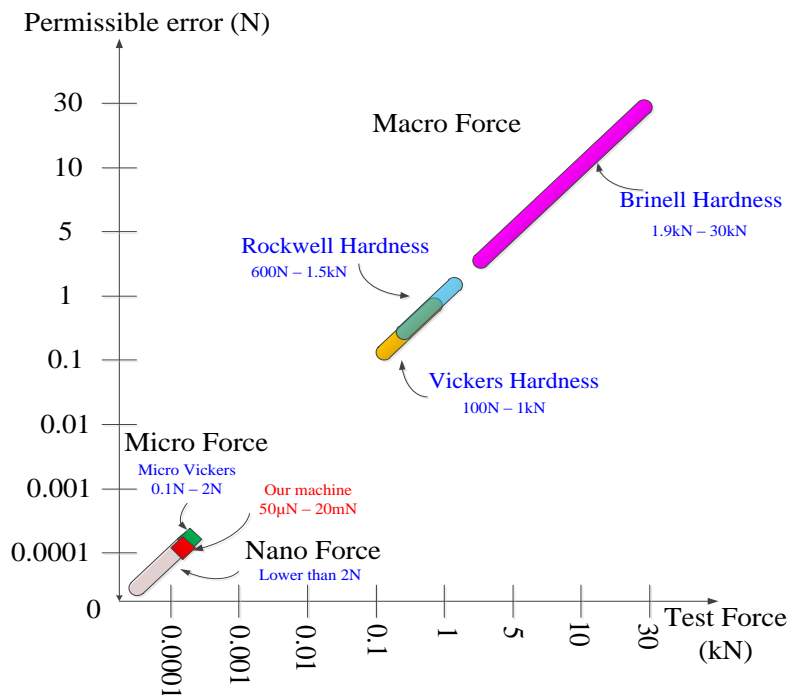
Figure 1.7 Hardness testing force range

1.1.3.1 Macroindentation hardness.

The macroindentation is applied to tests with a larger test load, such as 1 kgf or more. There are various macroindentation tests such as Vickers hardness test (HV), Brinell hardness test (HB), Knoop hardness test (HK), Meyer hardness test, Rockwell hardness test (HR) and Shore hardness test.

1.1.3.1.1 Rockwell hardness

The Rockwell hardness testing method is forcing an indenter (diamond cone steel or hard metal ball) into the surface of test piece in two steps under specified conditions. The Rockwell indenter and the Rockwell hardness block are shown in Fig. 1.8. The Rockwell hardness can be determined by measured the permanent depth h of indentation under preliminary test force after removal of additional test force [1-9].

(A)   (B)

Figure 1.8 (A) The Rockwell indenters. (B) The certified hardness block

The general Rockwell test procedure is shown in Fig.1.9 at first, the indenter is approached the material surface with a preliminary force (F_0) applied. Then hold the constant force for a period of time (dwell time). After that, the indentation depth is mark as a reference first position. Then an additional force is applied to increase the applied force to the total force level (F). The total

(A)   (B)
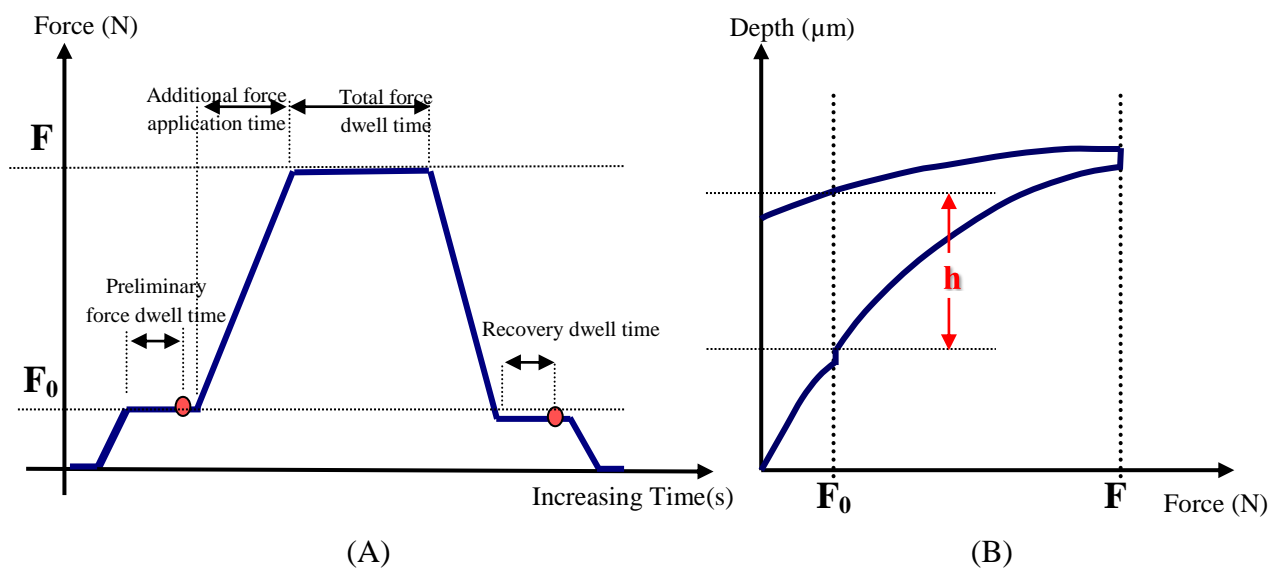
Figure 1.9 (A) Rockwell hardness testing cycle. (B) The indentation depth versus a testing force

force is held constant for a set of time period, after that the additional force is removed. The test force returned to the preliminary force level. After holding the preliminary force constant a set time period, the indentation depth is measured for a second position. Finally, removed the indenter from the test material. The deviation between the first and second indentation depth position, *h* is then used to calculate the Rockwell hardness number.

The Rockwell hardness number is calculated from the difference in the indentation depths before and after application of the total force, while maintaining the preliminary test force. The difference in indentation depths is measured as *h*(in mm). The calculation of the Rockwell hardness number is dependent on the specific combination of indenter type and the forces that are used. For Rockwell scales that use a sphere conical diamond indenter; the regular Rockwell hardness, i.e., HRA, HRC, HRD and the Rockwell Superficial Hardness, i.e., HR15N, HR30N, HR45N is calculated from Eq. 1.4 and 1.5, respectively.

$$Regular\ Rockwell\ Hardness = 100 - \frac{h}{0.002mm} \dots\dots\dots\dots\dots\dots(1.4)$$

$$Rockwell\ Superficial\ Hardness = 100 - \frac{h}{0.001mm} \dots\dots\dots\dots\dots\dots(1.5)$$

For scales that use a ball indenter; the regular Rockwell hardness, i.e., HRB, HRE, HRF, HRG, HRH, HRK and the Rockwell Superficial Hardness, i.e., HR15T, HR30T, HR45T is calculated from Eq. 1.6 and 1.7, respectively.

$$Regular\ Rockwell\ Hardness = 130 - \frac{h}{0.002mm} \dots\dots\dots\dots\dots\dots(1.6)$$

$$Rockwell\ Superficial\ Hardness = 100 - \frac{h}{0.001mm} \dots\dots\dots\dots\dots\dots(1.7)$$

1.1.3.1.2 Vickers hardness

The Vickers hardness test was developed in 1921 by Robert L. Smith and George E. Sandland at Vickers Ltd. It can be used for all metals and has one of the widest scales among hardness tests. It is mostly used for small parts and thin sections. The Vickers hardness is based on as optical measurement. The basic principle is forced a diamond indenter in the form of a right pyramid with the square base and with a specified angle between opposite faces at the vertex into the surface of a test piece. Then measured the diagonal length of the indentation on the test piece surface after removed the indenter. Finally, the average of
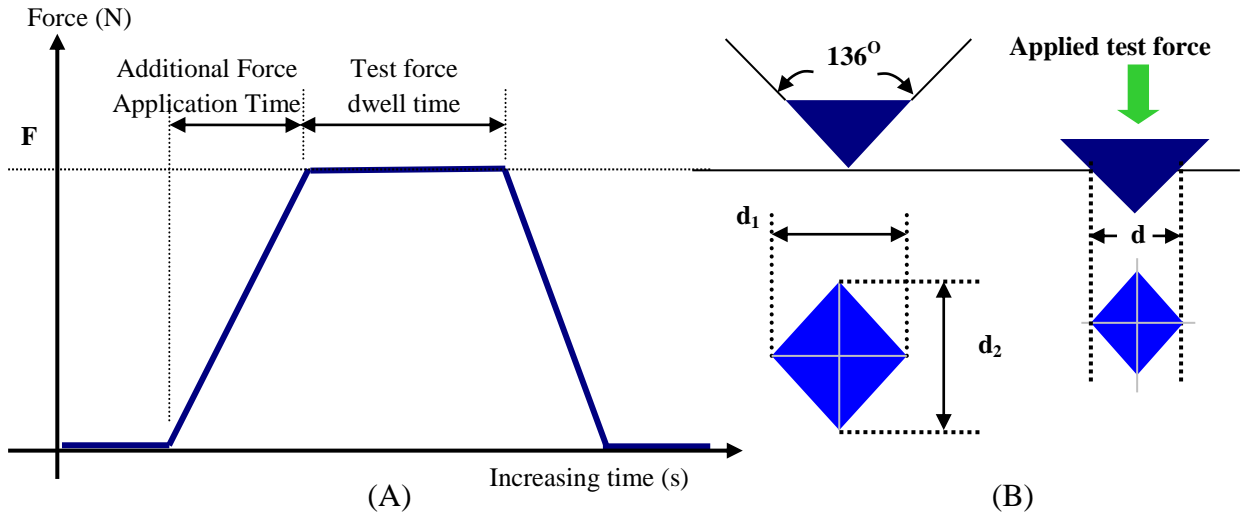
Figure 1.10 (A) Vickers hardness testing cycle. (B) The diagonal of an indentation

diagonal lengths is used to calculate the Vickers hardness number [1-10]. The HV number is then determined by the ratio *F/A* where *F* is the force applied to the diamond in kilograms-force and *A* is the surface area of the resulting indentation in square millimeters. *A* can be determined by the equation as follows:

$$A = \frac{d^2}{2\sin\left(\frac{136°}{2}\right)} \approx \frac{d^2}{1.8544} \dots\dots\dots\dots\dots\dots\dots\dots\dots\dots\dots(1.8)$$

$$HV = \frac{F}{A} \approx \frac{1.8544F}{d^2} \dots\dots\dots\dots\dots\dots\dots\dots\dots\dots\dots(1.9)$$

Where;

F is the testing force (N).

d is an arithmetic mean of the two diagonals length d_1 and d_2 (mm)

When the mean diagonal of the indentation has been determined the Vickers hardness may be calculated from the formula, but is more convenient to use conversion tables. The Vickers hardness should be reported like 800HV/10, which means a Vickers hardness of 800, was obtained using a 10kgf force. Several different loading settings give practically identical hardness numbers on uniform material, which is much better than the arbitrary changing of scale with the other hardness testing methods. The advantages of the Vickers hardness test are that extremely accurate readings can be taken, and just one type of indenter is used for all types of metals and surface treatments. Although thoroughly adaptable and very precise for testing the softest and hardest of materials, under

11

varying loads, the Vickers machine is a floor standing unit that is more expensive than the Brinell or Rockwell machines. The Vickers hardness can be converted in SI units (MPa or GPa) by multiply 9.807 for HV to MPa, and multiply 0.009807 for HV to GPa.

1.1.3.2 Microindentation hardness

The microindentation tests [1-11, 1-12] typically have forces up to 2N and produce the indentations about 50μm. It has been widely employed in the literature to describe the hardness testing of materials with low applied loads. It can be used to observe changes in hardness on the microscopic scale. Unfortunately, it is difficult to standardize microhardness measurements, i.e., it has been found that the microhardness of almost any material is higher than its macrohardness. Additionally, microhardness values vary with load and work-hardening effects of materials [1-13]. A basic principle of a microhardness is impressed a diamond indenter of specific geometry into the surface of the test specimen using a known applied force from 1 to 1000 grams force (gf). The hardness number is based on the surface area of the indentation divided by the applied force, a hardness units in kgf/mm² can be given. The two most commonly used as a microhardness tests are the Vickers hardness test (HV) and the Knoop hardness test (HK).

The Knoop hardness test was developed by at the National Bureau of Standards (NIST) in 1939[1-14]. The indenter used is a pyramidal diamond that produces an elongated diamond shaped indentation. It is particularly used for very stiff materials or thin sheets, because the elongated pyramid only creates a shallow impression.

The basic principle is pressed the pyramidal diamond indenter into the polished surface of the test material with a known force, for a specified dwell time, normally 10 - 15 seconds. The tests are mainly done at test forces from 10gf to 1000gf, so a high powered microscope is necessary to measure the resulting indentation size. After the dwell time is complete, the indenter is removed leaving an elongated diamond shaped indent in the sample. The size of the indent is determined optically by measuring the longest diagonal of the diamond shaped indentation. The Knoop hardness number is a function of the test force divided by the projected area of the indent. The diagonal is used in the following formula to calculate the Knoop hardness. The geometry of this indenter is an extended pyramid with the length to width ratio being 7:1 and

respective face angles are 172 degrees for the long edge and 130 degrees for the short edge as shown in Fig. 1.11(B). The depth of the indentation can be approximated as 1/30 of the long dimension [1-15]. The Knoop hardness *HK* or *KHN* is then given by the equation as follows:

$$HK = \frac{load(kgf)}{indentation\ area(mm^2)} = \frac{P}{C_p L^2} \dots\dots\dots\dots\dots\dots\dots(1.10)$$

Where;

L is the length of indentation along its long axis(mm).

C_p is the correction factor related to the indenter geometry and the units of force and diagonal, ideally 0.070279. *P* is the testing force (kgf)[1-16].

The Knoop number normally ranges from HK60 to HK1000 for metals, will increase as the sample gets harder. A typical Knoop hardness is specified as 650HK0.5, where; 650 is the calculated hardness. 0.5 is the test force in kg.
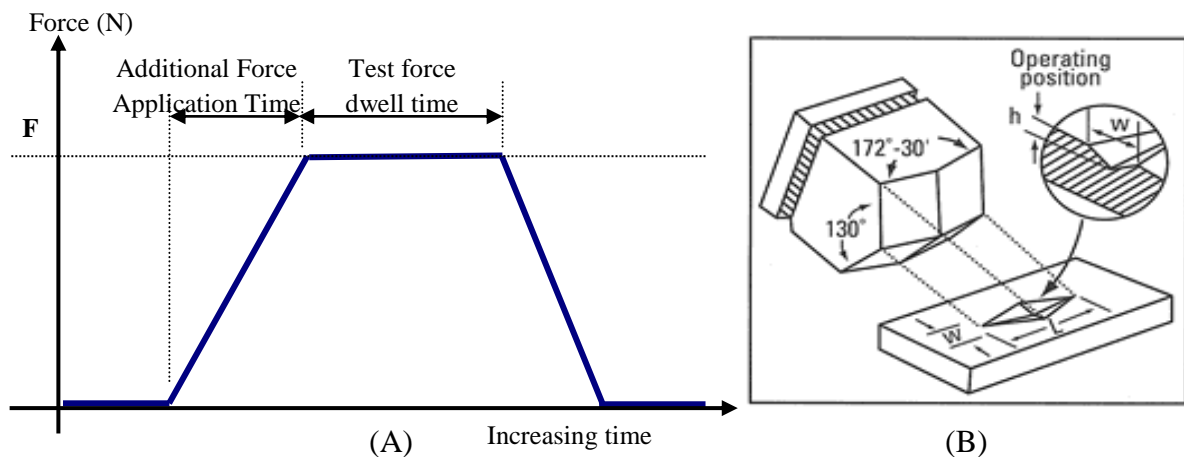
Figure 1.11 (A) Knoop hardness testing cycle. (B) The Knoop indenter and the indentation

1.1.3.3 Nanoindentation hardness

The nanoindentation [1-17, 1-18] techniques used to obtain mechanical properties from very small volumes of material. This method was developed to measure the hardness and elastic modulus of a material from indentation load–displacement data obtained during one cycle of loading and unloading. Nanoindentation test typically have forces lower than 2N. It is originally applied with the Berkovich triangular pyramid indenter as shown in Fig. 1.12. However, Oliver and Pharr [1-18] have realized that it can be applied to a variety of axisymmetric indenter geometries including the sphere. A schematic depiction

13
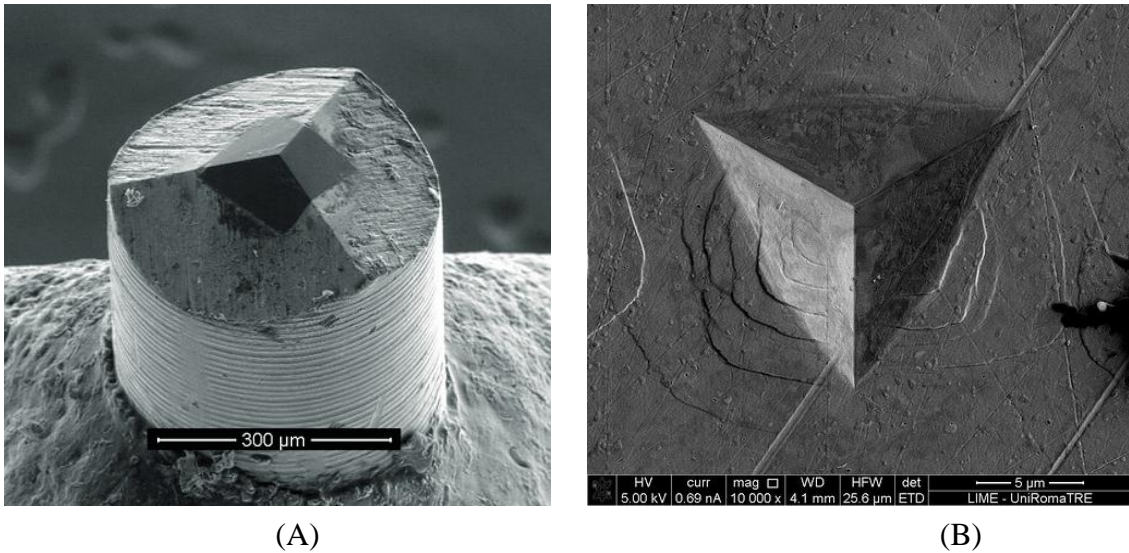
Figure 1.12 (A) Berkovich indenter tip. (B) The Berkovich indentation observed by SEM

of a typical data set obtained with a Berkovich indenter is shown in Fig. 1.13(A) where the parameter P defines the testing load and the displacement h qualified to the initial un-deformed surface. During loading, the deformation is supposed to be both elastic and plastic as the permanent hardness impression forms. It is assumed to be only the elastic displacements are recovered during unloading. The deformation of the material under test is the elastic natures of the unloading curve. There are three important quantities that must be measured from the P-h curves, i.e., the maximum load P_{max}, the maximum displacement h_{max}, and the
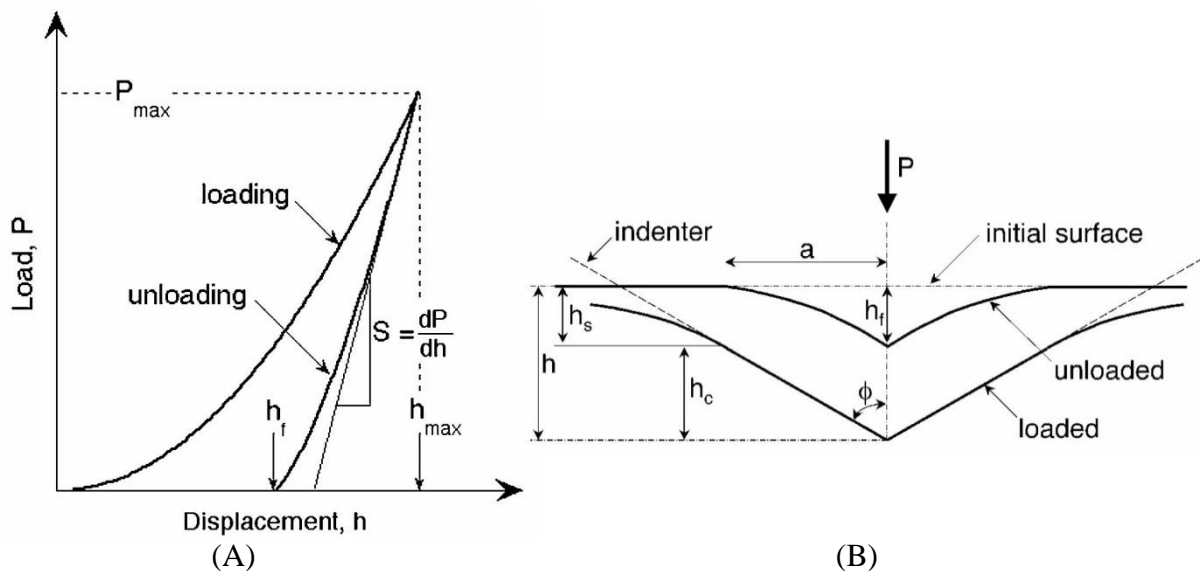
Figure 1.13 (A) Schematic illustration of indentation load–displacement data showing important measured parameters. (B) Schematic illustration of the unloading process showing parameters characterizing the contact geometry [1-18]

14

elastic unloading stiffness $S = \mathrm{d}P/\mathrm{d}h$. There are defined as the slope of the unloading curve during the first stages of unloading (also called the contact stiffness). The accuracy of hardness and modulus measurement depends on how well these parameters can be measured. Another important quantity is the final depth h_{f}, the permanent depth of penetration after the indenter is fully unloaded. The analysis used to determine the hardness H, and elastic modulus E, is principally the method proposed by Doerner and Nix [1-19]. Their method is less complicated because it is a linear curve fit of the selected minimum to maximum data. However, it is limited because the calculated elastic modulus will decrease as more data points are used along the unloading curve. The Oliver-Pharr [1-18] nonlinear curve fit method to the unloading curve data is usually well approximated as the power law relation given by:

$$P = \alpha\left(h - h_f\right)^m \dots\dots\dots\dots\dots\dots\dots\dots\dots\dots..(1.11)$$

Where;

h is the variable depth.

h_f is the final depth.

α and m are power law fitting constants.

The exact procedure used to measure H and E is based on the unloading processes shown in Fig. 1.13(B). It is assumed that the behavior of the Berkovich indenter can be modeled by a conical indenter with a half-included angle ϕ, that gives the same depth to area relationship $\phi = 70.3°$. The basic assumption is that the contact edge sinks-in manner can be described by models for indentation of a flat elastic half space by rigid indentions on a simple geometry [1-20 to 1–28]. However, this assumption is only described the sinks-in behavior at the contact edge. It does not define the pile-up of material at the contact edge, which is occurred in some elastic–plastic materials. Assuming that pile-up is negligible, the elastic models that show the amount of sink-in h_{s}, is given by:

$$h_s = \epsilon\,\frac{P_{max}}{S} \dots\dots\dots\dots\dots..\dots\dots\dots\dots\dots.(1.12)$$

Where;

ϵ is a constant, which depends on the geometry of the indenter.

Using Eq. (1.12) to approximate the vertical displacement of the contact edge, it follows from the geometry shown in Fig. 1.12(B). That the depth along the contact area is made between the indenter and the specimen $h_c = h_{max} - h_s$, is:

$$h_c = h_{max} - \epsilon \frac{P_{max}}{S} \dots\dots\dots\dots\dots\dots\dots\dots\dots(1.13)$$

Assuming that *F(d)* is an area function (the indenter shape function) describes the cross sectional area of the indenter at a distance *d* back from its tip, the contact area *A* is:

$$A = F(h_c) \dots\dots\dots\dots\dots\dots\dots\dots\dots\dots\dots..(1.14)$$

This function must carefully be calibrated because the deviations from non-ideal indenter geometry are caused the accuracy of the contact area. These deviations can be quite severe near the Berkovich indenter tip, where some rounding predictably occurs during the grinding process. Although a basic procedure for determining the area function was presented as part of the Oliver-Pharr's original method [1-25], new improved [1-18] have made significant changes to it in recent years. The hardness can be given by the equation below, relating the maximum load to the indentation area.

$$H = \frac{P_{max}}{A} \dots\dots\dots\dots\dots..\dots\dots\dots\dots\dots.(1.15)$$

This definition of hardness may deviate from the traditional hardness measured, if there is significant elastic recovery during unloading. Because the relation is based on the contact area under load applied not the residual hardness impression. However, this is dominate only in extremely small values of *E/H* materials [1-26]. The slope of the curve, *dP/dh*, upon unloading is indicative of the stiffness *S* of the contact can be given by:

$$S = \beta \frac{2}{\sqrt{\pi}} E_{eff} \sqrt{A} \dots\dots\dots\dots\dots\dots\dots\dots(1.16)$$

Where;

β is a geometrical constant. In the original method for measuring hardness and modulus, the dimensionless parameter β was taken as unity.

A is the projected area of the indentation.

E_{eff} is the effective elastic modulus defined by

$$\frac{1}{E_{eff}} = \frac{1-v_s^2}{E_s} + \frac{1-v_i^2}{E_i} \dots\dots\dots\dots\dots\dots\dots\dots..(1.17)$$

Where;

E_i and ν_i is the elastic modulus and the poisson's ratio of the indenter, for diamond indenter tip E_i is 1140 GPa and ν_i is 0.07. The Poisson's ratio of the specimen ν_s, generally varies between 0 and 0.5 for most materials and is typically around 0.3.

The nanoindentation technique has been widely used to evaluate mechanical properties of materials at the micro and nano-scale, especially hardness and elastic modulus. It can be used to characterize organic, inorganic, soft or hard materials and coatings. Examples are thin and multilayer PVD, CVD, PECVD, photoresists, paints, lacquers, and many other types of films and coatings. Bulk material surface mechanical characterization can also be performed on hard or soft materials, including metals, semiconductors, glasses, ceramics, composites, biomimetic and in vitro biomaterials. The accuracy and precision of the data are assured by having the lowest thermal drift currently available of any nanoindentation [1-27].

1.2 Loading methods and mechanism of indentation hardness machine

One of the most important parameters in any hardness machines is the loading method and the mechanism of the machine. The loading mechanism and force sensor have been improved significantly over the last 20 years. There are two typically type of the loading method used in recent day, the deadweight type and the electronic force type. The deadweight type is the most accurate and high long term stability of the generated force. However, for a very low force scale (lower than 2N) is very difficult to control, because the friction is dominate. Each loading method might suitable for another hardness testing method described as follows.

1.2.1 Deadweight type

The traditional hardness testers employ the deadweight systems. It is very simple and reliable method to apply and hold the testing force. With respect to operating convenience, deadweight type does not require a power source and can generate a stable and precise output pressure to be applied. Especially, if high testing force range is required. The deadweight system utilizes a series of

incremental, stacked weights in conjunction with a lever and pivot point to apply a magnified test force at the indenter. Minor loads are applied by spring or small weight.

The loading methods of hardness machines are different as forces necessary for various hardness testing methods are different. In general, the hardness machines are built for the different testing methods, such as; Rockwell, Vickers or Brinell. As shown in Fig. 1.14 is the principle of a deadweight Rockwell and Vickers machine. The Rockwell testing method (60, 100 and 150kgf) differ from the Vickers (187.5kgf) and Brinell (3000kgf) by employing a preliminary test force. The Vickers and brinell machines are required only a single force step. Deadweight type have been performing hardness indentations since the Rockwell hardness test was developed in and are still a popular and efficient way to perform a hardness test. In general, deadweight type is more precise devices providing very low uncertainties based on percent of reading rather than full scale. However, for a very large force hardness test methods are not a problem to of the deadweight application, but for very low force hardness test methods likes Microvickers, Knoop or nanoindentation (lower than 2N), the spring or counter weight have are required. This counter weight might cause a mechanical friction and may the source of pour generated force long term stability. It also very difficult to control applying the weights in a deadweight system. To apply the test force, the weight has to be moved, and stopping it quickly without overload and oscillation creates a problem. Recently, the

(A)   (B)
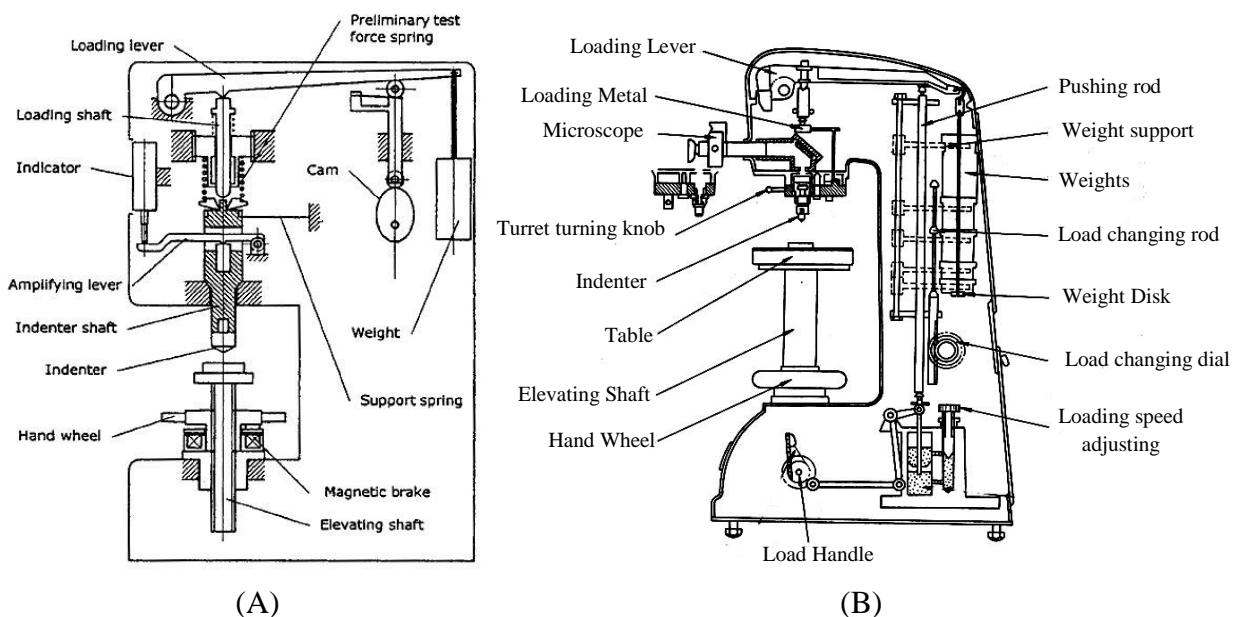
Figure 1.14 Loading mechanism of (A) Rockwell machine and (B) Vickers machine

electronic force generator techniques have been developed as an alternative method of load application. Moreover, it is very difficult to make such nanoindentation test force with the deadweight type.

1.2.2 Electronic force type

The electronic force is an innovator technology that utilizes motor/encoder control and a load cell or force transducer to apply and regulate the load. It can constantly monitor and adjust the applied force. Moreover, eliminating force errors and increasing tester accuracy and repeatability. The closed-loop control schematic diagram shown in Fig. 1.15(A) is a very simple generated and controlled force system. It is composed of the microcontroller that controls an actuator drives the indenter which is attached at the end of loadcell down to the specimen. It means that during applying force, the indentation force can be monitored and controlled in the same time. As shown in Fig. 1.15(B) the electronic force hardness tester from Wilson hardness an Instron company. This Rockwell machine can generate force from 3kgf up to 150kgf with very small overall structure.

(A)   (B)
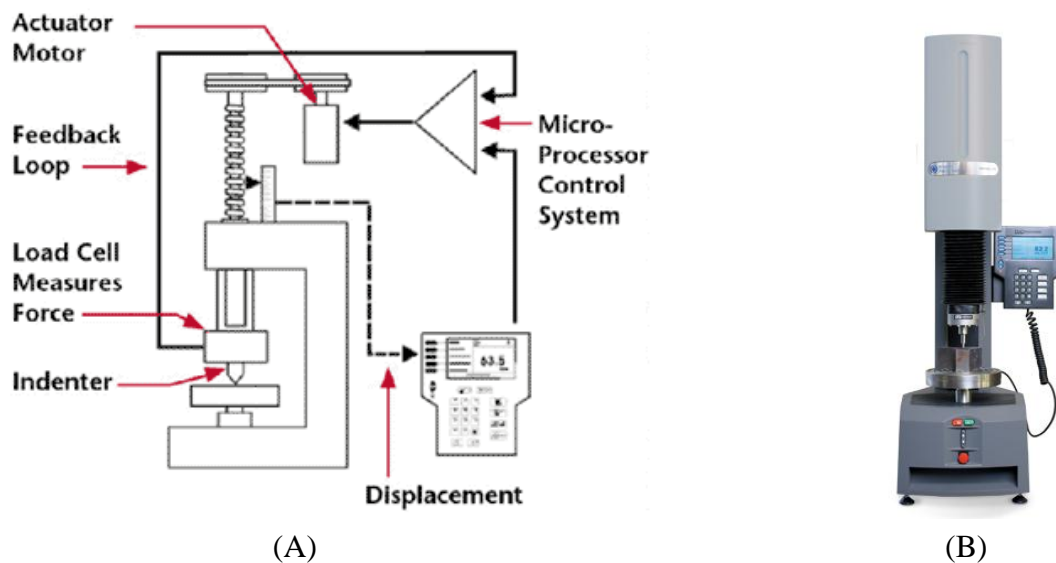
Figure 1.15 (A) Electronic force closed-loop control diagram. (B) Rockwell 2000 series hardness tester from Wilson hardness an Instron company [1-28]

Regarding to the nanoindentation hardness [1-29] there are various mechanisms and methods that have been designed to complete nanoindentation hardness tests. One method of force application was introduced by Pethica [1-30] in 1983. The basic principle is using a coil and a permanent magnet assembly on a loading column to drive the indenter downward as shown in Fig.

<center>(A)   (B)</center>
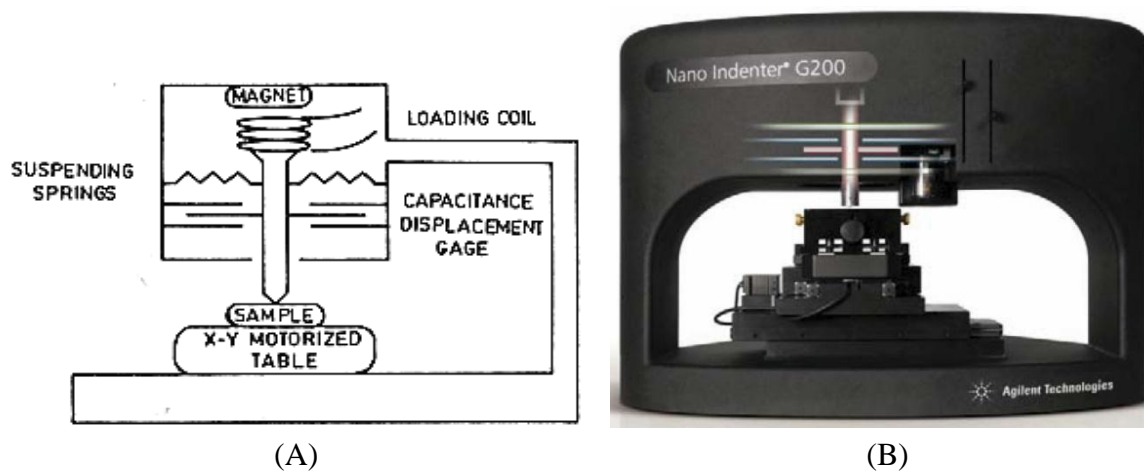
Figure 1.16 (A) Electronic force loading mechanism for nanoindentation, an electromagnetic actuation.[1-2] (B)The Nano-Indenter G200 from Agilent company[1-31]

1.16(A). This configuration looks familiar the driver from an audio speaker, voice coil actuator (VCA). By varying the current (*I)*, through the coil, a magnetic field is generated that interacts with the magnetic field of the permanent magnet. The loading column is suspended by springs, which damps external motion and allows the load to be released slightly to recover the elastic portion of deformation before measuring the indentation depth. In Fig. 1.16(B) is shown the commercial nanoindentation machine from Agilent Company, the Nano-Indenter G200. This machine using the electromagnetic actuation that can produce the testing force up to 10N (required high load option) with 50nN generated force resolution.

Another force actuation method using the electrostatic force was proposed by Lilleodden et al [1-32] in 1995. The basic principle mechanism structure is shown in Fig. 1.17(A). In this method the test force is produced by an electrostatic force generated between the center plate and the upper or lower plate of a three-plate transducer system, i.e., by applied AC signals 180° out of phase with each other to the top and bottom plate. The applied load is proportional to the square of the voltage, the AC signals are picked up by the center (floating) plate and the sum of the signals corresponds to a displacement of the plate. To apply a load, a DC voltage offset is applied to the lower plate of the transducer that electrostatically attracts the center (floating) plate downward [1-33]. In Fig. 1.17(B) is shown the commercial nanoindentation machine from Hysitron Company, the TI 950 TriboIndenter. This machine using an electrostatic actuation that can produce the testing force from 30nN up to 10N (with dual head option) with 1nN resolution.

(A)   (B)
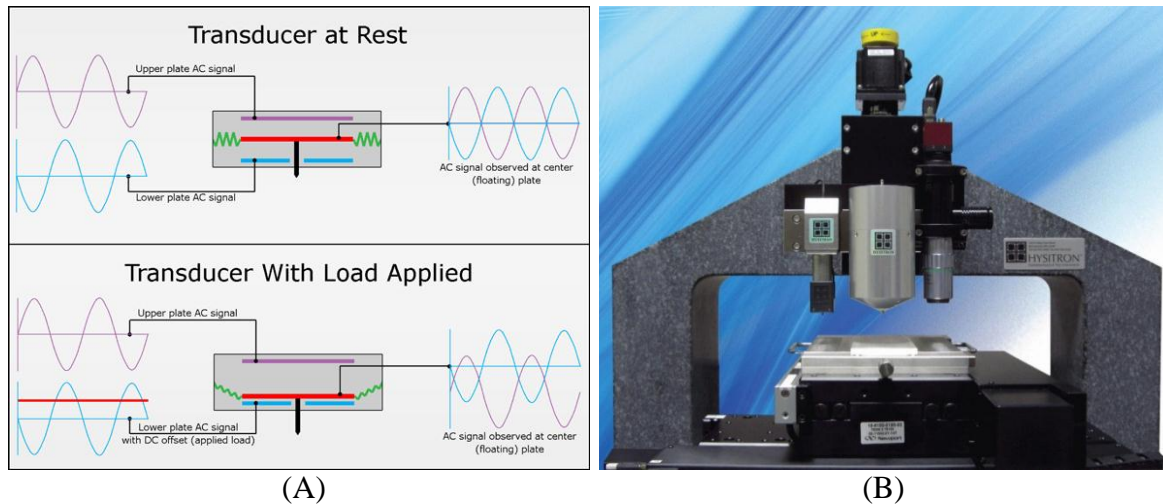
Figure 1.17 Electronic force loading mechanism for nanoindentation by using (A) electrostatic actuation and (B) the spring-based force actuation [1-33]

(A)   (B)   (C)
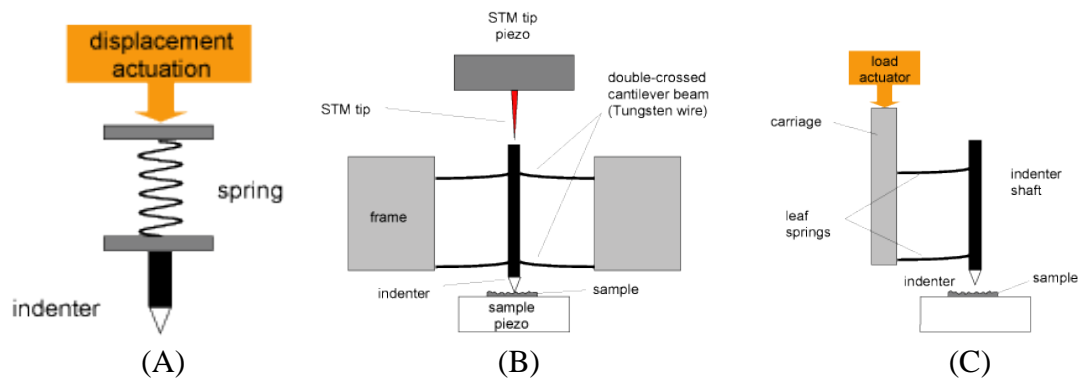
Figure 1.18 (A) Electronic force loading mechanism for nanoindentation by using load trough spring actuation. (B) The spring-based force actuation. (C) The long range piezo driver and elastic element [1-29]

Another method for produces force is the application of load through spring technique. The indenter shaft and the indenter tip are attached and support by spring while the displacement actuator generates pushing force as shown in Fig. 1.18(A). In 1989, Burnham and Colton [1-34] were propose another actuation by using a piezo actuator incorporates with a set of crossed wires as shown in Fig. 1.18(B). The indenter is supported by double crossed cantilever beam (tungsten wire) and push down by the piezo actuator pass through the scanning tunneling microscopy (STM). In 1992, Bell et.al [1-35] was proposed another approach technique by using the load trough spring method. As shown in Fig. 1.18(C) the indenter shaft and the indenter tip is attached with long range piezo driver and an elastic element. When the indenter is moved downward by the piezo driver, the elastic element resists the movement and creates a force.

Not only an electronic force type able to constantly measure the test force being applied, but the components used in this type inherently advance themselves to a much simpler design than those in a dead-weight type. As mentioned, dead-weight systems require levers, pivots and other friction-inducing components to function efficiently (see Fig. 1.14). On the other hand, an electronic force system's main component is a load cell or stain gauge. This compact, low-weight device provides an electronic output proportionate to the force applied to it. With this design, sources of error between the indenter and the test force are eliminated. For example, friction in the actuator is so excessive that the desired force is not applied to the indenter, i.e., the load cell constantly checks itself to make certain that only the correct test forces are applied to the indenter.

Even though, the electronic force type is very easy to control the generated force. It may be used in place of deadweight type because they may be cheaper and offer more portability. However, deadweight type still provides advantages that must be considered. Moreover, deadweight testers are generally less susceptible to environmental temperature effects on performance accuracy.

1.3 Equipment to measure indentation depth

Another influence factor for hardness measurement is the depth measuring device [1-29], because high accuracy of the depth measurement provides high position of hardness value. The lever actuated dial gauge employed for indentation depth measurement on commercial Rockwell hardness testers (Fig. 1.19). Meanwhile, most Rockwell standardizing machines were employed the
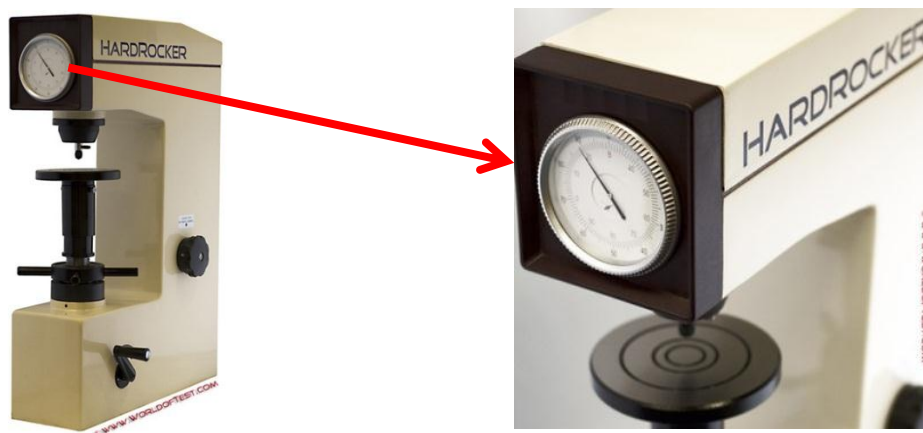
Figure 1.19 The commercial hardness testing machine illustrate the dial gauge, equipment for indentation depth measurement[1-36]

measuring microscopes for measuring indentation depth. For Vickers and Brinell machines, the indentation depth during an indenting process is not necessary, because the hardness value from these methods are the dimensions size of the indentation.

The nanoindeatation described a hardness value by the relation between indentation depth and impressed force during an indentation process. The high accuracy and resolution depth measuring device required to be used. The capacitive sensor technique shown in Fig. 1.19(A) is one of the high resolution displacement measurements. The basic structures composed of two capacitors with three metal plates are placed with a small gap between them and a voltage is applied to the plates, an electric field will exist between the plates. This electric field is the result of the difference between electric charges that are stored on the surfaces of the plates. The amount of existing charge determines how much current must be used to change the voltage on the plate. The capacitance between two plates is determined by the plates size, a gap size and the material between plates (dielectric). In practically capacitive sensor, the plates size and the dielectric material (air) remain constant. The only variable is the gap size. Based on this assumption, the different between C_1 and C_2 are results of the gap sizeΔ. The capacitive sensor technique can provides high precision of displacement with very small foot print. As shown in Fig. 1.20(B) is the layout of nanoindentation machine employed with capacitive gauge for measure the indentation depth. [1-37]

Another displacement sensor commonly used is the linear variable differential transformer (LVDT) [1-38]. The principle layout is shown in Fig. 1.21(A). It composed of three coils, a primary coil (A) placed at centered

(A)   (B)
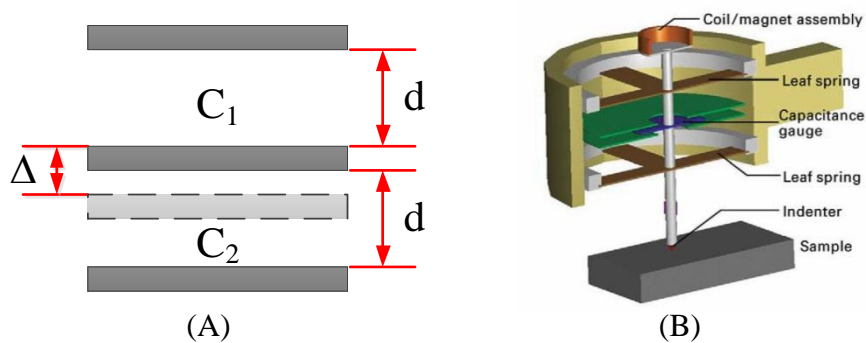
Figure 1.20 (A) Capacitive sensor and (B) the differential capacitor technique for measure the indentation depth [1-31]
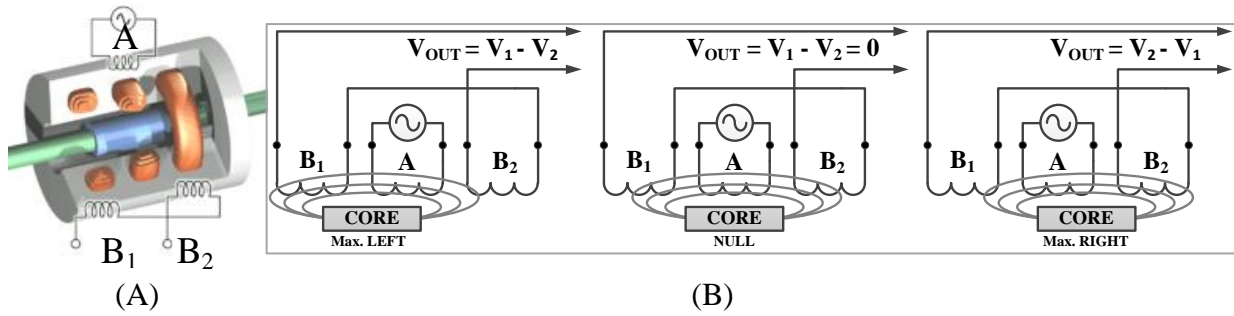
Figure 1.21 (A) Cutaway view of the LVDT [1-38]. (B) And the differential voltage output varies with core position [1-39]

between a pair of secondary coils (B1 and B2), symmetrically spaced about the primary. The cylindrical ferromagnetic core moving inside those coils, attached to the object whose position is to be measured. In Fig. 1.21(B) [1-39] when the LVDT's core is in different axial positions, current is driven through the primary coil with a constant amplitude AC source causing an induction current to be generated through the secondary coils, B_1 and B_2. The magnetic flux thus developed is coupled by the core to the nearby secondary coils, B_1 and B_2. If the core is located midway between B_1 and B_2, equal flux is coupled to each secondary so the voltages, V_1 and V_2, induced in coils B_1 and B_2 respectively, are equal. At this reference midway core position, known as the null point, the differential voltage output, $(V_1 - V_2)$, is essentially zero. Besides, if the core is moved closer to B_1 than to B_2, more flux is coupled to B_1 and less to B_2, so the induced voltage V_1 is increased while V_2 is decreased, voltage output is resulting in the differential voltage $(V_1 - V_2)$. On the other hand, if the core is moved closer to B_2, more flux is coupled to B_2 and less to B_1, so V_2 is increased as V_1 is decreased, voltage output is equal to $(V_2 - V_1)$. When compare between LVDT and Capacitance gauge, the measurement range of the LVDT is larger. However, the capacitance gauge has better measurement resolution. In Fig. 1.22
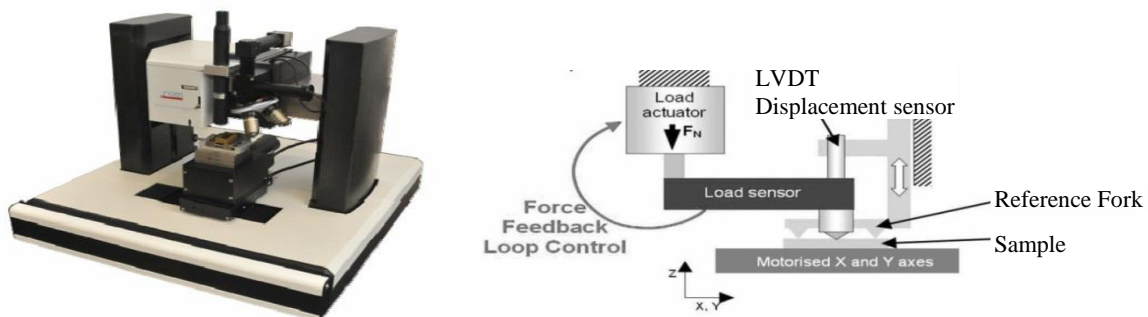
Figure 1.22 The CSM microscratch test, MST employed the LVDT to monitor the penetration depth [1-27]

24

has shown the CSM microscratch test machine. This machine is an open platform, can be operated in various including microindentation with monitor the indentation depth by the LVDT.

For the cantilever based system, the laser displacement sensors are the best selective depth measuring device (Fig. 1.23(A)). Because non-contact style, not affect to weight or vibration of the stylus. Another non-contact depth sensor is the laser interferometer. The basic principle is shown in Fig. 1.23(B). A linearly polarized laser beam passes through a λ/4 retarder (a quarter-wave plate) and it becomes circularly polarized. Then pass through a polarizing beam-
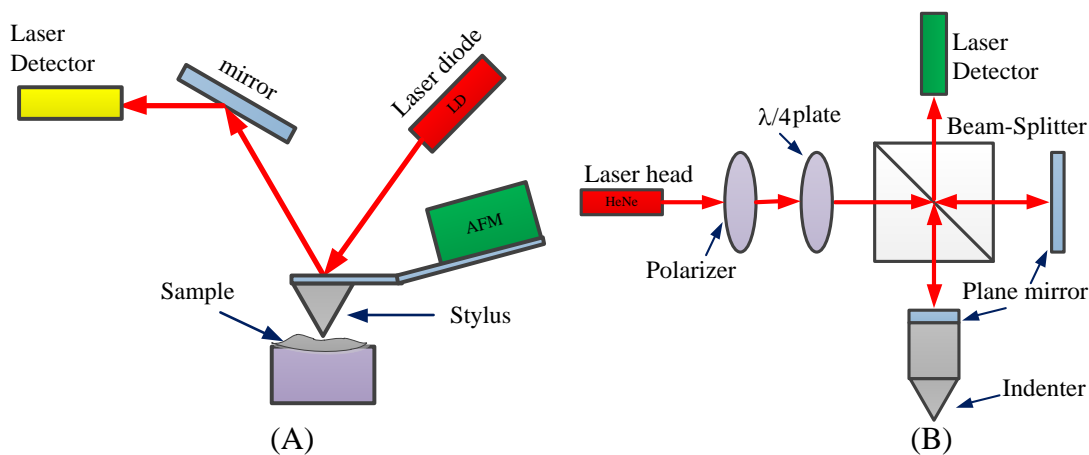
Figure 1.23 (A) The optical lever method application on cantilever based system [1-29]. (B) Laser interferometer setup to measure the indentation depth
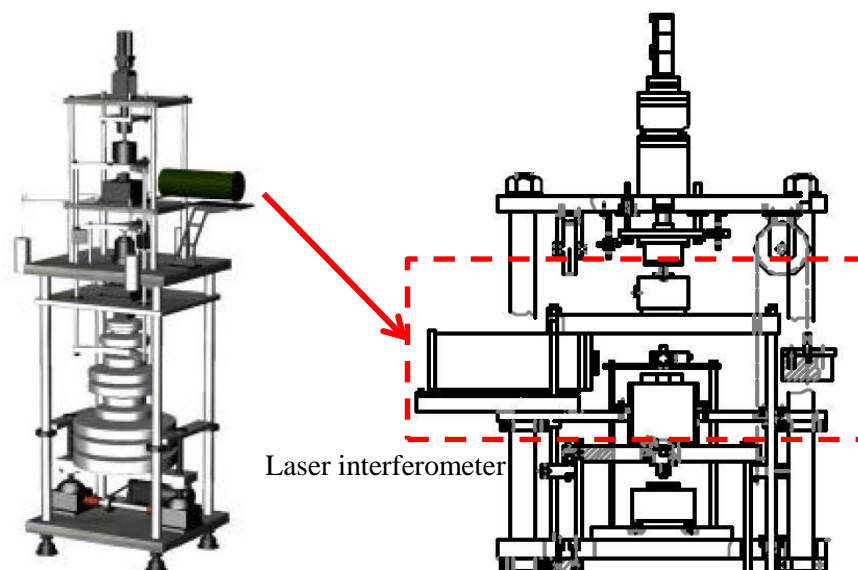
Figure 1.24 The hardness calibration machine employed laser interferometer to measure the indentation depth [1-40]

splitter then splits the output beam into reference mirror and the moving mirror (indenter). Then reflex back and interfere at the beam-splitter, after that pass through the detector. This phase information can then be used to deduce direction and therefore the position of the moving mirror (indenter).The resolution of laser measurement method depends on the wave length(λ) of the laser used. For example, by using the HeNe laser ($\lambda \approx 632.8nm$) in the interferometer system, the simple measurement resolution can be reached 300nm($\lambda/2$). The laser interferometer also increasingly employed in the Rockwell standardizing machine. For example, the deadweight type hardness calibration machine model HSM-RV (Fig. 1.24) employed the laser interferometer to measure the indentation depth. The manufacturer has claimed the depth resolution at $0.01\mu m$ (10nm).

1.4 Research motivation

As mention before, the hardness test has been widely used for determine the strength property of material for nearly hundred years. The conventional hardness (Rockwell, Vickers or Brinell) can be used with a large specimen or high stiffness materials. Recently, the size of materials and machined components to be checked keep decreasing because down-sizing trends of products. In term of conventional hardness testing methods, the indentation depth or the dimension size of the indenter imprint are used to calculate hardness. So, the accuracy of hardness depends upon a measuring device. For microscale or bio materials, the force applied in hardness testing should be as low as possible because the stiffness of these materials are also very low. Therefore, it is difficult to obtain good accuracy in material properties using the conventional hardness testing machine. For these reasons, nanoindentation testing is becoming very important for determining the mechanical properties of such bio materials especially materials in microscales. The nanoindentation testing method is similar to the conventional hardness test in that it requires pressing an indenter of known geometry and mechanical properties under predefined conditions into the test material. It provides a continuous record of variation in testing force as a function of indentation depth when the indenter penetrates the specimen. The slope of the unloading curve has commonly been used for calculate elastic modulus as discussed in Section 1.1.3.3. In order to achieve such a microhardness test, the loading force of the indenter should be applied precisely to the material without shock or vibration. There are a number of mechanisms and methods for nano and microforce range generators as

discussed in Section 1.2. Each method has its distinct advantages and disadvantages.

Recently, many commercial nanoindentation machines [1-41 to 1-43] have been available in the market. However, those machines come with huge structures that cause thermal drift as well as cost problems. As shown in Fig. 1.25 the typical size of the commercial machine is approximately 500mm in height and the arm length is around 300mm, which is made of some metals. Then with 1 degree temperature change, the uncertainty is about 5μm. Thus, these machines should be installed in such a special temperature controlled room, where the temperature change is less than 0.1 degree. The size of our small robot is approximately 2 cubic inch, and then the measurement uncertainty might be less than 0.5μm even the temperature change of 1 degree. Generally speaking, when the size of machine becomes one tenth, then one tenth uncertainty from the thermal effect can be expected. Furthermore in the case of biological applications or some other kinds of applications that require a special chamber, most commercial machines are too large to be implemented in a small chamber. Recently, microrobot technologies have become well known, i.e., microrobots has fine mobility with microscopic resolution and can work in small areas [1-44 to 1-47].
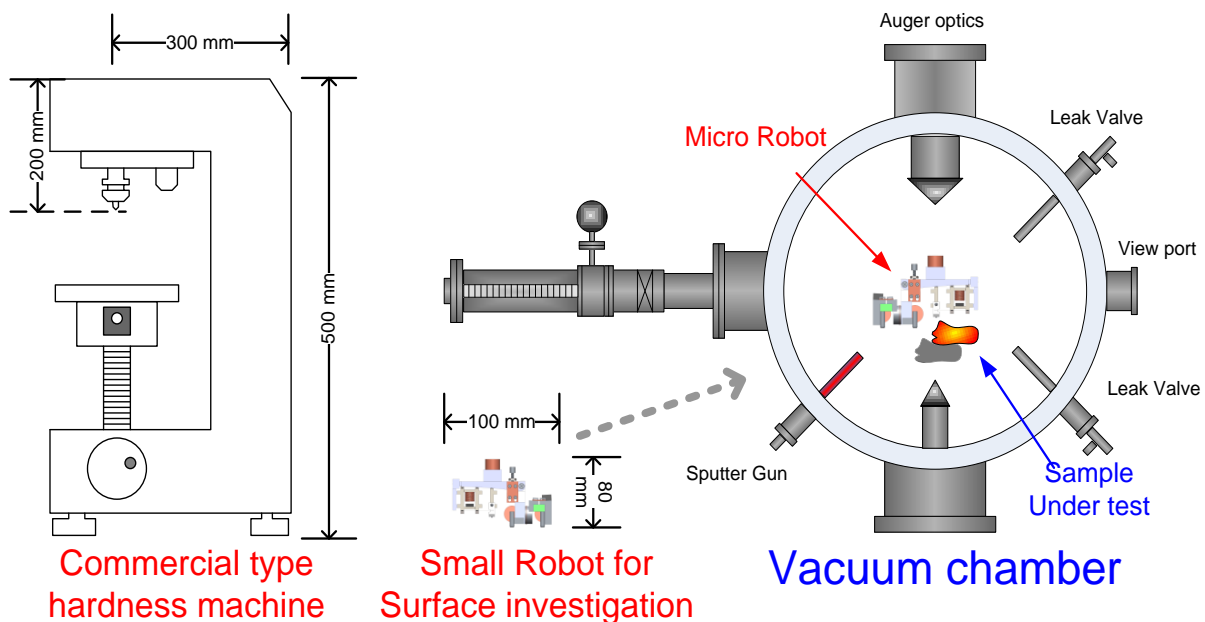
Figure 1.25 approximately size comparison between the commercial type hardness machine and the original microsurface investigation robot. The robot aim to operate inside small chamber
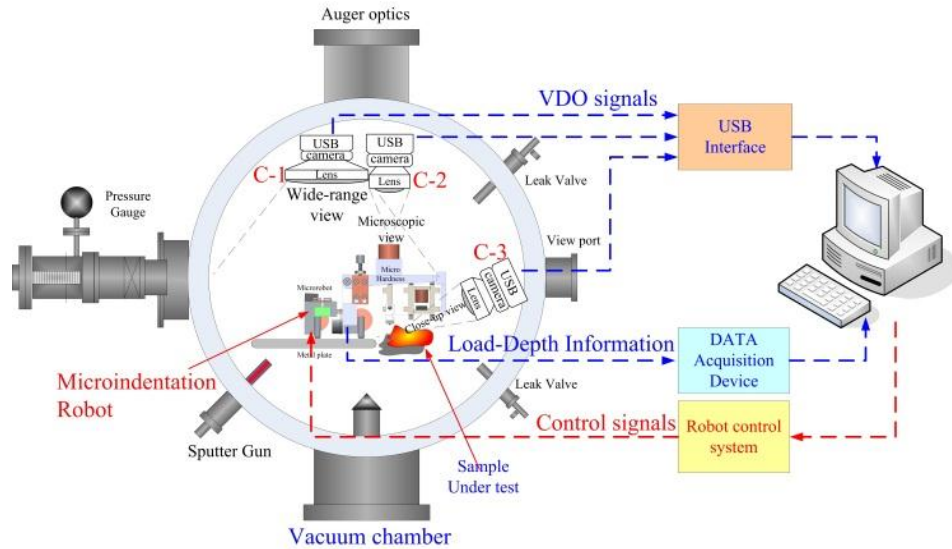
Figure 1.26 Microdiagnostics robot with hardness and stiffness testing navigation based on multiple vision images
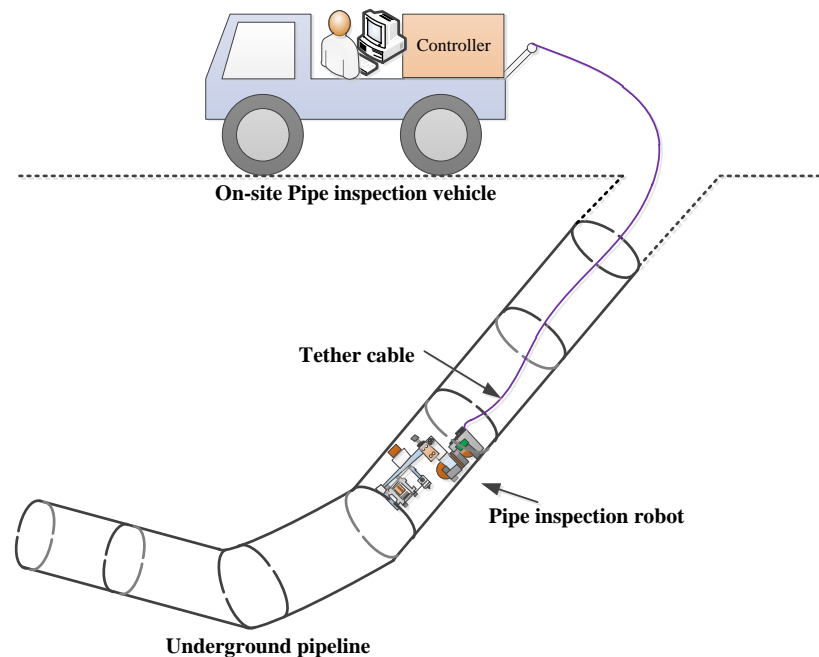
Figure 1.27 On-site service for underground pipeline inspections

As the first step in this research, we focus on fabricating a microhardness and stiffness measuring system with a couple of downsized instrumentation designs and microrobotics. In our final application, this unique measurement system with very small body and high mobility can be employed for purposes such as performing microsurface investigation in a special chamber. With the help of an image processing technique, the vision based coordination system with the local close-up view and the overall global view has been developed to identify the locations of small robot and the indenter precisely with high

28

accuracy over the working range. As shown in Fig.1.26, the conceptual view of the down-sized instrumentation microhardness and stiffness measuring robot with the position control by multi vision images navigation is presented.

Moreover, the mobility of this robot can be given an advantage point in the situation that the material to be tested is installed inside the small area such as the underground pipeline system. Recently, many troubles occur in pipelines because corrosion, cracks and mechanical damages from the unexpected reasons. To maintenance such pipelines are very difficult because most of the problems are occurred inside the pipe material. With the mobility and capability of this robot, it can make an inspection along the pipe surface inside the pipeline. And then the material problems can be identified. The conceptual view of the pipe inspection robot as shown in Fig. 1.27.

This research is organized as follows; Section 2 introduces the microindentation mechanism, as well as the machine layout and configuration including the basic performance. Section 3 presents the compact size piezo-driven microrobot including its basic performance. After that the combination between the microindentation mechanism and the microrobot will be described. Section 4 describes the vision based navigation system for tracks and controls a microrobot position. Then presents the robot position control using the vision based navigation system, including the path control under wide range and microscopic views, respectively. After that presents the performance of the robot tracking system, including the repeatability experimental results of this navigation system. Finally, section 5 summarizes this paper and the future works.

CHAPTER 2. MICROINDENTATION MECHANISM

2.1 System layout and configuration

In this section presents the original handmade microforce generator in order to give small force to the indenter. This is built from Voice coil actuator (VCA) technique associated with tandem parallel leaf spring. The parallel leaf spring mechanism can produce the rectilinear displacement of the platform without any friction. At first, the design of microforce generator and its basic performance are described respectively. The layout of VCA associated with tandem parallel leaf spring is shown in Fig. 2.1. It is composed of two parts, the actuator part Fig. 2.1(A) is a VCA that is implemented with parallel leaf spring and the sensor part Fig. 2.1(B) is also a parallel leaf spring with strain gauges and an indenter. Finally, Fig. 2.1(C) demonstrates the combination between an actuator part and sensor part.
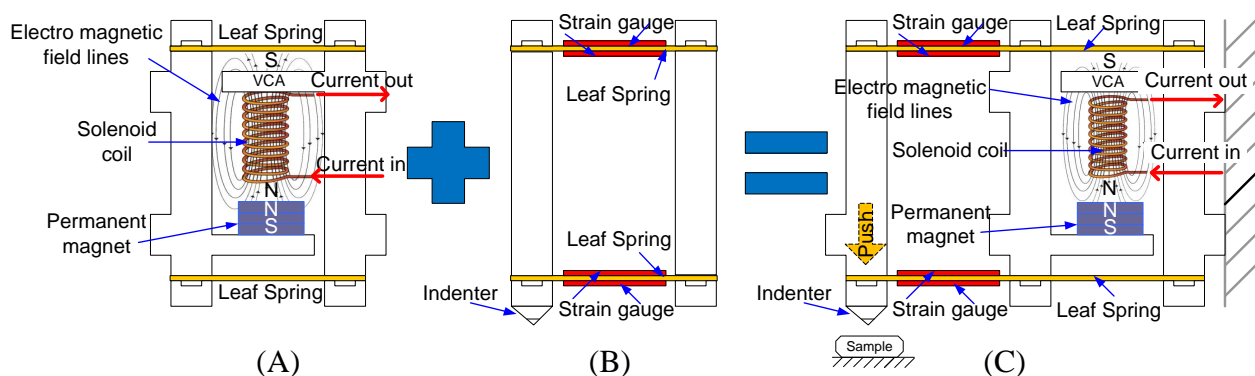
Figure 2.1 Layout of the microindentation mechanism, (A) Actuator part, (B) Sensor part and (C) the combination layout between (A) and (B)

The actuator part in Fig 2.1(A) consists of two frames (L-bar) supported by parallel leaf spring. There is a solenoid coil placed on the top side of L-bar, down side is a permanent magnet. This layout is well known as "voice coil actuator" (VCA). It is used as displacement actuator in this machine. When an electric current is supplying to the coil, the magnetic field will push the coil (and the attached VCM arm) outward if the north and south poles of the two magnetic fields are lined up together (north to north, and south to south), or pull the voice coil inward if they are lined up oppositely (north to south, and south to north). Thus, this actuator can be generated and controlled the displacement of a moving arm by control the current supplied. The sensor part shown in Fig 2.1(B)

demonstrated a layout of a sensor part. It consists of another parallel spring with strain gauges. Four strain gauges are attached on the both side of each leaf spring. Thus, the bending actions of the indenter arm can be detected. Finally, a combination between an actuator part and the sensor part, it becomes to a microforce generator mechanism. Thus, this layout can allow giving such a small precise displacement to the indenter as well as can detect the force applied to the indenter so that the depth-force curve can be characterized. In the next section, the microforce generator mechanism will be described. Then the basic performance of this mechanism will be discussed at the end of this chapter.

2.2 Microforce generator mechanism

2.2.1 Design of voice coil actuator (VCA)

The Voice Coil Actuator (VCA) is a very simple positioning actuator device. It is composed of a coil of wire and a permanent magnetic similar with the layout inside a sound speaker (Fig. 2.2). A speaker works based on the principle of an electromagnetism, which is an electromagnet is positioned in a constant magnetic field created by a permanent magnet. In speakers, the permanent magnets surrounding a voice coil (which is a solenoid coil) mostly a coil copper wire. The solenoid is attached to a cone of the speaker. When the current passes through the solenoid, it turns into an electromagnet. The electromagnet does have North Pole and South Pole, depends on which way the current is traveling in the solenoid coil. Then these two magnets (permanent magnet and electro magnet) interact with each other, so the directions are
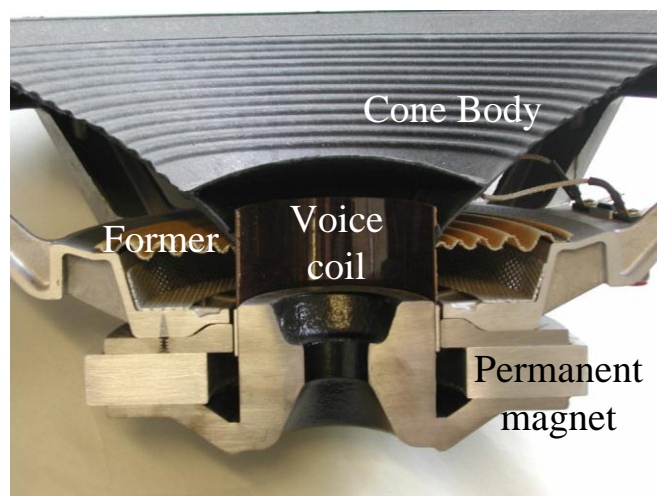
Figure 2.2 Cutaway picture of a sound speaker, demonstrates the voice coil (solenoid coil) and a permanent magnet layout [2-1]

repulsion and attraction. If the current was supplied only one way and the positive end of the electromagnet is attracted to the negative pole of the permanent magnetic field, the voice coil gets pushed away from the permanent magnet that surrounds it. On the other hand, when the alternating current is supply, the electromagnet's polar orientation switches. Then the coil is pulled back to the permanent magnet. During the moving actions of the coil, it pushes and pulls the speaker cone passed through the former. This action vibrates the air in front of the speaker, creating sound waves.

The actuator part in this research consists of two L-bars and two parallel leaf springs. They are assembled as show in Fig. 2.3. The solenoid coil is set on the top side of the frame and the permanent magnet is done on the bottom side. This layout is well known as a VCA. The magnetic fields are produced by electric current, which electric current carrying conductor in a magnetic field will be produces a force perpendicular to the direction of the electric current and the magnetic field. The generated force depends on length of the conductor in the magnetic field and electric current supply. In this actuator, the turn number of solenoid coil is important as it should generate appropriate force enough to activate the parallel spring with the required range. The electric current to the coil is limited at the possible lowest level so that the heat generation also could retain at the minimum level. From the view point of the microhardness and microstiffness test, the practical range of the displacement of the indenter is required as 50μm and that of the force is done as 10mN with ±1.5% tolerance [2-2]. Then, for the actuator part, we assigned the displacement generated range
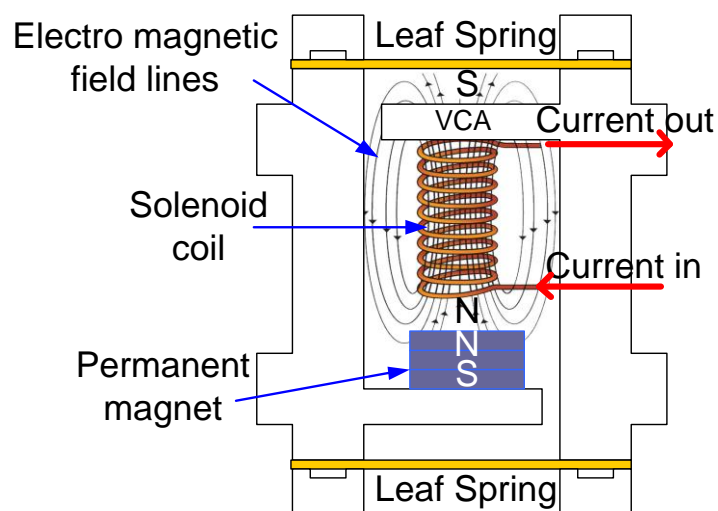
Figure 2.3 Layout of the actuator part

at 100μm and the pushing force at 20mN, which this operation range is about 200% of the microhardness operation range required. And the electric power at the coil should be limited less than 1W to prevent the thermal problem. Then its dimension size should small enough to be implemented in microrobot, which will be described in section 3.

Many experiments on magnetic repulsion with permanent magnets have been done [2-3 to 2-6], here we can discuss the force that generated by solenoid and permanent magnet. The magnetic force repulsion depends inversely on the separation r (meter). A simple law that we may have supposed to estimate the force F (N/m) that can be generated by two magnets as given in equation (2.1).

$$F = k\,\frac{M_1 M_2 V_1 V_2}{\mu_0 r^n} \dots\dots\dots\dots\dots\dots\dots\dots\dots\dots(2.1)$$

Where;

M_1 and M_2 is the magnetization of each magnet (can be given by $M=B_0/\mu_0$).

V_1 and V_2 is the volume of each magnet (meter^3).

μ_0 is the permeability of space ($\cong 4\pi \mathrm{x} 10^{-7}$ tesla·meter/ampare).

k is the constant coefficient that can evaluate from the experiment and the exponent n can be determined in many cases as the magnetic flux analysis is so complicated [2-7]. Here we have to negotiate the relation between the generated magnetic force and the spring constant, so that the range of position can be appropriated.

In Fig. 2.3 is shown the parallel leaf spring supporter. This simple parallel leaf spring mechanism can produce rectilinear displacement of platform. Even though it has positioned error due to angle of bending of platform (we will discuss in this issued later on section 2.6). Nevertheless, we must fabricate the VCA that is small enough to implement in microrobot. The size should be smaller than 5mm in width, 25mm in length and 25mm in height. The thin plate phosphor bronze (50μm thickness) is used to fabricate the parallel mechanism. Then the static performance of the parallel leaf spring mechanism k is also given as follow equation (2.2). And the spring parameter is shown in Fig. 2.4.
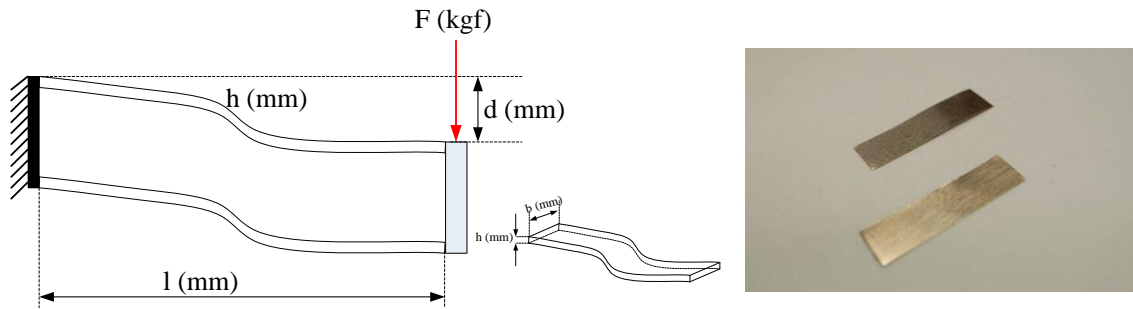
Figure 2.4 Parallel leaf spring parameters

$$K = \frac{4bh^3E}{l^3}\dots\dots\dots\dots\dots\dots\dots\dots\dots\dots\dots\dots(2.2)$$

Where;

E is Young modulus of Phosphor bronze is 112.7 x 10^9 N/m^2

l is length of leaf spring is 0.0105m

h is thickness of leaf spring 50µm = 0.00005m

b is width of leaf spring 5mm = 0.005m

$$K = \frac{4bh^3E}{l^3}$$

$$K = \frac{4 x 0.005(m) x 0.00005^3(m^3) x 112.7 x 10^9(N/m^2)}{0.0105^3(m^3)}$$

$$K = 243.38(N/m)$$

Calculation result from equation (2.2) shows spring constant of the parallel spring mechanism equal to 243.4 N/m.

Because of structure size limitation, the solenoid that will be used in this VCA is limited at 200 turns with 10mm in height and 5mm in diameter. Then the size of permanent magnet is limited around 5mm in diameter and 3mm in height. And we did select the 0.3 Tesla cylindrical type Nd-Fe-B permanent magnet, with dimension 4mm in diameter and 2mm in height for this VCA. The solenoid coil is fabricated from copper wire with 0.2mm diameter. The magnetic field at the center core of a coil is calculated from equation (2.3). An electromagnetic field sources are essentially dipolar in nature, having a north and south magnetic pole. In this machine, the action between permanent magnet and solenoid coil is push direction (North Pole to North Pole). The amount of the current applied is means of controlling the magnetic force produced. The programmable power

supply (HP-6632A) is used as a current control unit. The current supplied was limited at lower than 0.5A, due to temperature product from high current supply can disturbed another sensing part. The programmable power supply is controlled by computer, which program by Labview from National Instrument Company.

$$B = \mu n I \ldots\ldots\ldots\ldots\ldots\ldots\ldots\ldots\ldots\ldots\ldots..(2.3)$$

Where;

B is magnetic field at the center of solenoid (Tesla),

n is N/L (turns/m)the number of turns per unit length, N is 200 turns, L is 0.009

I is current (amperes), I from 0.05A to 0.5A

μ is permeability of the core, μ_{copper} is 1.2566380 x 10^{-6} (H/m)

N = 200 turn, L= 0.009 m, μ_{air} = 1.2566380 x 10^{-6} (H/m),

n = 200/0.009 = 22,222.22 (turn/m), I = 0.05 A to 0.5 A

Then B = (1.2566380 x 10^{-6}*22,222.22*(0.05 to 0.5))

= 0.0014 to 0.014 Tesla

The solenoid coil parameters and the fabricated coil are demonstrated in Fig. 2.5 (A) and (B), respectively. The calculation result from equation (2.3) shows the estimation value of magnetic field at the center of solenoid is about 0.0014 – 0.014 Tesla, along 50mA to 0.5A current supply.

(A)   (B)
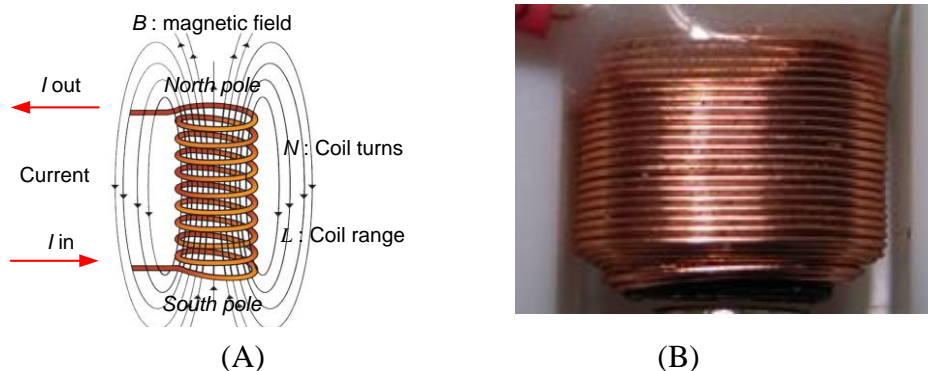
Figure 2.5 (A) Solenoid coil in actions when supplied the current. (B) The fabricated solenoid coil

2.2.2 Experiment on repulsive force

After we specified the VCA size and the turns of solenoid including the permanent magnet dimension, then we made a primary experiment on repulsive force between solenoid and permanent magnet. The experiment setup is shown in Fig.2.6. In this experiment, a solenoid and a permanent magnet which is the same specification with our requirement is used, both are placed in the same y axis, with their opposite poles facing and it was supported by very low stiffness metal plate(which long 200mm to reduce spring constant). The parallel leaf spring can keep permanent magnet in same plane position. By supplied an electric current to a coil the permanent magnet that supported by parallel spring will push up because the repulsive force between two magnetic fields. Then using weight set (100mg up to 3g) as an addition force against the magnetic force. When the repulsion magnetic force equals to the addition weight, then the separation r was measured along each solenoid current supply I(A) from 0.03A up to 0.5A as shown in Fig. 2.7. The graph at the separation range lower than 300μm is shown and the start point of x-axis at 120μm, due to the initial position of electromagnetic force from solenoid. The force F estimation results of our design parameters from equation (2.1) (shown by dash line) and the experiment data (shown by solid line) is quite similar with each other. The constant coefficient k and the exponent n should be carefully defined and consider in many parameters based on experiment results, so in this experiment,

(A)   (B)
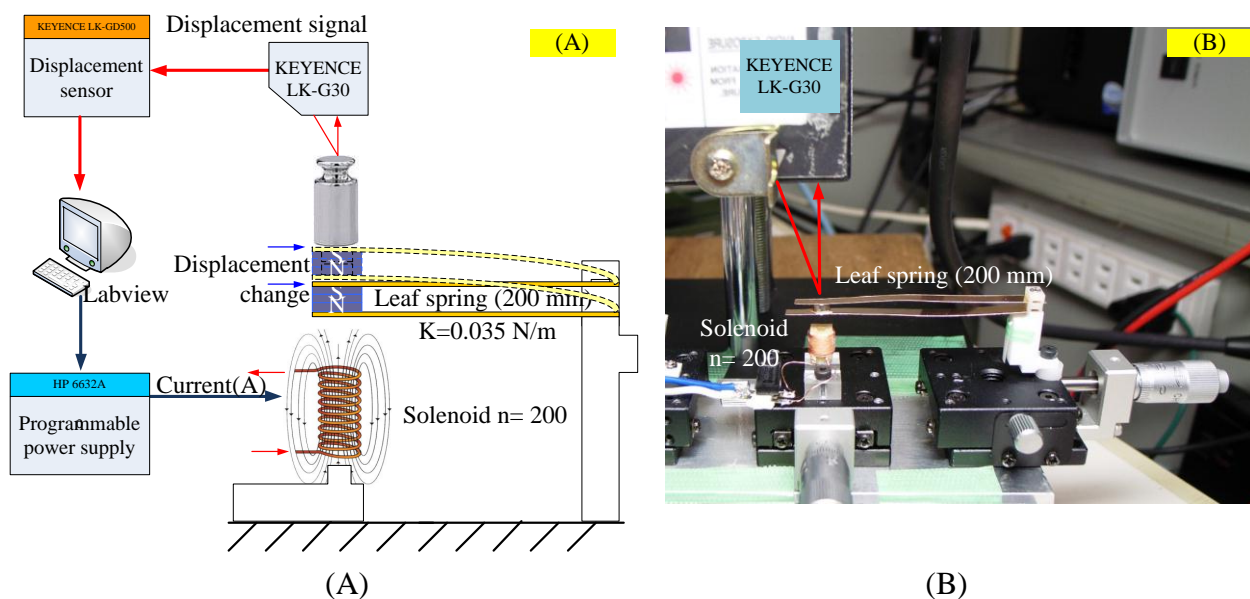
Figure 2.6 Experiment setup for determining the repulsive force between solenoid and permanent magnet, (A) Setup diagram and (B) Equipment setup
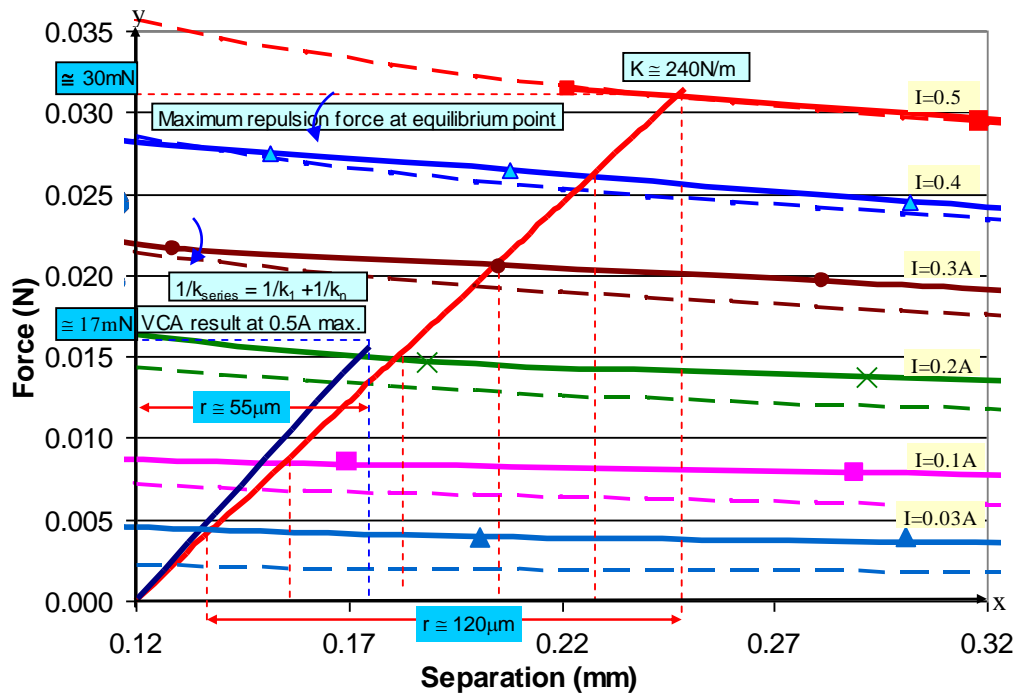
Figure 2.7 Repulsive force between solenoid and permanent magnet (dash line from calculation, and solid line from primary experiment) of each current supply, compare with the design value of main structure spring constant and the force generated experiment results of the fabricated VCA

the desired constant coefficient k is 1.4×10^7 and the exponent n is 0.2, these values are only available with the same size of experiment coil not valid for other. However, in this research view point, the investigation with these parameters is not the main concern and the research objective is focusing on the generated force value rather than the magnetic relation.

From the experiment results, the maximum repulsion force from this solenoid at 0.5A current supply to the permanent magnet is around 30mN. Here the operation performance of magnetic force has been proposed, then we could design the spring constant of VCA structure from these results. As we wish that the displacement operation range of VCA should be around 100 to 120μm, so we can design a spring constant as 240N/m. Considering the magnetic force and the parallel spring force can be balanced from 0.03A to 0.5A current input, it is presumed that the workable range is 120μm. Then we can find out the spring constant k of VCA regarding to the limitation of VCA size and operation range. Thus the minimum thickness of the spring should be around 30μm to 50μm. Because, if it thicker than 50μm then the k would be larger than 240N/m,

on the other hand if we use thinner than 30μm, then it cannot support the whole structure weight.

Under the conditions of the displacement range, the required force generation, the acceptable part size as well as the minimum electric power, the turn number of the coil and the components sizes were carefully decided with the negotiation of the trade-off management. The phosphor bronze 50μm thin plates were selected and the dimension of the parallel leaf spring was designed, and then the actuator part was fabricated as shown in Fig. 2.8.
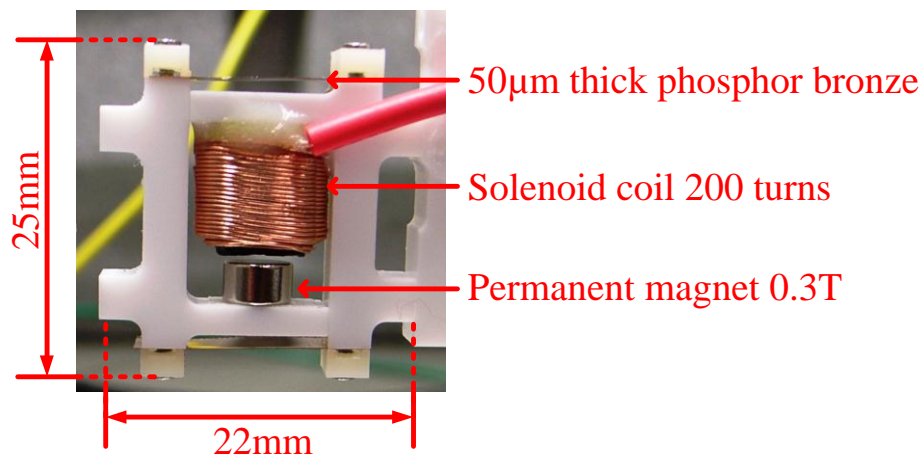
Figure 2.8 The fabricated voice coil actuator (VCA) associated with tandem parallel leaf spring

2.2.3 Experiment on displacement generated

After the microdisplacement generator was fabricated, then the basic performances such as the linearity and resolution of generated displacement were checked. These performance tests were test without any loads applies, only the magnetic force pushed against the spring force of the main structure.

This performance test was conducted with the DC current of 1.5mA step incrementally from 0.0A to 0.5A, and the current was decrease from 0.5A to 0.0A. The laser displacement sensor (Keyence LK-G30) is used to determine the behavior of moving L-bar arm as a consequence of the current. The schematic diagram of equipment setup in this experiment is shown in Fig. 2.9. Then resolution, linearity and operation range of microdisplacement generator machine were checked precisely as shown in Fig. 2.10 and Fig. 2.11, respectively.
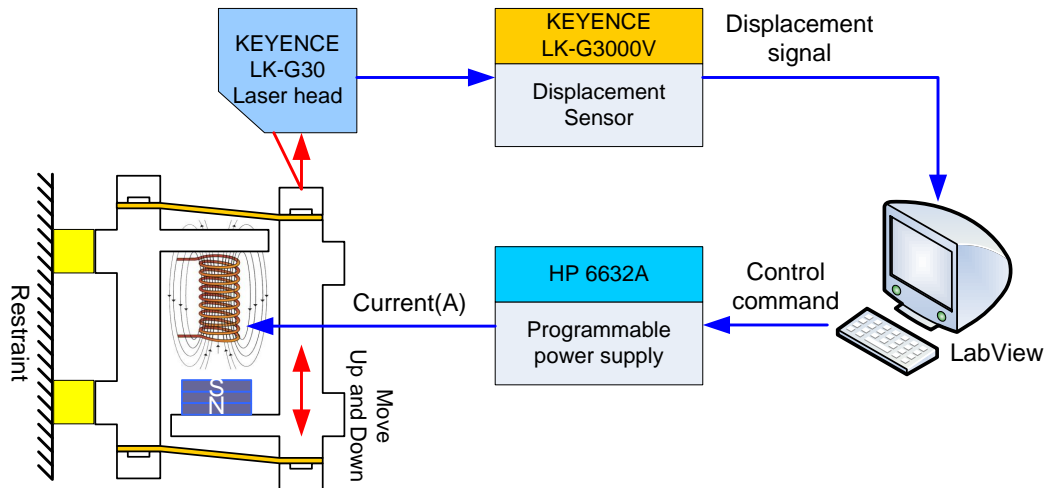
Figure 2.9 Control diagram of the solenoid coil

From the experiment, it was clear that this machine could generate displacement up to 280μm with 0.5A current supply. When comparing these experiment results with the estimation results (Fig. 2.7), it is obviously shown that this fabricated VCA could generate the displacement larger than the calculation value. There were the dimension size and the assembly error. The most sensitive part is the parallel spring, at the edge of clamping nut on both of L-bars might cause some bending. It may reduce the overall spring constant to lower than the expected value.
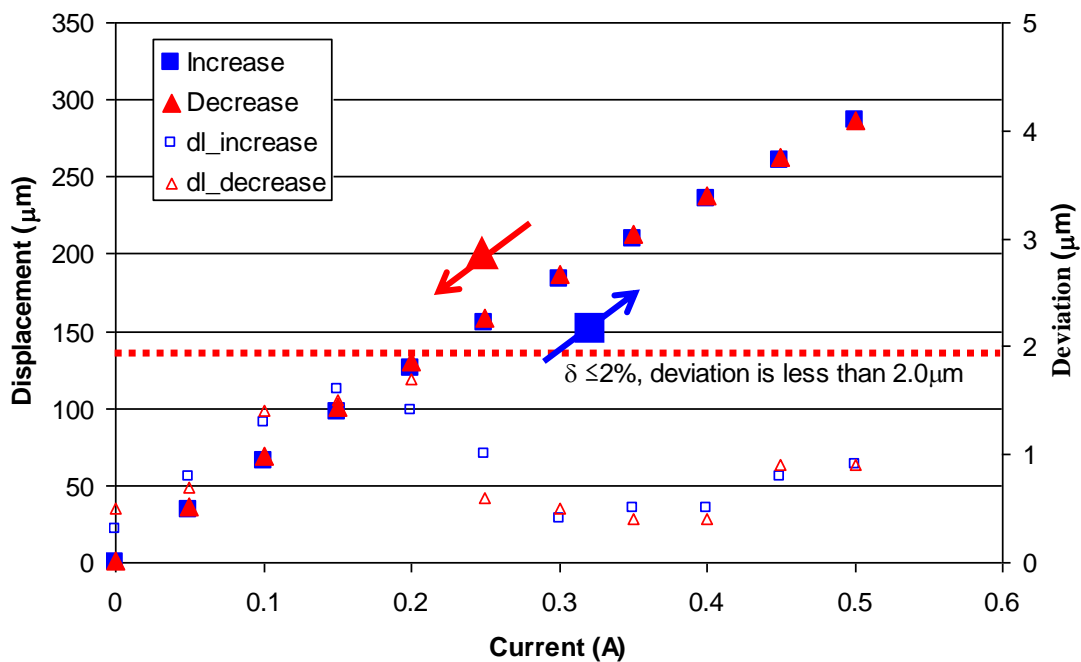
Figure 2.10 Experiment results with the displacement of the paralleled spring driven by VCA
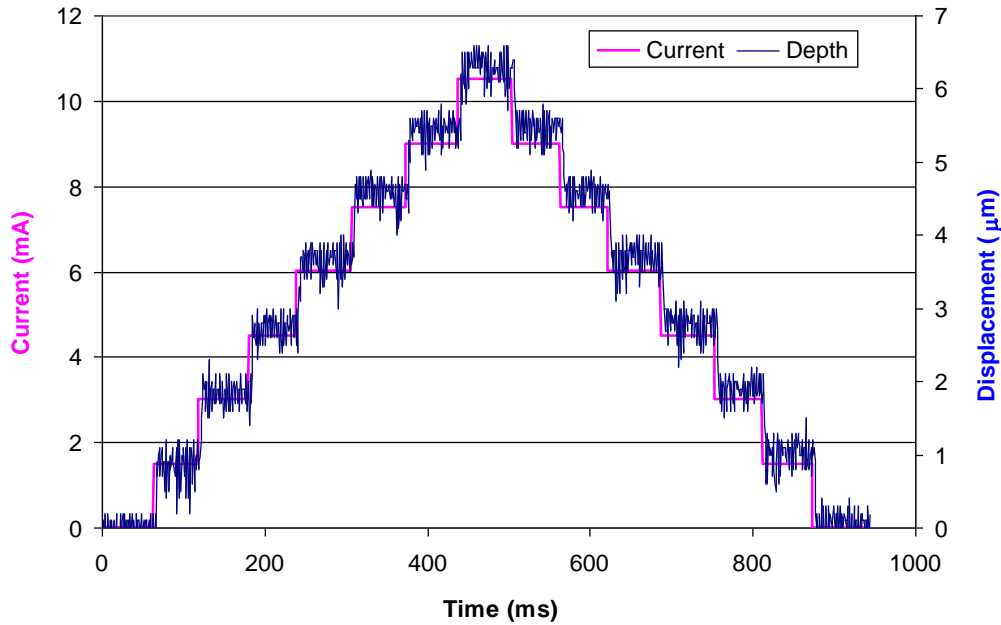
Figure 2.11 Experiment results with the step response to the input current

Furthermore, the solenoid was made by hand, the winding process cannot guarantee that its shape would perfect. However, these operation range results can be accepted as the performance results are better than our requirement.

The resolution result shows that the displacement 1µm can be given with 1.5mA step current supply. The linearity graph shows the completely same behavior for increasing and decreasing direction of generated displacement. By a series of measurements, the deviation δ is less than 2µm. It is found that this machine can be provided good linearity and repeatability with the range of the generated displacement.

2.2.4 Force sensor unit

In order to measure the generated microforce precisely, another sensing part should attached to the actuation part. Another parallel spring with strain gauges force sensor is shown in Fig. 2.12. Here four strain gauges(model: KSPH-4-2K-E4) are attached on the both side of each leaf spring and the full bridge electric circuit can get the signal that can indicate the acting force. Resistance change of sensing part due to bending action of leaf spring was magnified 200 times by bridge amplifier (KYOWA DA-710A). Then the output can be measured and schematic diagram is shown in Fig. 2.13.

41
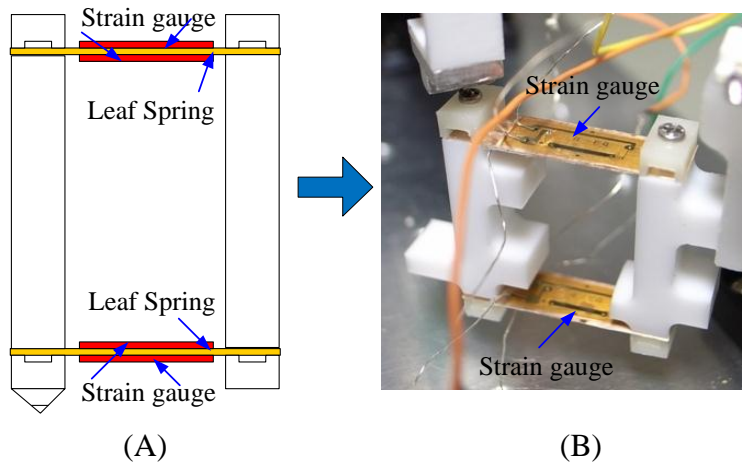
Figure 2.12 The force sensor unit associated with tandem parallel leaf spring, (A) diagram layout and (B) the fabricated unit

After the sensor was built, then it is attached to the actuator part as shown in Fig 2.14. The test force can be generated by displacement change of L-bar arm of force generator mechanism. The expected force can be measured and controlled by the force sensing feedback signal. The control diagram of this small force generator mechanism is shown in Fig. 2.15.

The solenoid coil is controlled by programmable power supply (Agilent 6632A). When in operation, an electric current activate a coil push a permanent magnet that attached with the sensor part downward. Assume that the sensor part touch a sample surface, the bending action of parallel leaf spring on the sensor part can be monitored. Resistance change of sensor part was amplified by
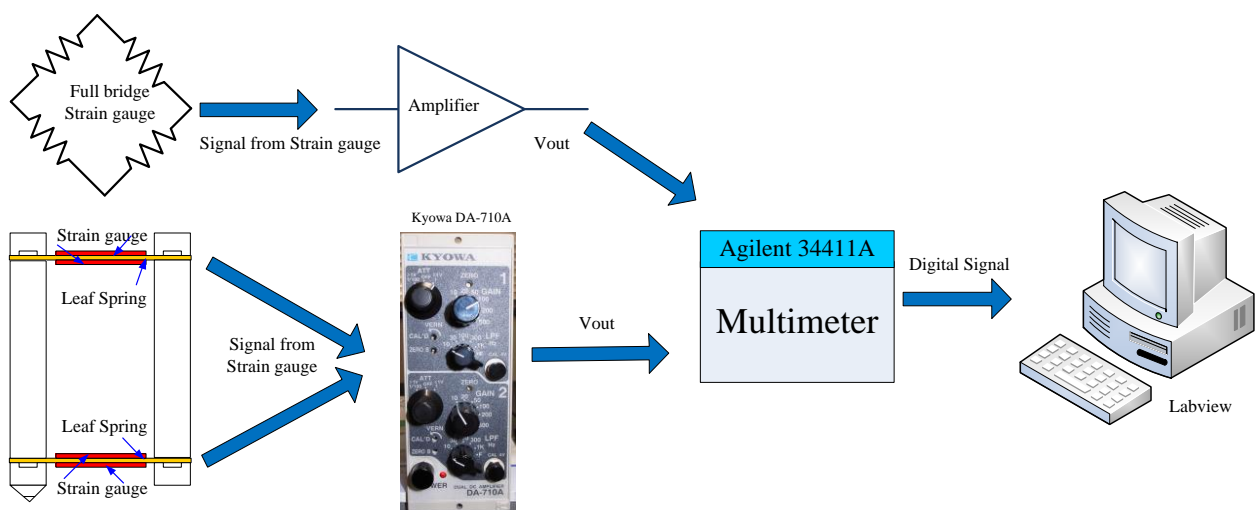
Figure 2.13 The schematic diagram of force sensor unit, composed of bridge amplifier (DA-710A), the multimeter (Agilent 34411A) and PC

42

(A)   (B)
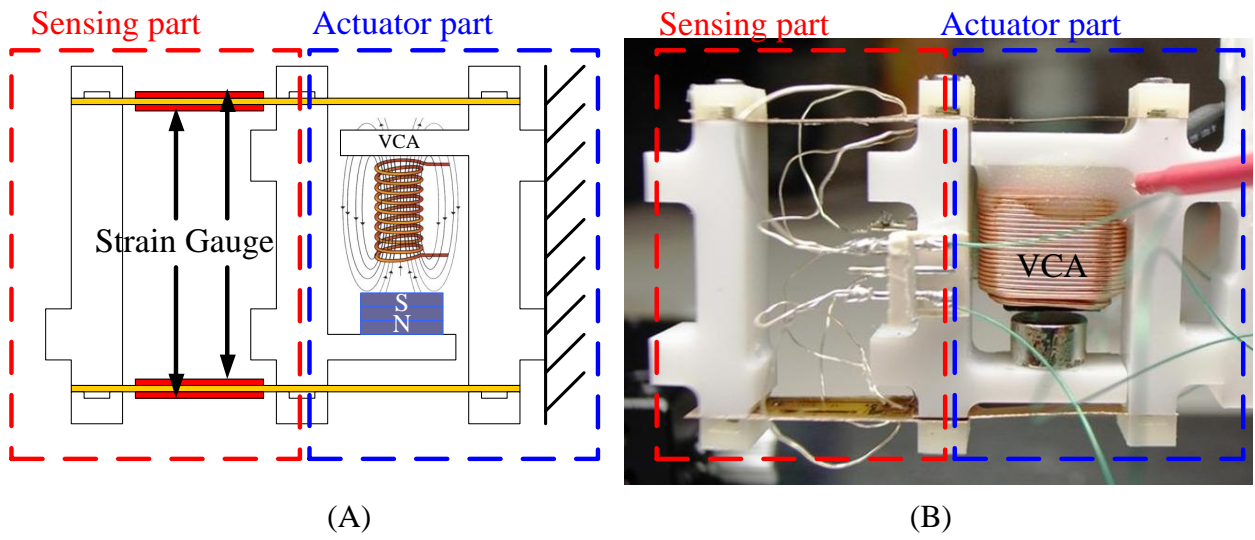
Figure 2.14 The force sensor unit associated with tandem parallel leaf spring, (A) diagram layout and (B) the fabricated unit
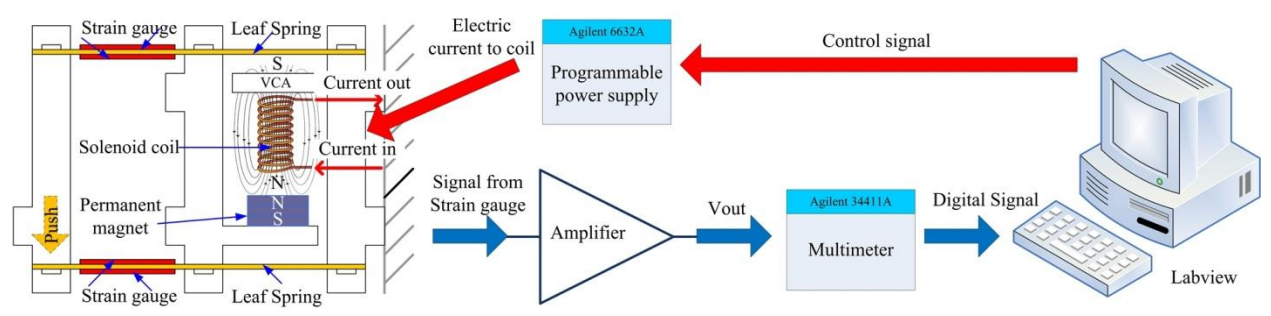
Figure 2.15 Feedback control diagram of a microforce generator mechanism

an amplifier. Then voltage out from amplifier circuit is measured out by six and a half digits multi meter (Agilent 34411A).

       The force sensor element works as a feedback signal, the force value can be generated from displacement generator machine and the set point of force can be measured and limited by force sensing signal. After attached the sensor part to the actuator part, we organized an experiment the determined basic performance of a sensor part as the diagram in Fig. 2.16. The experiment procedure is pushed a pressure plate of sensor part on rigid body by using a movement of the actuator part (activate the VCM). The displacement change of VCM's arm was measured by KYENCE laser displacement sensor. The moving step of a VCM composed of large step and small step test, large step: 0.02A per step start from 0.05A to 0.5A and small step: 0.3mA per step start from 0.05A to 0.063A. Then measure the voltage output from a sensor part simultaneously with displacement behavior of the moving VCM's arm (data from KYENCE
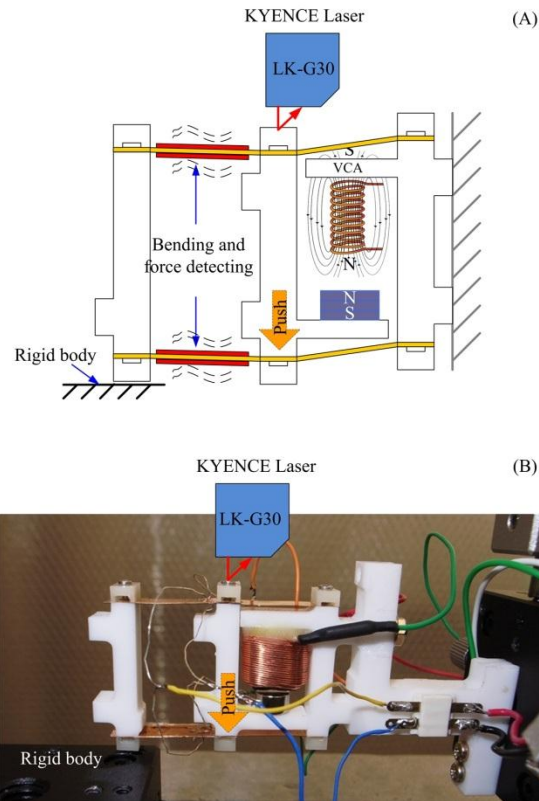
Figure 2.16 (A) Schematic diagram and (B) Experiment setup for determined the basic performance of a sensor part after attached to the actuator part

laser). The experiment results are shown in Fig. 2.17 and 2.18 for large step and small step, respectively.

After the strain gauge force sensors are attached, and then the displacement generated performance can be checked by using a laser displacement sensor. The experiment results in Fig. 2.17 and 2.18 can be read as follows; the pink line demonstrates output signal from the sensor part, the value is indicted on left hand side Y axis. The blue line demonstrates displacement behavior of a moving L-bar which attached to the VCA, the value is indicated on right hand side Y axis. Finally, red line indicates the current input to the coil, the current value is shown on right hand side Y axis same as the displacement axis. The experiment results have shown that, the sensitivity of this sensing part is about 0.1μm at 0.3mA current input step. There is no displacements change or bending behavior from input current less than 0.3mA. Form rang 0.05-0.5A current input, it can moves 50μm of displacement change. The bending action that readout from the sensor part is almost the same with the behavior of the L-bar moving arm, which readout from laser displacement. That means the bending behavior of a sensor part can be used as a force feedback signal.
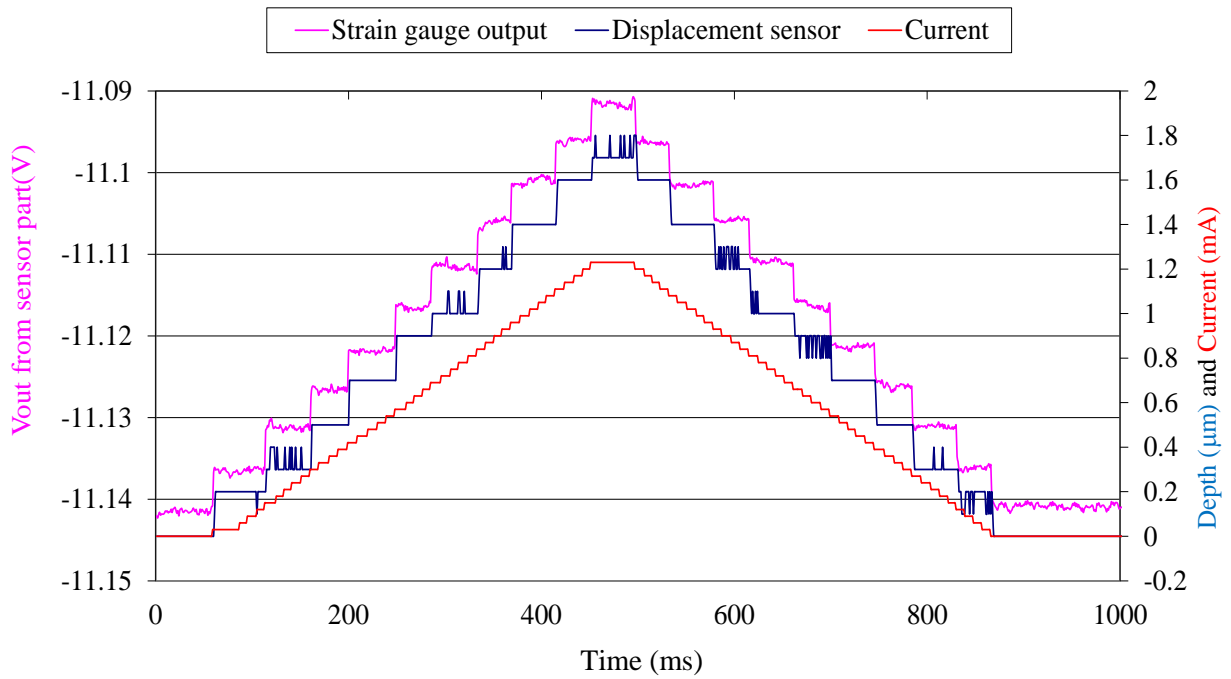
Figure 2.17 Experiment result of small step movement
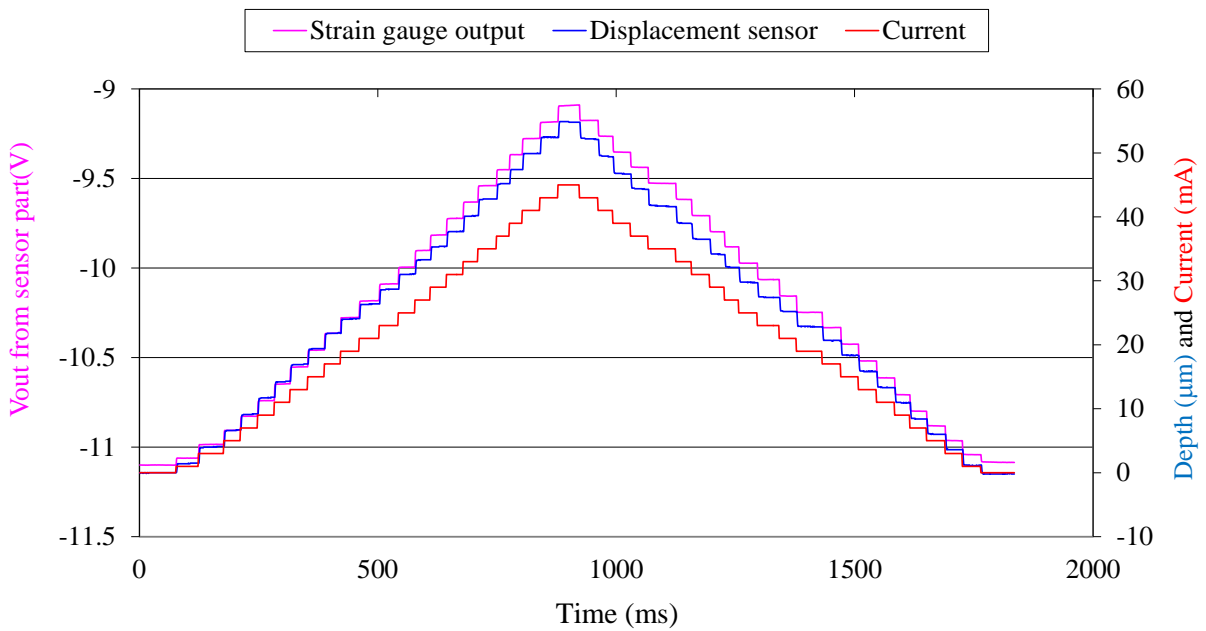
Figure 2.18 Experiment result of large step movement

The generated forces given by this mechanism were calibrated by using the commercially available 50mN standard load cell (Kyowa LVS-5GA). The experiment setup is shown in Fig. 2.19 and the experiment result is shown in Fig. 2.20. The result has shown the generated force in the both directions (increase and decrease) have a good linearity with less hysteresis at the maximum current supply at 0.5A. Here the deviation of the generated force was ±0.9% of testing force with 20 times measurements over one hour in the uncontrolled room temperature. With ISO standard the tolerance of testing force within ±1.5% of testing force should be confirmed.
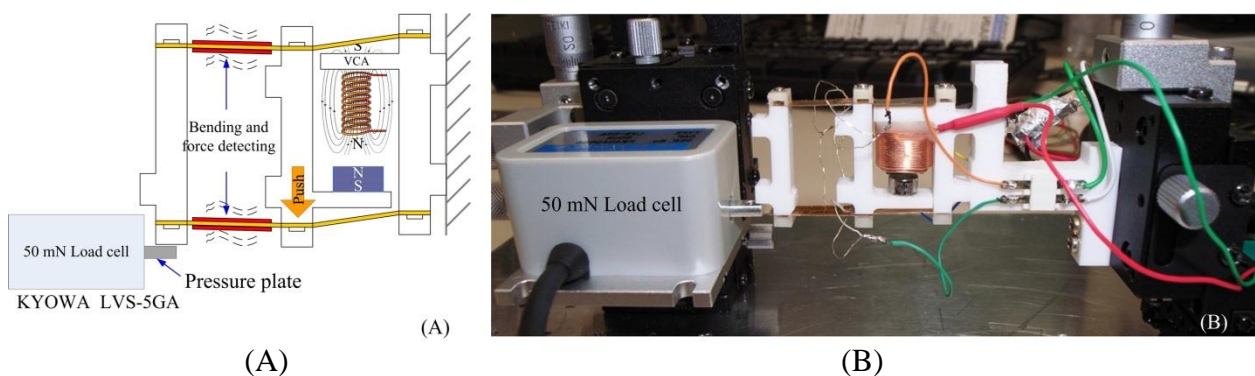
Figure 2.19 (A) Schematic diagram and (B) Experiment setup for generated force verification
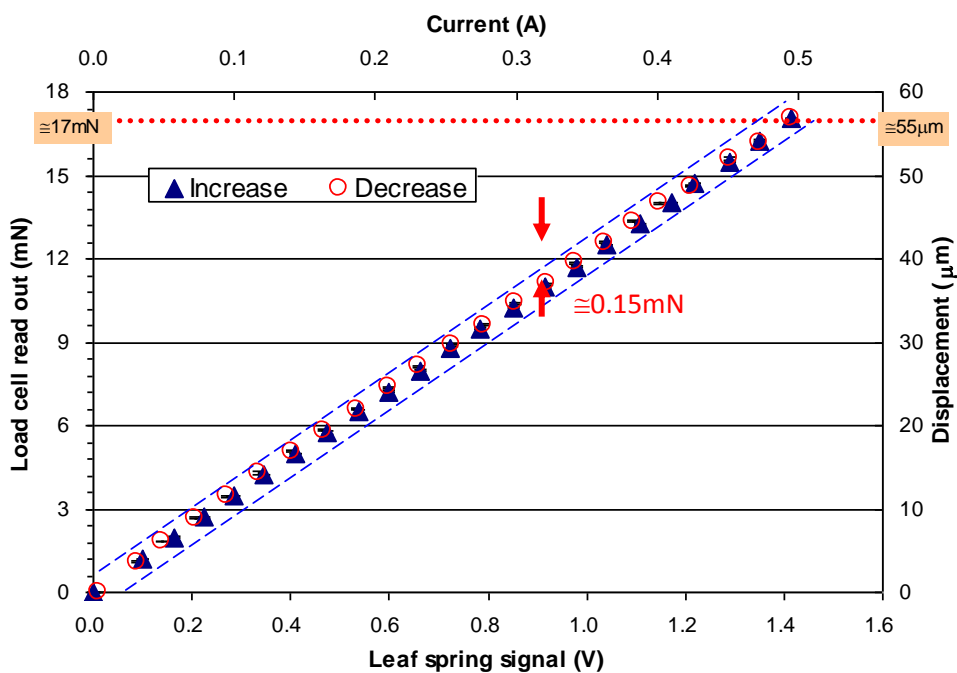
Figure 2.20 Experiment results with the relation between the generated force and the displacement. The force comparison between standard load cell and output from leaf spring with 20 measurements inside temperature controlled room temperature
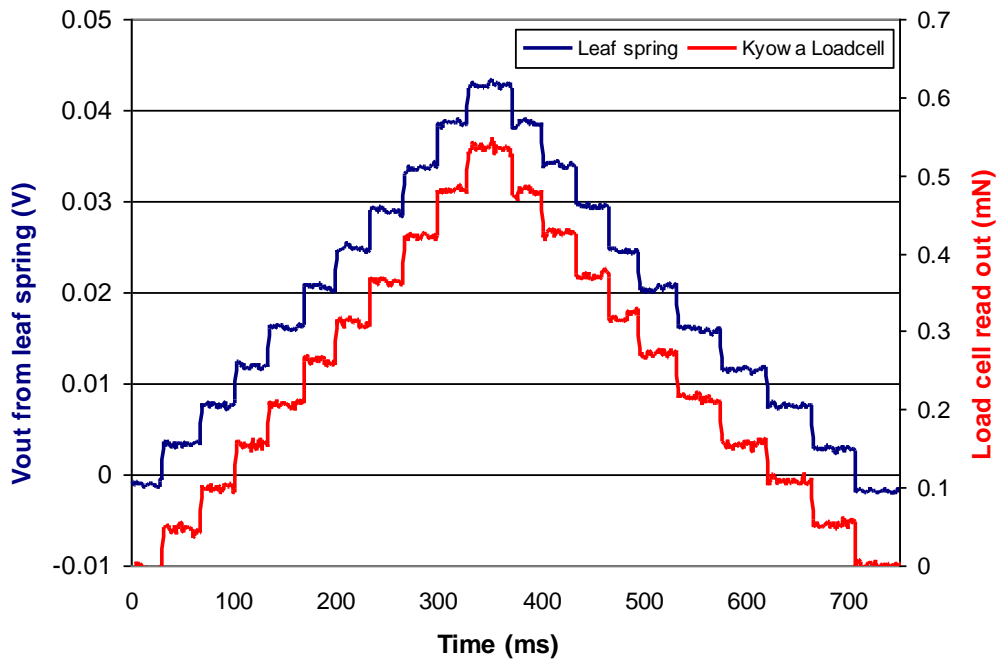
Figure 2.21 Experiment results with the resolution of the generated force

It is clear that this generated force range is over 15mN, which is can be covered our requirement for the operation range. Then the displacement change due to pushing against the load cell also was measured. It is about $55\mu m$ at 17mN maximum generated force which is smaller than the displacement generated without any loads applies (Fig. 2.10). When this machine operates without load, the whole spring constant is equal to parallel spring constant. But when it is pushing against the sample, then the overall spring constant should be considered the stiffness or spring value of that sample as a series of spring ($1/k_{series}=1/k_1+1/k_n$).

In Fig. 2.7 the pressure plate is pushed down to load cell then a combination of parallel spring constant the stiffness of load cell could discuss with the blue line. Thus, we might say that the samples that we want to test should have appropriate stiffness less than the stiffness of parallel spring, and then the actuator can operate without any problem.

Moreover, the experiment result in Fig. 2.21 shows the output signal of force sensor unit, compared with milli-Newton force value from load cell. It is clear that the resolution of generated force is approximately about 0.05mN, which is cover the accuracy requirement at 0.5% of testing force. It has a good repeatability within 15mA step current supply over the range. And also there is

47

a very small noise signal of generated force, even at one resolution (50µN). This means the microforce machine has shown a good ability to generate soft load controlled without any shock or impulse attack. Thus, the force generating mechanism is possible to be employed for the force generator in microhardness and microstiffness testing machine.

2.3 Displacement sensor for indentation depth of the indenter

At this moment the actuator part and the sensor part are combined together. The basic performance in term of generates and control force has shown good linearity with high resolution. In this section another important sensor for hardness machine, which is the depth measuring device is described. In order to use the hardness measuring system in inside a small chamber as our proposed, the smallest depth measuring device is required. Regarding to section 1.3 in chapter 1, the best depth sensor that compatible with this hardness mechanism is the linear variable differential transformer (LVDT). Because a small package with high resolution of displacement measurement, LVDT become a sensor of choice. The overall system control diagram of the microhardness mechanism after attached with depth measuring device as shown in Fig 2.22. The depth sensor is designed to place at the top of the indenter rod on the sensor part, aims to detect the displacement behavior of the indenter. The data acquisition card (model. NI DAQ 6259) is used to acquire depth signal from the LVDT, and then raw data is passed through filter software.
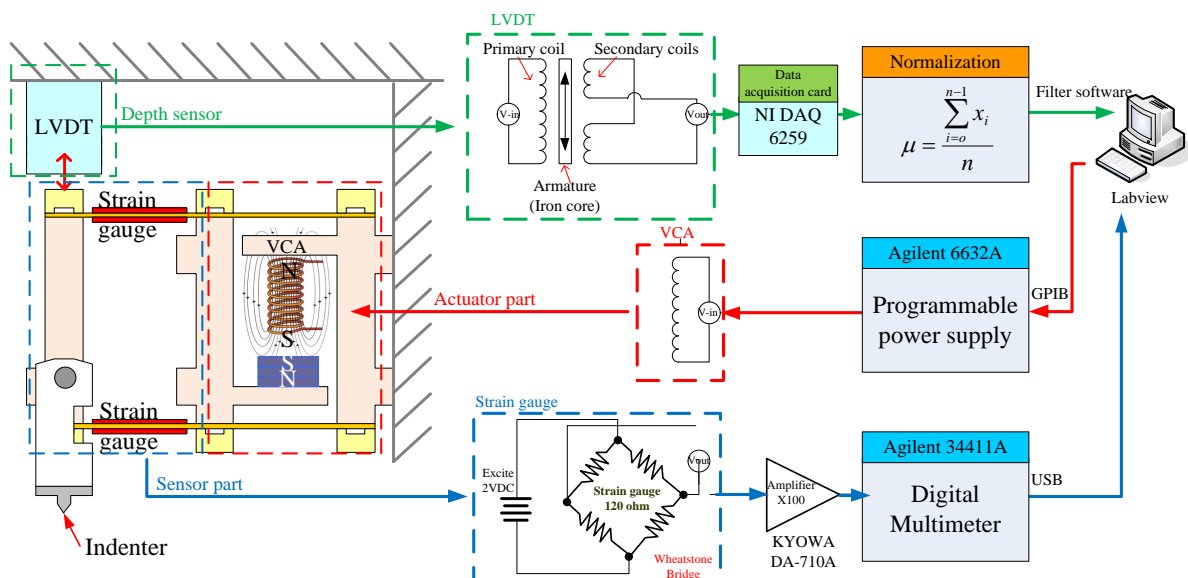
Figure 2.22 Overall system control block diagram
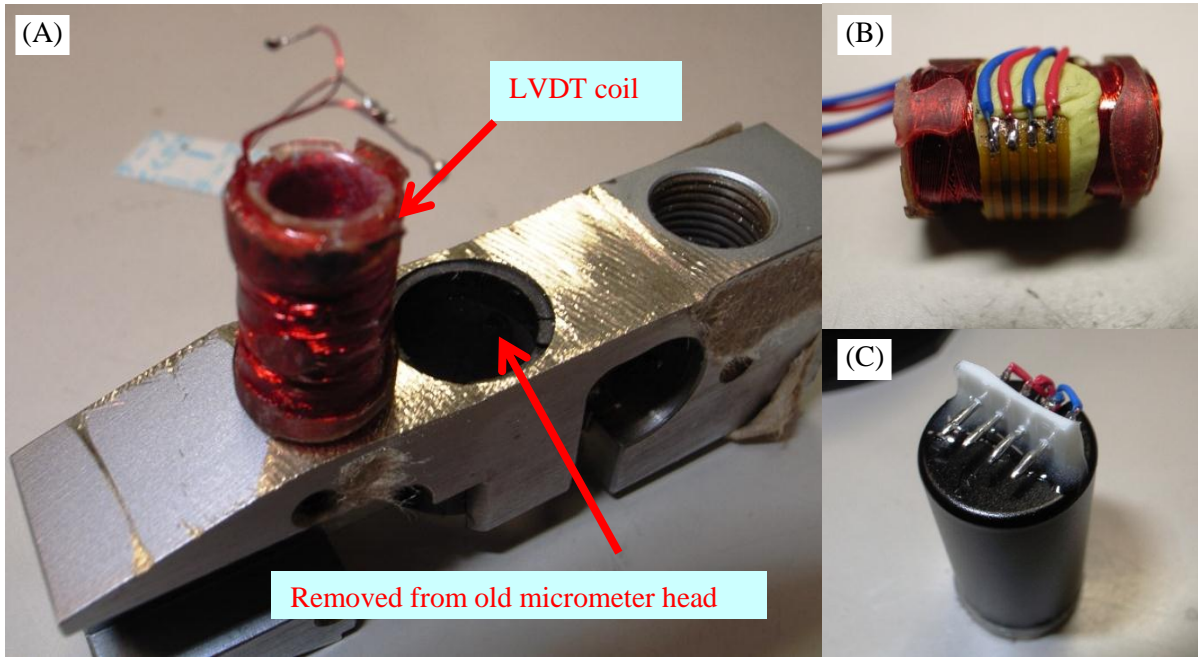
Figure 2.23 (A) The LVDT coil is removed from the micrometer head. (B) Wire holder to prevent the fragile LVDT wires. (C) The LVDT inside an enclosure package
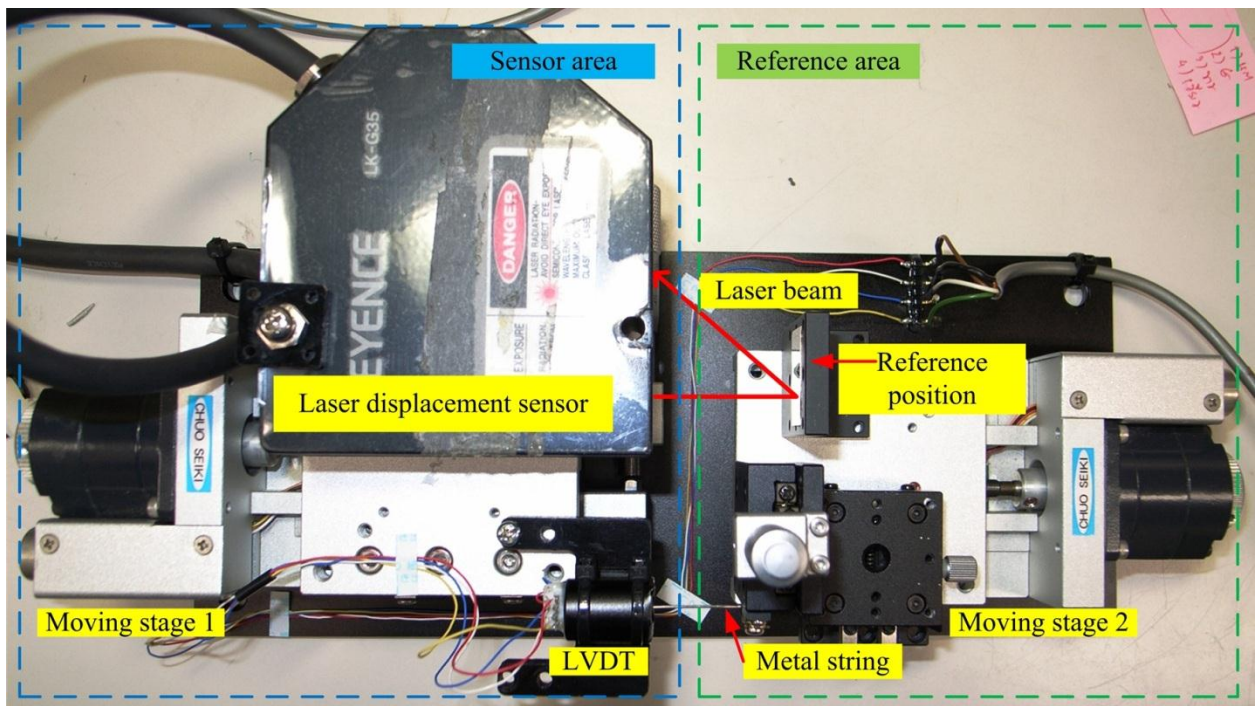
Figure 2.24 Experiment setup for LVDT performance test

We developed depth sensor for our hardness machine by using LVDT-based technique, which was found in inside of the micrometer head of an old electronic micrometer made by the Mahr Company as shown in Fig. 2.23 (A).

However, the micrometer package is too big but we have a limitation of space, so we had to make the depth-measuring device as small as possible. In Fig. 2.23(A) the LVDT coil was removed from the micrometer head. In Fig. 2.23(B) has shown the hard disk pair wire was used as wire holder to prevent the LVDT coil wire from damage, because it is very fragile. Then the LVDT was inserted into plastic tube and covered by metal plate and then made a connector as shown in Fig. 2.23(C). The experiment setup for determine a performance of LVDT is shown in Fig. 2.24. The displacement change of a metal string was measured by laser displacement sensor and it was compared with the voltage output from LVDT.

The experiment setup is separated into two areas, a sensor area and a reference area. Both areas are place on the same table but different moving stage. At the sensor area side, the LVDT and a laser are placed and fixed position on the same moving stage and same plane axis. On another side (reference area), the reference mirror and a metal string are also placed and fixed on the same moving stage. Because misalignment produces a cosine error the cause the laser or LVDT to measure a displacement shorter or longer than the actual distance traveled. Moreover, the Abbe error can be occurred if the axis of measurement is offset from the axis of interest. To avoid such errors from an angular misalignment between the sensor area and the reference area, the precise alignment between sensor area and reference area is required. In this experiment, the alignment setup is done by using ruler. At the first, the face of laser displacement sensor must be the same plane axis with the face of LVDT. Also, the face of laser must be parallel with the face of reference mirror. Meanwhile, the metal string must be inserted at the center of LVDT with the perpendicular direction. When the alignments process has done, then the experiment is ready to carry on. The moving stage has a capability to move within 1μm resolution. When the moving stage on the reference area is moved, the reference position of a laser and the metal string of a LVTD will moves simultaneously. So the laser readout and LVDT readout data should be the same behavior. The comparison result between laser and LVDT is shown in Fig. 2.25(A), the Fig. 2.25(B) is shown close up data of Fig. 2.25(B). The result has shown that the behavior of a metal string during changing a position can be detected by LVDT, with almost the same behavior that a Laser detects the reference position. The comparison results between LVDT and Laser have shown a conversion parameter from voltage output of LVDT and the displacement change measured by Laser.
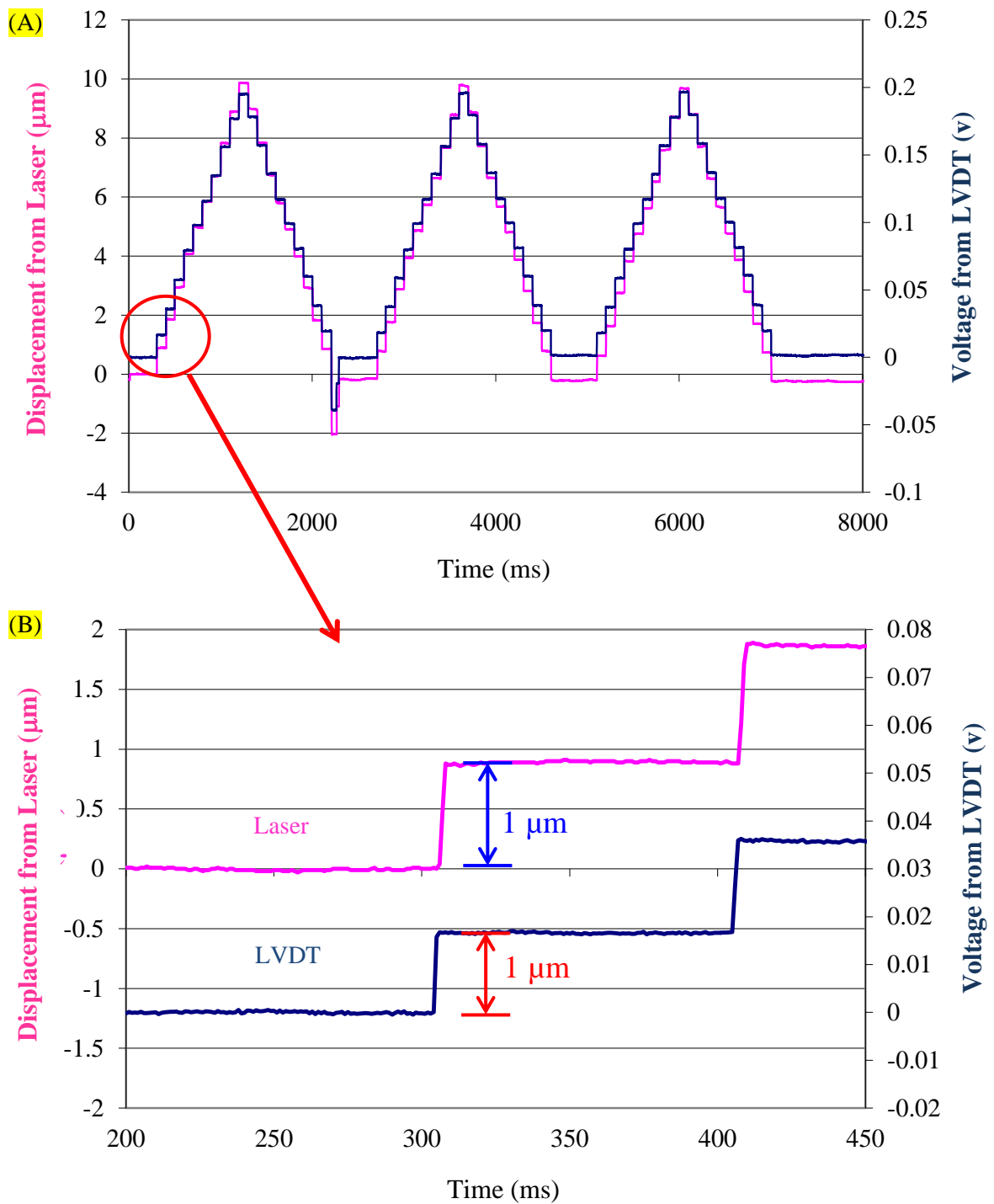
Figure 2.25 (A) Comparison result between LVDT and Laser displacement.
(B) Close up data shows the same behavior of both devices

51
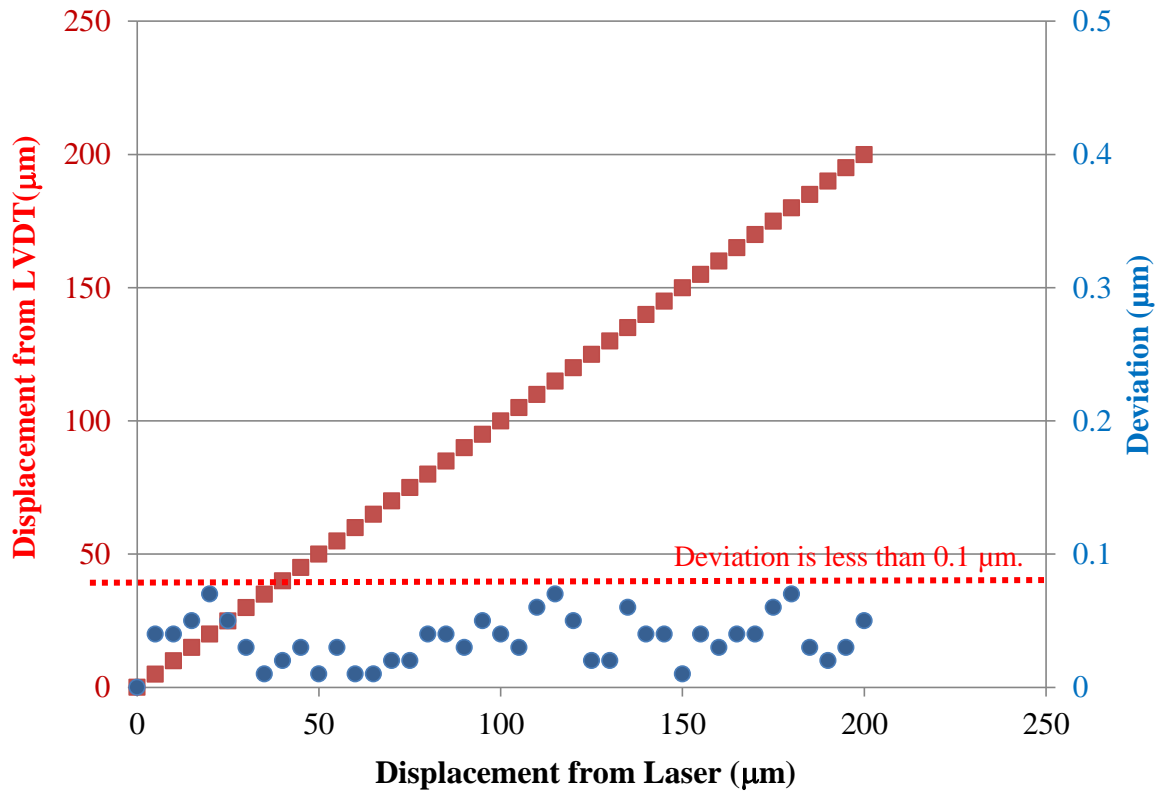
Figure 2.26 Calibration results of LVDT by using Laser displacement sensor. Red squares are the results of each calibration point. Blue circles are the deviation at each calibration point

From the results, one micrometer of Laser is about 20mV of LVDT voltage output. After that the calibration process of LVDT by using Laser is carried on. The equipment setup is the same with previous experiment shown in Fig. 2.24. There are three rounds of calibration process; the calibration step is start from 0μp to 200μm, with 5μm resolution. The moving stage of reference area is moved until the laser read 5μm each step, then record V-out from LVDT. The calibration result is shown in Fig. 2.26. From calibration result it is clear that have a good repeatability with wide measurement range (200μm) with deviation less than 0.1μm.

At this moment, the microhardness mechanism complete with controlled generated force and the depth measuring device. In next section the combination of each part is described.

2.4 A combination of microforce generator and depth measuring device

In this section presents a combination of microforce generator mechanism and depth measuring device, it become to the microindentation hardness mechanism as shown in Fig. 2.27. The layout and the fabricated of the prototype microhardness measurement machine are composed of actuator part, force sensor part, depth sensor part and the microindenter. The control diagram is shown in Fig. 2.22. The microforce can be given to the stylus tip that is set at the end of the tandem parallel leaf spring and can check the force applying the target surface by detecting the bend of the parallel spring. For our purpose, this mechanism has the indenter with cone angle 60° and tip radius 2µm at the bottom of pressure plate as the indenter of hardness machine. Thus, we need another displacement sensor to measure the depth of this indenter on machine. As shown in Fig. 2.27, the compact head of LVDT is set and the thin rod from the indenter can pass through this LVDT. This prototype version of microhardness machine can generate force by VCA up to almost 17mN and control generated force set point by using feedback signal from strain gauge on tandem leaf spring. And the LVDT displacement sensor can be monitored the indentation depth during whole dwell time.

(A)   (B)
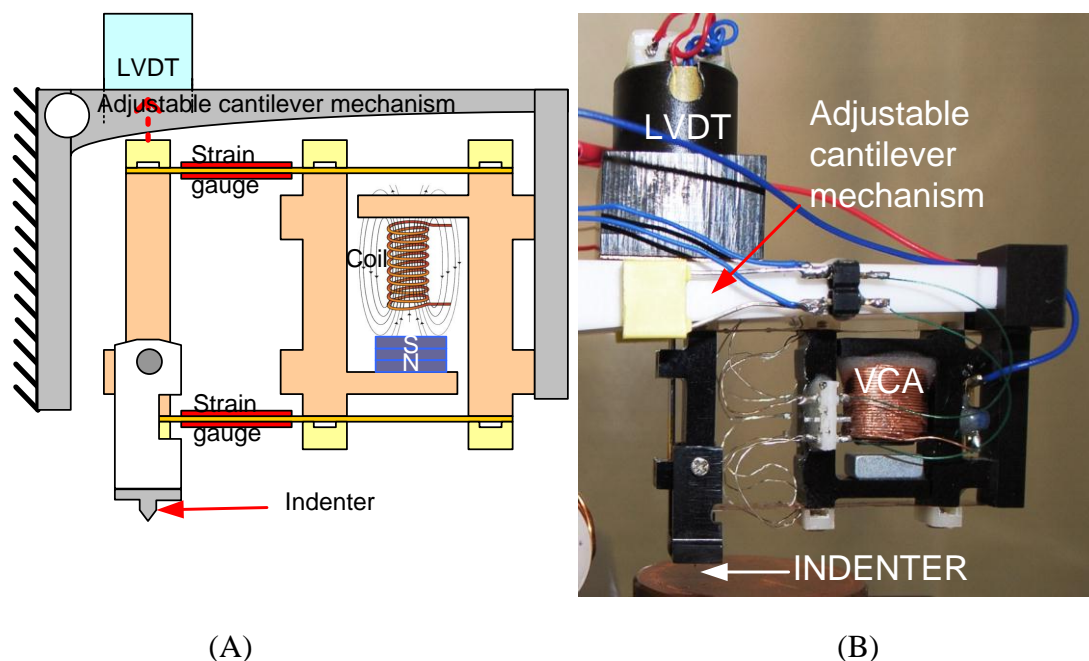
Figure 2.27 (A) Diagram layout and (B) fabricated of the prototype of microhardness machine
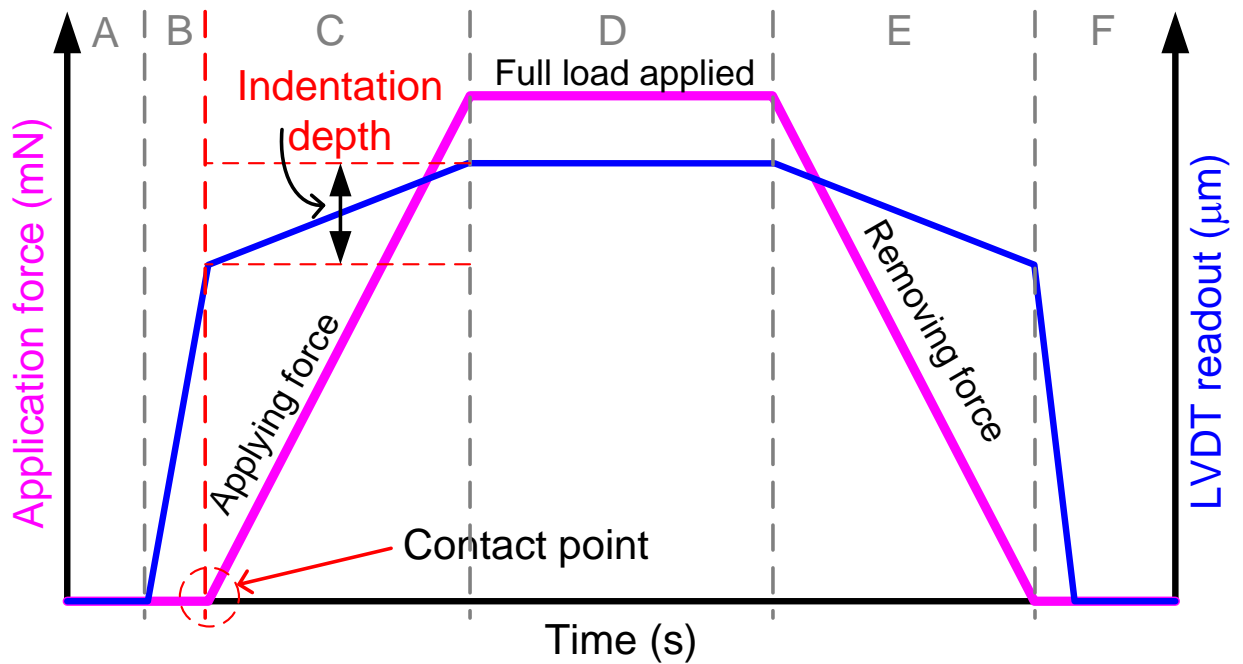
Figure 2.28 The testing cycle behavior of indentation depth from LVDT readout and the application force from strain gauge. It is separated by region A to F for each status

As shown in Fig. 2.28 is the testing cycle behavior of the indentation depth and the application force during the whole measurement process. At the first region A, the VCA is activating and adjust the balance point to manage the initial state; there is a reset of the residual depth and force in this point. And then at region B, the VCA is pushing the indenter downward to the sample. At this state there is no force apply to the sample, due to the indenter is pushing in the air. When the indenter is approaching and contacts to the sample surface at B to C junction, with the help of the sensing part on tandem parallel spring the applied force signal is obviously increasing. Then the read out of LVDT corresponds to the indentation depth. At the region D is the maximum force application. Finally, the force is removed at region E until the indenter is leaved from the sample surface in region F. The control sequence of this system can be managed by PC with Labview program.

2.5 Heartzian's contact

In this section presents the experiment on contact between the indenter and the specimen surface. When the diamond indenter tip and the specimen surface are brought into close proximity to each other, it is necessary to be considering the mechanics of contact between solids. The nature of the stresses arising from the contact between two elastic was first studied by H. Hertz 1881[2-8 and 2-9]. The contact between an indenter and a specimen involves both elastic and plastic deformations [2-10]. The contact profile is shown in Fig. 2.29.
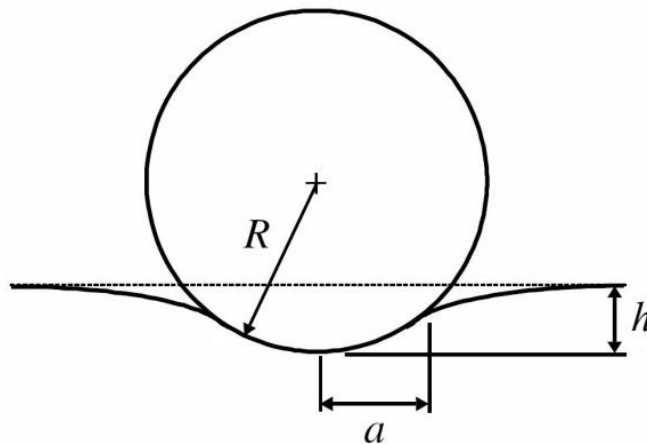
Figure 2-29 Contact between a sphere and the flat surface [2-11]

After the microindentation hardness mechanism finished, then the experiment on an indentation is carried on and presents in this section. The 30HV gold block is used as a specimen under test. The testing forces in this experiment are 5, 10, 15 and 20mN. Then the diameter of an indentation is compared with the contact mechanic calculation by Eq. 2.4. Which is an elastic contact between two curved surfaces, the radius of the circle of contact a is given by:

$$a = \left(\frac{3PR}{4E^*}\right)^{1/3} \quad \dots\dots\dots\dots\dots\dots\dots\dots\dots\dots\dots\dots\dots(2.4)$$

Where;
P is the indentation load (N).
R is the combined radius of the contacting surfaces (m).

$$R = \left(\frac{1}{R_i} + \frac{1}{R_{sp}}\right)^{-1} \quad \dots\dots\dots\dots\dots\dots\dots\dots\dots\dots\dots(2.5)$$

For our machine is in case of a sphere on a flat surface ($R_{indenter}$ is 1µm (0.000001m, $R_{specimen}$ is ∞), R is the radius of the indenter.

$$R = \left(\frac{1}{0.000001} + \frac{1}{\infty}\right)^{-1}$$

$$R = 0.00001$$

The quantity E^* is the combination between an elastic modulus (N/m²) of the indenter and the specimen is given by:

$$E^* = \left(\frac{1-v_1^2}{E_1} + \frac{1-v_2^2}{E_2}\right)^{-1} \dots\dots\dots\dots\dots\dots\dots(2.6)$$

Where;

v is Poisson's ratio of a indenter tip v_1 and the specimen v_2.

Regarding to the specification of our hardness mechanism, the modulus of the diamond indenter is $E_{diamond}$ = 1140GPa, (1.22×10⁹ N/m²) with poissions's ratio $v_{diamond}$ = 0.07. The modulus of the specimen (30HV block made of gold) is E_{gold} = 78GPa, (78X10⁹ N/m²) with poissions's ratio v_{gold} = 0.44. From Eq. 2.6, the combined elastic modulus is calculated by:

$$E^* = \left(\frac{1-0.2^2}{1.22x10^9} + \frac{1-0.44^2}{78x10^9}\right)^{-1}$$

$$E^* = 1.25435x10^9 \, {}^N\!/_{m^2}$$

From Eq. 2.6, the radius of a circle contact is calculated by:

$$a = \left(\frac{3Fx0.000001m}{4x1.25435x10^9 {}^N\!/_{m^2}}\right)^{\frac{1}{3}} (m)$$

$$a = \left(\frac{3x10^{-6}xF}{5.01741x10^9}\right)^{\frac{1}{3}} (m)$$

The experiment results on contact stress which is applied with 5, 10, 15 and 20mN test force on 30HV block are shown in Fig.2.31 to 2.34. And the circle contact that is calculated from Eq.2.6 and compares with the experiment results is shown in table 2.1 and demonstrated in Fig. 2.30.

Table 2.1 Calculation results and measurement results on the indenter circle contact

Force(mN)	Hertzian contact diameter, 2a (µm)	Measurement result		Error	
		d1 (µm)	d2 (µm)	d1 (µm)	d2 (µm)
5	0.696	3.142	4.377	2.446	3.681
10	0.876	4.818	6.426	3.942	5.550
15	1.003	5.725	8.847	4.722	7.844
20	1.104	7.19	12.292	6.086	11.188
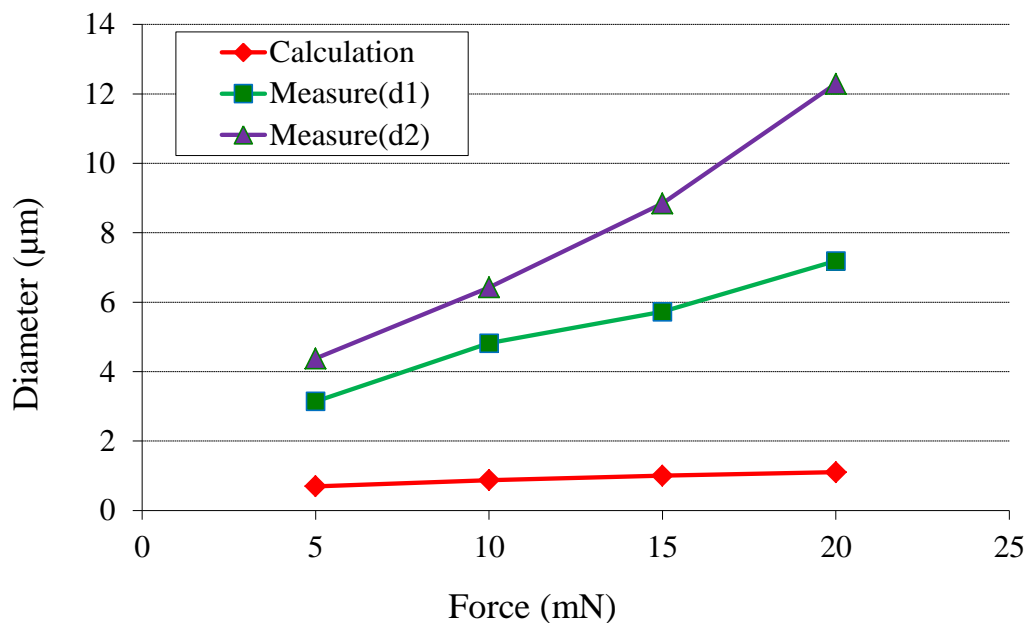
Figure 2.30 Comparison between the calculation results and measurement results of the indenter circle contact with various testing force on 30HV gold block

The Hartzian model was successfully applied to system that the low load applied with very small adhesion force [2-12]. However, the experiment on contact-mechanics of the AFM tip shape have shown disagree results between SEM images and the calculated values, because the AFM tips geometry were changed during applied force [2-13]. In our experiment, the comparison result in Fig 2.30 has shown that the calculation values and the measurement results are quite difference. Especially d2 measurement value has extreme error about 12µm deviated from calculation value. One possibility of non-agreement results can be explained in Fig 2.31 the theoretical heartzian's contact defined the radius of the circle of contact *a* is an elastic contact between curved and flat surface as shown in Fig. 2.31(A). While in practically, the contact area at a specified depth of the indentation depends not only on the shape of the indenter
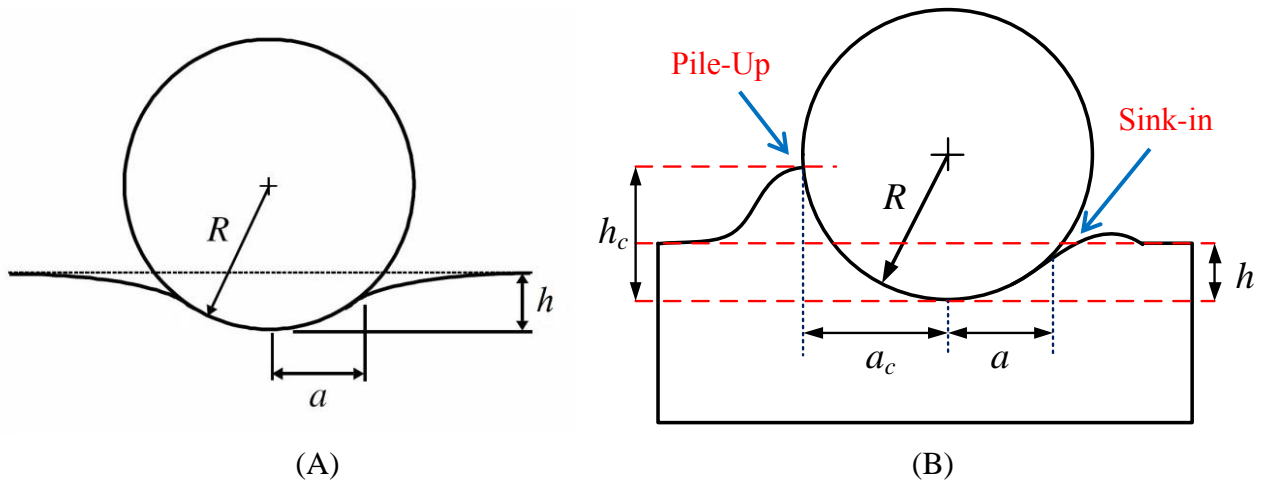
Figure 2.31 Comparison between (A) the theoretical heartzian's contact and (B) the practical measurement

but also on the elastic–plastic behavior of the materials being indented [2-14 to 2-16]. For hard materials the volume of material displaced by indentation is pushed out to the sides of the indenter and forms a pile-up that makes the contact area larger than the cross-sectional area of the indenter. In case of soft materials, the volume of material displaced by indentation is sinking into the center of the indentation called a sink-in effect that makes the contact area smaller than the cross-sectional area of the indenter. Moreover, because the indentation angle of the parallel spring mechanism produced both pile-up and sink-in behavior (Fig. 2.31(B)). The indenter cannot penetrate into material, and then the main structure is pulled down the indenter arm produced bending angle. From the experiment results shown in Fig. 2.32 to 2.35, the error becomes larger when the testing force is increasing. Here one of the limitations of this machine is discovered in this experiment. To reduced effect of indentation angle, the testing force generates from this mechanism should be lower than 15mN. And the material under test should softer than 30HV.

One factor that produced large or small indentation angle of parallel spring mechanism is the gap between indenter tip and specimen surface. To reduce indentation pile-up and sink-in problem, this indentation gap should be carefully defined. The experiment in section 2.6 is presented the appropriate indentation gap of this mechanism.

5mN
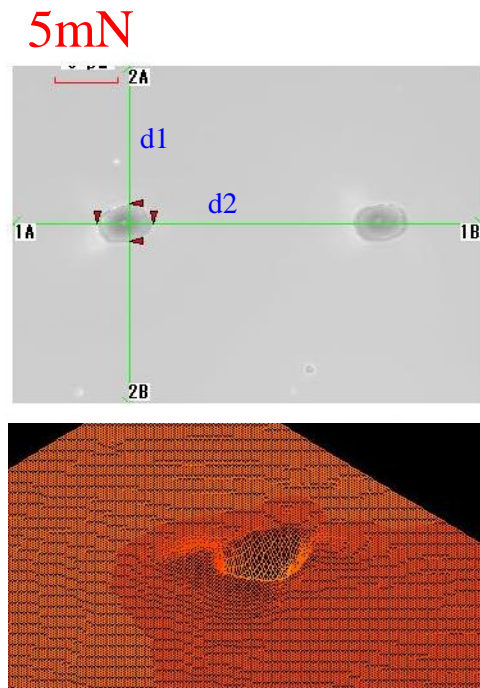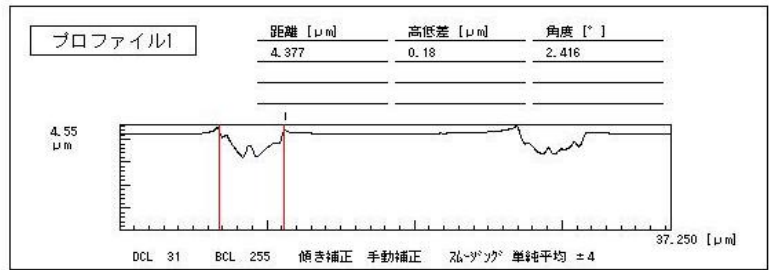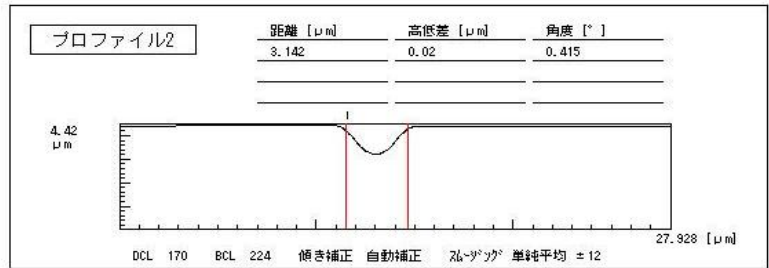
Figure 2.32 Indentation profile on gold block surface with 5mN testing force
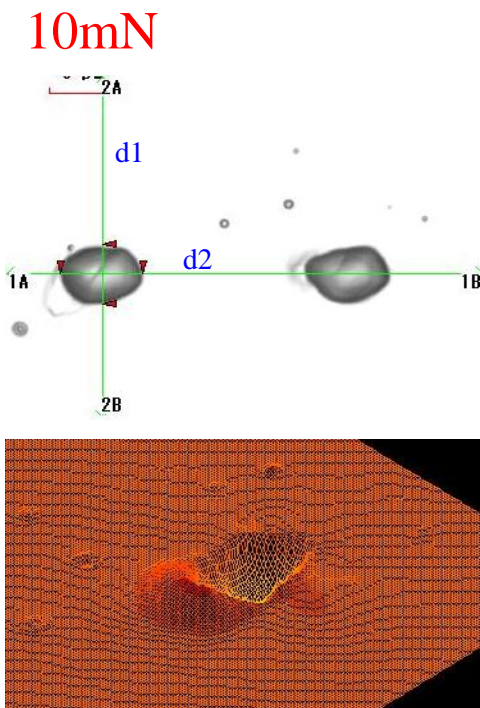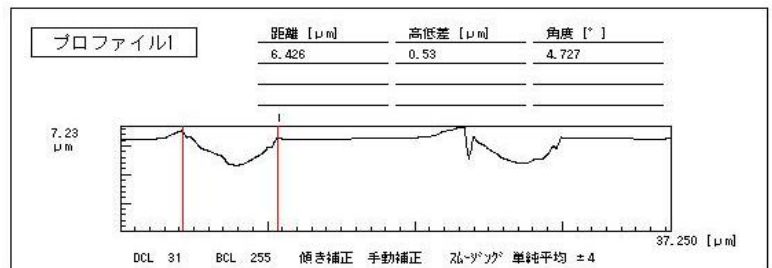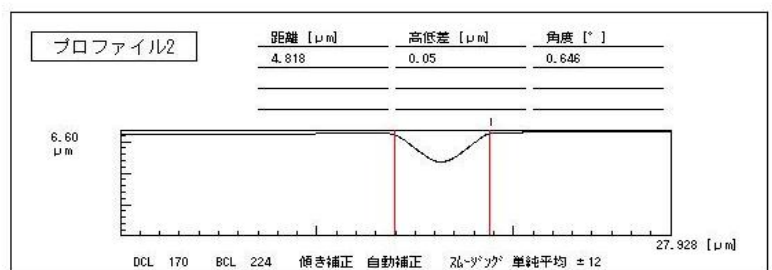
10mN

Figure 2.33 Indentation profile on gold block surface with 10mN testing force

15mN
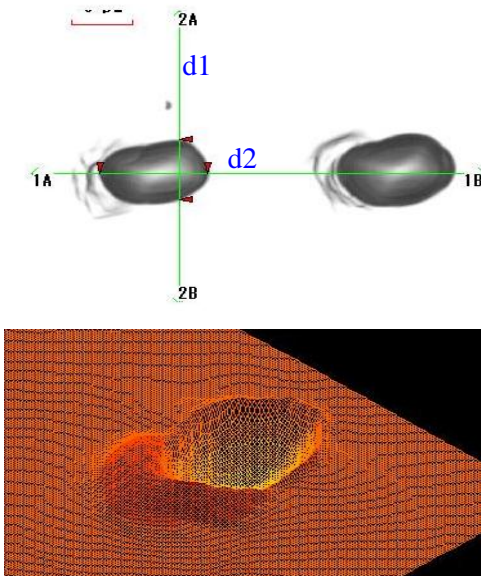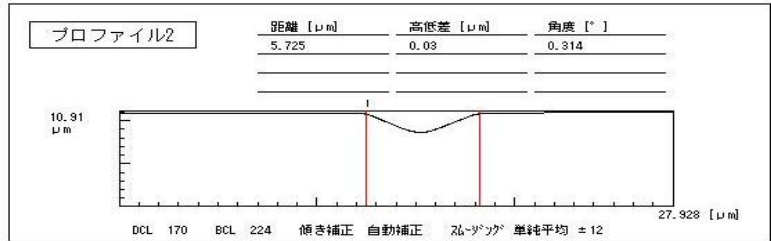
Figure 2.34 Indentation profile on gold block surface with 15mN testing force

20mN
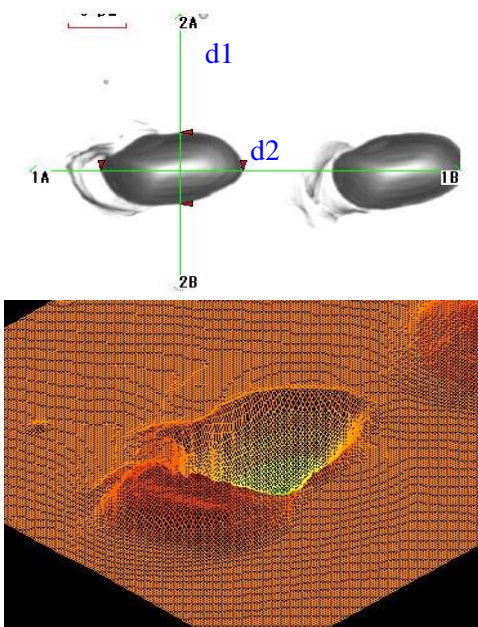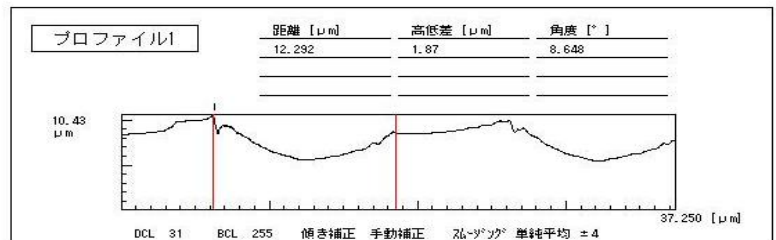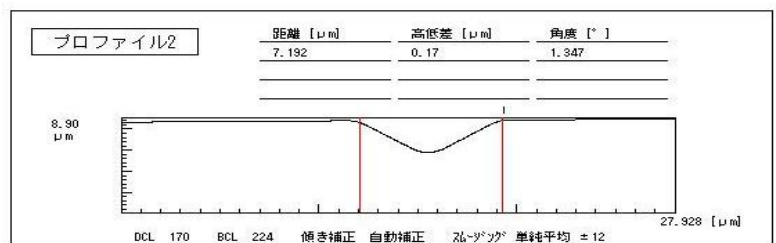
Figure 2.35 Indentation profile on gold block surface with 20mN testing force

60

2.6 Gap between the indenter and specimen surface

From the previous experiment results on Fig 2.32 to 2.35 have shown elliptic imprint indentation. Assumed that, this is a problem of the main structure deformation, because the indenter cannot penetrate into specimen surface then the bending action occurred. Another dominant factor is the gap between indenter and the specimen surface. Because the tandem structure has a linear movement limitation, this gap might a cause of problem. In this section described the effect of the distance of indenter from the specimen surface by using both simulation with finite element analysis (FEA) and the indentation experiment. The purposed of this experiment are that to find out the elliptic imprint problem and to verify the behavior of the indentation angle at different indenter gap. The FEA simulation is concerned only the movement behavior of the indenter rather than the material properties of the machine structure. While the indentation experiment is focused of the indentation imprint with several indenter gap. At the beginning, the simulation with FEA software is present and then the indentation experiment with certified hardness block is described, respectively.

2.6.1 Simulation and boundary conditions

The FEA software (Solidworks) is used to simulate the behavior of the main structure of this mechanism with three different indentation gaps (0μm, 40μm, and 100μm). The dimensions sizes as well as all materials parameters are well-defined close to the fabricated machine. For example, main structure using ABS material with elastic modulus 2×10^9 N/m^2 and Poissions ratio 3.94, the indenter tip using diamond with elastic modulus 1.22×10^9 N/m^2 and Poissions ratio 0.07, finally the specimen using pure gold(similar with 30HV hardness block) with elastic modulus 7.8×10^{10} N/m^2 and Poissions ratio 0.42. The boundary conditions in this simulation are shown in Fig.2.36 with 100mN external force applied to the lower L-Bar frame in the perpendicular direction, which is same as the pushing force from VCA. Applied contact sets with no penetration at the vertex of indenter tip and the face of specimen. Applied solid mesh type ant the FE mesh control element size is 300μm with ratio 1.5, total nodes are 87,550 nodes and total elements are 52,945 elements. The FEA mesh for indentation gap simulation is shown in Fig. 2.37. And the simulation results from each indentation gap are presented from Fig. 2.38 to 2.43.
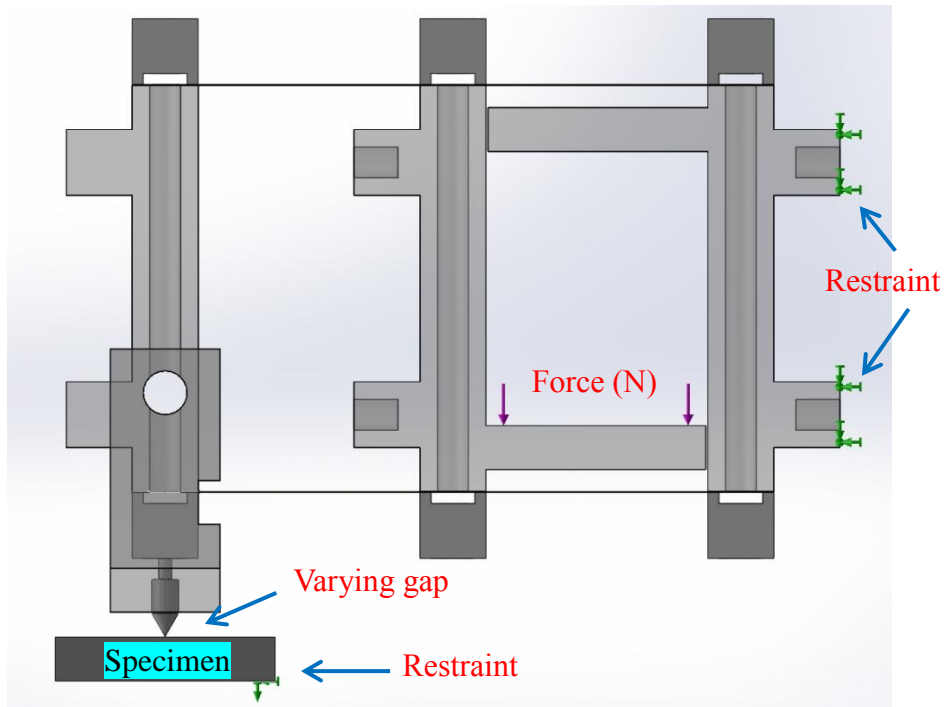
Figure 2.36 Boundary conditions of the simulation
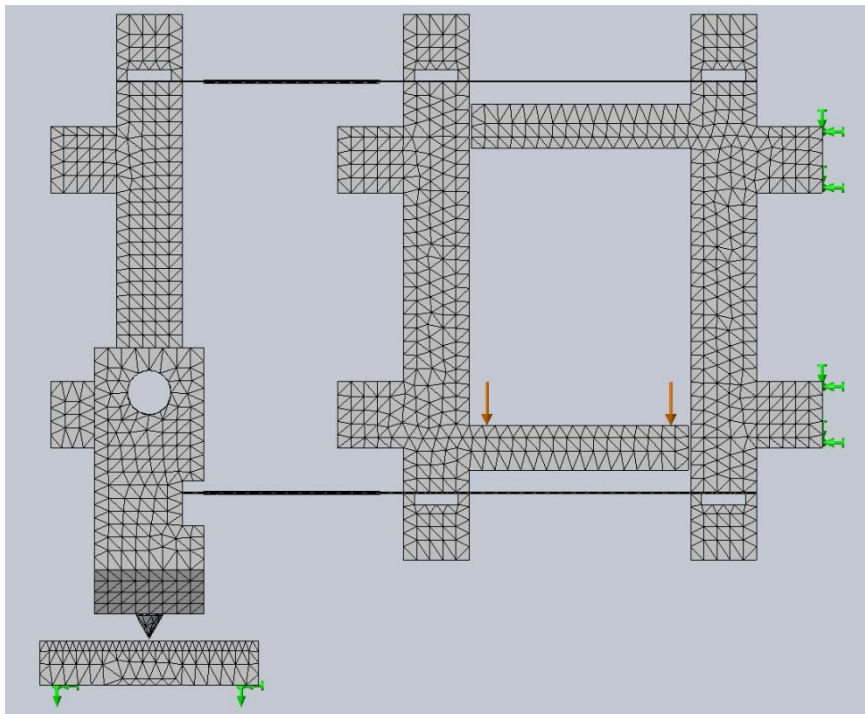
Figure 2.37 FEA mesh for the indenter gap simulation. The number of nodes and elements are 87,550 and 52,945 respectively
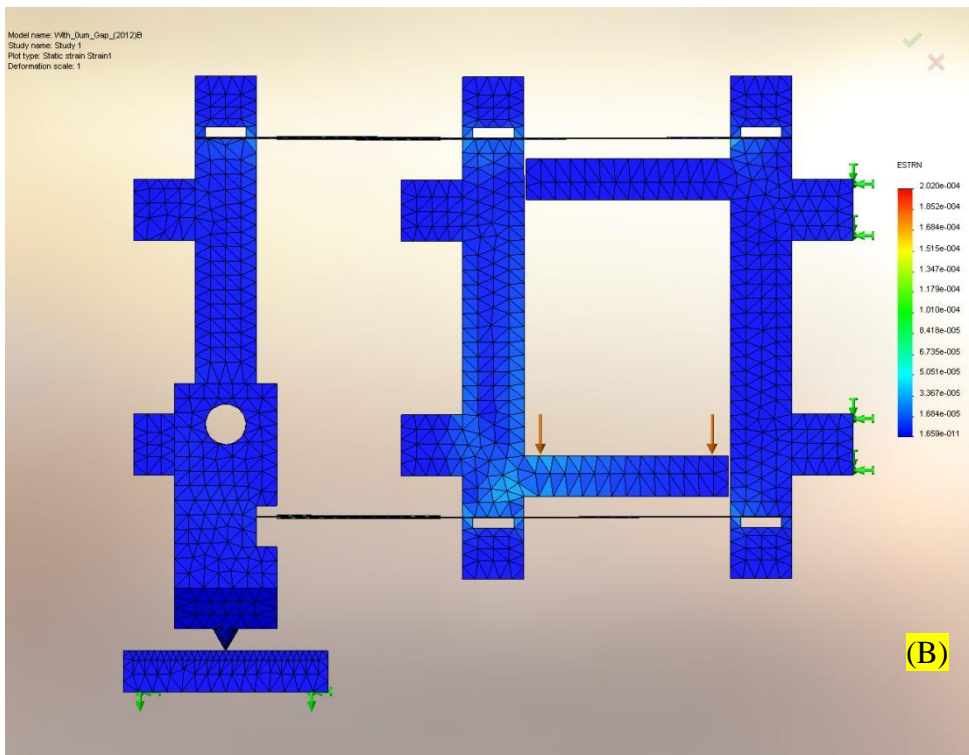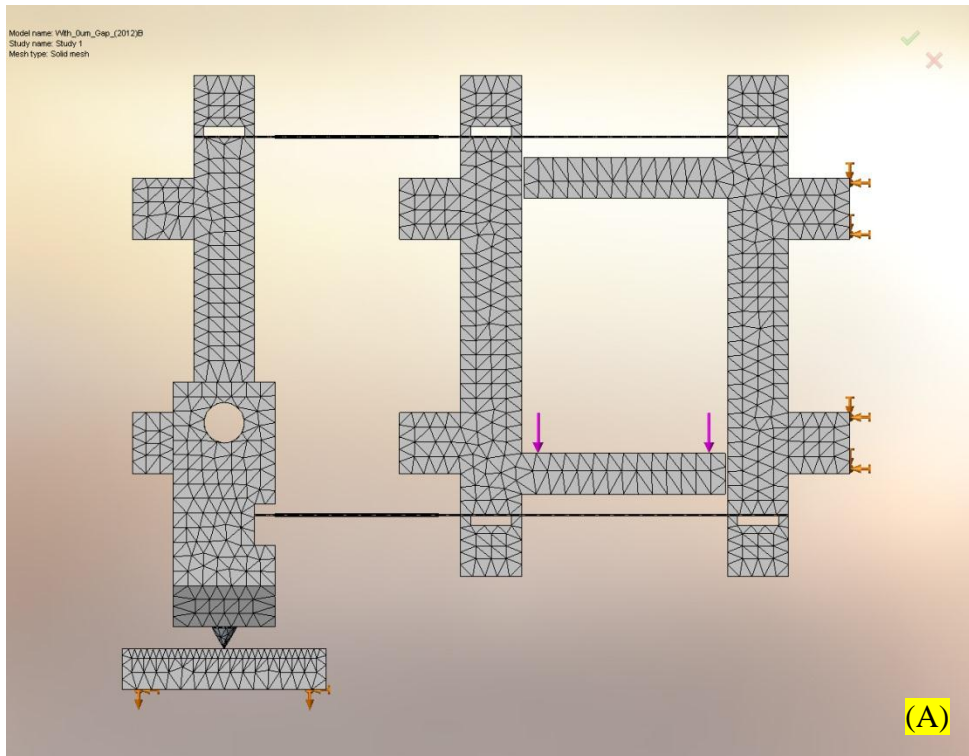
Figure 2.38 FEA simulation result at 0µm indenter gap (A) without deform and (B) with deformed result
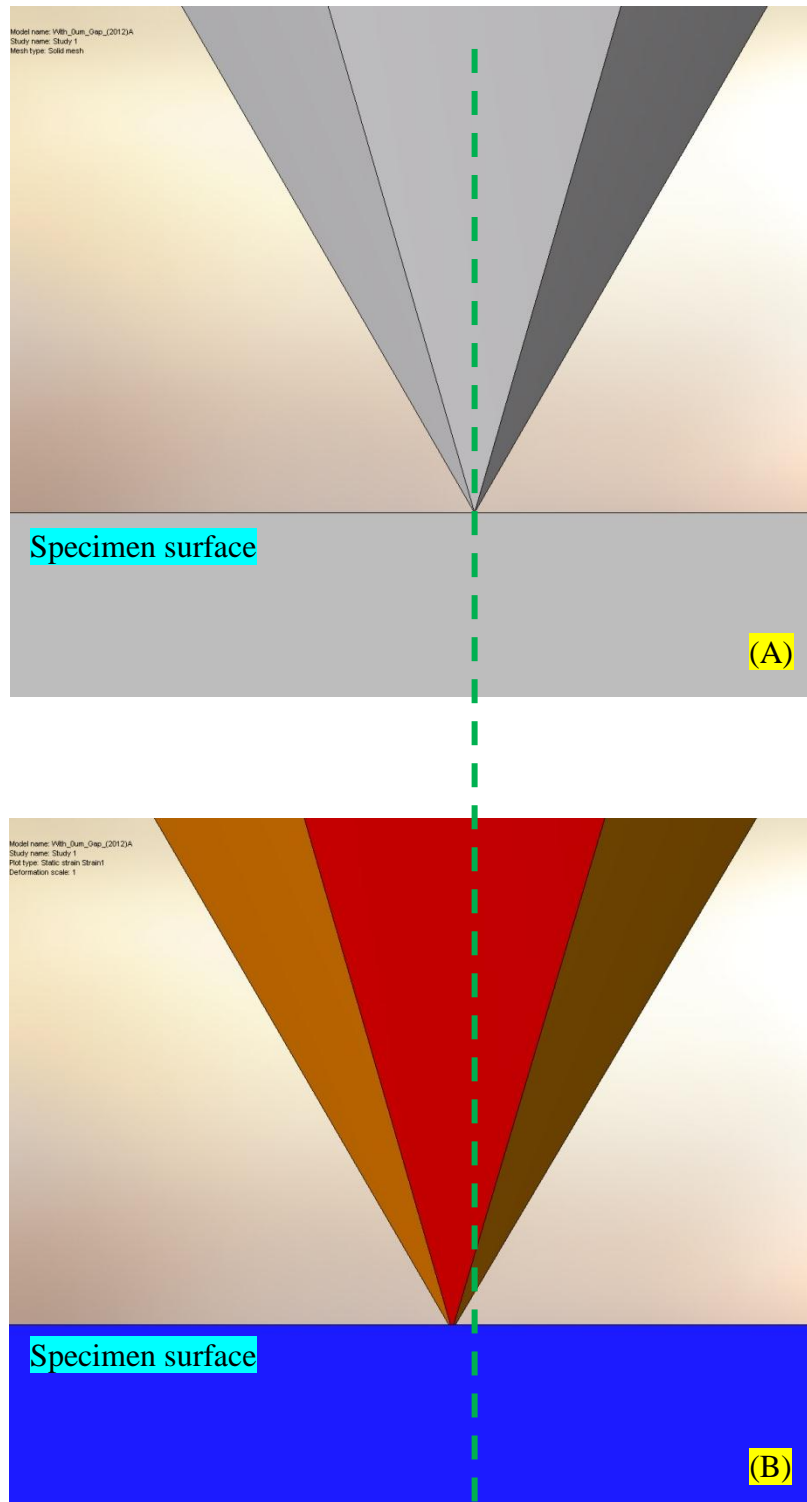
Figure 2.39 Close up view at the indentation contact point with 0μm indenter gap FEA simulation result, (A) without deform and (B) with deformed result
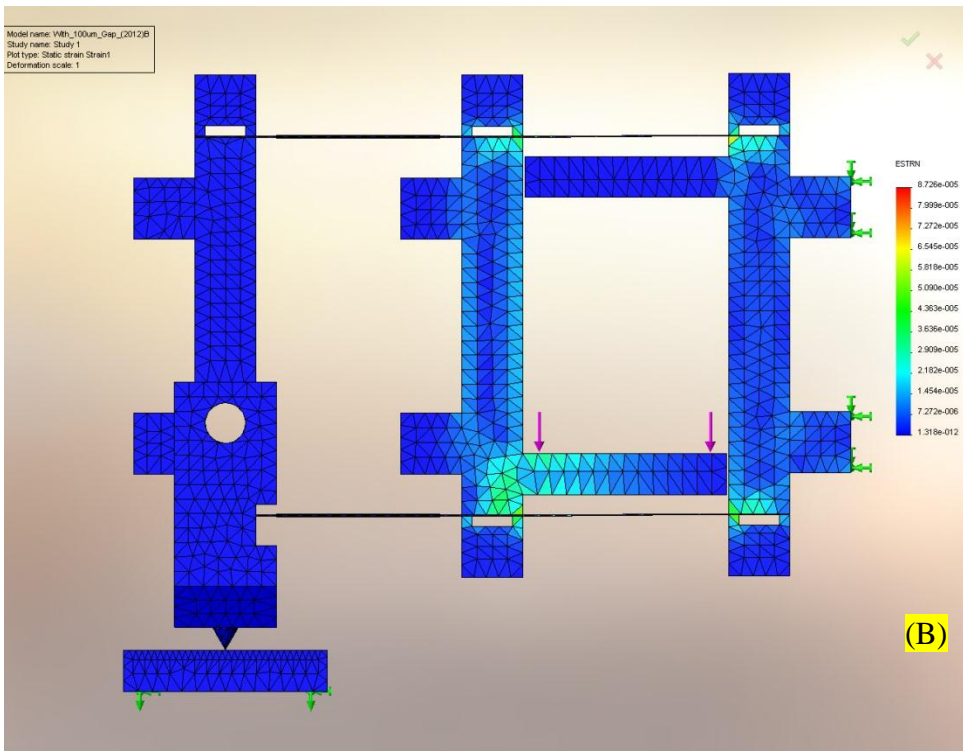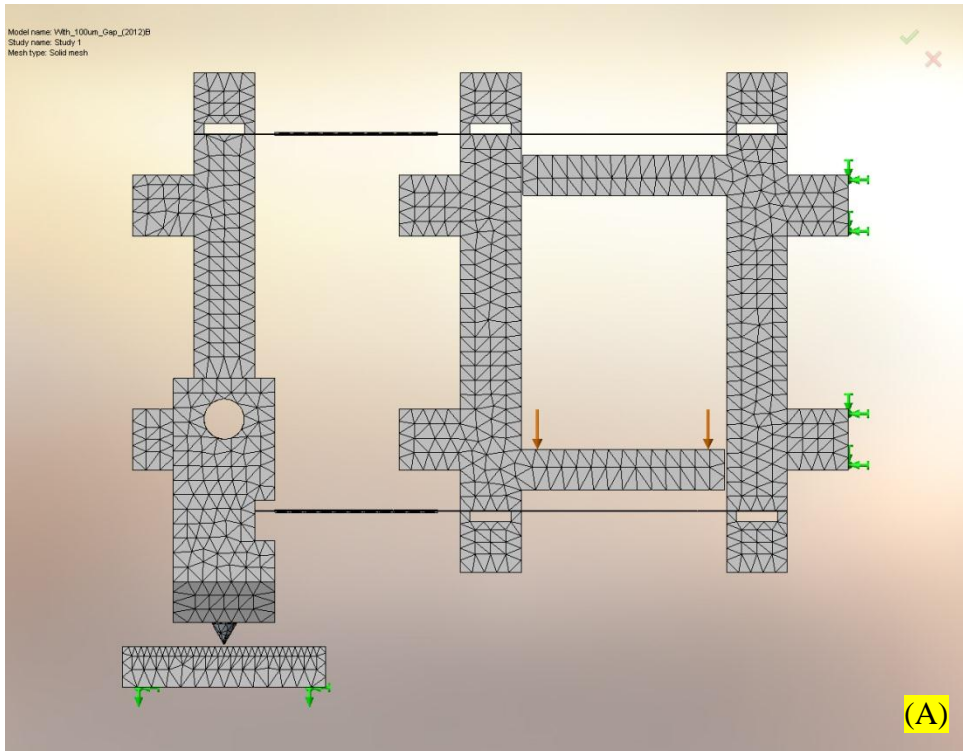
Figure 2.40 FEA simulation result at 100µm indenter gap (A) without deform and (B) with deformed result
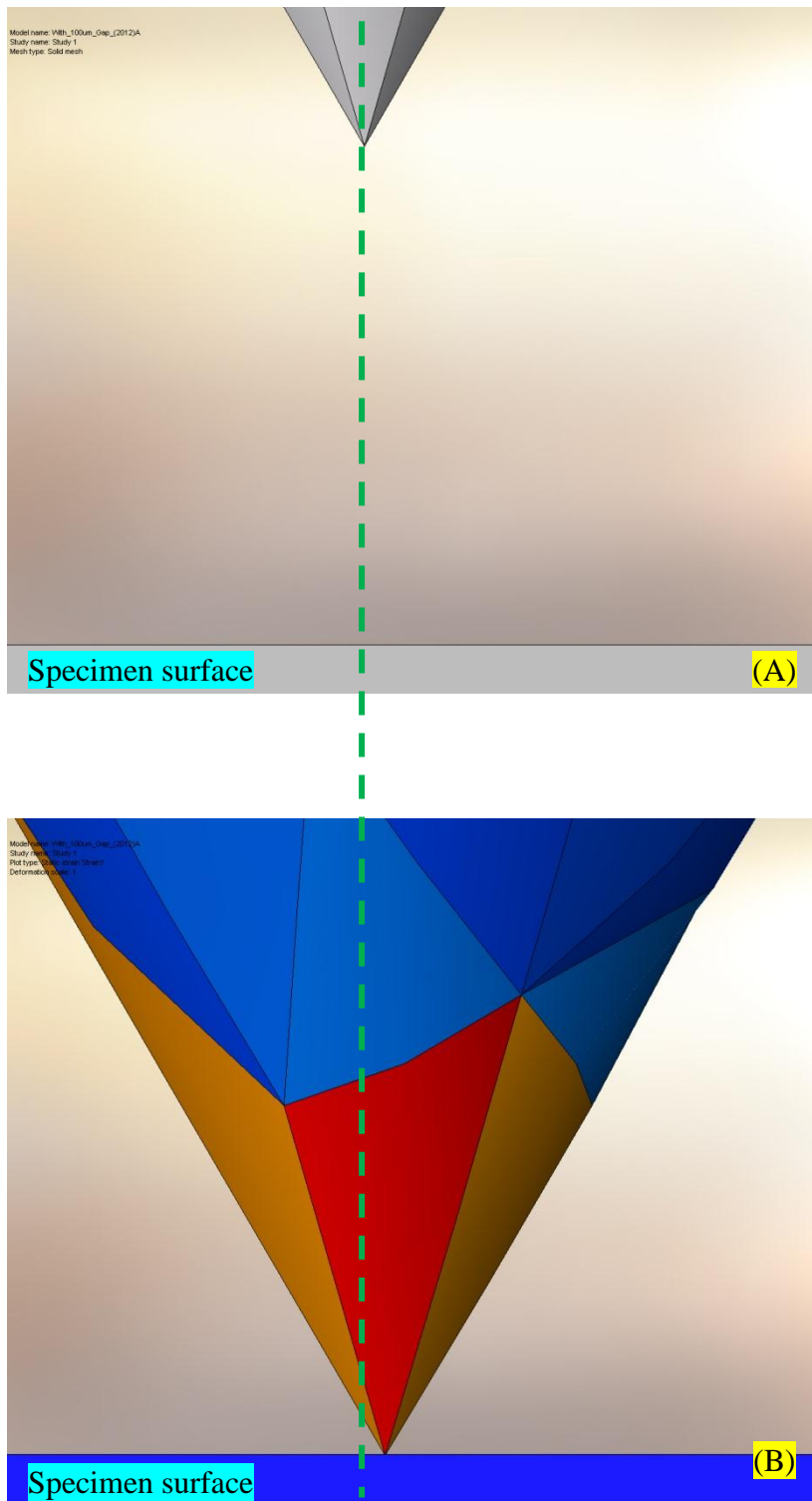
Figure 2.41 Close up view at the indentation contact point with 100µm indenter gap FEA simulation result, (A) without deform and (B) with deformed result
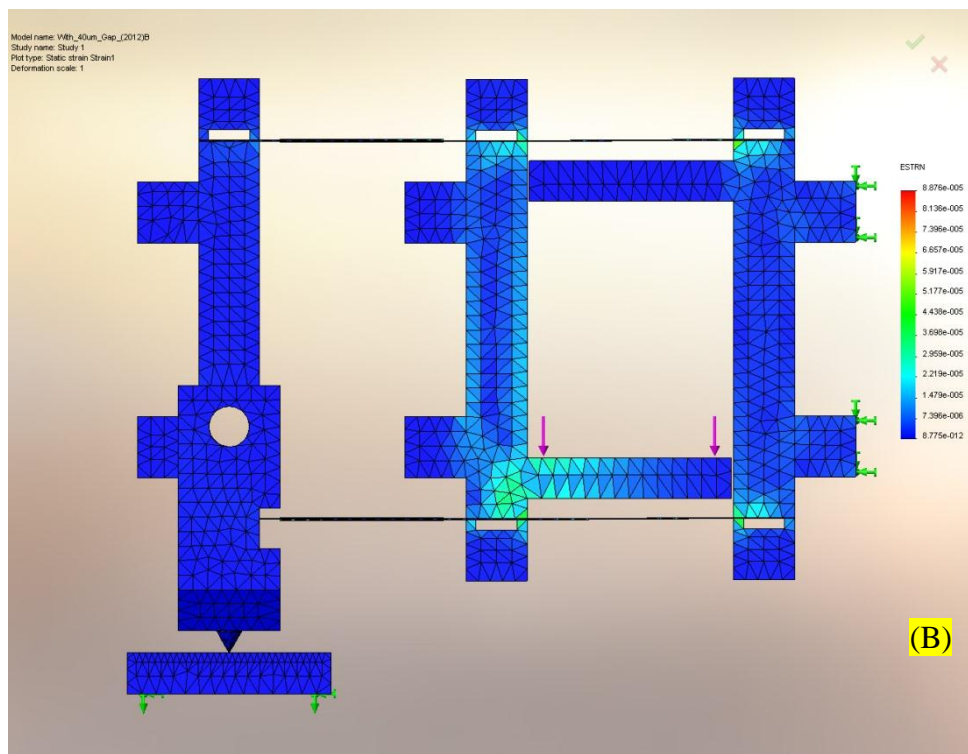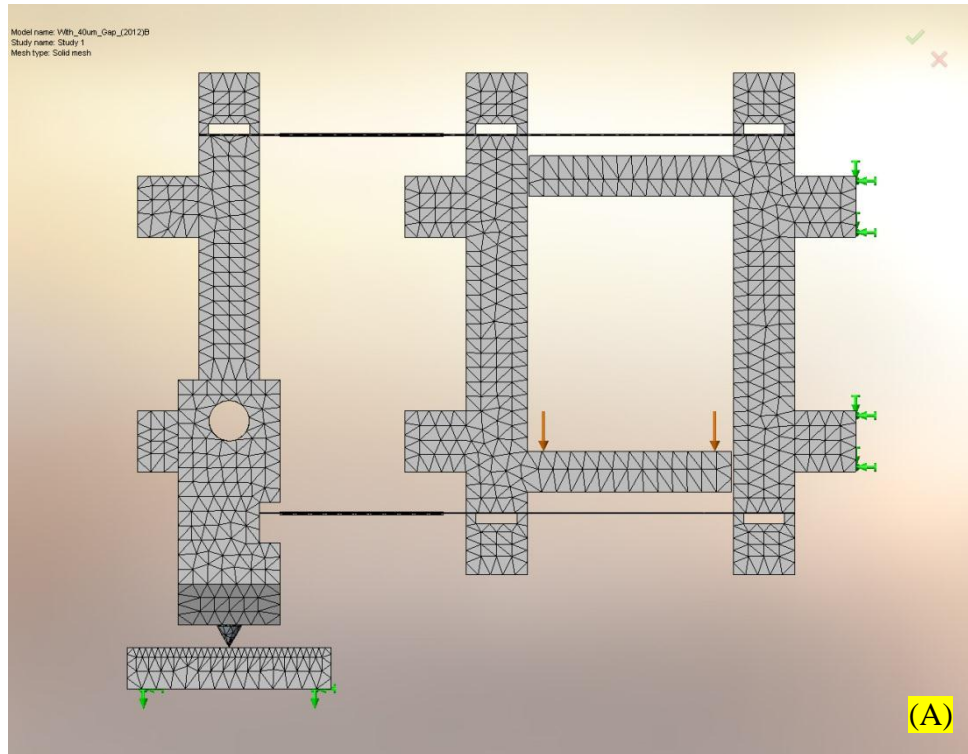
Figure 2.42 FEA simulation result at 40µm indenter gap (A) without deform and (B) with deformed result
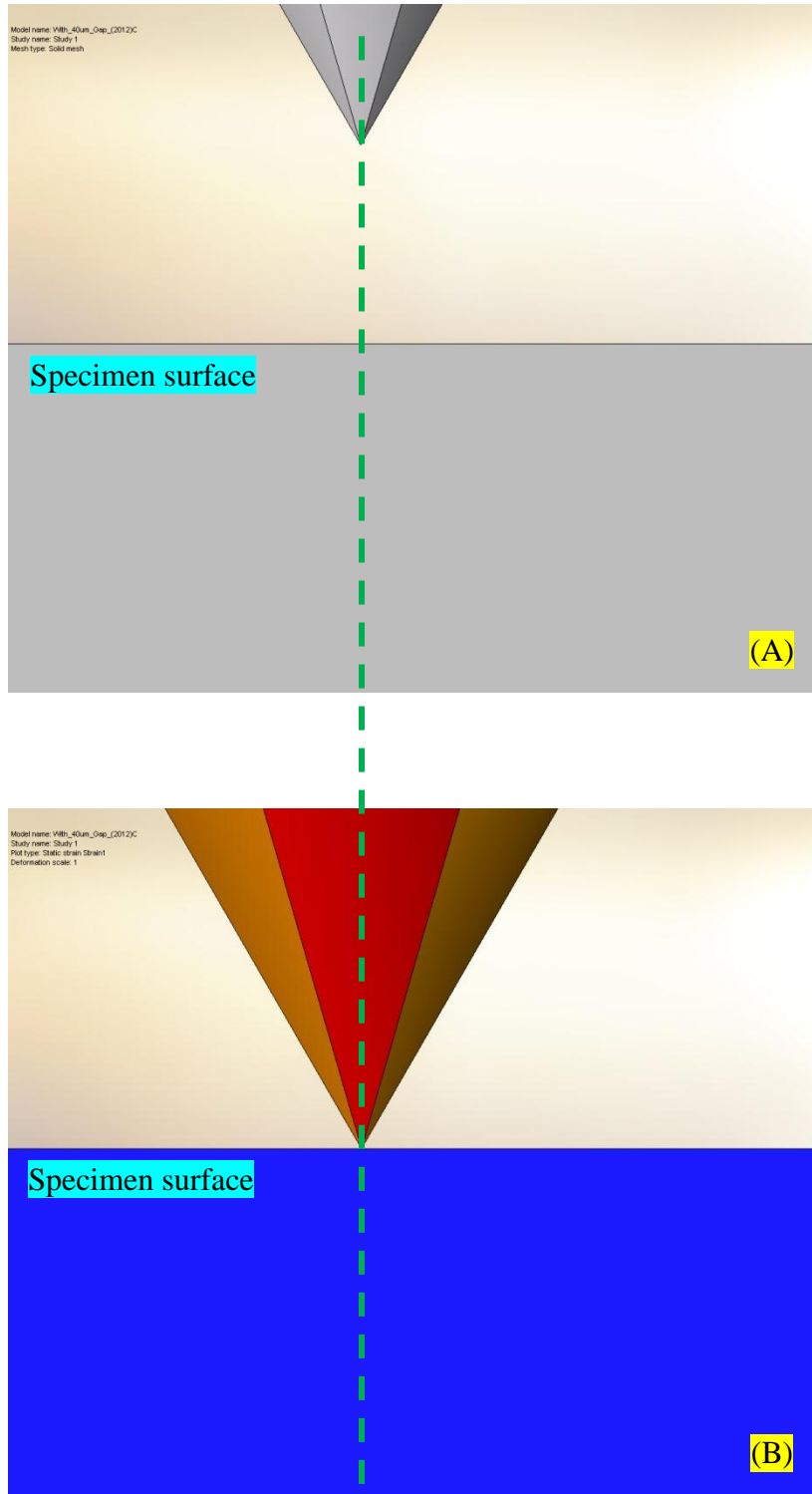
Figure 2.43 Close up view at the indentation contact point with 40µm indenter gap FEA simulation result, (A) without deform and (B) with deformed result

When the indenter that attached with the parallel mechanism making an indentation without gap between the indenter tip and specimen surface, the simulation result has shown that the indenter was pushed forward as shown in Fig 2.38 and 2.39. While, indenter gap is increased to 100μm, the simulation result has shown that the indenter was pulled backward as shown in Fig. 2.40 and 2.41. On the other hand, with 40μm indenter gap the simulation result has shown that the indenter is making contact with vertically to the specimen surface as shown in Fig. 2.42 and 2.43. Here the simulation results with different indenter gaps have shown variety of indentation behavior. Next, the indentation experiment with certified hardness block is presented. And then the results can be compared at the end of this section.

2.6.2 Indentation experiments with different indenter gaps.

In this experiment the 30HV certified hardness block was used as the specimen under test. The test procedure is that making a series of indentation with 5mN, 10mN and 15mN on the specimen with different indenter gaps, i.e., indenter gap are varied from 10 to 100μm. After a series of indentation have done, then 3D profiles of each indentation are measured as shown in Fig. 2.44. Finally, the diameter and the concentric error of each indentation are measured and compare the measurement results with the simulation results as shown in table 2.2.

As mention before, we are not much concerned about the exactly movement of the structure in simulation test. The simulation results that shown in table 2.2 are only the estimation from the simulation results. The main concerned is the indentation behavior from different indenter gaps. From the simulation results in Fig. 2.38 to 2.41 have shown that the indentation direction is not perpendicular with the specimen surface. Because a tandem structure is pushed/pulled the indenter from the main structure. And also from the simulation results in table 2.2 the concentric error of the indentation is increased with increasing indenter gap. The experiment results with various indenter gaps also described with the same way with the simulation results. In Fig. 2.44 at the indenter gap that are large than 40μm, the indentation shape are begin to elliptic. It is clear that the level or distance between indenter and surface under test can give different meaning of indentation. Here another limitation of out machine is discovered, that is the indenter gap should be smaller than 40μm.
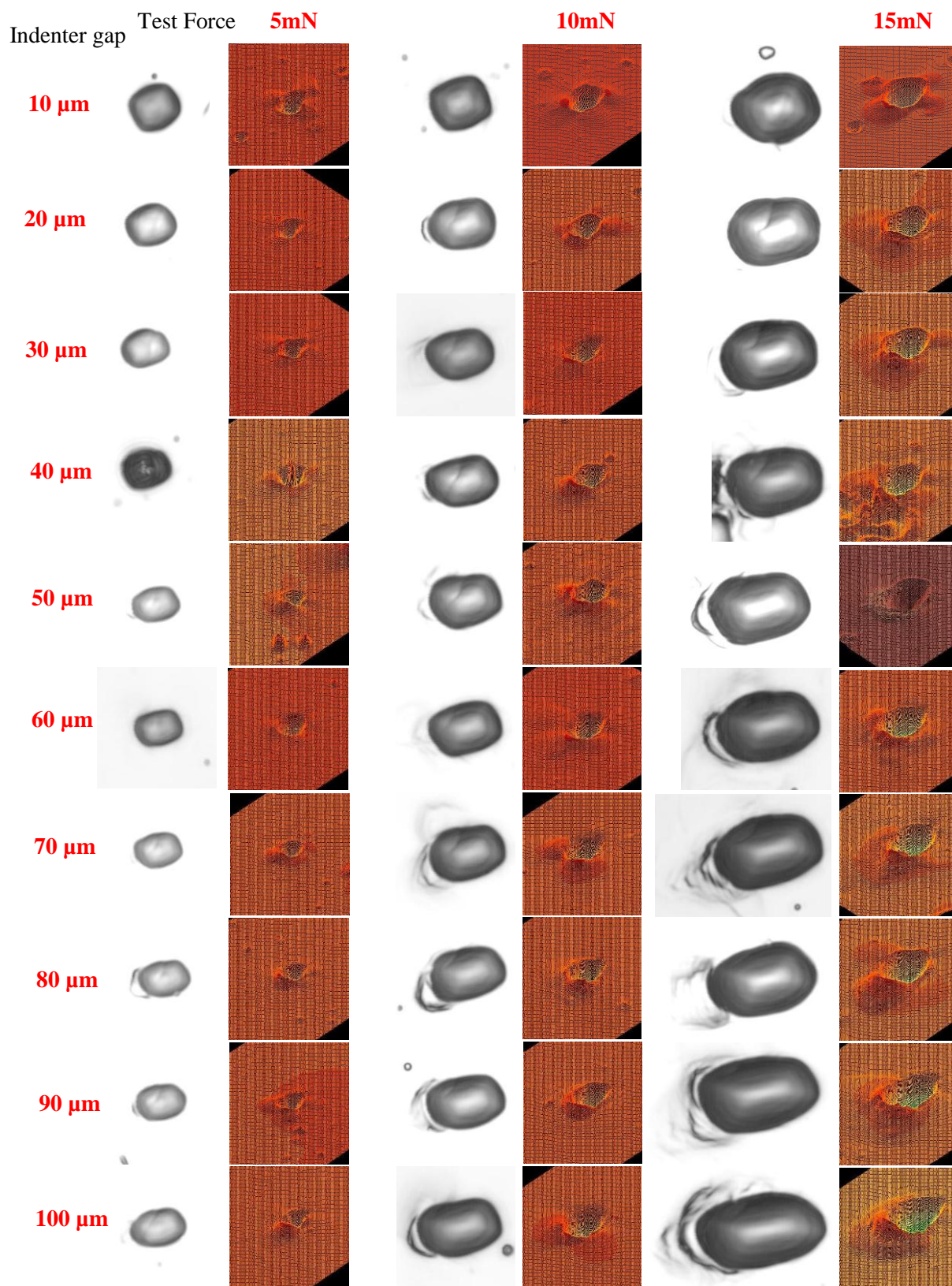
Figure 2.44 Indentations 3D profile on 30HV block with different test force and different indenter gaps

Table 2.2 Effect of the indenter gap on each test force

Force	Inderter Gap	Measurement			Simulation
(mN)	(μm)	d1(μm)	d2(μm)	Concentric Error(μm)	Deviation from perpendicular point(μm)
5	10	4.183	4.631	0.22	-0.04
	20	4.05	4.711	0.33	0.00
	30	3.526	4.374	0.42	0.03
	40	3.716	4.784	0.53	0.07
	50	4.218	5.164	0.47	0.10
	60	3.509	4.737	0.61	0.14
	70	3.592	5.328	0.87	0.17
	80	3.675	5.654	0.99	0.21
	90	3.67	5.295	0.81	0.24
	100	3.632	5.333	0.85	0.28
10	10	4.797	5.564	0.38	
	20	4.507	6.387	0.94	
	30	4.363	6.207	0.92	
	40	4.368	6.691	1.16	
	50	4.577	6.851	1.14	
	60	4.594	6.741	1.07	
	70	4.855	7.104	1.12	
	80	4.684	7.1	1.21	
	90	4.879	7.291	1.21	
	100	5.028	7.891	1.43	
15	10	6.491	7.828	0.67	
	20	6.151	8.588	1.22	
	30	6.244	9.097	1.43	
	40	6.094	8.835	1.37	
	50	5.8	9.364	1.78	
	60	6	9.425	1.59	
	70	6.334	9.989	1.83	
	80	6.16	10.363	2.10	
	90	6.976	10.962	1.99	
	100	6.552	11.874	2.66	

2.7 Basic performance

After successful in measurement system and control system of machine, this section presents an experiment on indentation on certified hardness blocks. The 30HV and 100HV certified hardness block is used as unit under test, picture of the hardness blocks is shown in Fig. 2.45. According to block certificate, these two hardness blocks were certified by three forces range, 1kgf, 0.1kgf and 0.01kgf. The lowest testing force is 10gf (100mN), which is larger than our machine. This experiment may cause a lower test force effect, that the indentation size is increased with decreased test force [2-17]. However, only 30HV and 100HV blocks that available in the market at this moment.

The experiment procedure as follows; making an indentation with three level of testing force (5mN, 10mN and 15mN) on surface of both hardness blocks. In the experiment, controlling force application and force removal time are 30s. The holding time at maximum force is 30s, as the pattern of testing cycle shown in Fig. 2.28. Then the indentation 3D profile is investigated by 3D laser scanning microscope as shown in Fig. 2.46. After that, the elasticity of blocks is investigated by the indentation load-depth curve as shown in Fig. 2.47 and 2.48 for the indentation load-depth curve on 30HV and 100HV, respectively. Finally,
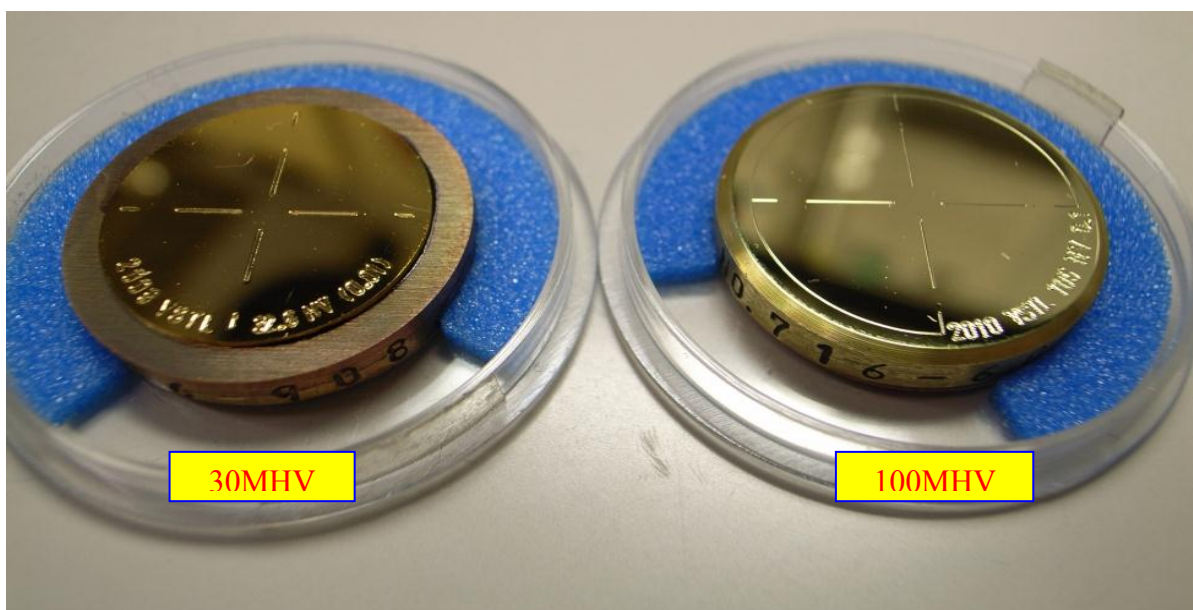
Figure 2.45 30HV and 100HV certified hardness blocks
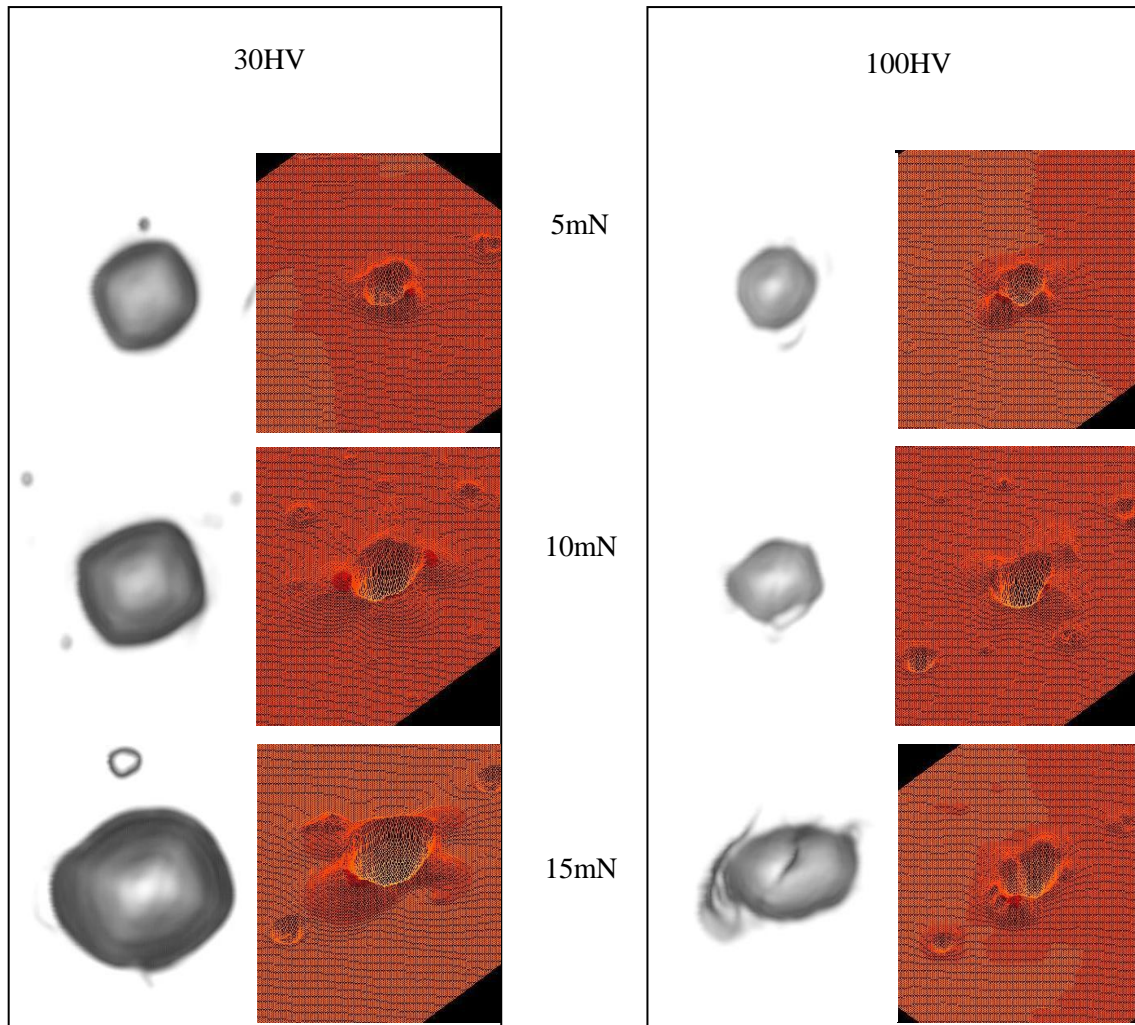
Figure 2.46 Indentation 3D profile of 30HV compare with 100HV

the diameter of each indentation on each force are measured and compared with the maximum depth from load-depth curve as shown in table 2.3.

From 3D profile of indentation on 100HV with 10mN tested force has shown elliptic print dimension. That is a limitation of machine performance. Because 50μm tick of phosphor bronze is used as leaf-spring to hold all structure together. The leaf-spring might be cause of problem. The main structure cannot with stand 10mN test force on harder surface, because reaction force is larger than a stiffness of main structure. The geometric of indenter print is changed due to the rotation of cantilever when indenter cannot penetrate into harder surface. So, from this issue we make a decision to limit operation range of this machine at 10mN test force on surface that softer than 30HV, to avoid damage of moving part of this mechanism.

Table 2.3 Diameter of indentation compare with maximum depth from load-depth curve

Test Force	100HV			30HV		
(mN)	d1(μm)	d2(μm)	Depth(μm)	d1(μm)	d2(μm)	Depth(μm)
5	3.24	3.59	0.50	4.18	4.63	0.90
10	3.49	4.53	1.20	4.80	5.56	0.50
15	3.85	5.83	2.00	6.49	7.83	3.00
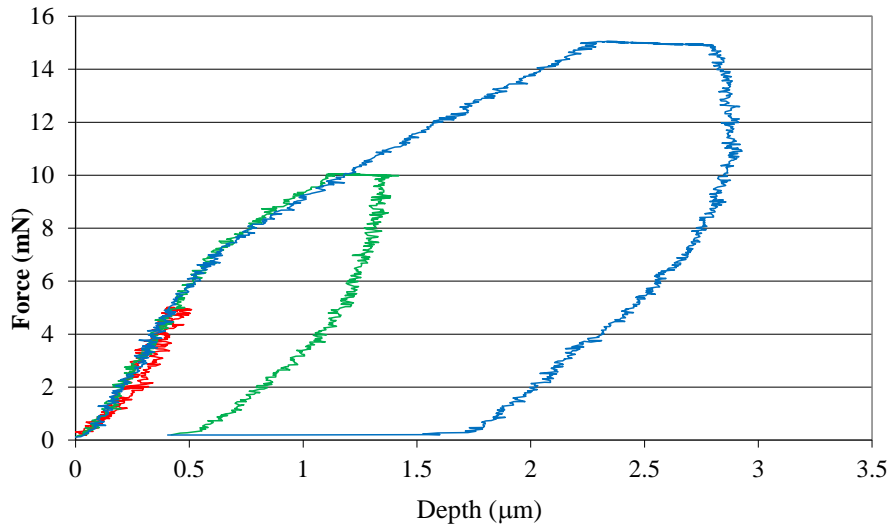
Figure 2.47 Indentation load-depth curve of 30HV certified block at 5mN, 10mN and 15mN testing force
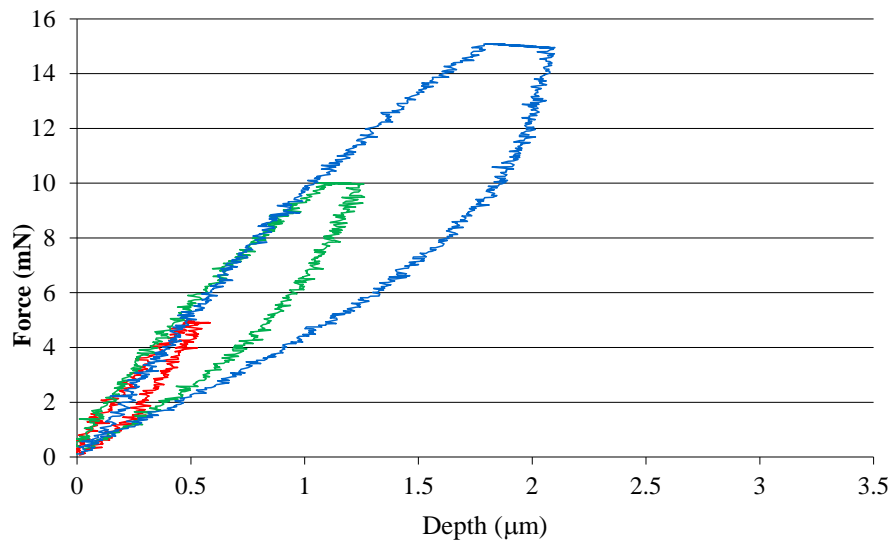
Figure 2.48 Indentation load-depth curve of 100HV certified block at 5mN, 10mN and 15mN testing force

Because non-standard using of indenter, testing cycle and force applied; even certified hardness blocks were used as reference material, but we cannot compare the load-depth curve directly with load-depth curve that come from standard machine. Regarding to researching on effect of indenter shape [2-18], the 60° conical indenter and Berkovish indenter were compared. Their results show 0.25μm maximum depth from load-depth curve of Berkivish indenter and 0.37μm from 60° cone indenter at hardness about 100HV by 10mN test force. For 60° cone microindenter as conform to standard, it should have tip radius less than 0.3μm which is very sharp when compare with our stylus tip indenter (2μm tip radius). This evident has shown that this machine should obtain maximum depth on 100HV at 10mN test force lower than 0.3 μm. But from the result on table 2-2 shown result at 10mN test force on 100HV block has maximum depth at 2μm, which is five times deeper than commercial machine. We can evaluate the degree of hardness from the comparison with the results of 30HV and 100HVs standard blocks although the load-depth curve from our machine is different from the results of standard machine.

2.8 Discussion

In this chapter the first prototype of microhardness machine was constructed and described that the simple mechanical structure of parallel leaf spring mechanism and small voice coil actuator can generate force in micronewton range. This machine can provided the best resolution of generated force at 50μN per step with good linearity, less vibration and less hysteresis up to maximum range 20mN. In the experiment results, the ability of this machine has been presented by the reasonable hardness results when compare with the 30HV and 100HV certified hardness blocks. The experiment also demonstrated the limitation of this micromechanism. This microhardness mechanism is capable to measure with the material that softer than 30HV with the maximum testing force at 15mN, and 40μm indenter gap. On next chapter, the implementation of this micromechanism with the microrobot will be presented. And then the surface stiffness investigation on several BIO samples are described the machine performance.

CHAPTER 3.MICROINDENTATION ROBOT

3.1 Piezo driven inchworm microrobot

3.1.1 Principle and structure design

The tiny robot driven by the piezoelectric transducers are capable of working even in the vacuum SEM chamber with the microscopic positioning resolution has been developed [3-1]. As shown in Fig. 3.1 that is the diagram picture and the photo of the fabricated inchworm robot, it has the dimensions with 30mm in width, 50mm in length and 30mm in height. The small robot is consisting of two front and rear electromagnetic legs. They are connected with two piezoelectric actuators for providing the accurate inchworm locomotion on metal ground surface. The equipment to control this robot is composed of robot driver model ERP-1201k, the data acquisition PCI-NI 6723 and PC. The control diagram is shown in Fig. 3.2. This microrobot can control step movement by supply voltage to piezoelectric transducers simultaneously with electromagnetic
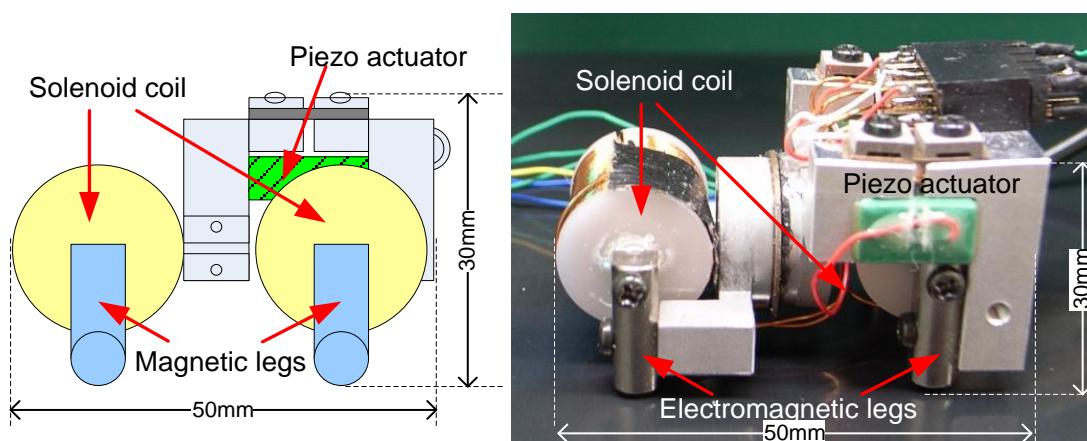
Figure 3.1 Diagram picture and photo of the original inchworm microrobot
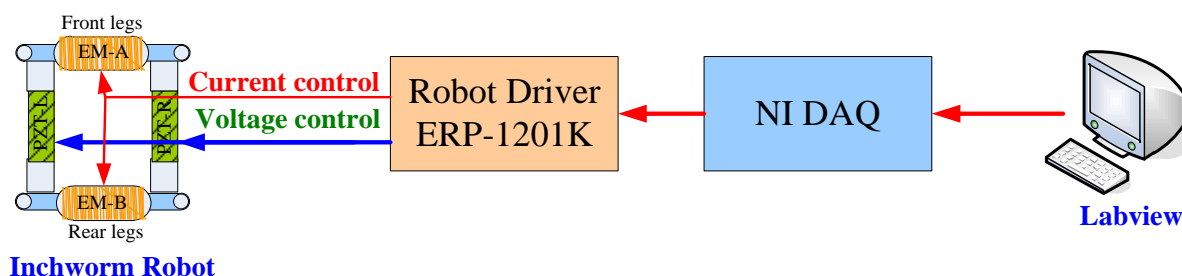
Figure 3.2 Control diagram for inchworm robot

legs coil current control. By using Labview, the DAQ card is generated precise voltage output waveform sent to robot driver. The control waveform can be transferred to electromagnetic legs current control and piezoelectric transducers voltage control by a robot driver. The control algorithm of this robot is presents in the next section.

3.1.2 Robot control algorithm

This robot is employed as a microlocomotion platform since it can provide very high resolution movement. Shown in Fig. 3.3 that is the motion control sequence of robot for forward movement. At first, there is no electric current and voltage supplied to electromagnetic legs (EM-A and EM-B) and piezoelectric transducers (PZT-R and PZT-L), respectively. Then the front and rear legs is free, and the piezoelectric transducers are in initial state. In the next phase, the electromagnetic B(EM-B) which is the rear legs of a robot is activated to clamp on metal ground surface by electric current that supplied to EM-B. On the other hand the front legs (EM-A) are still free from electric current. Meanwhile, a pair of piezoelectric transducers (PZT-R and PZT-L) can expand by supplied a positive voltage cycle. Because of the rear legs (EM-B) are clamped, so the front legs (EM-A) are pushed by the expanding of PZT-L and PZT-R. Finally the front legs are fixed by supplied electric current to EM-A,
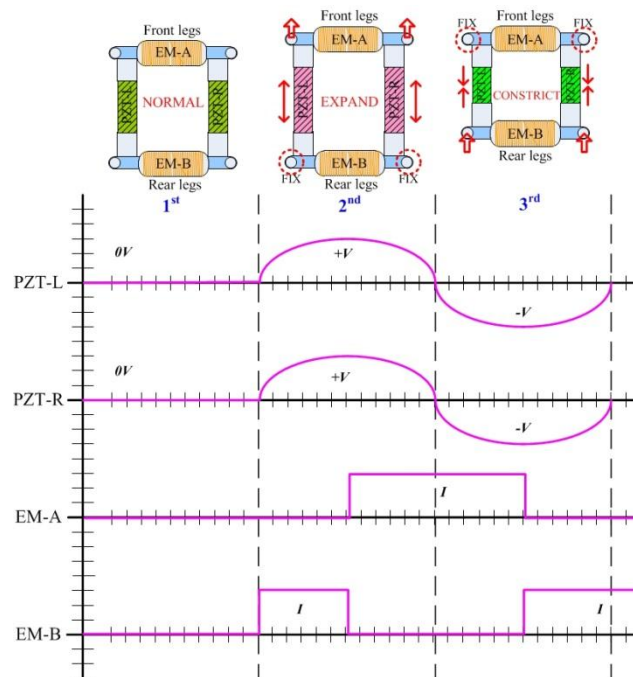
Figure 3.3 PZT and electromagnetic legs control timing diagram for forward direction
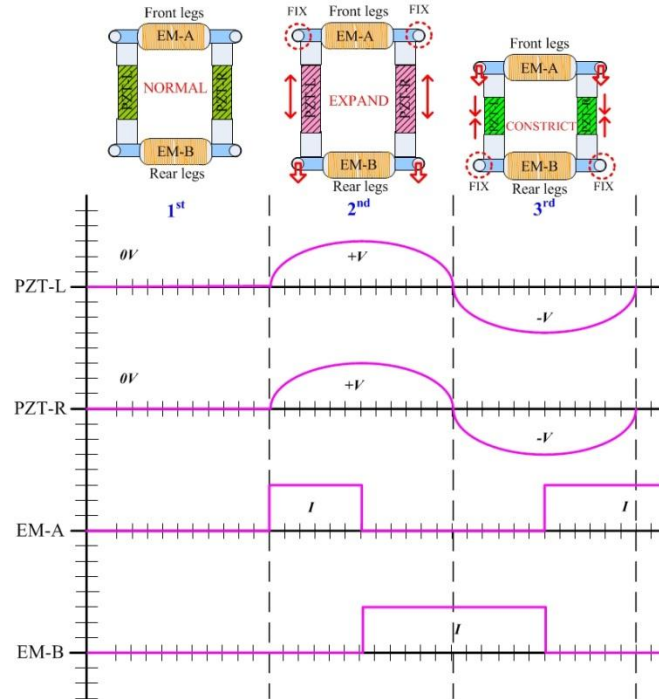
Figure 3.4 PZT and electromagnetic legs control timing diagram for backward direction

on the other hand the rear legs (EM-B) are free from electric current. Meanwhile, the PZT-R and PZT-L are constricting by supplied the negative voltage cycle. During this phase, the rear legs (EM-B) are pulled by PZT-R and PZT-L, as the front legs are fixed. When repeat this sequence, the robot will move forward precisely with a manner of inchworm locomotion. When this sequence is given with an opposite pole, then the movement of a robot will be backward direction as shown in Fig. 3.4.

The turning motion control of this robot is much more complicated than forward or backward directions. The motion control timing diagram for turn right is shown in Fig. 3.5. At the first rear legs(EM-B) are fixing then supplied different phase voltage signal to PZT as shown in the 1st stage of Fig. 3.5 (PZT-L is expanding while PZT-R is constricting). At this stage the front leg right (EM-A-R) side is pulling back while another front leg (EM-A-L) is pushing forward. After that in the 2nd stage, front legs (EM-A) are fixing and the reversed phases signal are supplied to PZT (PZT-L is constricting while PZT-R is expanding). At this stage the rear leg left side (EM-B-L) is pulling back while another rear leg (EM-B-R) is pushing forward. When repeat this sequence, the robot will turning right precisely with a manner of inchworm locomotion. When

this sequence is given with an opposite pole, then the movement of a robot will be turn left direction as shown in Fig. 3.6.
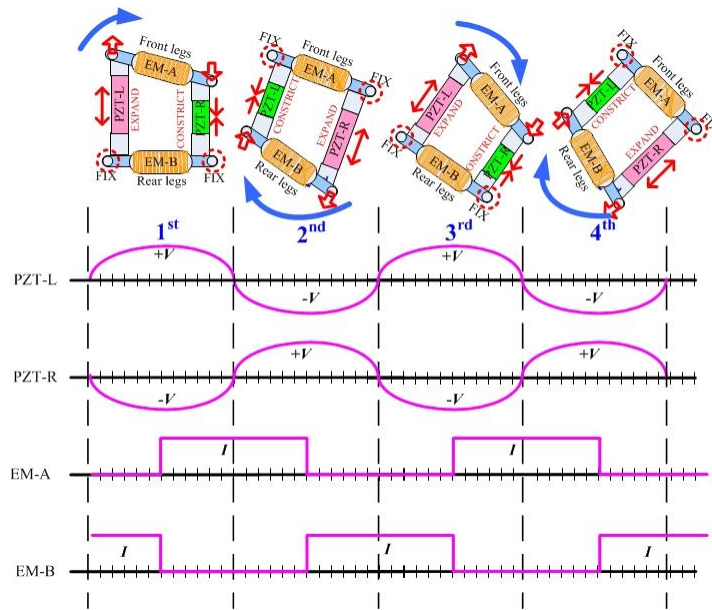
Figure 3.5 PZT and electromagnetic legs control timing diagram for turn right direction
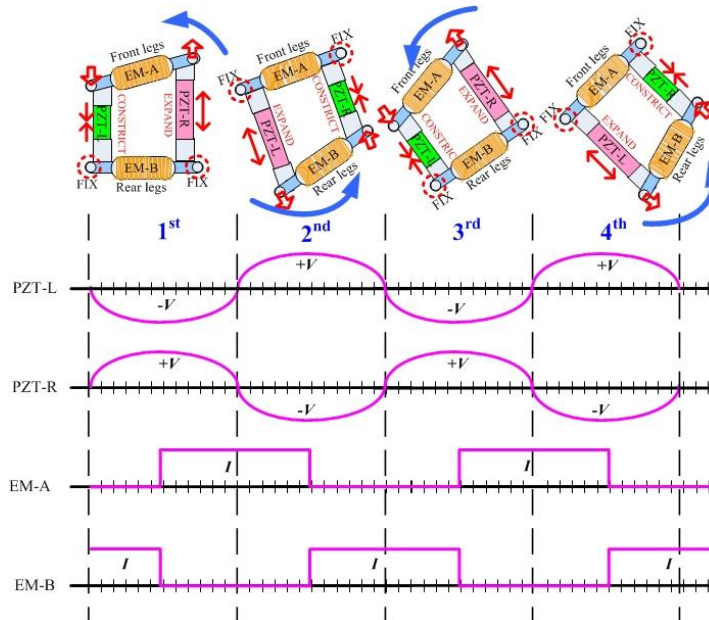
Figure 3.6 PZT and electromagnetic legs control timing diagram for turn left direction

3.1.3 Robot movement performance test

In this section presents the basic performance of a robot. Previously, this robot is moving without any guidance or position feedback control, so the experiment is separated into two parts, the step resolution test and repeatability test. The experiment setup for resolution of a robot movement is shown in Fig. 3.7. The laser displacement sensor (LK-G30) is used to detect the movement behavior of a robot in one dimension. For this experiment, a robot is moved only forward (FW) and backward (BW) directions, there are no turn right (TL)
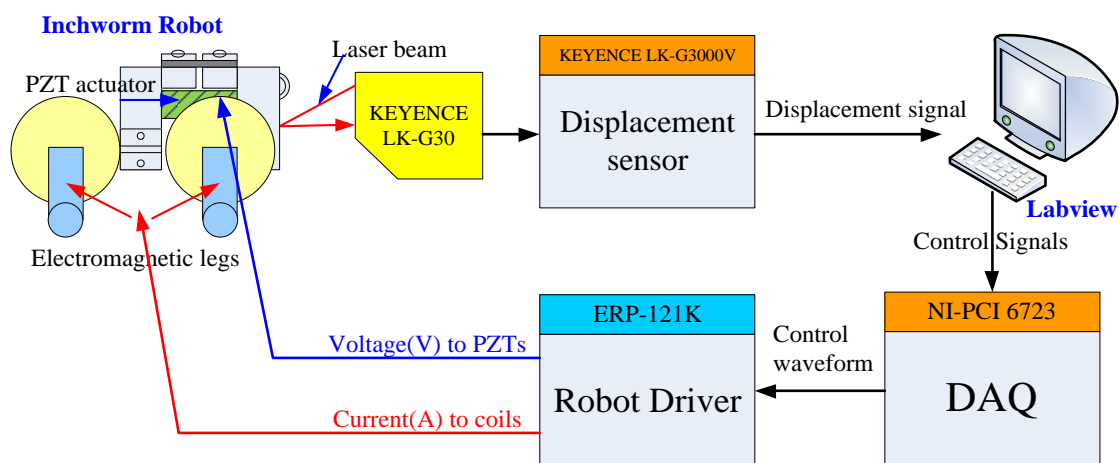
Figure 3.7 Experiment setup for robot movement performance test
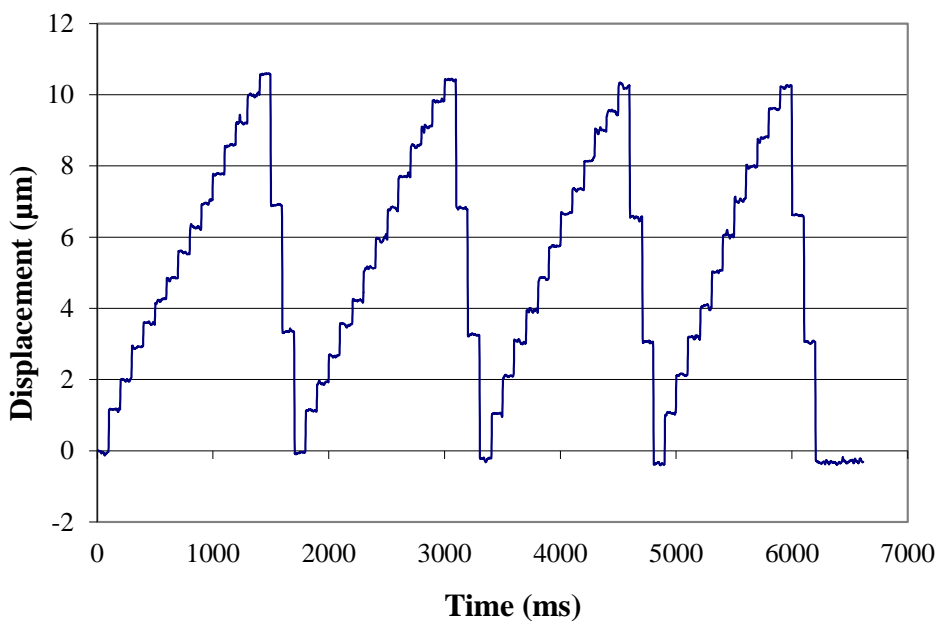
Figure 3.8 Resolution experiment results on step movement of the microrobot (measured in four times forward and backward directions)

or turn right (TR). At the first, a robot is moved forward (FW) with lowest voltage input (2V) in ten steps, then move backward (BW) to the start position. Repeat these processes in four rounds. During a robot is moving, the position of a robot is monitored by Laser displacement sensor.

The resolution test result is shown in Fig. 3.8. The result has shown that, this locomotion movement has step resolution about 1µm per step for forward (FW) direction and about 3.5µm per step for backward (BW) direction. It has good repeatability even movement without guidance or feedback control. However, moving forward and backward is different step resolution.In the resolution test, the behavior of a robot was monitor with one dimension by one laser displacement sensor. In the experiment on repeatability test, the behavior of a robot during move is monitored in two dimensions by microscope with image processing. The marker that is a representative of a robot position is placed at the center top of a robot. The coordinate of a marker was transferred to a position unit in micrometer by using image processing technique.   The experiment setup is shown in Fig. 3.9. In this experiment, a robot is move in four directions, forward (FW), backward (BW), turn right (TR) and turn left (TL). At the first a robot is moved forward (FW) to 1 mm far from the start point, and then move backward (BW) to the start point. Next, a robot is turned right (TR) to 0.5 mm far from the start point, and then turn left (TL) back to the start point. The experiment result is shown in Fig. 3.10. The result has shown
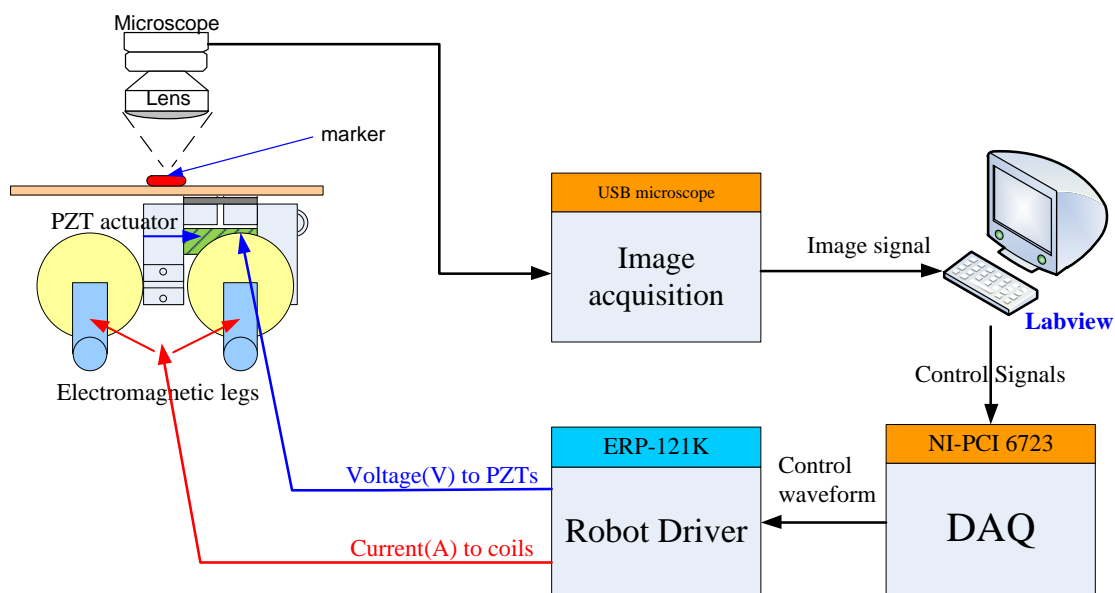
Figure 3.9 Experiment setup for repeatability test

82
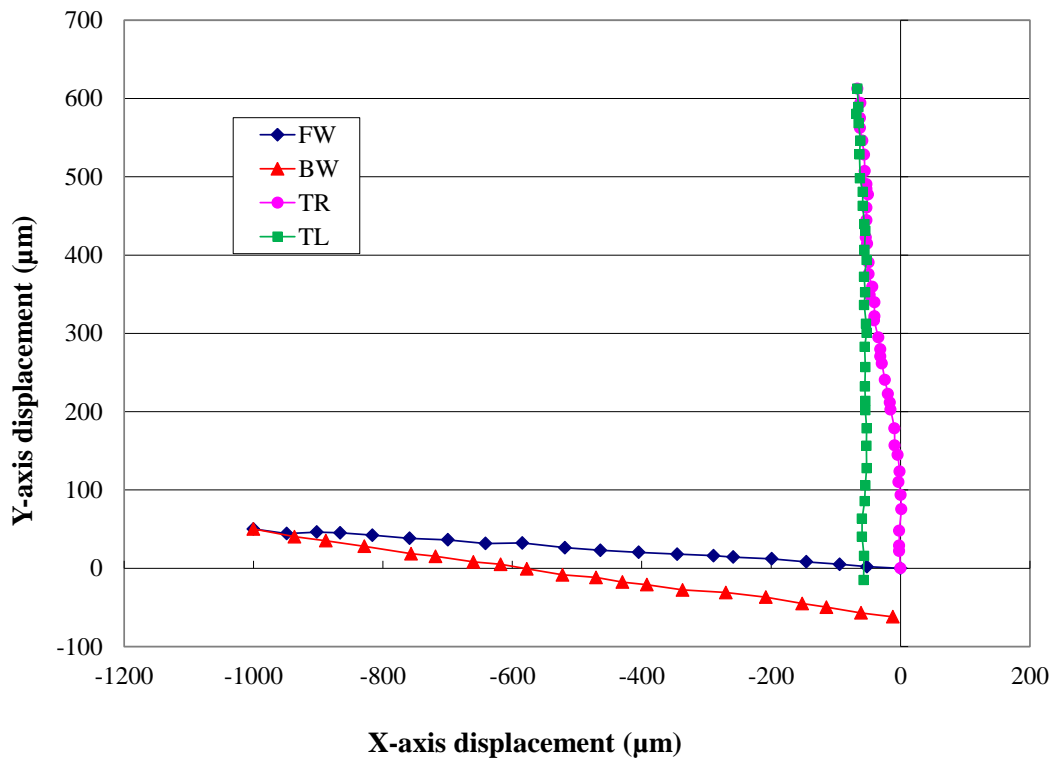
Figure 3.10 Repeatability experiment on step movement of microrobot. Measured in four directions, Forward (FW), Backward (BW), Turn right (TR) and Turn left (TL)

that, this robot have a very bad repeatability movement. After move forward for a large distance (1 mm) then move backward to the start point with same direction, the displacement error is about 80 μm. For turning actions, the position error is about 80 μm after turned right for 0.5 mm and turned left to the start position.

The repeatability of a robot depends on ground surface and the weight to carry. Moreover, this robot does not have any position feedback, so it moves without any guidance. For precise movement position, the navigation system for this robot is required. On next chapter, the navigation system of this robot is described.

3.2 A combination of microindentation mechanism and microrobot

In this section describe the combination between the hardness and stiffness measurement mechanism and the piezo driven microrobot. At first, the microhardness and stiffness testing robot and its control system are described and then the basic performance of a robot is depicted respectively.

3.2.1 Assemble of microrobot with small force indenter

In order to merge the measurement mechanism and the microrobot into one system, special holding mechanism is required. In Fig. 3.11 is shown the design of a prototype of the microindentation robot. It is composed of the measurement mechanism that is assembled on a microrobot by using the adjustable cantilever mechanism. This cantilever mechanism is able to adjust the measurement mechanism angle. By adjusting the cantilever to the proper position then indenter can be perpendicular to the surface of the specimen.
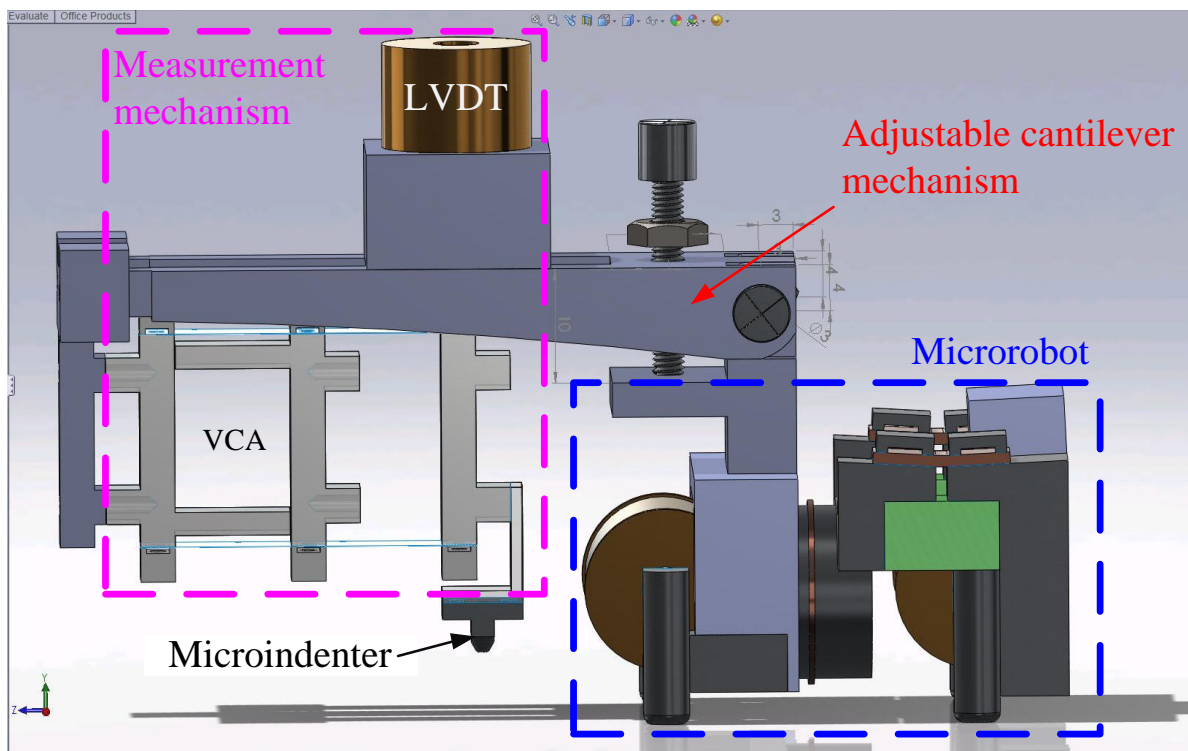
Figure 3.11 Solidwork design of a microindentation robot
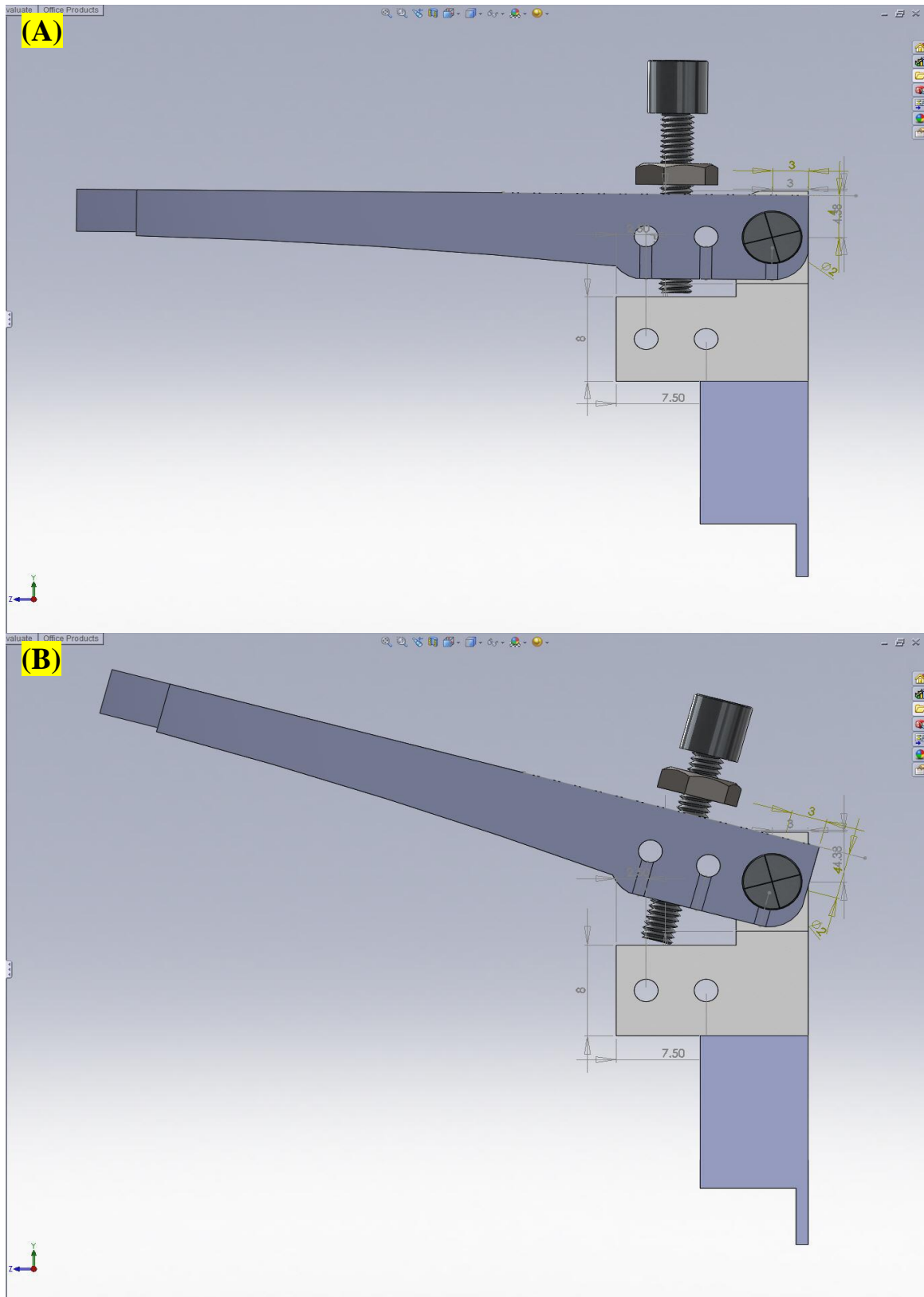
Figure 3.12 Design of the adjustable cantilever mechanism (hanger), which is able to adjust the angle of a measurement part. (A) normal state and (B) lift- up position
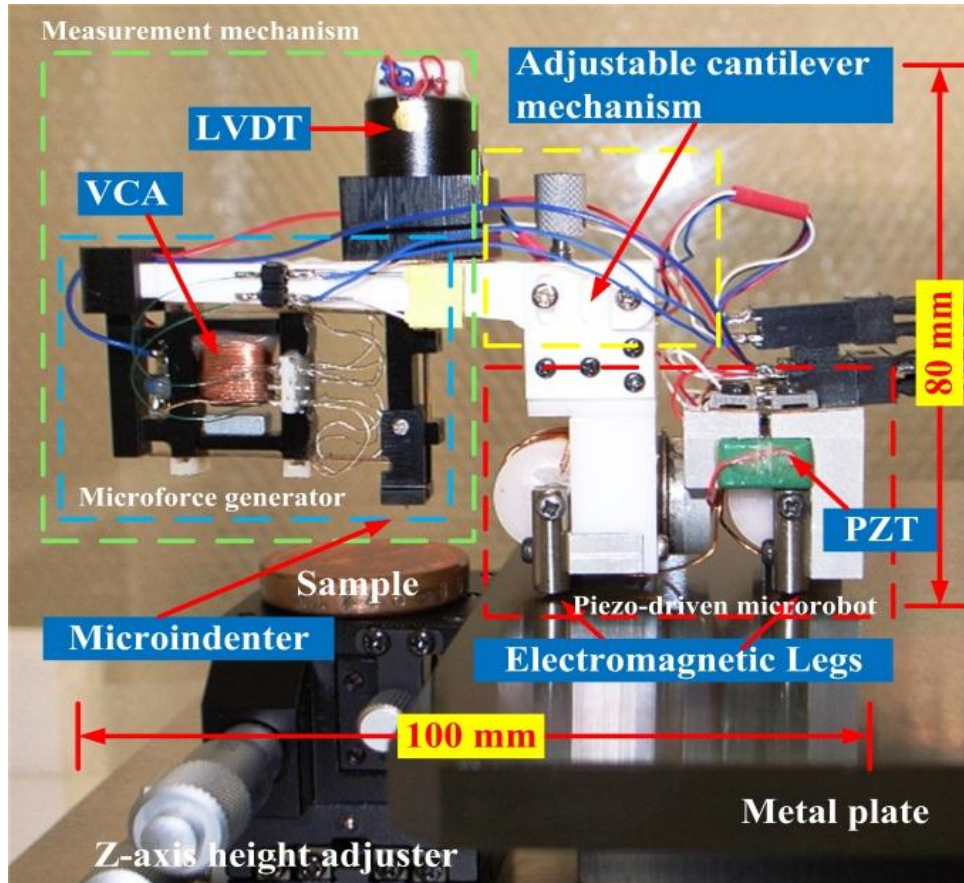
Figure 3.13 The prototype of the microindentation robot

The design of the hanger part is shown in Fig. 3.12. The robot should have a mechanism that can control the gap between indenter tip and surface under test with find angle adjustment. After the finished the machining process of a cantilever, then the measurement mechanism is implemented on a microrobot with supported by the adjustable cantilever mechanism as shown in Fig. 3.13. The target sample to be measured is set on the height adjustable z-stage and the initial gap between the indenter tip and the surface of sample are precisely positioned. The control diagram of this microindentation robot is shown in Fig. 3.14. The PC with several signal boards are employed to control a robot movement, the indentation process finally the indentation load and depth signals. At the first, the PC can send the specified signals to the robot driver so that the piezoelectric transducers and the magnetic legs can activate with the appropriate waveforms simultaneously. When the small robot arrives at the measurement area, then the gap between the indenter tip and the surface under test can be close within 40 μm by adjusting the z-stage that carries the sample. The small robot can start to make an indentation on the samples under test. The
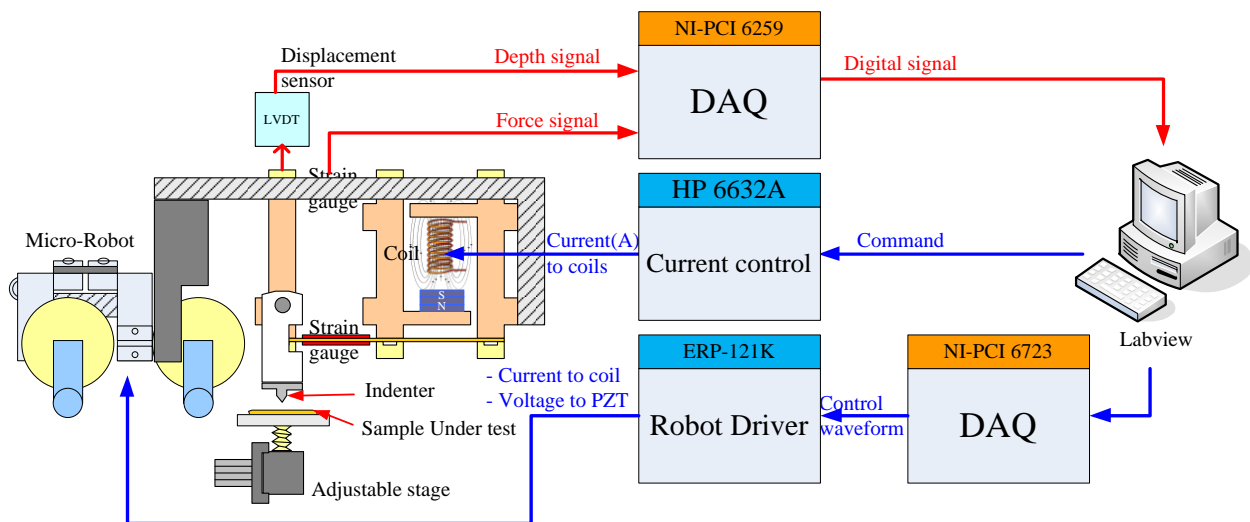
Figure 3.14 Control diagram of the microindentation robot

VCA can be controlled carefully by programmable power supply (HP6632A) and it can push down the sensing part with the microindenter to the sample. During the indentation process which controlled testing cycle, the behavior of the indenter including testing force and indentation depth can be monitored by the force sensing part and LVDT. When the indentation process is finished, PC can indicate a load-depth characteristic of the measuring point automatically. Then a robot will move to the next destination to be checked position. After finished the assembled process, at this moment the microindentation is ready to survey on the surface of a specimen. The experiment on indentation test with the microindentation robot is described on next section.

3.2.2 Experiment on mobility of the microrobot

Recently, microrobots have been widely used for many applications, it has fine mobility with microscopic resolution and can work in small areas [3-2 to 3-5]. The environments in which these robots are supposed to operate are narrow and potentially complicated spaces or hazard to human, such as pipe system in nuclear plant [3-6]. To present the mobility of our microindentation robot, a robot must walk to the measurement position in a narrow space. The pipe simulation was built from transparent plastic bottles with diameter about 9cm. It is composed to be a complicated shape; the schematic diagram is shown in Fig. 3.15(B). The total distance from start point to measurement area is about 70cm. The robot has to walk inside this pipe to reach the target. The operation of a robot during walk to the target is shown in Fig. 3.16. Once it arrives the target; the robot must do a surface investigation on the artificial sample with defect. The sample was made from plastic part with very flat surface. On the measurement surface, the small hole diameter about 2mm was drilled and filled in with gum glue as shown in Fig. 3.15(A). When the robot arrives at the measurement area, then it can start making an indentation on the sample surface with manual control by operator. The measurement area is designed pass through the glue hole, each indentation have about 100µm separation. Finally, the experimental results pertaining to the load-depth characteristics of the sample surface are summarized in Fig. 3.17.

(A)   (B)
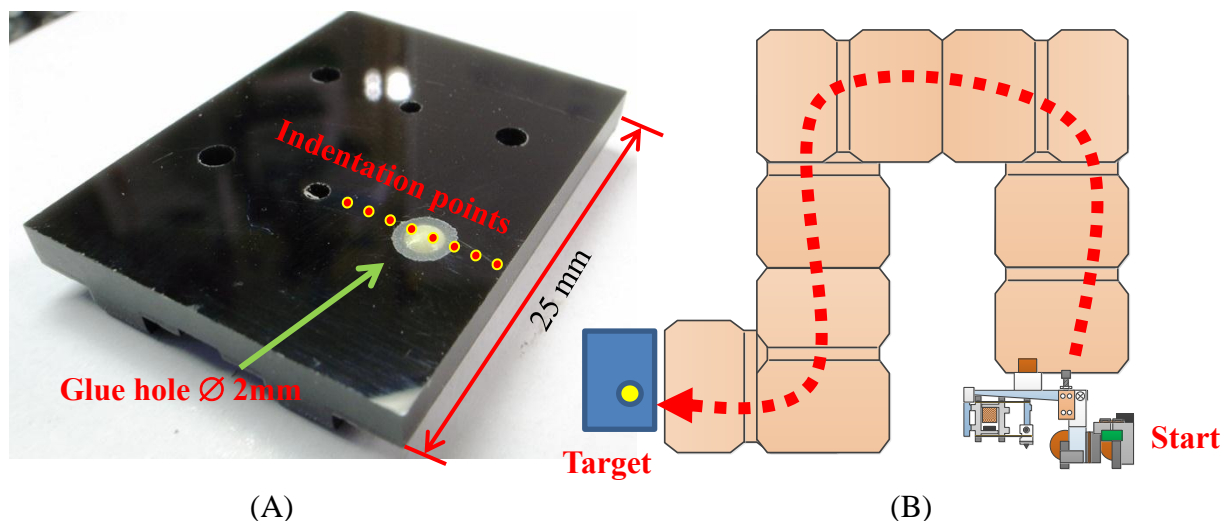
Figure 3.15 (A) Artificial sample with small defect. (B) The schematic diagram presents the robot path walks through the pipe
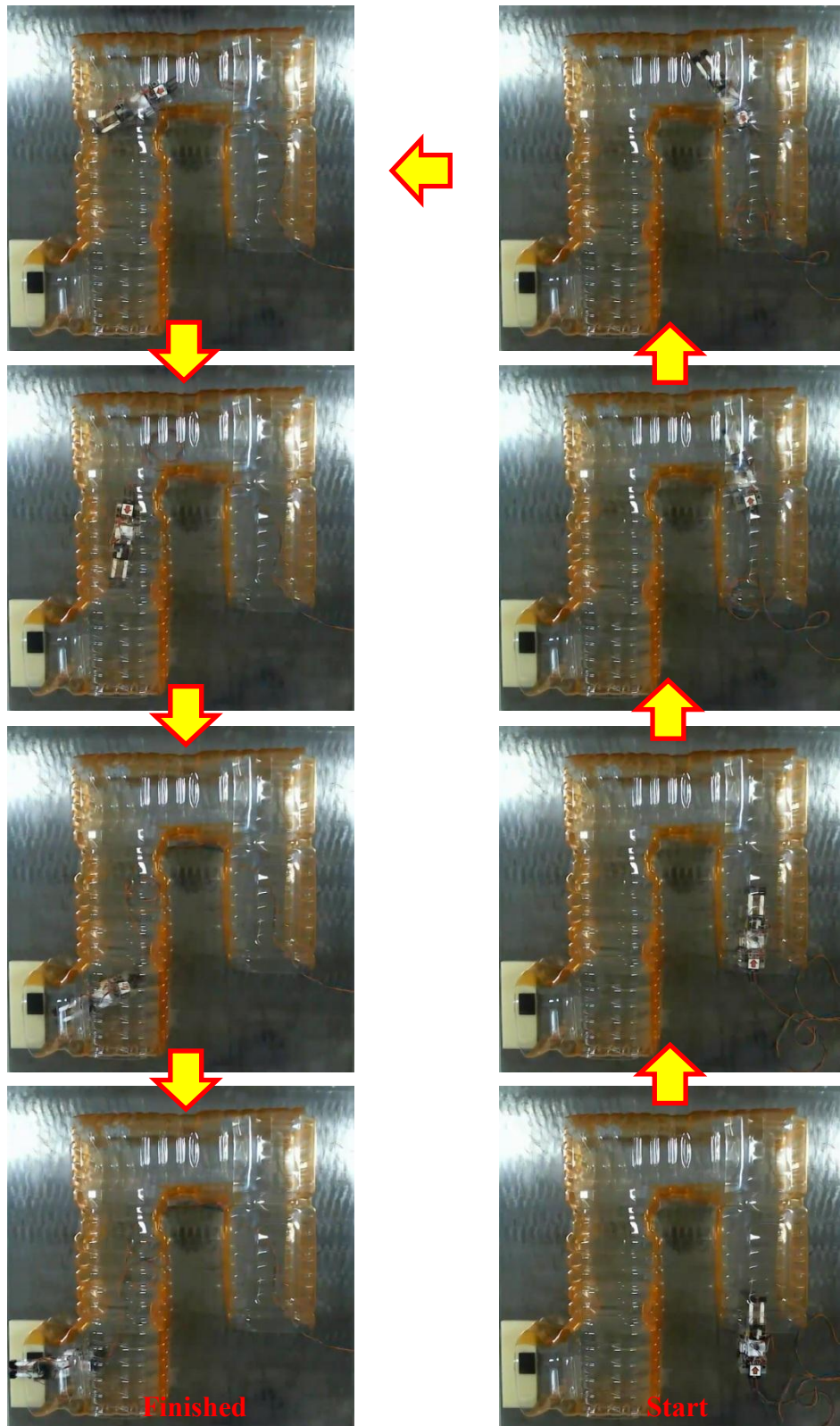
Figure 3.16 The robot walk through the pipe, start from the bottom right to the bottom left
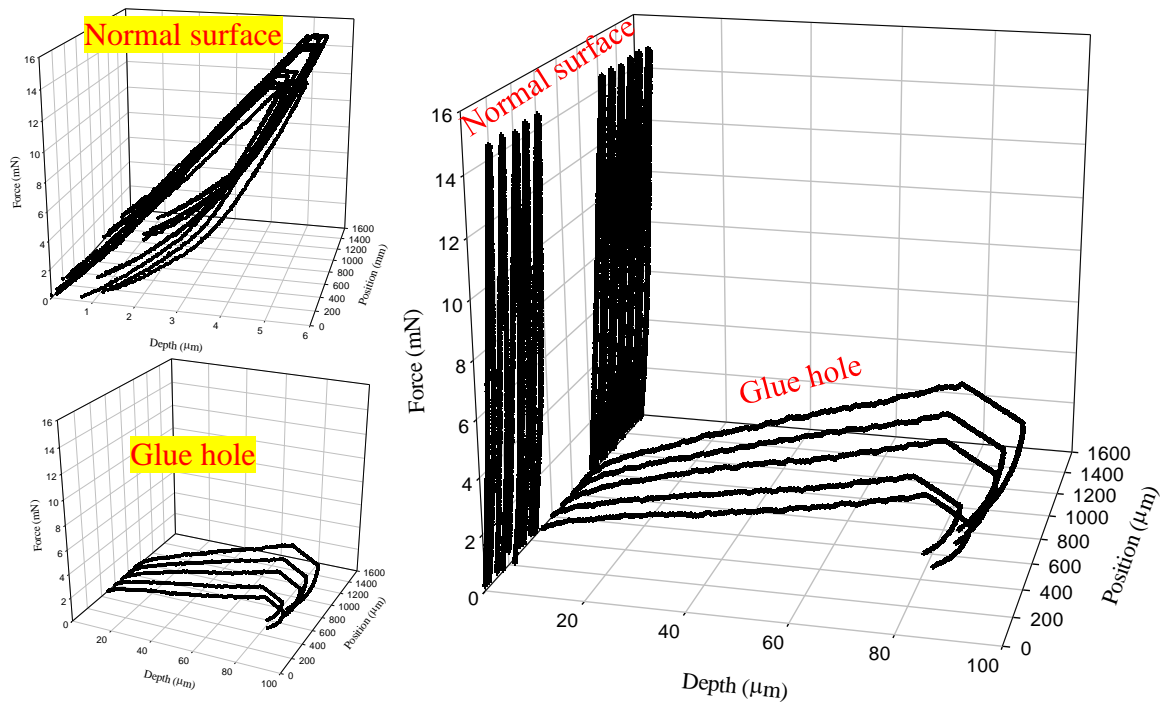
Figure 3.17 Indentation load-depth curves present the problem area on a glue hole with very deep indentation depth compare with normal sample surface

The experimental results load-depth characteristics of the artificial sample with defect surface are summarized in Fig. 3.17. Because the glue surface is very soft and high elastic, then the indentation load-depth characteristic of a glue surface must be different from a normal sample surface. From the load depth results, the different degree of hardness on the different surface characteristic can be checked in this experiment, and several load-depth curves can be identified. The strange behavior of the load-depth curves evidently comes from the effect of a glue hole.

Moreover, the mobility of this robot is presented from this experiment, i.e., the target at the end of a completed pipe can be reached. Obviously the robot mobility goes beyond another actuator. This is only the first step of this research; the application at the working area (such as nuclear plant) is going on the future work.

3.2.3 Indentation experiment on BIO samples

Usually, the rubber hardness measurement scales, i.e. Shore A, B, C, D, DO, O, OO M and IRHD are used to evaluate the hardness of soft materials such as elastomers and plastics [3-7]. In case of bio materials, the rubber hardness test method might be an appropriate method for determined the hardness value. Previously, Robert Katz and friends [3-8] have investigated the hardness of the wheat kernal by using a modified Barcol impressor. The Barcol impressor [3-9] is a portable hardness tester. It is generally used on soft materials and performed using similar test method with the Shore D hardness, i.e., elastomer hardness with round indenter tip. The hardness is measured from the indentation depth of the penetration of the indenter on the test object. On the other hand, our machine is performed using microindentation technique. The hardness is determined by load-depth characteristic compared with the indentation load-depth of the reference material, i.e. hardness block. Recently, there is no experiment on soft materials with this technique. Here, the performance of our machine will be present by the indentation experiment on several bio materials such as human nail, rice grains and finally human tooth.

3.2.3.1 Indentation on human nails

Regarding to the experiment results on chapter 2, this measurement mechanism can be operating with the specimen that is softer than 30HV. So, the biomaterials seem to meet this requirement. In 1971, J.R.K. Robson and H.D.EL-Tahawi had investigated hardness on human nails by using Knoop hardness [3-10]. Their results have shown harder nails and more hardness distribution range on the malnourished group. So, we have got a motivation from their research and selected the human nails as the first bio specimen. The cross section of the nail structure is shown in Fig. 3.18. Nails are made of a translucent fibrous protein called keratin. It's made in the matrix under the nail root in the mantle deep below the visible part of the nail. The lunula or whitish crescent is part of the matrix. The portion of the nail is called the nail body or plate. As the nail grows from the matrix, the plate moves along the nail groove located between the nail and the nail wall or eponychium. At the opposite end of the nail is the free edge, which extends beyond the fingertip. [3-11]
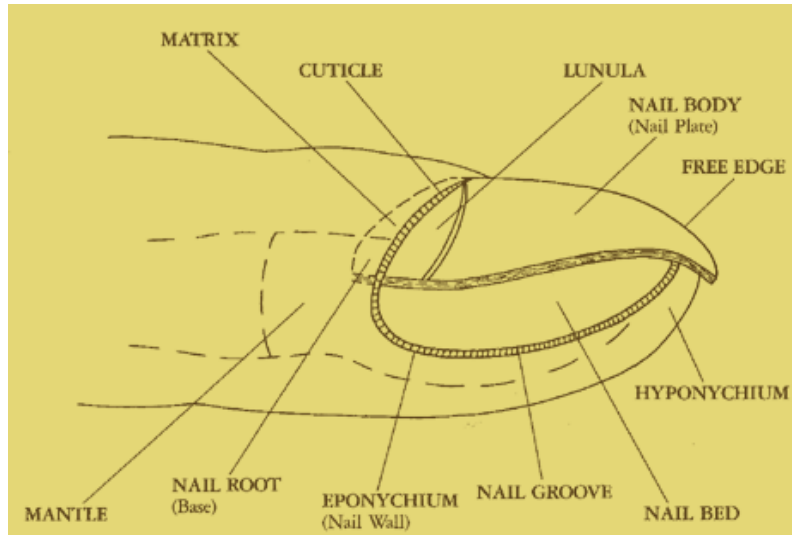
Figure 3.18 Cross section of the nail structure [3-11]

The fingernails sample were collected from three ages human sources. The first was a group of children age lower than five years old. The second was a group of 20-40 years old adults. And the last was a group of people over 60 years old. Free edge finger nail was clipped not less than 2mm × 2mm and fixed on a plastic plate by epoxy glue as shown in Fig. 3.19.

The nail sample has no polishing process, because it is difficult to control the polished surfaces for 3μm indentation depth. Twenty indentations by 10mN testing force were done on each sample. The indentation load-depth results of each sample group are shown in Fig. 3.20. And the average value (mean of group) of the indentation load-depth on each group is shown in Fig. 3.21.
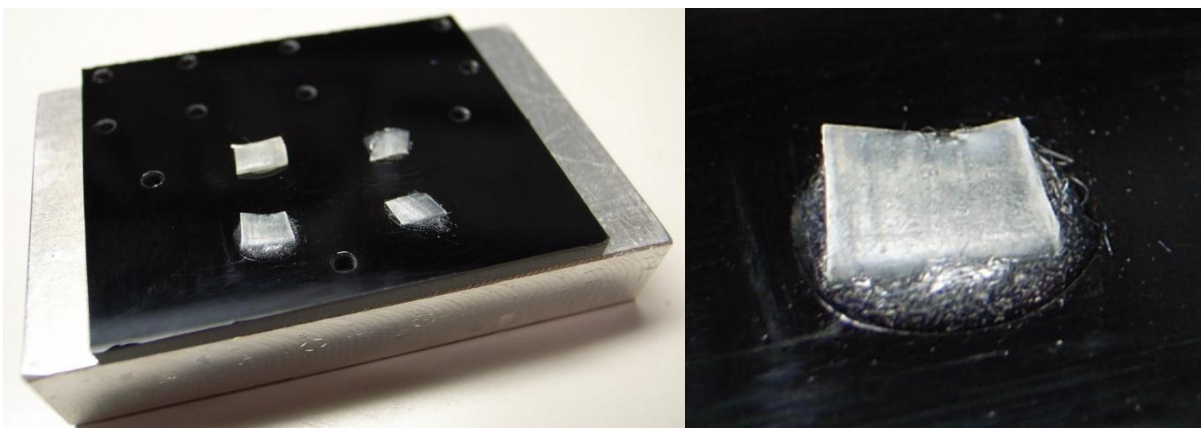
Figure 3.19 Finger nail sample were clipped in 2×2 mm, and placed on plastic plate by epoxy glue
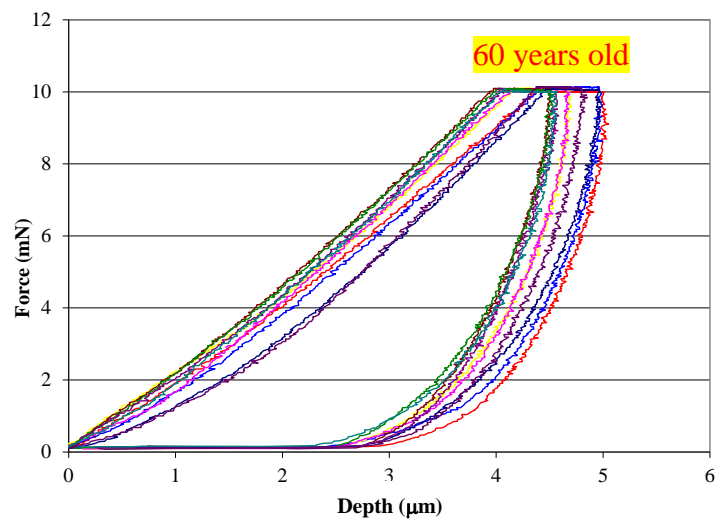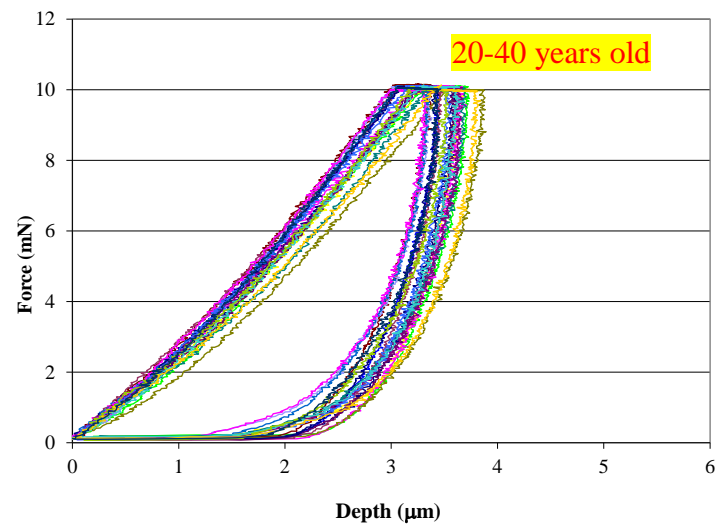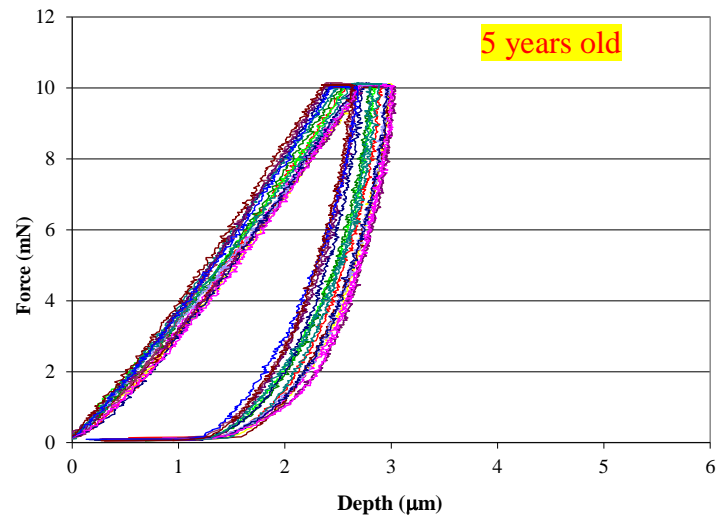
Figure 3.20 Indentation load-depth curves of each sample group
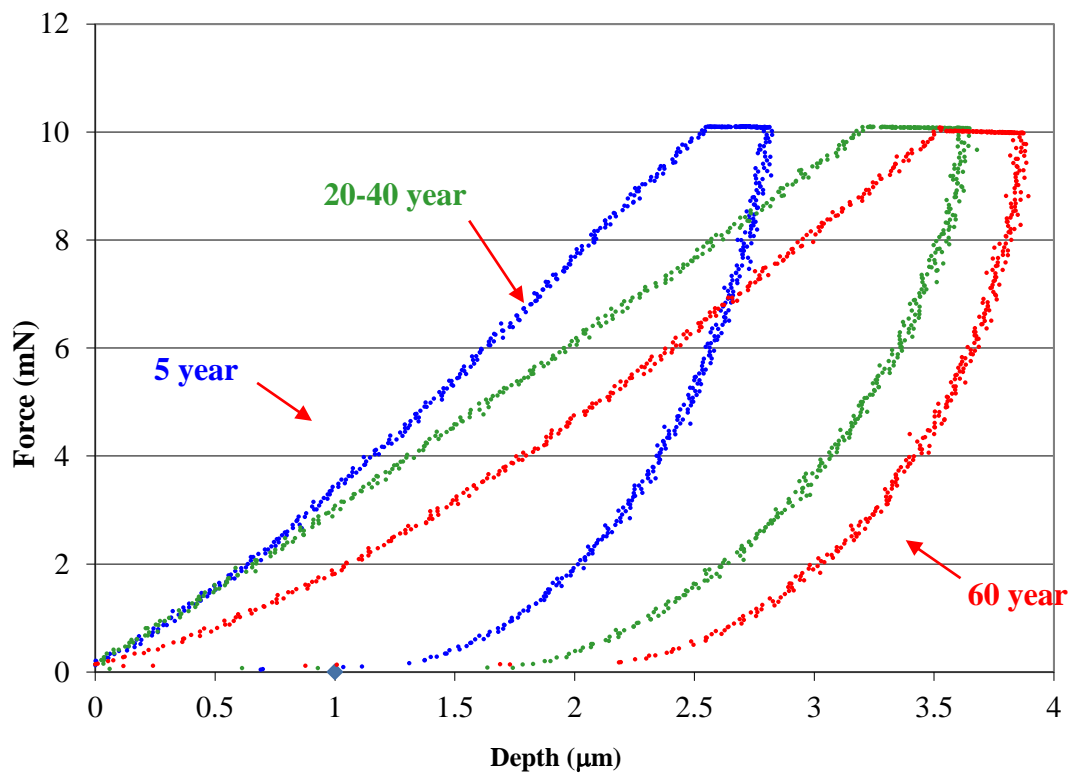
Figure 3.21 Mean of group of the indentation load-depth curves from each sample group

Here the nails sample is transported with the accurate interval distance with the small inchworm robot. Then the multiple indentations were applied along the robot path as shown in Fig. 3.22. The 3D profile of the nail indentation show very rough surface, some of the indentation was indented on crack or hole and some of them indented on pile up surface. This bumpy surface has effect to distribution of load-depth curve stiffness value. Some of the strange load-depth curve was deleted before doing average section. The nail is actually similar in structure to the hair which made of keratin, which is a tough protein. So, the growth rate of human nail not only depends on age, but it is dependent on many factors, such as nutritional status, the season and activities [3-12]. From load-depth curve results as shown in Fig. 3.21, we might be able to say that the group of 5 year old child has high stiffness of nail rather than another group. This may because the children have nail repairing process or nail growing rate faster than adult and old people. So, their nail surfaces have less scratch and minor pore when compare with another group. The lowest stiffness of nail is belonging to group of old people who have age over than 60 years. From the surface scan by microscope we found that nails surface of old people have many scratches due to, they use fingers for many actions in their everyday

life. Moreover, the nail repairing process or growth rate of old people seems too behindhand than other groups [3-12]. On the other hand, the load-depth curves show that babies' (or children) nails are harder than adults and older people's nails. This data is amazing.

We know that infant nail is very soft when compare with teenager or young man, but these experiment results are only surface indentation depth is not over than 5µm. The load-depth shows high stiffness on babies' nails means, the indenter cannot penetrate in to nail surface due to very high-density surface. Moreover, for low stiffness and softest load-depth curve of older peoples nail means, the rough and less density surface is very easy to indent. By the way, it is obviously showing that human nail has hardness level lower than 30HV when compare load-depth curve with last experiment results on the certified hardness block. From this experiment, the elasticity of human nails was checked and then the several load-depth curves can be given. It is clearly that the distribution of surface elasticity can be detected, and it can give us the potential performance to investigate the microsurface characteristics of the sample, including the microinside defect identification.
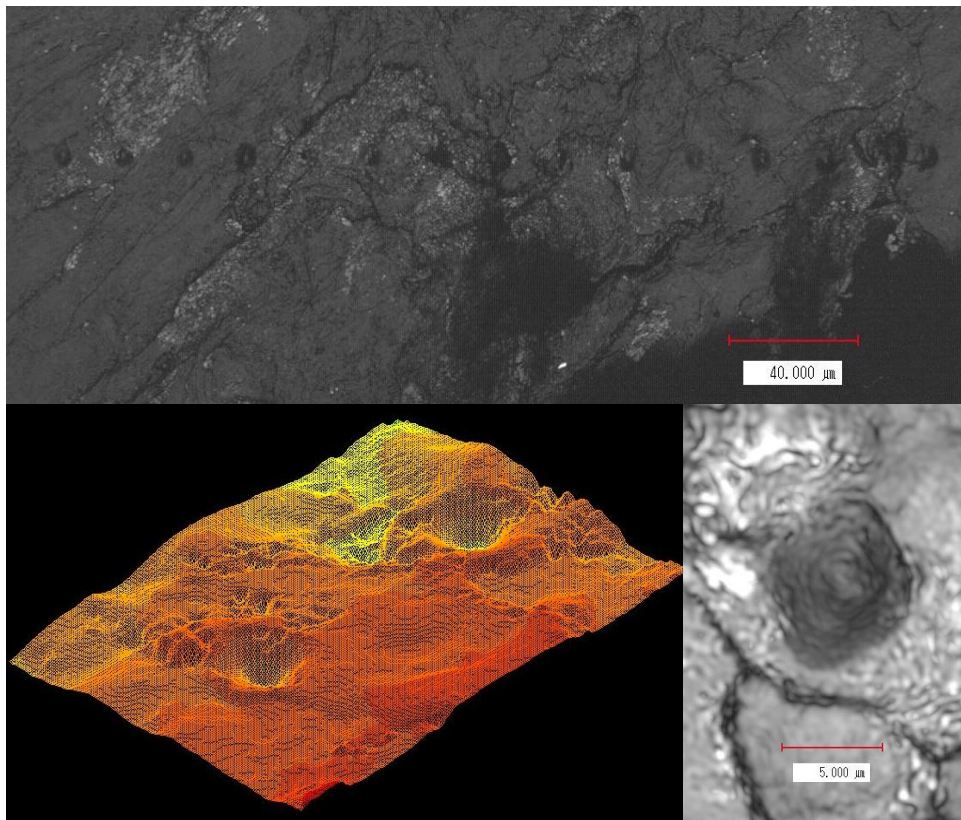
Figure 3.22 3D profile of the indentation on human finger nail

3.2.3.2 Indentation on rice grains

The rough rice consists of an outer protective covering, hull, bran (pericarp, seed-coat and nucellus), aleurone layer and the endosperm. After removing the outer husks of the grain by rice huller, it becomes to brown rice if continue milling process to removing the bran, thereby creating white rice [3-13]. The outer layers and internal structures of rice grain in shown in Fig. 3.23.

In this experiment three types of white rice grain were used as a sample, which is Japanese rice that has short grain rice, Thai rice and sticky rice, which is medium and long grain rice, respectively. Each kind of rice is divided into two categories, cooked and uncooked state. The Japanese rice and Thai rice was cooked by boiling process, but for sticky rice was cooked by steamer. We determined the stiffness of rice grain by series of indentation up on a rice grain surface with 10mN test force. The rice seed are placed on a plastic plate by epoxy dry fast glue as shown in Fig.3.24. All measurement processes are finished within one hour after glue dried, because the humidity inside the seed also desiccated depends on time.
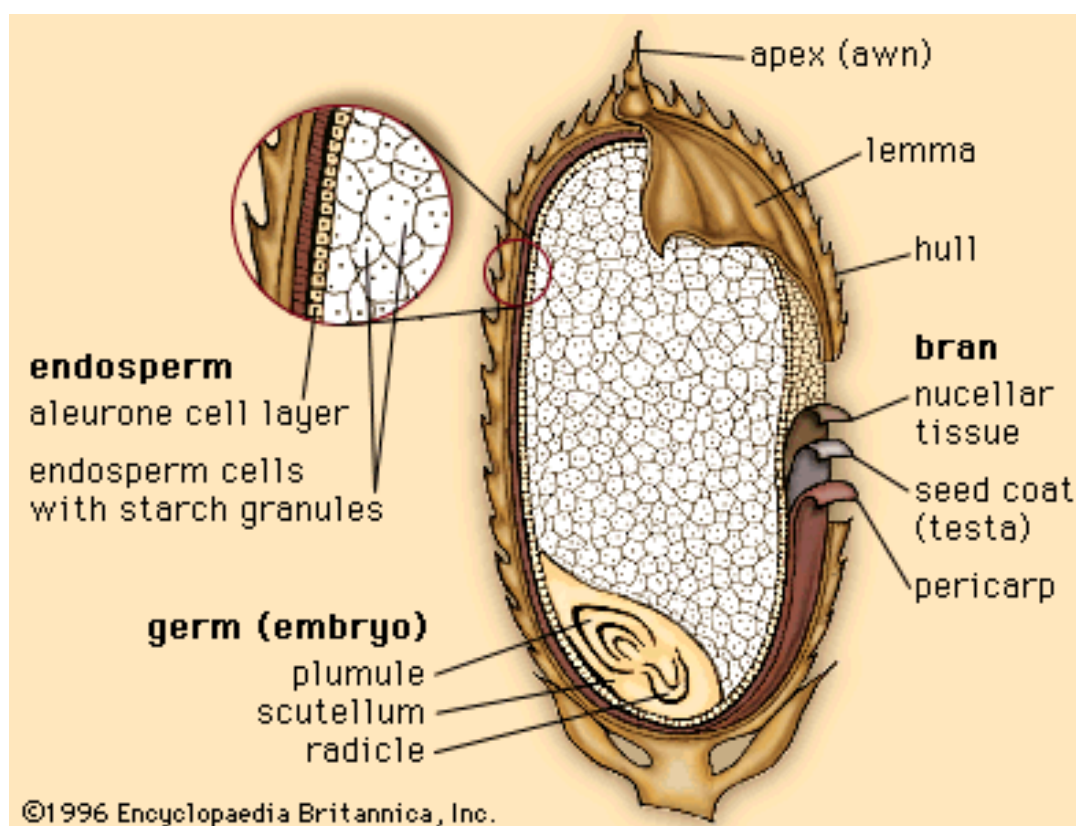
Figure 3.23 Outer layers and internal structures of rice grain [3-14]

| Japanese rice uncooked | Sticky rice uncooked | Thai rice uncooked |
| Japanese rice cooked | Sticky rice cooked | Thai rice cooked |
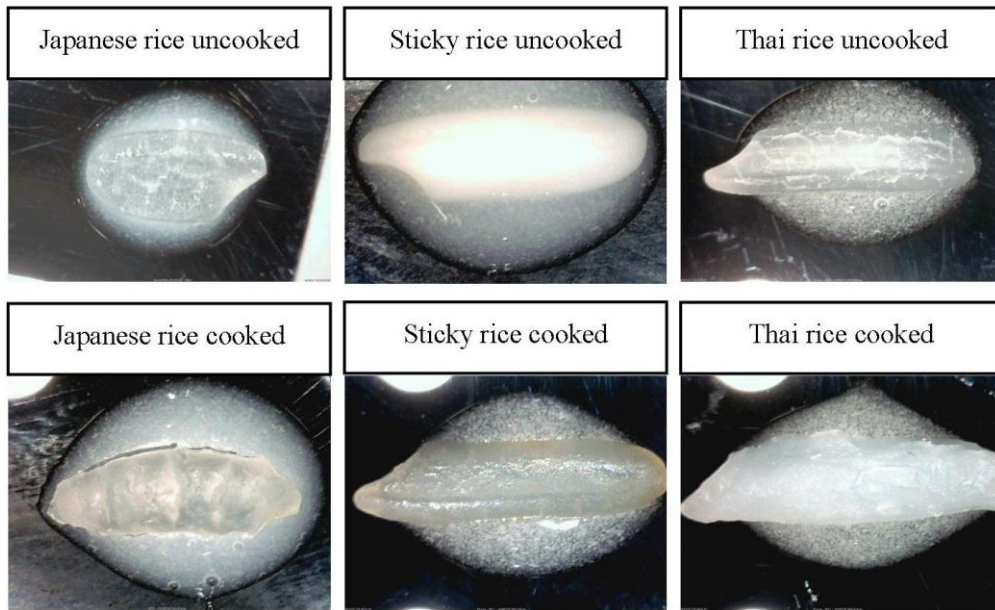
Figure 3.24 Rice grains are placed on the substrate with epoxy dry fast glue

| Japanese rice uncooked | Sticky rice uncooked | Thai rice uncooked |
| Japanese rice cooked | Sticky rice cooked | Thai rice cooked |
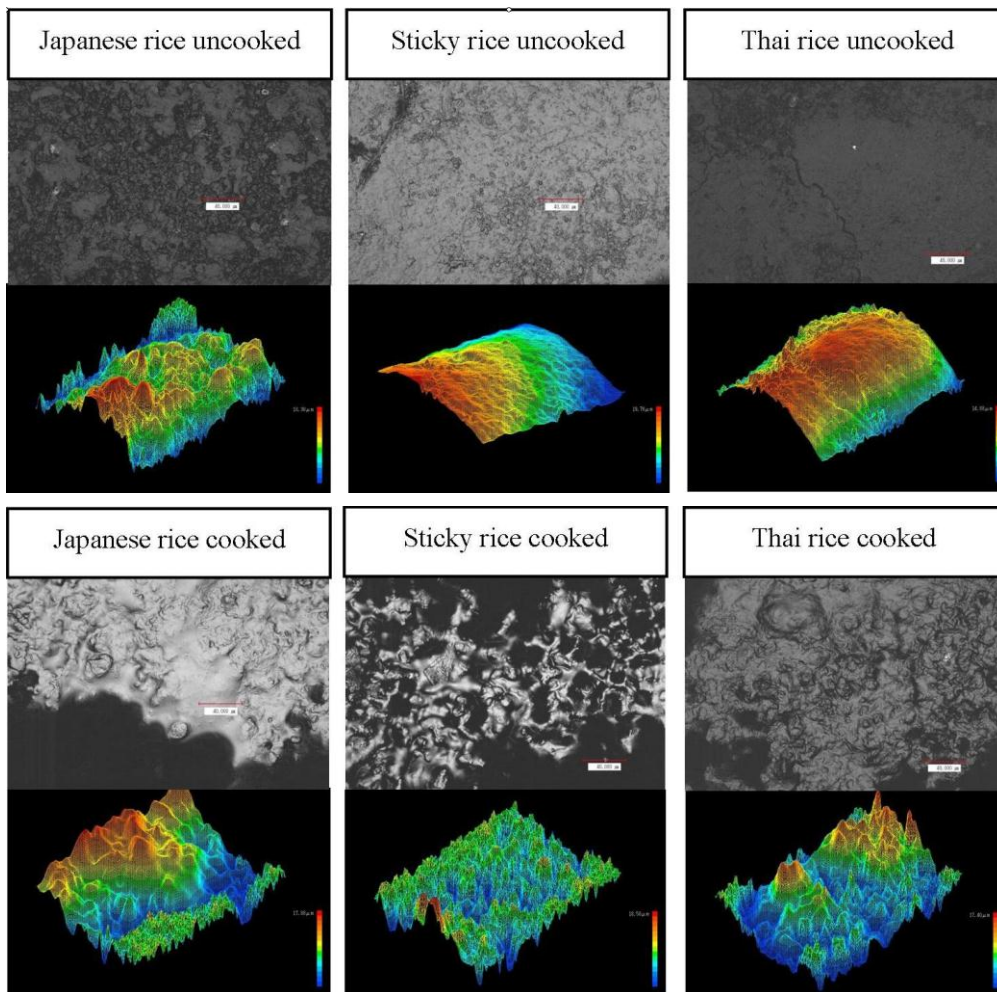
Figure 3.25 3D profile of the indentation on rice grains
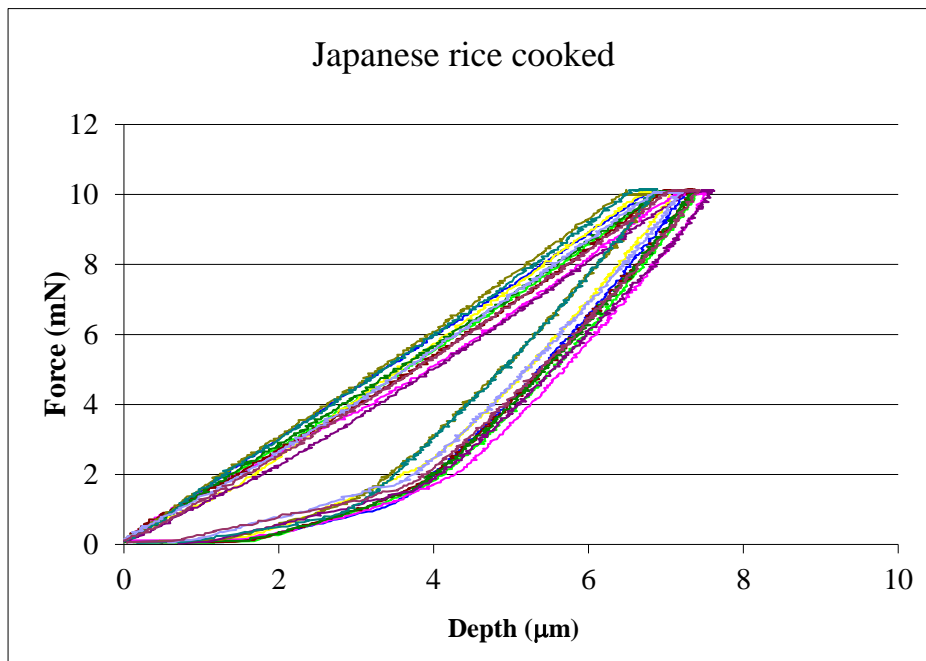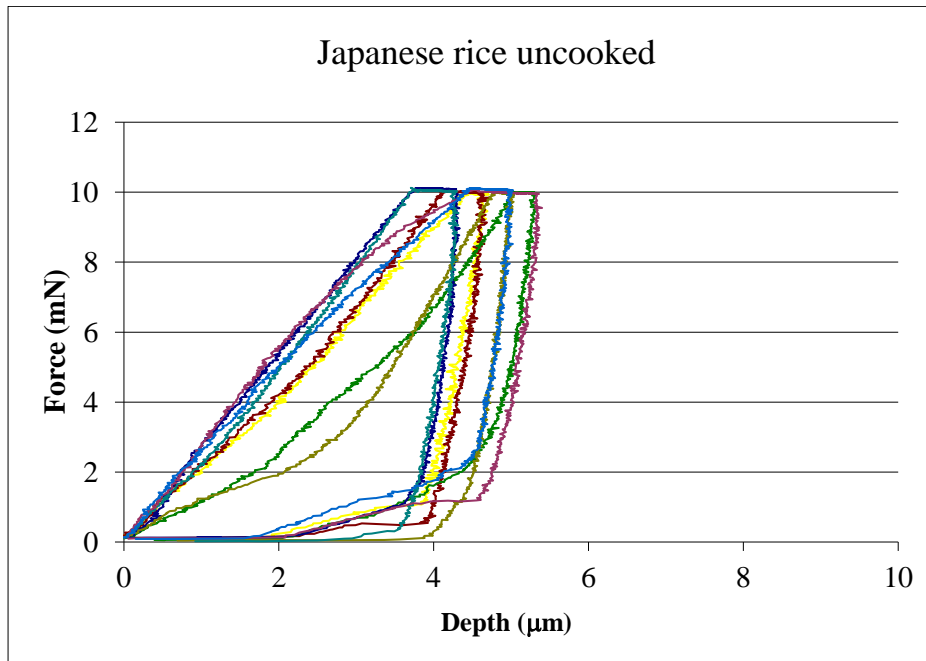
Figure 3.26 Indentation load-depth curves of Japanese rice uncooked and cooked
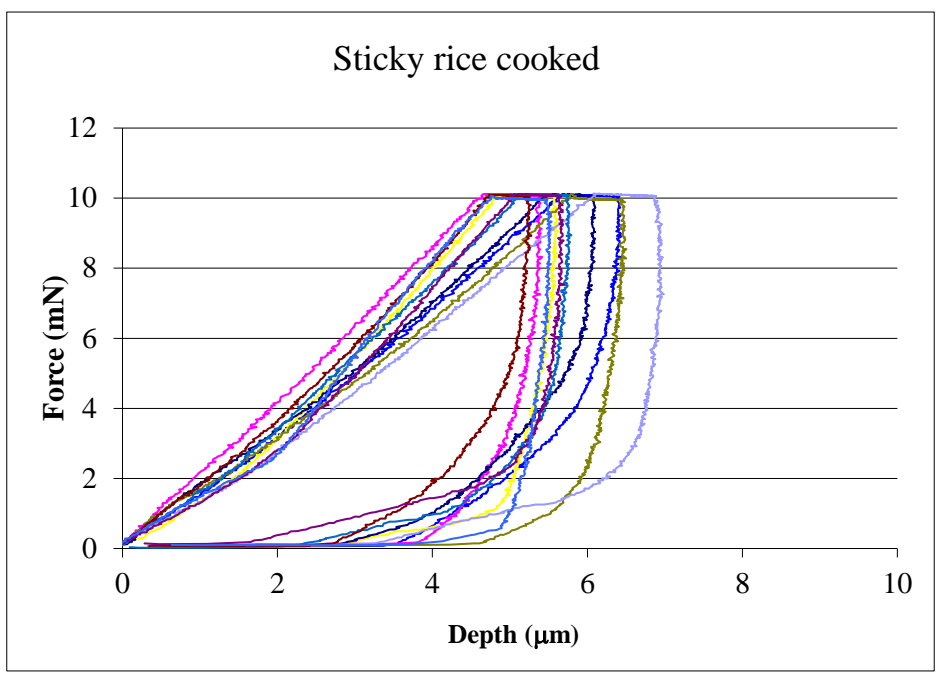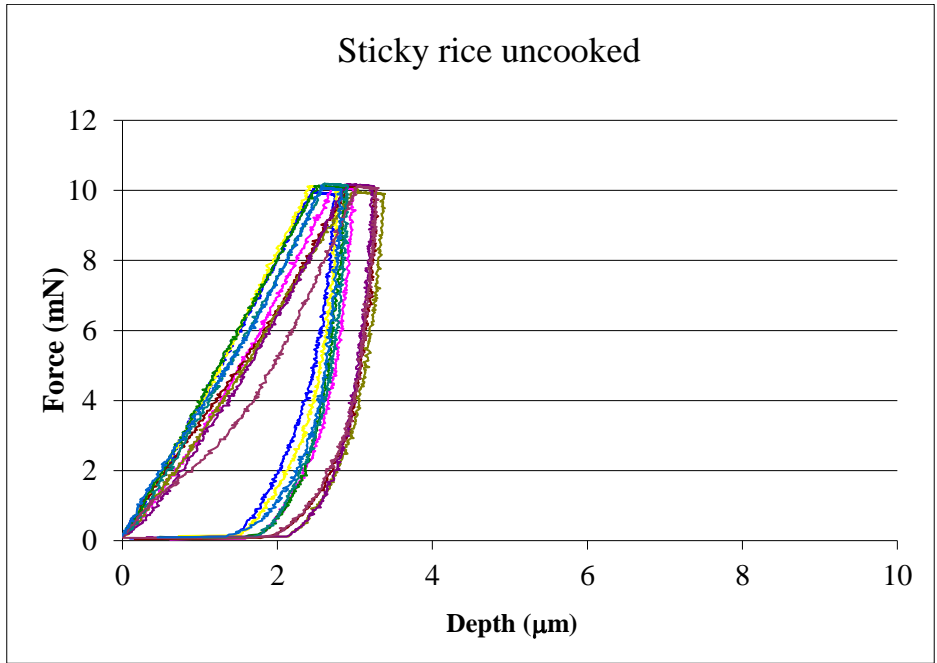
Figure 3.27 Indentation load-depth curves of sticky rice uncooked and cooked
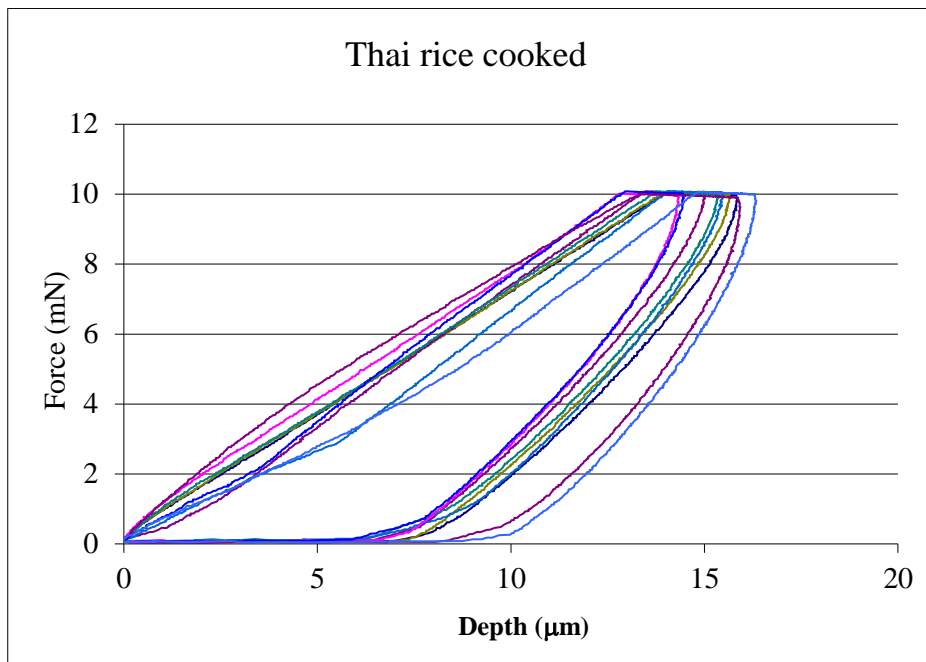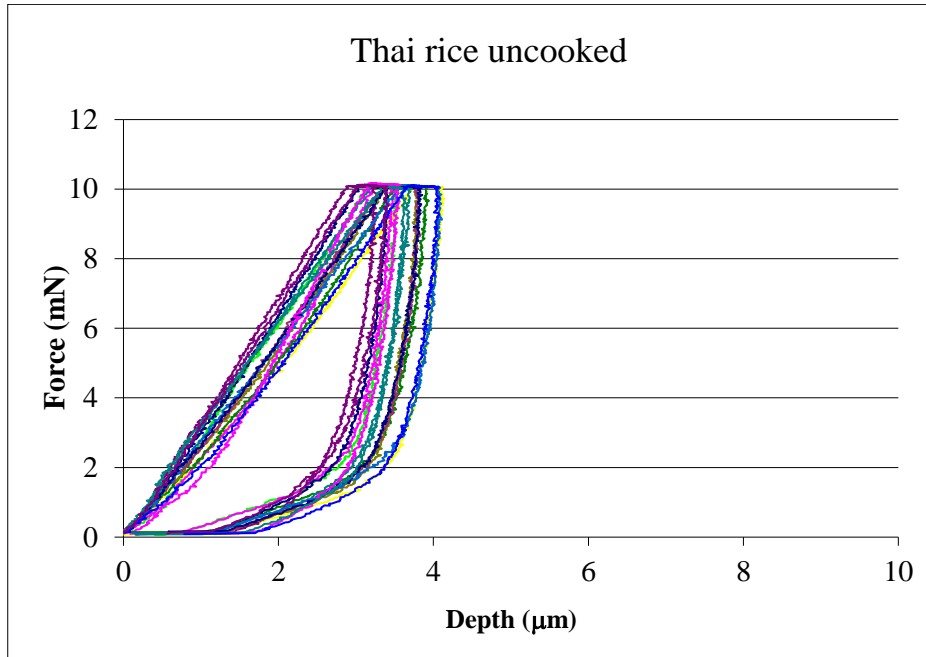
Figure 3.28 Indentation load-depth curves of Thai rice uncooked and cooked
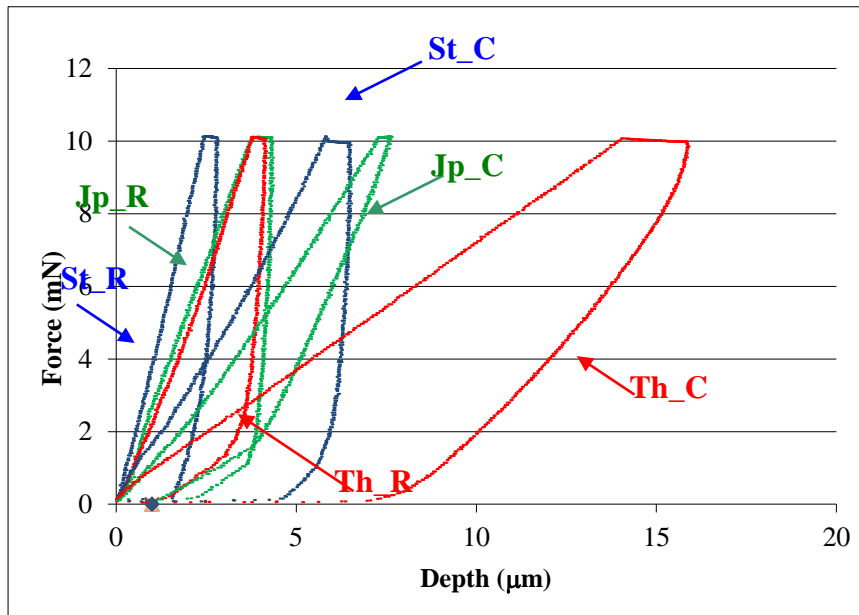
Figure 3.29 Mean of group of the indentation load-depth curves of rice grains, here the letter R is the representative of "uncooked", the letter C means "cooked"

By using laser scanning microscope, the 3D profile surface of each grain is illustrated in Fig. 3.25. Surface of rice grain before and after cooked fairly different, especially sticky rice surface before cooked its surface very smooth but after cooked it became to very rough surface. The series of indentation load-depth curves are shown in Fig. 2.26 to 2.28 for the results of Japanese rice, Sticky rice and Thai rice, respectively. And then the average values (mean of group) of indentation load-depth on each group are shown in Fig. 3.29.

From load-depth result shown in Fig.3.29 it has shown that the sticky rice uncooked is the most heard rather than another type. The stiffness on each uncooked not too different between each other, Thai rice and Japanese rice seem similar stiffness but for sticky rice, it looks harder. It is obviously notice that, after cooked all of the rice grain become softer than before, and the softest cooked rice is the Thai rice. These experiment results are only surface investigation; indentation depth is not over than 5µm for uncooked rice and 18µm for cooked. That means only the aleurone layer was investigated not endosperm layer. The stiffness and hardness value of rice is depends on many factors such as effect of moisture content, milling process or environment effect. So, results are only present an idea that the ability of this machine can be estimated stiffness of bio-material in degree of hardness or stiffness value.

3.2.3.3 Indentation on human teeth

The human teeth are extremely useful. They help you to tear, cut and break up your food into very small pieces so you can swallow it more easily. Humans have four kinds of teeth the incisors, canines, premolars and molars (Fig. 3.30) each carries out a different function. The eight incisors are the very front human teeth with rather flat surfaces, a straight sharp horizontal edge for cutting and biting the food. The four canine teeth are very strong, pointed corner teeth for tearing and shredding. The 8 premolars, used for the chewing of the food, are placed lateral to and behind the canine teeth, with a flat upper surface and 1 to 2 roots. The last twelve molars are the back human teeth. Molar teeth have much different tooth morphology with large and flat upper surface and 2 to 4 roots. Molars is the one of types of teeth with the largest of the permanent teeth, used for the final chewing and grinding of the food before swallowing. [3-15]

The human teeth are composed of four important parts, enamel, dentine, cementum and plup, the anatomy of tooth is shown in Fig. 3.31. The Enamel is the hardest tissue in the human body and even stronger than bone. It is composed of inorganic substances (96%) and organic substances (4%). The next is the Dentine, its layer is similar to the bone, it composed of 35% organic and 65% inorganic matter. Inside the dentine the pulp occupies at the center, it consists of soft connective tissue and blood vessels. Finally, the Cementum, it is a mineralized dental tissue which covers the roots of the tooth [3-16].
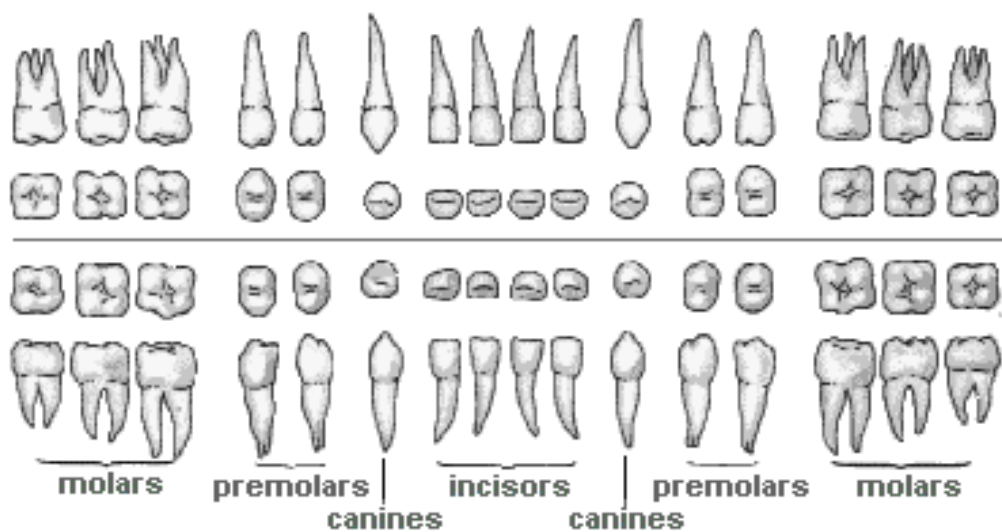
Figure 3.30 Diagram of human tooth [3-15]
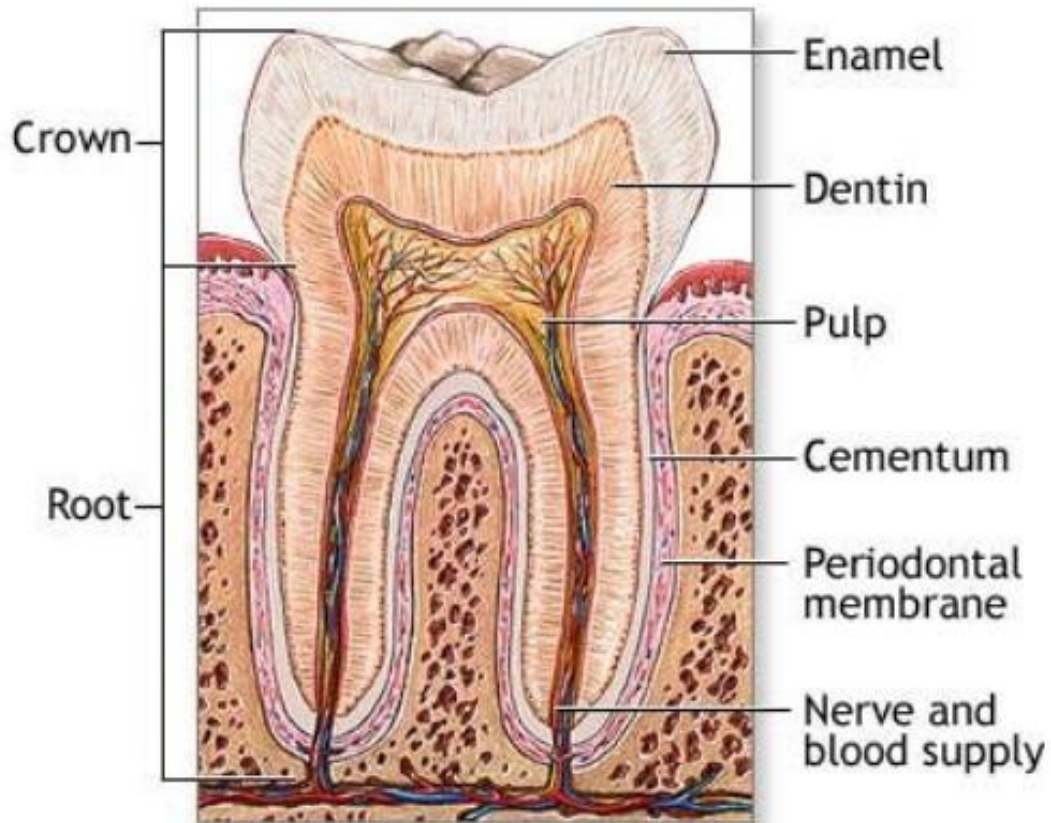
Figure 3.31 Anatomy of a tooth [3-17]

There are many researches about the tooth hardness investigations, because the study of teeth hardness is very important for understanding, for example, how toughness of tooth is change due to age and sickness. The hardness of human tooth has been explored by many of methods including indentation hardness [3-18, 3-19 and 3-20], scratch hardness [3-21], abrasion test [3-22] and the famous nanoindentation hardness [3-18]. From those methods, the average hardness value of enamel is around 250 to 360HV and for dentine is in the range from 30 to 60HV [3-23]. It has founded that the hardness values, of tooth decrease from the outer surface to the enamel and dentine junction until inner of dentine [3-24 and 3-25]. However, some other studies [3-18 and 3-26] have found only slight indications that the enamel is harder in the outer surface than in the enamel and dentine junction, but the difference were less than the standard deviation. Thus the uniformity of teeth is dominated, rather than the experiment area

Figure 3.32 Two incisors teeth samples (milk teeth and permanent teeth) before cut (Left). The teeth were placed on substrate by epoxy glue (Right) with polished surface
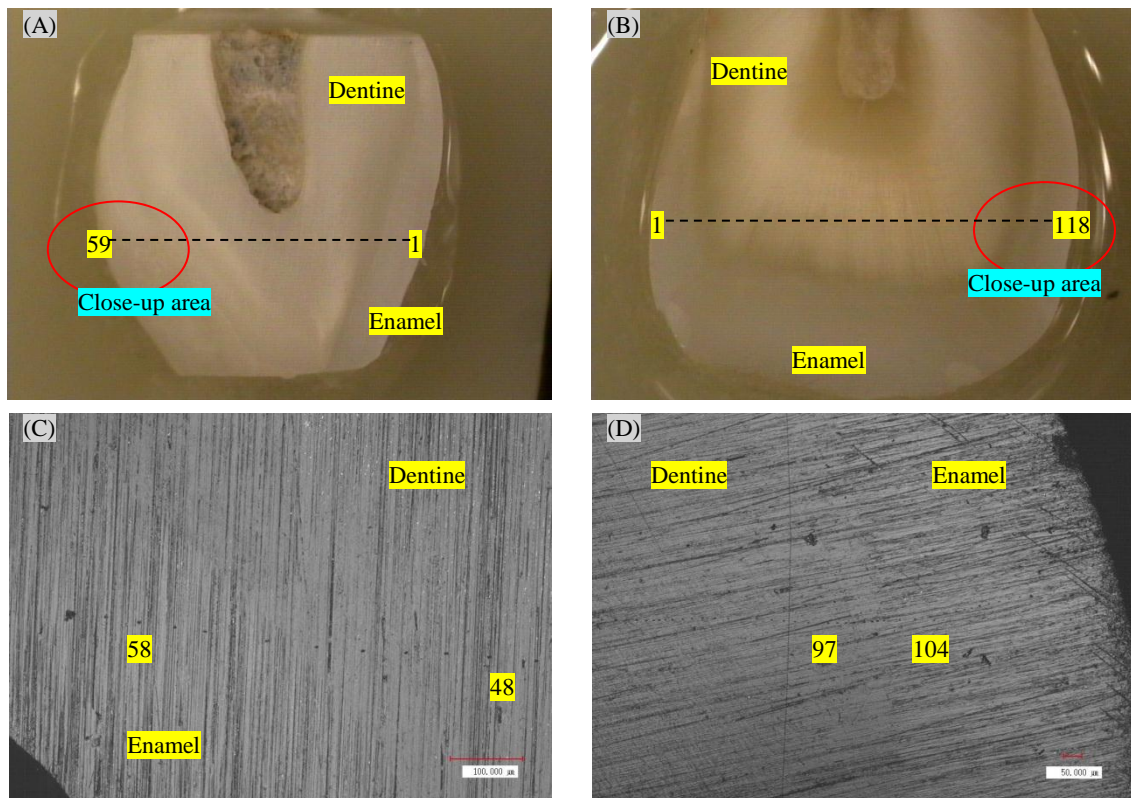
Figure 3.33 (A)The milk tooth and (B) the permanent tooth with vertical cut and indentation in transverse. 3D image from laser scanning microscope of the indentations on (C) milk tooth and (D) permanent tooth

In the experiment, two ages of incisors teeth were used as a sample under test. The teeth were cut vertically and placed both of them on the substrate with epoxy composite glue as shown in Fig. 3.32. One of the influence factors that affect the hardness measurement is the specimen preparation. If there is any tilt or bumpy surface, it can cause the indentation problem. So the teeth were polished by silicon carbide paper number 2000, in an increasingly way, with water. In transverse samples, the series of indentations were done from the enamel outer surface to dentine inner surface, going through enamel-dentine junction then dentine inner and enamel outer as shown in Fig. 3.33. The indentation process was done with 15mN testing force with 10s holding time at the maximum force. The series of indentation produce series of indentation load-depth as shown in Fig. 3.34 and Fig. 3.35 for milk tooth and permanent tooth, respectively. And then the average values (mean of group) of indentation load-depth on each group are compared with the indentation load-depth of 30HV and 100 HV as shown in Fig. 3.36.

From the experiment results load-depth characteristic on each indentation area compare with certified hardness blocks are shown in Fig. 3.36. We can conclude that, the hardest zone is the enamel of permanent tooth, it is nearly 100HV. And the softest area is the dentine of permanent tooth, because the
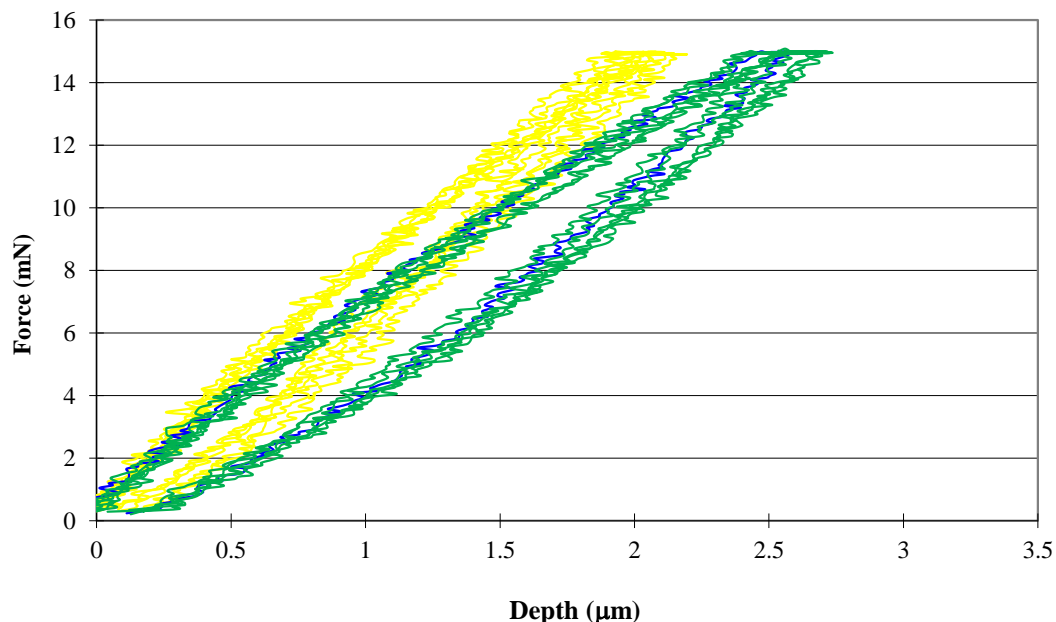
Figure 3.34 Indentation load-depth curves of milk tooth
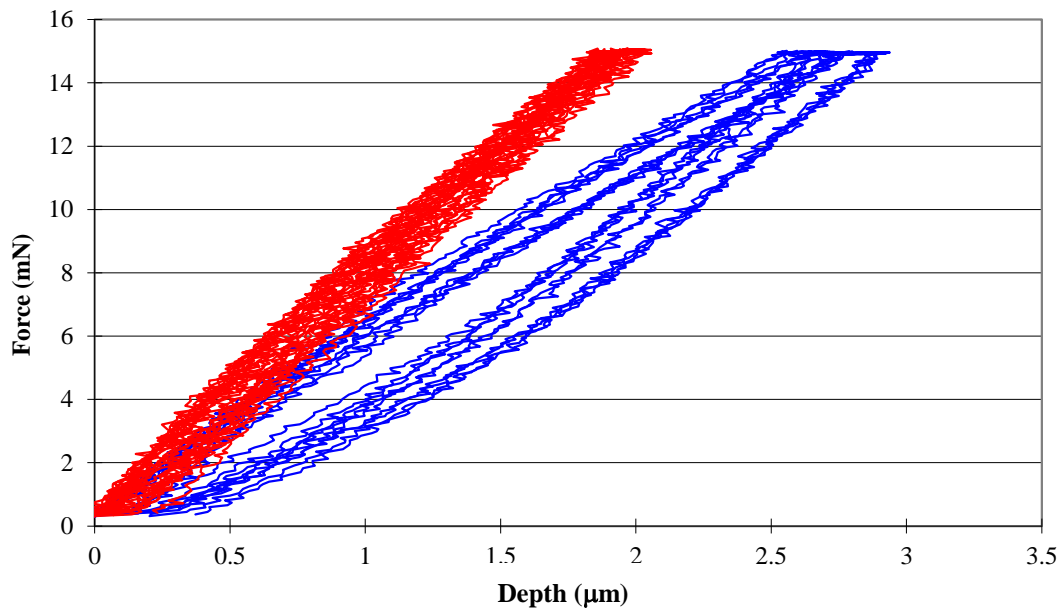
Figure 3.35 Indentation load-depth curves of permanent tooth
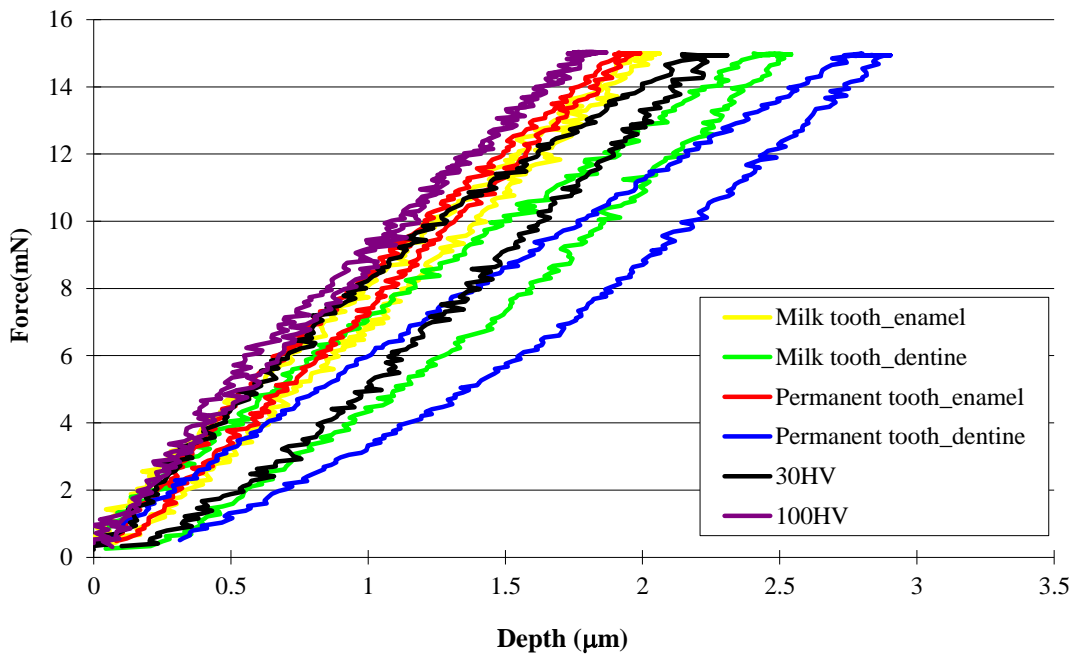
Figure 3.36 Mean of group of indentation load-depth curves of permanent tooth and milk tooth compare with load-depth curves of certified hardness block

indentation depth is lowest from group. Both section of milk tooth hardness is stay close together and placed between enamel and dentine of permanent teeth which is quite different each other. It may because of the milk tooth life time is just 5-6 years old so each layer is almost the same stiffness, meanwhile the permanent tooth life time is more than 50 years, so it apparently different for each area.

3.3 Discussion

In this chapter, the performance of a microrobot is presented in term of surface stiffness investigation on bio material. It is clearly that this measurement system can provide the reasonable surface investigation results. However, at this moment the robot is maneuver without position controlled. It is caused indentation position problem as shown in Fig, 3.37. The indentation path under manual control was not so precise straight line as an expected path designed. Moreover, the separations of each indentation were different. For these reasons, the robot navigation system is required in order to get the surface characterization with precise position control. On next chapter, the vision-based navigation system for robot path control will be described.

Figure 3.37 The series of indentions under manual position control

CHAPTER 4.VISION BASED NAVIGATION SYSTEM FOR ROBOT PATH CONTROL

In chapter 3, we succeeded in the development of the first prototype of a microindentation robot. This is a combination of a tiny piezo-driven microrobot and a small hardness tester. Here, a small mechanical loop provides the benefits of low thermal expansion and high mechanical stiffness as well as utilized the microrobot to expand the working range. The microindentation robot is used to investigate microscopic elastic behavior of certified hardness blocks by determining indentation load-depth curves. Although it can be operated without a position control system, the indentation pattern cannot be controlled precisely along a specified path. In this chapter, the conceptual view of the down-sized instrumentation microhardness and stiffness measuring robot with position control by multivision image navigation is presented as shown in Fig.4.1.

This chapter is organized as follows: Sections 4.1 introduces the image processing technique, the basic image formation, sampling technique, and the shape analysis are described. In section 4.2 describes the robot position control
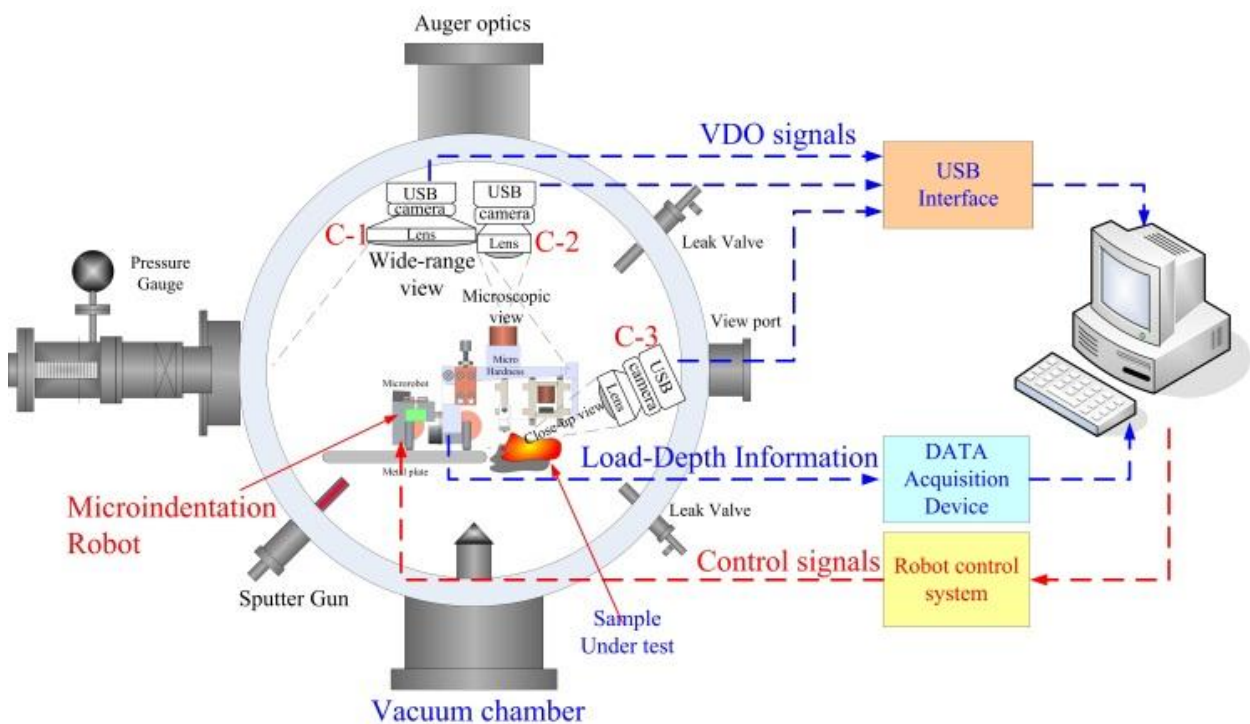
Figure 4.1 Microdiagnostics robot with hardness and stiffness testing, navigation based on multiple vision images

using the vision-based navigation system, including path control of wide range and microscopic camera views respectively. Finally, at the end of this chapter presents the performance of the microindentation robot with experiments on a human tooth inside a specified measurement area is also presented.

4.1 Basic image processing

In the early 19th century, the development of photography provided a mechanical instrument that can capture what the human eye could see. In 1950s, the development of the laser began to provide the light detector. This describes a starting point of the image processing system. However, the computer cost in the 1970s is limited the amount of developer. But in this century, almost all images can be seen in newspapers, books, advertising displays and on television have been processed digitally. The digital data that converted from analog signals involves three conceptual stages, i.e., sampling, quantization and coding. A set of computational techniques are used for analyzing and reconstructing the digital images. Image processing has extensive applications in many areas, including astronomy, medicine, industrial robotics, and a normal life. [4-1]

4.1.1 Image formation

The image formation can be simply described by the operation of the human eyes and the camera. The structure and operation of the eye is very similar to an electronic camera, and it is natural to discuss them together. Both are based on two major components, i.e., a lens assembly, and an imaging sensor. The lens assembly captures a portion of the light coming from an object, and focuses it onto the imaging sensor. And then the imaging sensor transforms the pattern of light into a video signal or electronic signal. The structures of an electronic camera and the human eye are shown in Fig. 4.2 and Fig. 4.3, respectively. The focus process of the electronic camera (Fig. 4.2) is achieved by move the lens toward or away from the imaging sensor. The amount of light reaching the sensor is controlled by the iris, i.e., a mechanical device that changes the effective diameter of the lens.
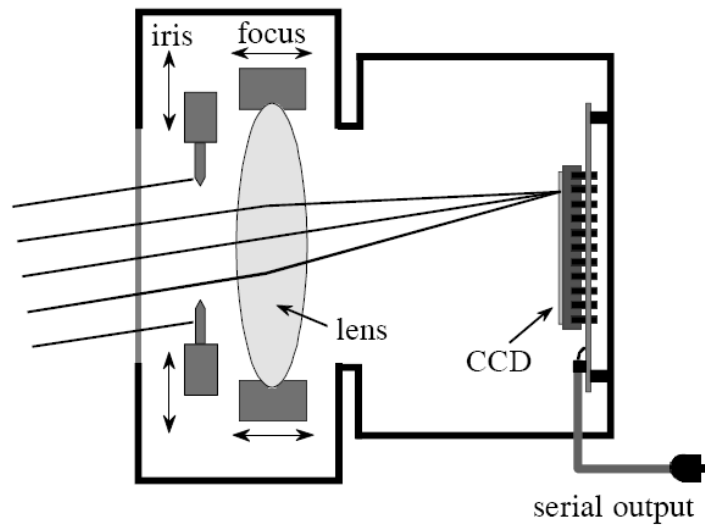
Figure 4.2 Diagram of an electronic camera [4-2]
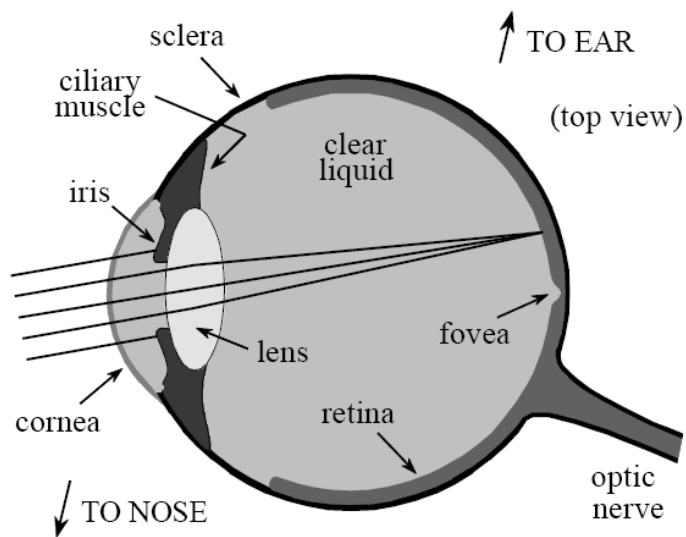
Figure 4.3 Diagram of the human eye [4-2]

The most common imaging sensor in present day cameras is the Charge-coupled device (CCD). The eye (Fig 4.3) is a liquid filled sphere (about 3cm in diameter), enclosed by a tough outer case called the sclera. The focus process is provided by the cornea, i.e., a fixed lens on the front of the eye. The focus is adjusted by contracting muscles attached to a flexible lens within the eye. The amount of light entering the eye is controlled by the iris, formed from opaque muscle tissue covering a portion of the lens. The rear hemisphere of the eye contains the retina, a layer of light sensitive nerve cells that converts the image to a neural signal in the optic nerve. [4-2]

4.1.2 Sampling and quantization

The computers organize an image as the arrays of digital numbers. As the images create a three-dimensional (3D) distribution of the irradiance at a plane, it is required to represent images as two-dimensional (2D) arrays of points. A point on the 2D grid is called a pixel. It represents the irradiance at the corresponding grid position and located on a rectangular grid. The position of the pixel is given in the common notation for matrices. The index m indicates the position of the row, and n represents the position of the column (Fig. 4.4). If the digital image contains $m \times n$ pixels, the index n runs from 0 to $n-1$, and the index m from 0 to $m-1$. The vertical axis (y axis) runs from top to bottom and not vice versa as it is common in graphs. The horizontal axis (x axis) runs as usual from left to right. [4-3]

(A)   (B)
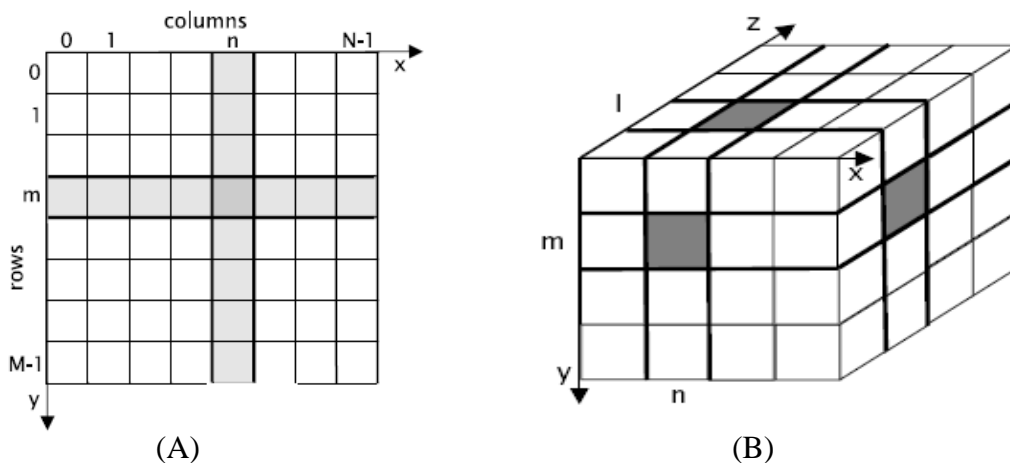
Figure 4.4 Representation of digital images by arrays of discrete points on a rectangular grid: (A) 2D image, (B) 3D image [4-3]

384x288 192x144

92x72 48x36
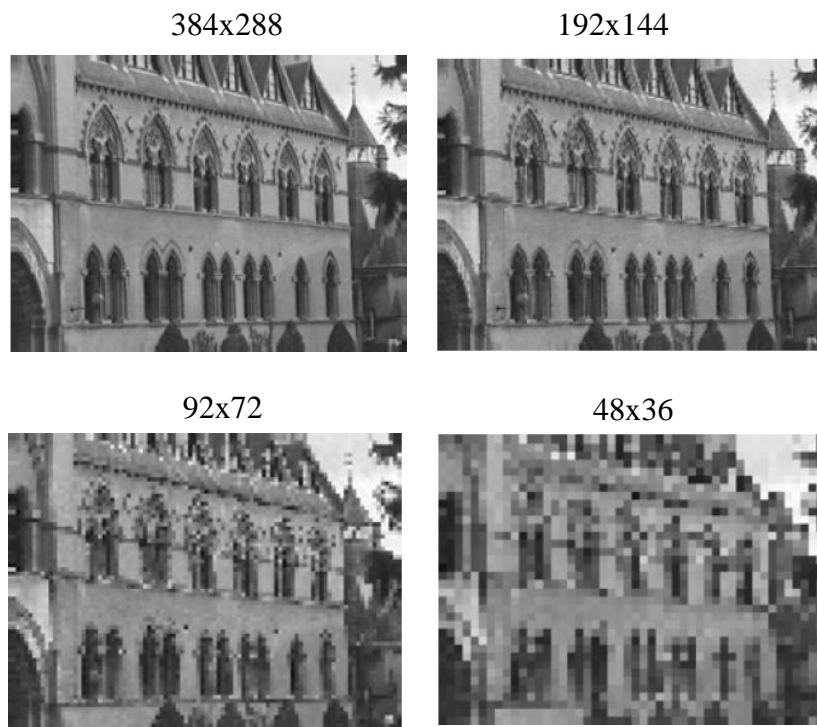
Figure 4.5 Effect of different sampling rates [4-4]

2 Levels 4 Levels

8 Levels 256 Levels
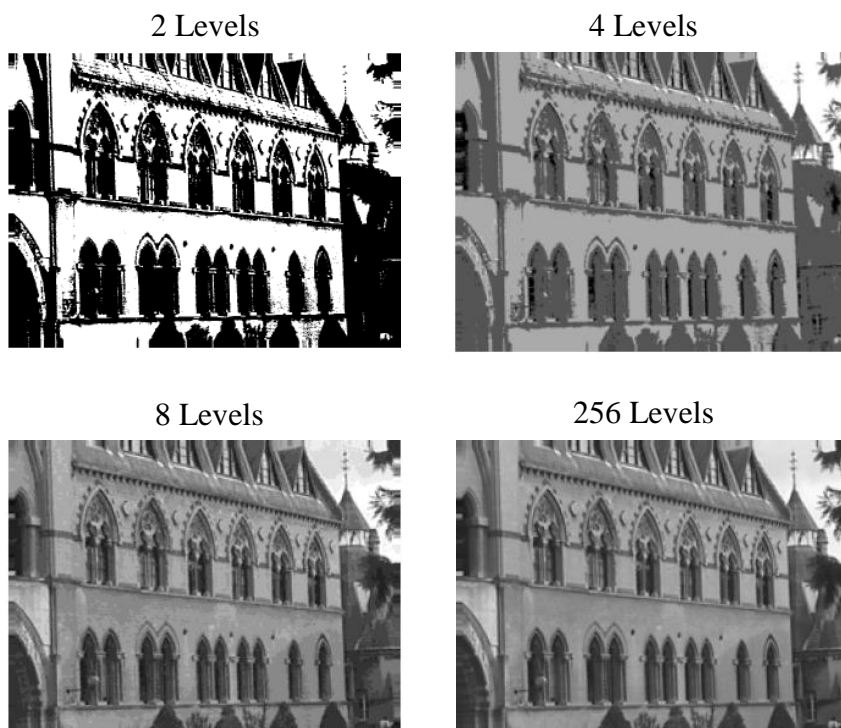
Figure 4.6 Effect of different quantization levels [4-4]

For use with a computer, the image must be digitized in both spatially and amplitude. Spatial digitization is the process that the intensities of light at each pixel location are read. Then more pixels present the resolution of the image. This technique is called sampling, as the light intensities are sampled at equally spaced intervals. A larger sampling rate will create a larger number of pixel data with better resolution. The effect of the sampling rate is shown in Fig. 4.5 it is indicate that the picture is clear and easy to recognize with the increasing of a sampling rate.

The voltage measured or charge read at each pixel is an analog value and must also be digitized. The digitization of light intensity values at each pixel location is called quantization. The resolution of an image can be changed due to the number bits used. For a 1-bits analog-to-digital converter, there are only two possibilities: "off" or "on" (0 or 1). And the quantization of 8-bits data, the maximum number of gray levels is 256. Obviously, the image will have 256 different gray levels.

The different quantization levels shown in Fig. 4.6 indicates that a low number of gray values produced a very difficult to recognize image. In printed images, 16 levels of gray values seem to be sufficient, but on a monitor we would still be able to see the gray value steps. [4-4 and 4-5]

4.1.3 Binary image

Binary images are used in many applications for example, identifying the orientations of objects. Sometimes the output of other image processing techniques is represented in the form of a binary image, for example, the output of edge detection can be a binary image (edge points and non-edge points). The binary images are images whose have been quantized to two intensity values. They are normally displayed 0 for black and 1 for white (for pixel values are 0 and 255). The example binary image that converts from color picture is shown in Fig. 4.7. The binary images are produced by thresholding a grayscale or color image, in order to separate an object in the image from the background. Usually the color of the object is black and the background color is white. It depends upon the thresholding level of the grayscale images. Choosing a threshold is very difficult, when the background and the interested object are close in gray level. The thresholding is the process that is divided an image into different levels. By select a certain grayness level of the image as a threshold and comparing each pixel value with the threshold, and then assigning the pixel to
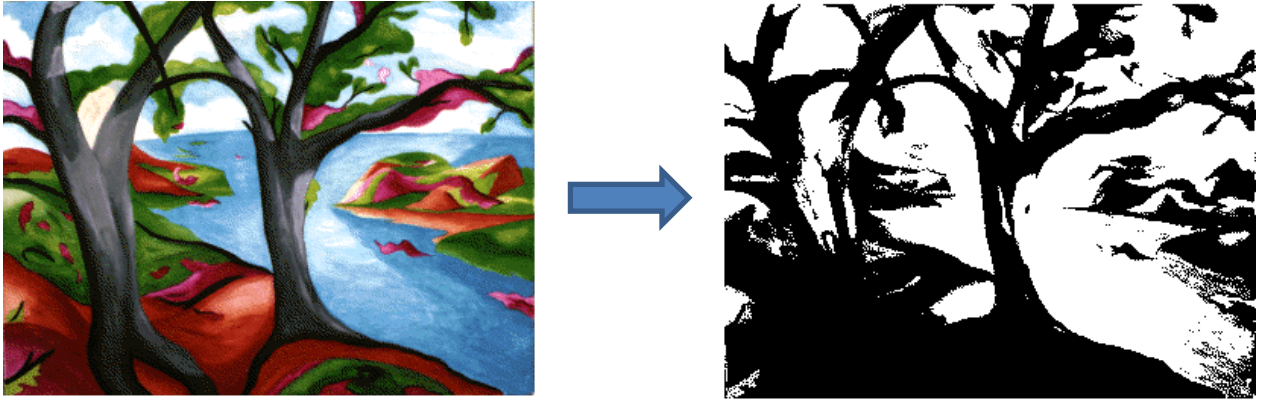
Figure 4.7 The example of a Binary image convert from color image [4-6]

| (a) Orginal image | (b) Thresholding image image | (c) Thresholding too low image | (d) Thresholding too high image |
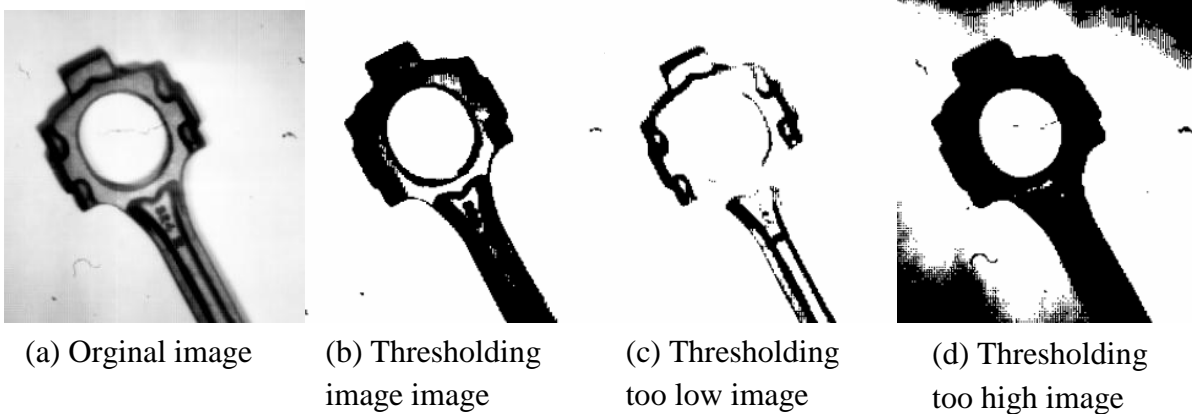
Figure 4.8 Thresholding of grayscale image [4-8]

the different portions or levels. It is depend on the pixel's grayness level, which is below the threshold or above the threshold. Thresholding can be performed at a single level or at multiple levels; the result of thresholding at different grayness levels is shown in Fig. 4.8. The level to be thresholding depends on the application, such as transforming an image into binary values, filtering operations, masking, and edge detection. [4-7 to 4-9]

4.1.4 Image detection

The image analysis is the techniques that extract information from images. And then this information can be used as image identification. There are several image analysis tasks for example, feature extraction, position analysis, size, orientation as well as image detection. The image detection is concerned with the existence or nonexistence status of being objects in an image. One of the most fundamental means of image detection is the template matching, in which a mockup of an object of interest is compared to all unknown objects in the image field [4-11 to 4-14]. If the template match between an unknown object and the template is sufficiently close, the unknown object is masked as the template object. As a simple example of the template-matching process, consider the set of binary black line geometric figures placed on white background as shown in Fig. 4.9(A). In this example, the triangle is the interested objective in the image field. And then the simple template for localization of the triangle is sequentially scanned over the image field and the common region between the template and image field is compared for similarity. The triangle template is shown in Fig. 4.9(B). [4-15]

The template matching technique is a very simple image detection technique. However, the accuracy depends upon many influences such as, noise, spatial and amplitude quantization effects, and structure of an object to be detected.

(A) Array of objects

(B) Triangle template
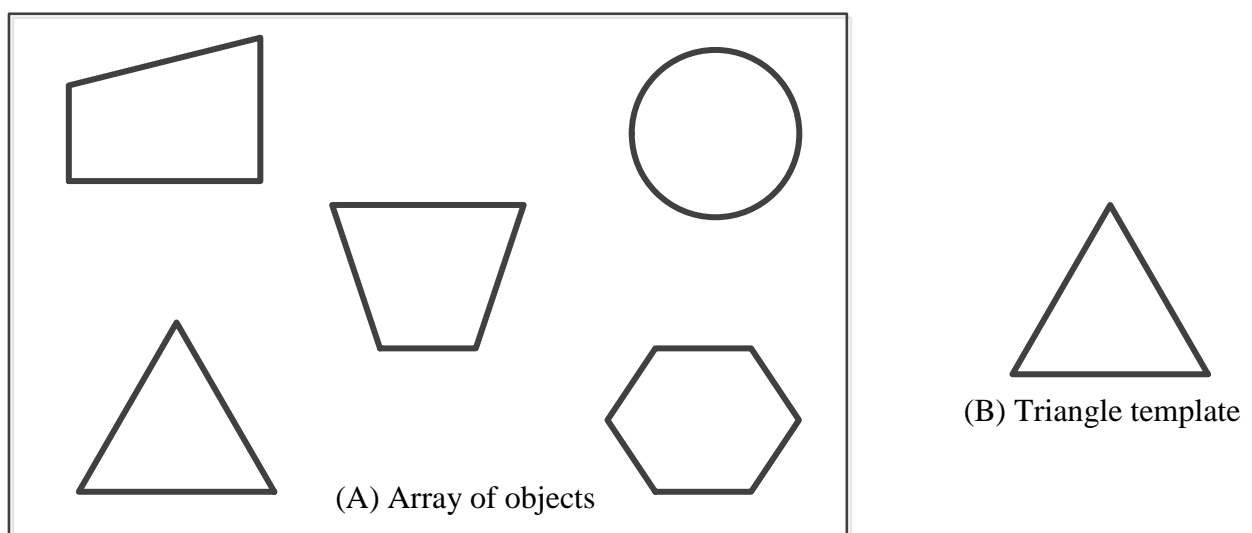
Figure 4.9 Template matching example, (A) Array of objects and (B) Triangle template

4.2 Robot path control with vision based navigation system

In a previous chapter a small robot with a microindenter was developed as shown in Fig.4.10. This section focuses on the vision-based navigation system for this small robot. The primary goal of this paper is the implementation of the microstiffness and hardness testing robot operating inside a small chamber. Several small CCD cameras with lens are thus employed in real-time path control. Such a vision-based sensory system [4-16] has been proposed for automatic assembly operation by a microrobot. The layout of CCD cameras in our setup is shown in Fig.4.11. The objectives of the setup are to provide the many viewpoints of the robot, the design of the trajectory path and the measurement point path.

The image processing technique used in this tracking system is commercially available (National Instruments Corporations) IMAQ Vision. An automatic color pattern matching technique is used in this system, so the movement of a small robot can be tracked and controlled with the help of LabView. Color pattern matching is able to accurately location object whose size varies and is
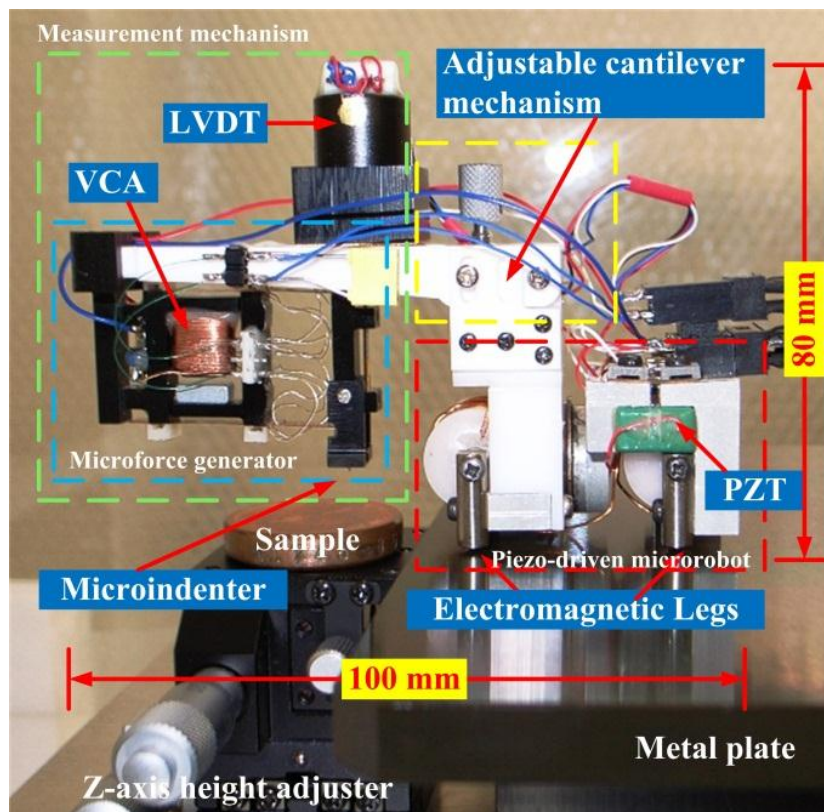
Figure 4.10 The prototype of the microindentation robot

rotated within 360°[4-17]. Color pattern matching is composed of two important parameters, i.e., a marker and a template. With the template pattern of the marker, the template is scanned in the image to get the matching position for shape and color sensitivity. The matching score is determined by the comparison of color and pattern between the marker and its template. The score of matching is related to how accurately the pattern model matches the marker found. The matched pattern is marked and the position of the marker is identified by a coordinate pixel from the whole picture. Such coordination is utilized as a representative of the marker position.

4.2.1 Experimental setup for calibration of the camera system

Two camera types a high-magnification type (C_1, C_3) and a wide view angle type (C_2) are employed in this tracking system as shown in Fig. 4.11. C_1 and C_2 cameras are placed on top of the robot. The C_1 camera has two operational functions. The first function is for the operator to observe a sample surface and check the area of interest. The second function is for the measured position to be fed back to the controller to maneuver the robot during the measurement process. First, the C_1 camera focuses on a red marker placed on the center axis of the LVDT case so that the indenter position can be detected. Second, the C_2 camera is placed next to C_1 so that it can monitor the overall behavior of the robot in the working range. Finally, the C_3 camera with a microscope lens with a long working distance is placed on the right side of the robot in order to observe the behavior of the indenter tip.
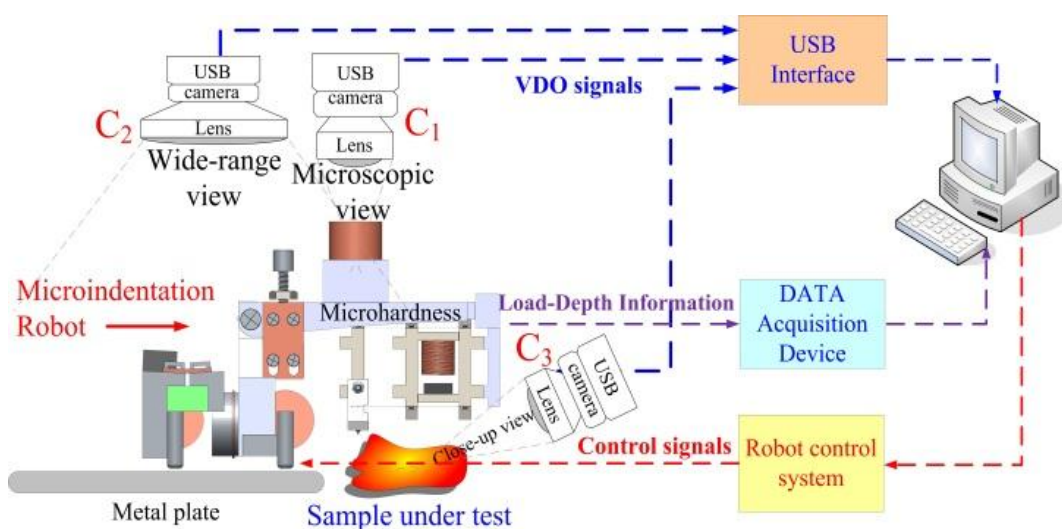
Figure 4.11 Multi-cameras based coordinate system for robot navigation

Because many cameras work together but at different scales and functions, verification of CCD camera pixel change due to the displacement change is required before implementation of the camera system.

In the experiment setup shown in Fig. 4.12 two precision-controlled X-Y stages are used as the displacement standard. The large stage has a moving range of about 50mm, while the small stage has 25mm. Both of them have the same movement resolution at 1μm per step. There are two markers, placed on both stages, whose shape and size are different for each camera. The cameras are set up to focus on the markers on the stage. When the stage is moving, the image of a marker that is monitored by a camera also moves. By comparing the image pixel change read out by a camera to the position of the marker on the moving stage, the CCD pixel is calibrated.
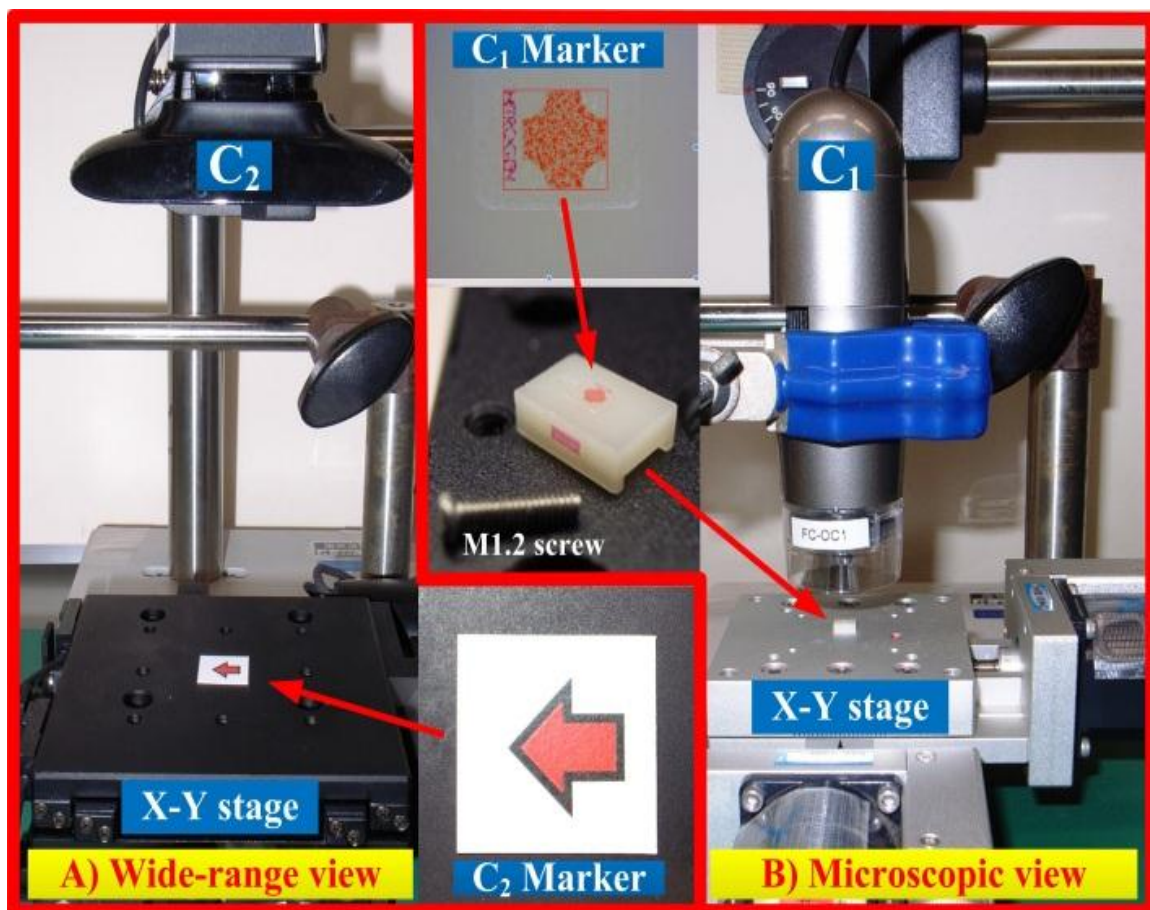
Figure 4.12 Experiment setup for calibration of cameras pixel change compare with the actual movement of X-Y controlled stage, (A) wide-range view and (B) microscopic view

4.2.1.1 Calibration in wide-range view

The wide-range view (C_2 camera) focuses on a large red arrow marker about 10×10mm placed on a large stage. The focusing length is fixed at 150μm per pixel. The C_2 camera has an effective CCD area of 1024×576 pixels. This implies that the operation range of C_2 is about 150×80mm. The calibration procedure of the C_2 camera is as follows: the stage is moved at 1mm per step from 0 to 50mm repeated ten times, and then the pixel read by tracking system is compared to actual stage movement. Experiment results are shown in Fig. 4.13. It is depicted that the accuracy of tracking system with the C_2 camera is achieved at ±1 pixel or about ±150μm.
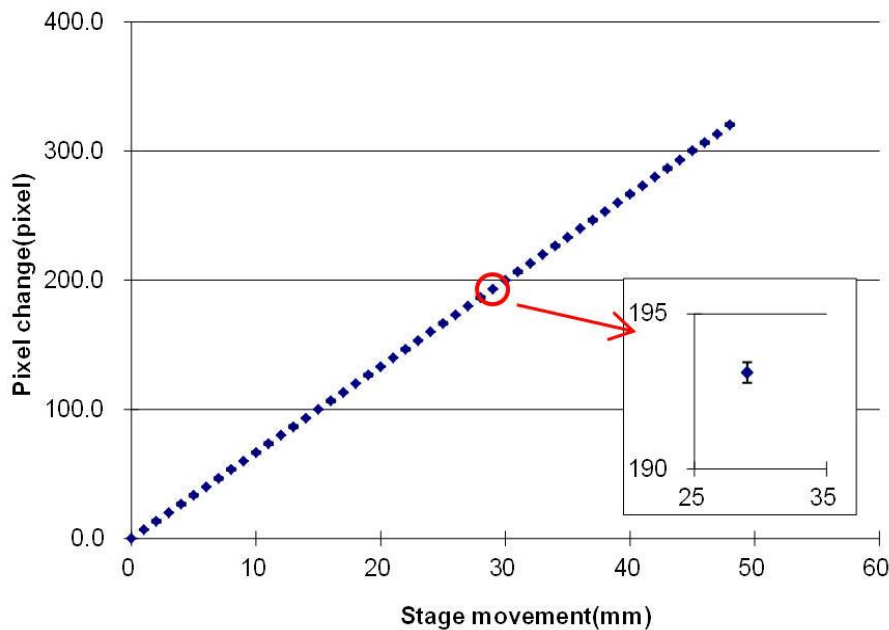
Figure 4.13 Comparison results between actual movement of a marker and a pixel change of C_2 camera (wide-range view)

4.2.1.2 Calibration in microscopic view

The microscopic view (C_1 camera) focuses on a marker shaped similar to a plus (+) sign. It is less than 1mm and is placed on the small X-Y stage. The focusing length is fixed at 2.5μm per pixel. The C_1 camera has an effective 1024×576 pixel CCD area, which indicates that the operation range of C_1 is about 3.2×2.3mm. The calibration procedure of the C_1 camera as follows: the stage is moved at 10μm per step from 0 to 2.5mm repeated ten times, then the pixel read by tracking system is compared to actual stage movement as shown
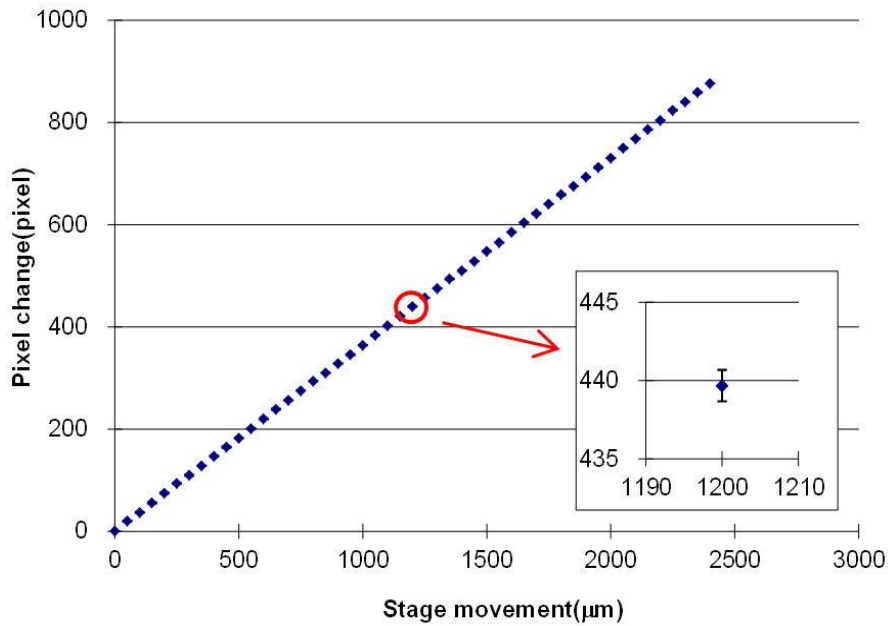
Figure 4.14 Comparison results between actual movement of a marker and a pixel change of C_1 camera (microscopic view)

in Fig. 4.14. It is indicated that the accuracy of the proposed technique with the C_1 camera is also achieved at ±1 pixel or about ±2.5μm.

Comparison results between the tracking camera and the controlled X-Y stage have shown that accuracy is achieved at ±1 pixel by both cameras. These results have reached the limit of the CCD camera at one pixel. After that, the image tracking system is implemented into the whole measurement system as shown in Fig. 4.15. The plastic chamber is 50cm wide, 30cm high and 30cm deep. The overall system, including the microindentation robot and the vision-based tracking system, is encompassed into the chamber.
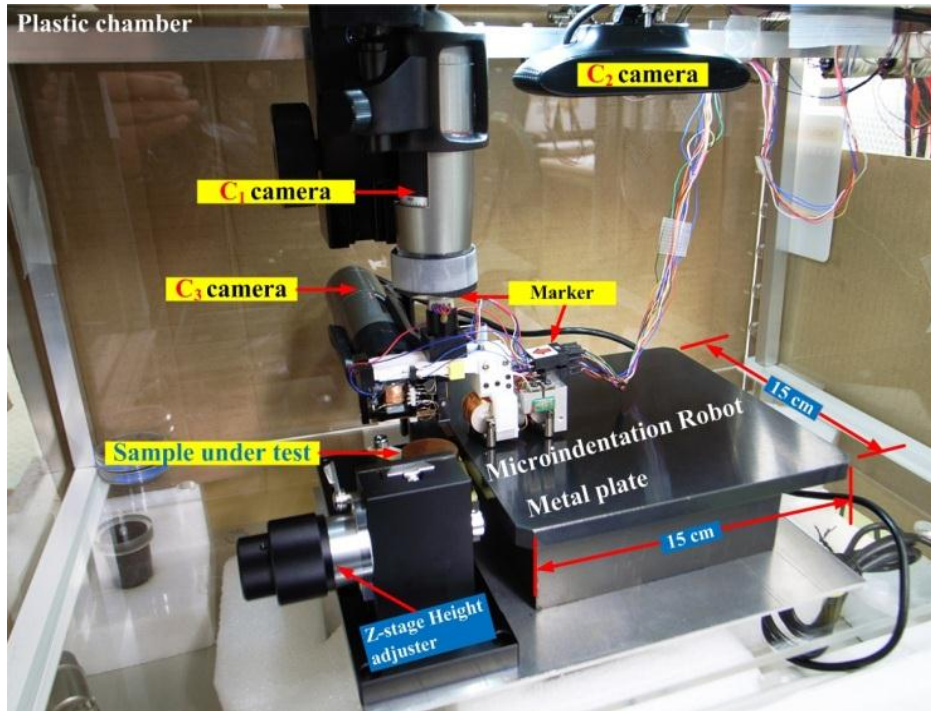
Figure 4.15 The vision based navigation system of the microindentation robot with three CCD cameras in the chamber
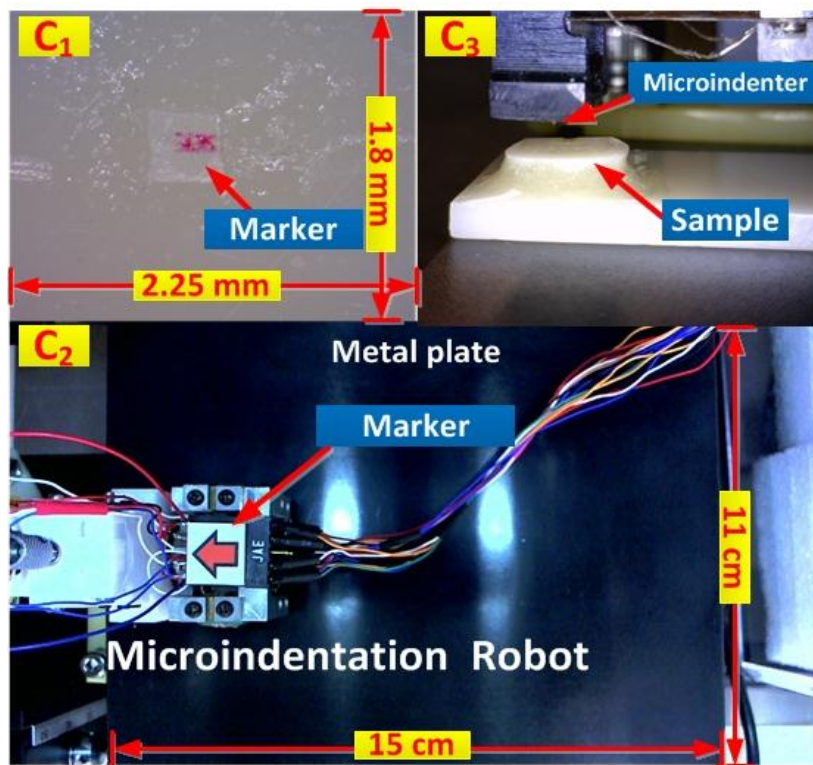
Figure 4.16 Camera views and the actual scale from C_1, C_2 and C_3 in the chamber

4.2.1.3 The lighting system

The working range of the camera system has been changed to make it appropriate to the chamber size, i.e., C_1 is set to 1.75μm/pixel with a full operation range of 2.5×2mm, and C_2 is set to 190μm/pixel with a full operation range of 150×100mm(Fig. 4.16). These scales come from calibration results between image pixels and the standard scale after all cameras are placed in positions inside the chamber. Then the lighting system is applied to the measurement chamber. Lighting system in the research can be separated into two categories, i.e., the lighting for wide-range camera and microscopic view camera. The wide-range lighting system is used two external LEDs (light emitting diode) setup at the top of measurement chamber as shown in Fig. 4.17(A), while the microscopic view camera is used internal ring LED as shown in Fig. 4.17(B). Both of them setup as the vertical incident-light system in which light is irradiated from a point substantially just above an object to be
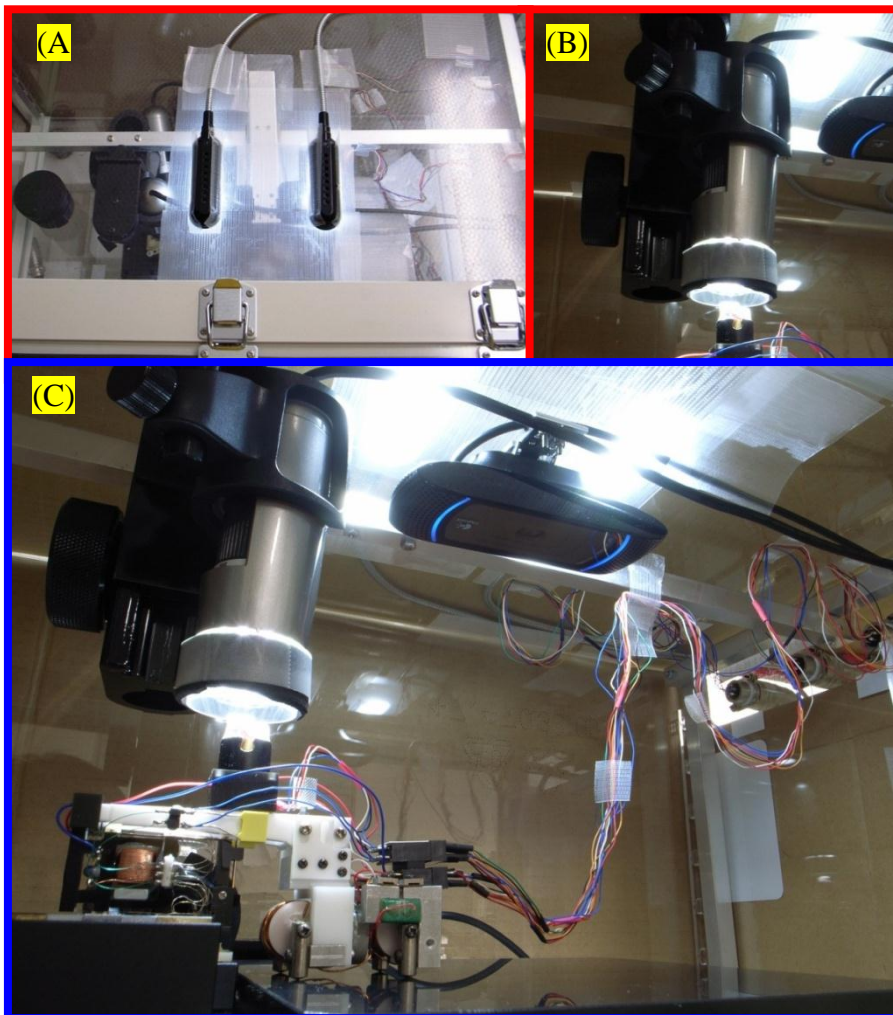
Figure 4.17 The lighting system. (A) External light for wide-range camera. (B) The internal ring light for microscopic view camera. (C) Overall lighting

controlled. The overall lighting system is shown in Fig. 4.17(C). The light source were chosen by conditions that the intensity must provide a quality image and available at low cost. Because the LEDs light intensity and chromaticity are largely vary due production process at the manufacturer, so the quality of an image to be captured must be checked. For the microscopic view camera that comes with internal ring light is not a problem, the quality of an image to be captured is brilliant as shown in Fig. 4.16(C_1). Meanwhile the external light for wide-range view camera is a custom built, so the image quality around the working area must be confirmed. It was determined by placing a marker at nine specific positions around working area. Then using color pattern matching to score the marker. If the score is over 80 point, this means the marker can be recognized. That means the light system is provided sufficient light intensity. The score result of each marker position is shown in Fig. 4.18. The results have shown that the external light system is provided a quality image. At this moment, the vision-based position tracking system is ready to track and control a robot's position. In the next section, a surface stiffness measurement process and a robot path control are described.
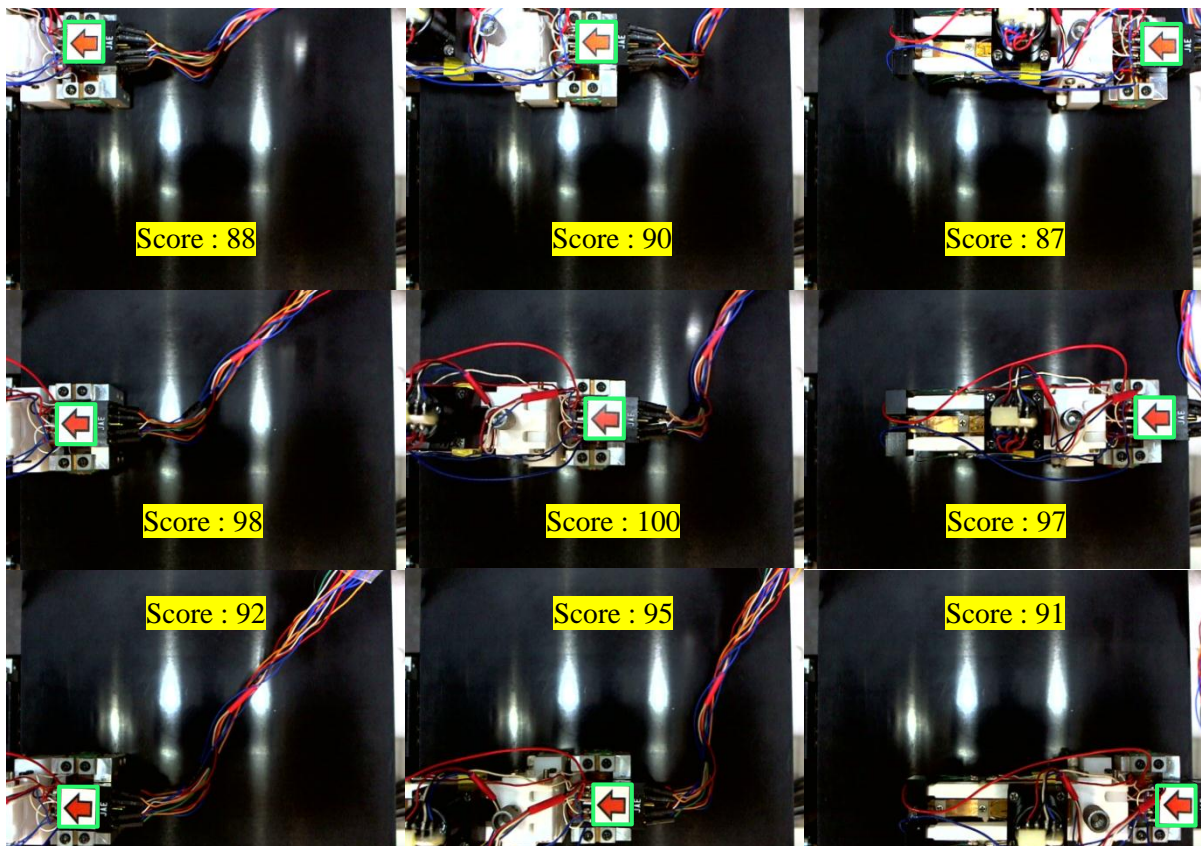
Figure 4.18 The marker and its score at several positions around the working area

4.2.2 Robot path control strategies

After the camera system is implemented in this section, the operational procedure of the tracking system is discussed as shown in Fig.4.19. The small robot is placed inside a parking area and the position of the robot is tracked and controlled by the C_2 camera. The sample is observed from another side by the C_1 camera for designing the measurement point. The path that is designed can be obtained by the user. Normally, it is assumed that the surface of the sample under test is clean and homogeneous so that points interesting for making the stiffness measurement are different texture areas. The user assigns the three biggest vivid color patterns on the sample as measurement points, and then
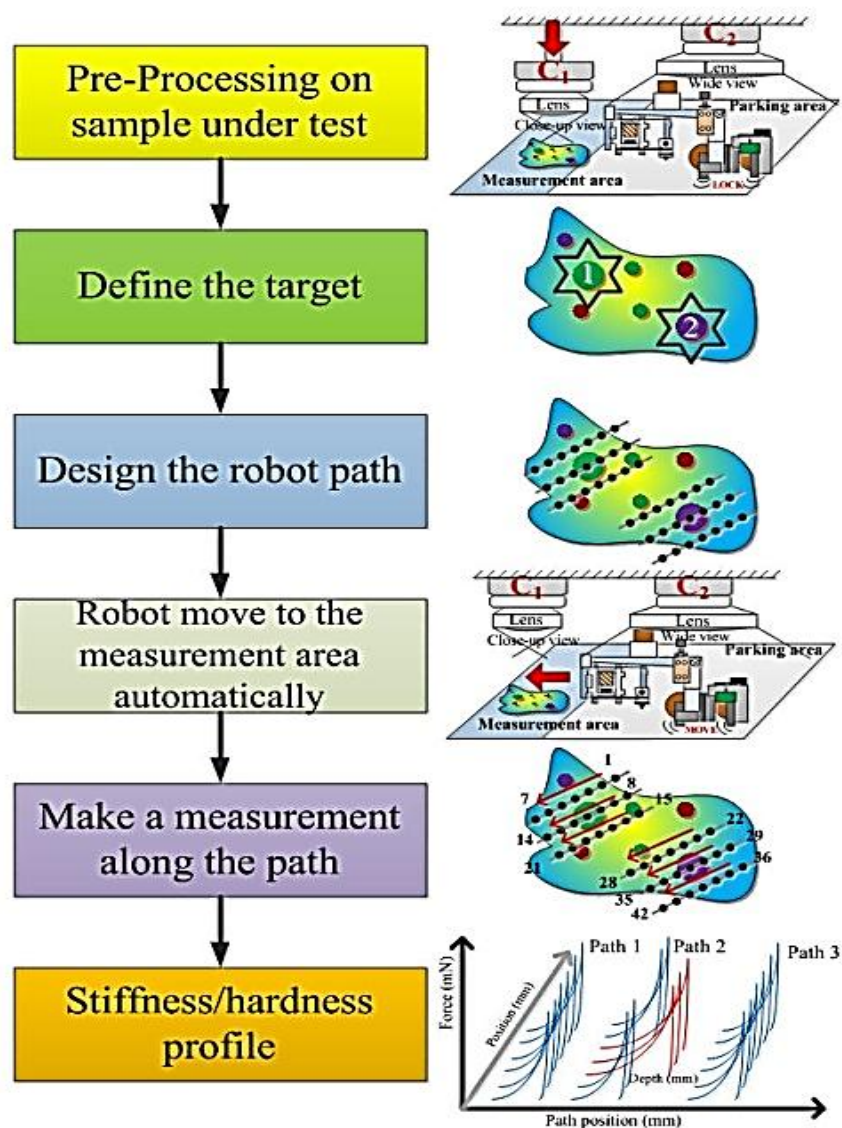
Figure 4.19 Measurement process algorithms

robot paths are designed to pass through a measurement point one line and outside each top and bottom one line as shown in Fig. 4.19. After designing of a measurement path point is finished, the C_2 camera provides the coordinates of a robot, and then a computer designs the geometric trajectory path. A robot is maneuvered along the designed trajectory path from the parking area to the measurement area automatically, controlled by the C_2 camera. After the robot reaches the measurement area, the robot makes an indentation along the designed measurement point path, which is controlled by the C_1 camera. Finally, the surface stiffness/hardness profile of measurement areas is identified.

Robot path control strategies in this research are divided by a camera view and its function, i.e., the wide-range view C_2 camera and the microscopic view C_1 camera. Robot position control procedures for these cameras are different, as described in the next two sections.

4.2.2.1 Path control for wide working range

The wide-range view C_2 camera, as shown in Fig. 4.16 is focused on the red arrow marker placed on the robot. This marker is a representation of the robot position and orientation angle. Robot path control in the wide-range view is depicted in Fig. 4.20. The path is produced by a combination of four movement actions, i.e., forward (FW), backward (BW), right turn (TR) and left turn (TL). As discussed in previous paper [9], this small robot is driven by piezo-actuators and electromagnetic legs in the manner of an inchworm. The robot is turned left or right by supplying a different phase signal to the piezo-actuators and electromagnetic legs simultaneously because the joint that connects the front and rear leg is not placed at the center of the robot. While the robot is turning, not only its angle changes but the turning movement also generates changed displacement. A marker cannot be placed at the position of the pivot point, furthermore, because such a point is covered by the robot itself. The relation between turning angle θ and y-displacement change is thus required in the TL and TR directions. Such a relation is determined by a series of turning actions, i.e., each TL or TR starts from $\theta = 0$ degree and goes to $\theta = 50$ degrees, as shown in Fig. 4.21. The standard curve fitting of the relation is shown in Eq. (4.1) and (4.2). These equations are used for calculating the deviation of the y coordinate, which is related to the robot when it turns from 0 to θ degrees and vice versa.
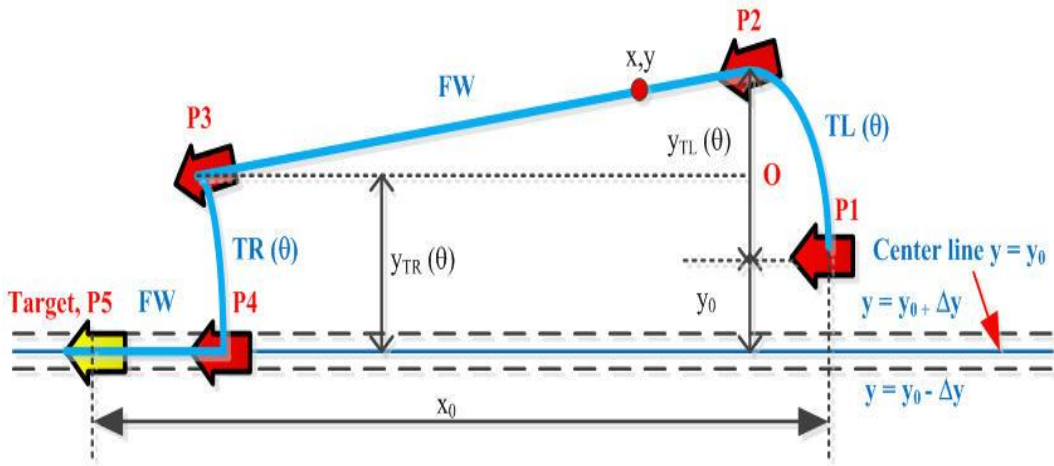
Figure 4.20 Robot path design algorithm for wide working range (C_2 camera)

$$y_{TL} = 0.0034\theta^2 - 0.7403\theta \dots\dots\dots\dots\dots\dots\dots\dots\dots(4.1)$$

$$y_{TR} = -0.0029\theta^2 + 0.7842\theta \dots\dots\dots\dots\dots\dots\dots\dots\dots(4.2)$$

Where;

y_{TL} and y_{TR} are y displacement corresponding to the orientation of the robot in a case of the robot turns left and turns right, respectively.

The center line ($y=y_0$) in Fig. 4.20 is the straight line which the robot reaches the target by only moving forward, without changing turning angle θ. To prevent problems from slippage, the center line requires an upper and lower limit ($\pm\Delta y$), which is specified by the user. Assuming that the robot is placed at P1, its orientation θ should be $\theta = 0°$ (if $\theta \neq 0°$, the robot must turn until $\theta = 0°$), the distance to the target is x_0. The relation of the turning angle, shown in Fig. 4.21 indicates that the robot needs at least 30mm space for turn θ into 50 degrees in both TL and TR movement. For this reason, distance x_0 (Fig. 4.20.) must be larger than 30mm if a robot stays off the center line ($y=y0$). If the starting position of a robot (P1) is placed near the target (P5), for example, the robot has to move back more than 30mm. On Fig. 4.20, a robot turns left θ degrees from P1 to P2 with distance y-displacement ($y_{TL}(\theta)$) and smallest turning angle θ calculated by Eq. (4.1) under the condition that OP3 must be smaller than x_0 in this equation
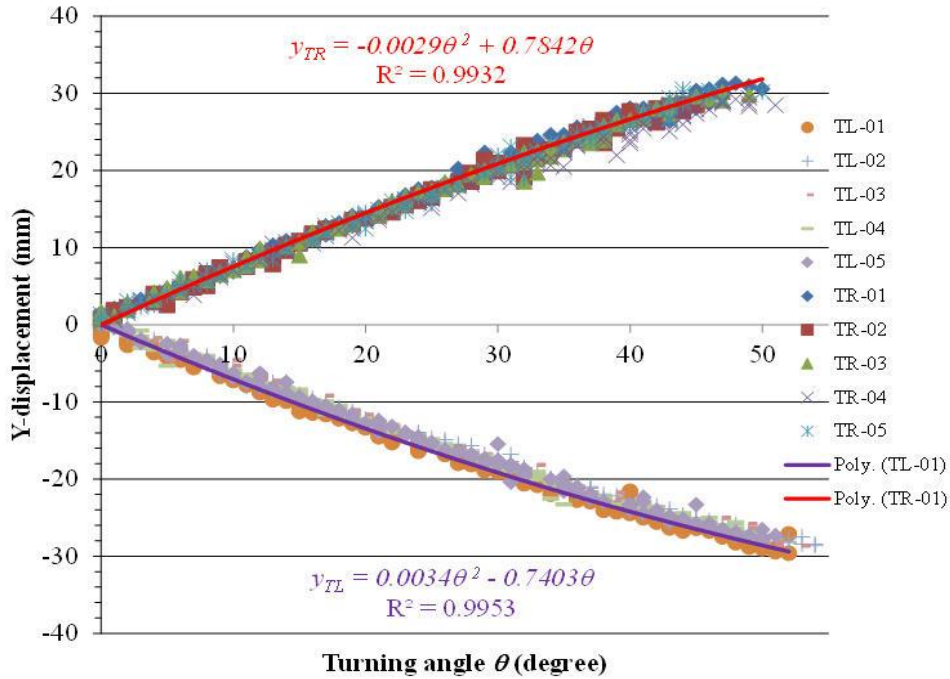
Figure 4.21 Turning angle and Y-displacement ability of the robot which is monitored by C_2 camera

$$OP3 = \frac{OP2}{tan\theta} = \frac{y_0 + y_{TL}(\theta) - y_{TR}(\theta)}{tan\theta} \ldots\ldots\ldots\ldots\ldots\ldots..\ldots(4.3)$$

Where;

θ is the turning angle.

OP3 is displacement from *O* to *P3*.

OP2 is displacement from *O* to *P2*.

y_0 is displacement from *P1* to center line.

y_{TL} and y_{TR} are y-displacement corresponding to θ when a robot turns left and turns right, respectively.

The smallest θ in Eq. (4.3) is established by increasing θ from 0° until condition OP3< *x0* is satisfied. The robot then turns to P2 with such a θ degree and moves forward to P3. Assume that the angle of θ does not change during movement and the coordinate of a robot is *x, y* point. Coordinate *y* of P3 is determined by the following condition:

$$y_0 - \Delta y < y + y_{TR}(\theta) < y_0 + \Delta y \ldots\ldots\ldots\ldots\ldots..(4.4)$$

Where; *Δy* is the tolerance limit specified by the user.

The condition in Eq. (4.4) is checked simultaneously while the robot is moving to P3. When the condition is satisfied, the robot turns right to P4, i.e.,

the θ degree become to 0°. With y-displacement $y_{TR}(\theta)$ calculated from Eq.(4.2), the robot then moves forward from P4 to target P5 with the x coordinate defined by

$$x_0 - \Delta x < x < x_0 + \Delta x \dots\dots\dots\dots\dots\dots\dots\dots(4.5)$$

Where; Δx is the tolerance limit specified by user.

The condition in Eq. (4.5) is checked simultaneously while the robot is moving to P5. Finally, the condition established by Eq. (4.5) is the target position. This control algorithm is similar wherever a robot (red arrow marker) stays below or above the center line.

4.2.2.2 Path control for microscopic working range

The microscopic view C_1 camera has an image with a working range of 1.8×2.25mm, as shown in Fig. 4.16 which operates on a very small marker size of about 100×200μm. The main function of C_1 is to track the position of a marker that is moves around inside the 1.8×2.25mm working area. A basic odometry reduction error method is utilized to decrease the deviation between the actual position of the marker and the target position. To reach the target, the deviation of the actual position and the target must be reduced to zero as shown in Eq. (4.6). On the way to reaching the target, equations Eq. (4.7) and (4.8) are checked simultaneously.
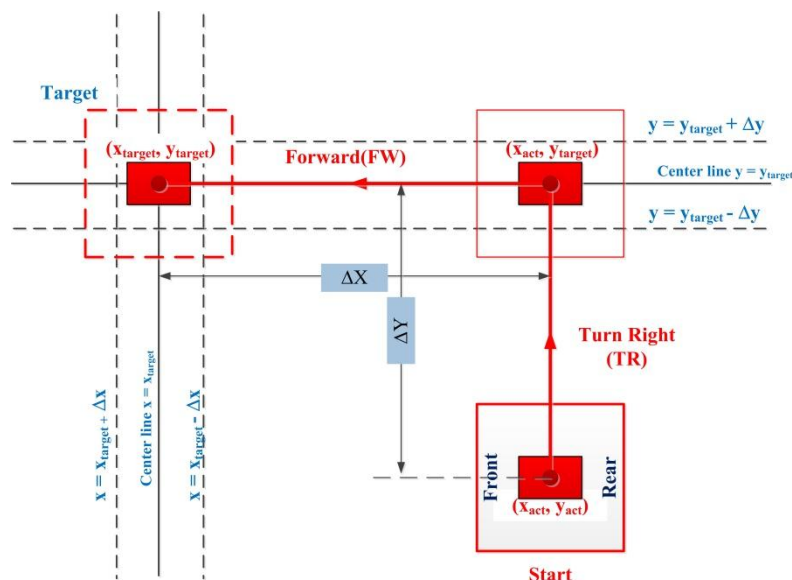
Figure 4.22 Robot path design algorithm for microscopic working range (C_1 camera)

$\Delta X = x_{act} - x_{target}$

$\Delta Y = y_{act} - y_{target}$

$$0 = \Delta X = \Delta Y \dots\dots\dots\dots\dots\dots\dots\dots\dots\dots\dots\dots\dots\dots(4.6)$$

$$Y_{target} - \Delta y < y_{act} < y_{target} + \Delta y \dots\dots\dots\dots\dots\dots\dots\dots(4.7)$$

$$X_{target} - \Delta x < x_{act} < x_{target} + \Delta x \dots\dots\dots\dots\dots\dots\dots\dots(4.8)$$

Where;

ΔX and ΔY are the deviation between the actual and target position of the marker. (x_{act}, y_{act}) is the position of the marker at the actual position.

(x_{target}, y_{target}) is the position of the center line of the target position and $\Delta x, \Delta y$ are the upper and lower limits specified by the user.

An example of operation is shown in Fig. 4.22 where the robot initially stays at the starting point inside the solid line square (x_{act}, y_{act}). The best way to attain the target inside the dashed-line square (x_{target}, y_{target}) is to move in a forward slanting direction to the right. However, the mobility of the robot is not precise in a such direction, i.e., movement leads to slip, so the robot has to move to the right side to position (x_{act}, y_{target}) by turning right (TR) within distance ΔY. During left or right movement, Eq. (4.7) must be satisfied. Finally, the robot moves forward (FW) within distance ΔX to target position (x_{target}, y_{target}), during forward (FW) or backward (BW) movement the Eq. (4.8) must be satisfied.

Here, robot path control strategies in the C_1 microscopic view and the C_2 wide range view are described, and then the repeatability of the tracking system by such cameras is described in the next section.

4.2.3 Basic performance

To demonstrate the performance of the tracking system, several experiments are presented in this section. The experiment concerning repeatability of the camera system is described first, and then the hardness/stiffness measurement performance test is described at the end of this section.

4.2.3.1 Wide-range path control

The reproducibility of wide-range tracking system is determined by the experimental setup shown in Fig. 4.23. The testing procedure is carried out by placing a robot at ten specific positions inside a parking area. The robot then navigates to the target following the robot path and the last position of the robot at the target is recorded. The last position of the robot is a representation of the reproducibility of the tracking system of the C_2 camera as shown in Fig. 4.24. Experiment results show that this tracking system achieves ±1mm within a 150×100mm working range.
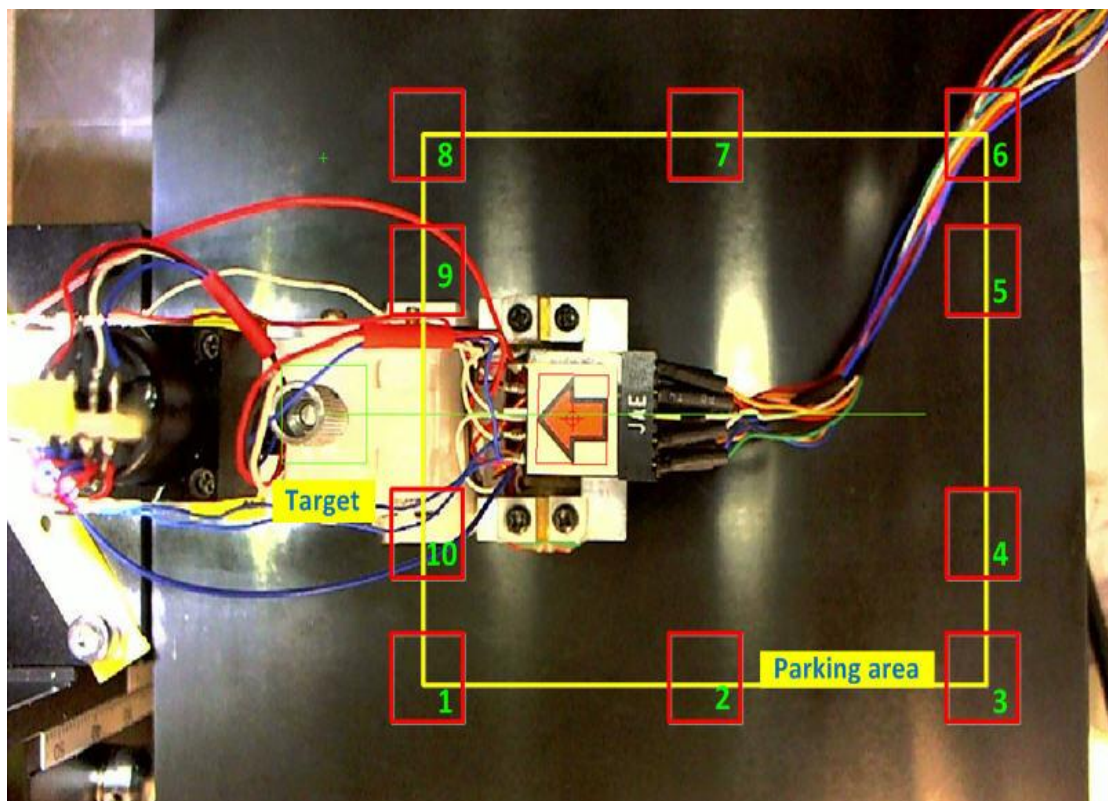
Figure 4.23 Experiment setup for wide-range path control
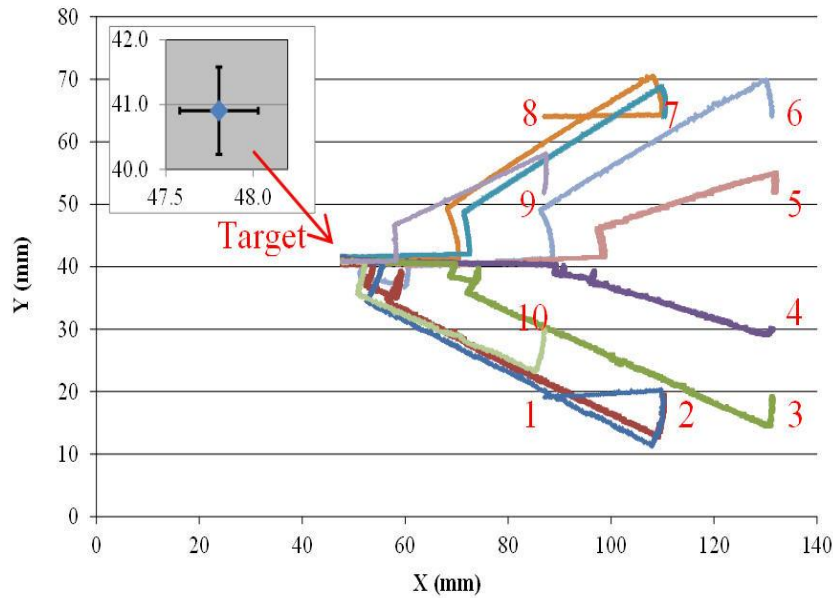
Figure 4.24 Repeatability experiment results of wide-range path control

4.2.3.2 Microscopic range path control

To carry out the repeatability test of microscopic view tracking system, the center of the working range is set as the center point because the pattern-matching technique recognizes a marker only when its shape is similar to the template. In the case of the C_1 camera view, when a marker is close to an image border, the shape of which is chanced, then the gap between the marker and image border is required to be 100mm because the marker size is about $200 \times 100 \mu m$. In the experiment, the target is assigned with four positions, FW, BW, TL and TR, at the edge of an image with another $100 \mu m$ free space as shown in Fig. 4.25. The robot then navigates into the fourth position in ten rounds (going and returning) for each position, starting from the center point, and the last position of the robot is recorded. The last position is a representation of the repeatability of the tracking system of the C_1 camera as shown in Fig. 4.26. Experiment results show that this tracking system achieved $\pm 3 \mu m$ within a $2.5 \times 2mm$ working range.

The operation of the robot during try to reach the target with different starting position is shown in Fig. 4.27. A robot can reach the target with the designed path control no matter the start point is below or above the center line.
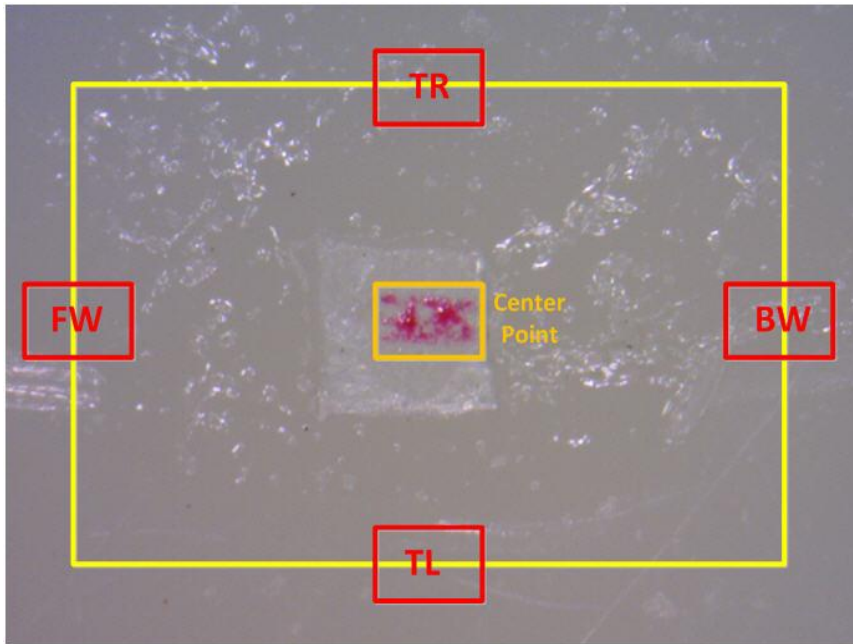
Figure 4.25 Experiment setup for microscopic range path control (In this picture is shown the marker that placed on the top of LVDT case)
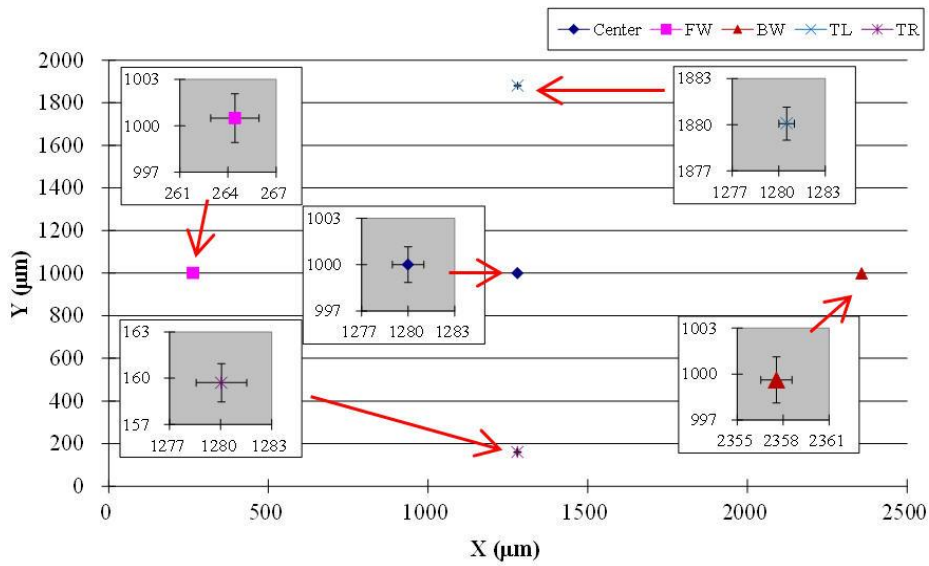
Figure 4.26 Repeatability experiment results of microscopic range path control
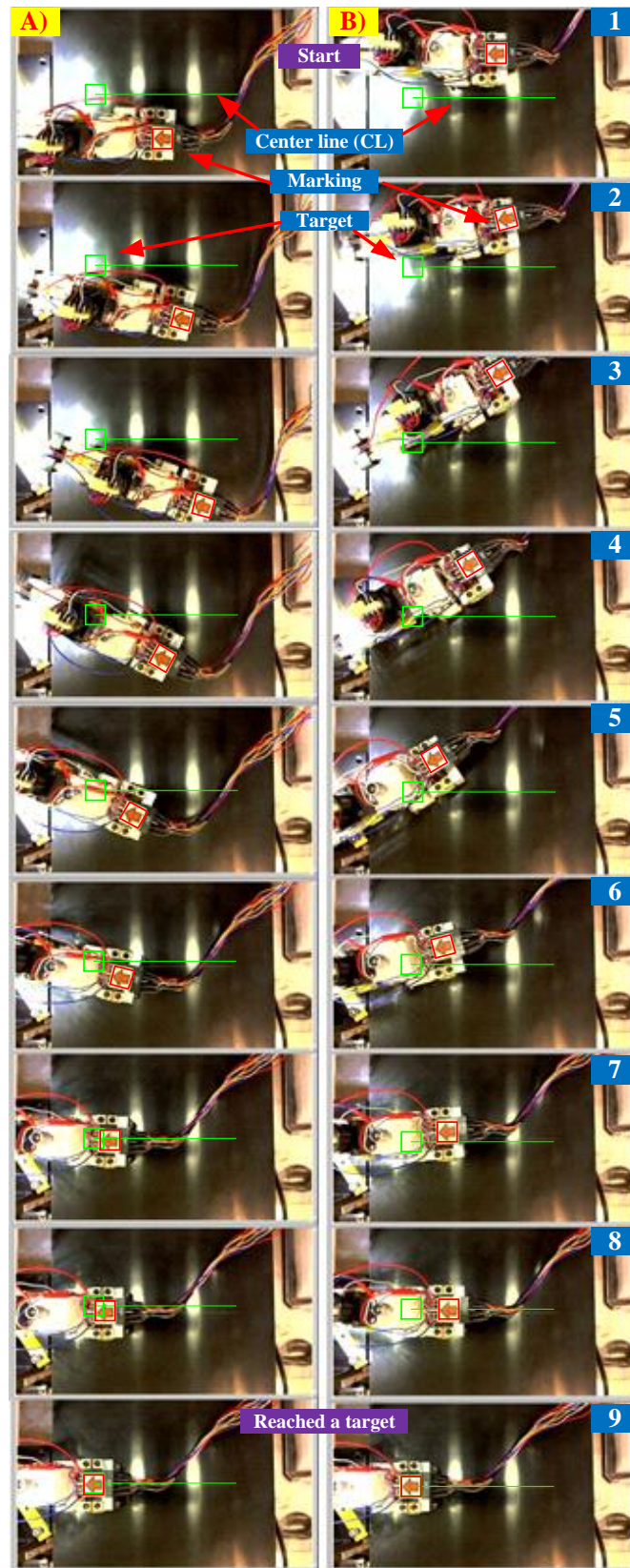
Figure 4.27 The robot during automatically reaches the target with different starting position, i.e., (A) below the center line and (B) above the center line

4.2.3.3 Sample measurement test

To investigate the performance of the tracking system, we propose one of the most difficult surface hardness investigations on a human tooth sample in this experiment. The tooth is composed of four important layers, i.e., enamel, dentine, cementum and pulp. Enamel is the hardest tissue in the human body, and is even stronger than bone. Next is dentine, whose layer is similar to bone. Inside dentine, pulp occupies the center, and consists of soft connective tissue and blood vessels. Finally, cementum, which is mineralized dental tissue, covers the roots of the tooth [4-18].

In the experiment, an artificial unhealthy tooth is used to investigate the performance of the tracking system. The tooth specimen is made from a human tooth from a 60 years old person. A series of holes in both the enamel and dentine regions of a permanent tooth have been made 200μm deep with the 50μm and 100μm drill bits shown Fig. 4.28(A). Elastomer glue is then inserted into all of the holes. The glue surface is very soft and highly elastic, so the indentation load-depth characteristic of the glue surface is different from a normal tooth surface. With the help of image processing, the user can easily designed the measurement path pass through a small glue hole on the dentine surface. There are four paths designed, two of which pass through the glue hole
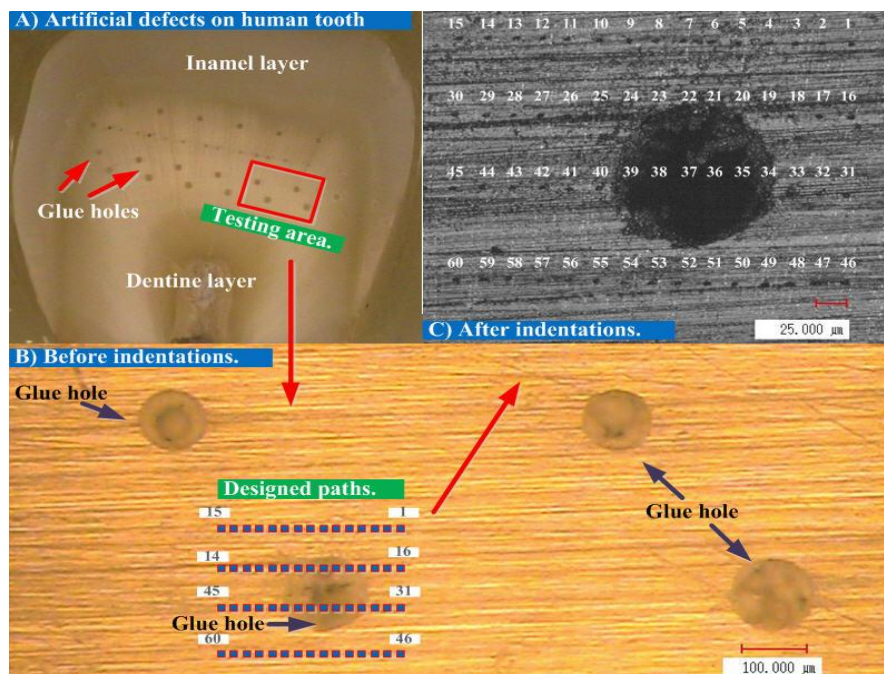
Figure 4.28 (A) Artificial defects on a human tooth. (B) The designed paths on a glue hole of a human tooth. (C) The series of indentations scan pass through the glue hole on dentine surface of a human tooth
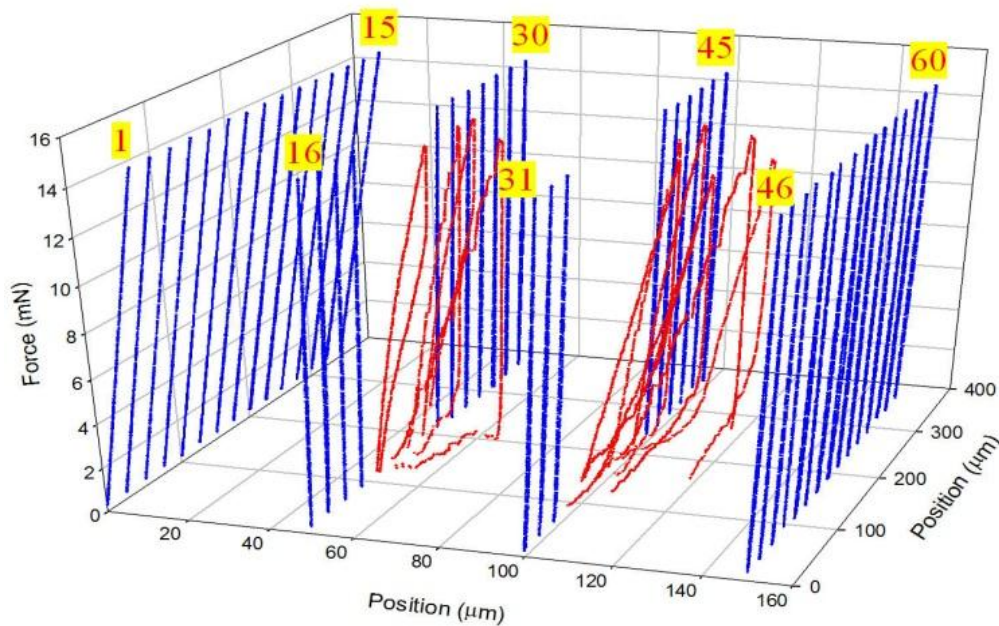
Figure 4.29 3D indentation load-depth curves present the problem area on a human tooth with very deep indentation depth compare with normal tooth surface

and others of which are on the dentine surface. Designated path points with 25μm separations are positioned as shown in Fig. 4.28(B). Indentation test force is fixed at 15mN and total dwell time with maximum force applied is 10 seconds. A close-up of the experiment area is shown in Fig. 4.28(C). In experimental results, the load-depth characteristics of the artificial unhealthy tooth surface are summarized in Fig. 4.29 where different degrees of hardness on different surface characteristic are checked in this experiment and several load-depth curves are identified. The second and third indentation paths showing the strange behavior of load-depth curves evidently comes from the effect of the glue hole.

4.3 Discussion

In this chapter, the first prototype of a microindentation robot combined with a vision-based navigation system has been constructed and described. The experiment results have indicated that the simple image processing technique provides the benefit of a micropositioning and the surface scan tasks. The improvement comparison between the indentation pattern before and after implemented the vision-based navigation system is shown in Fig. 4.30. It is cleared that the simple vision-based navigation controls the position of a small robot precisely. In the experiment, all of the measurement points that are

designed inside an enclosure chamber can be reached by a robot. And the last experiment results in this chapter have depicted that this measurement system capable to identify the microsurface stiffness as well as the inside defects on the bio sample.
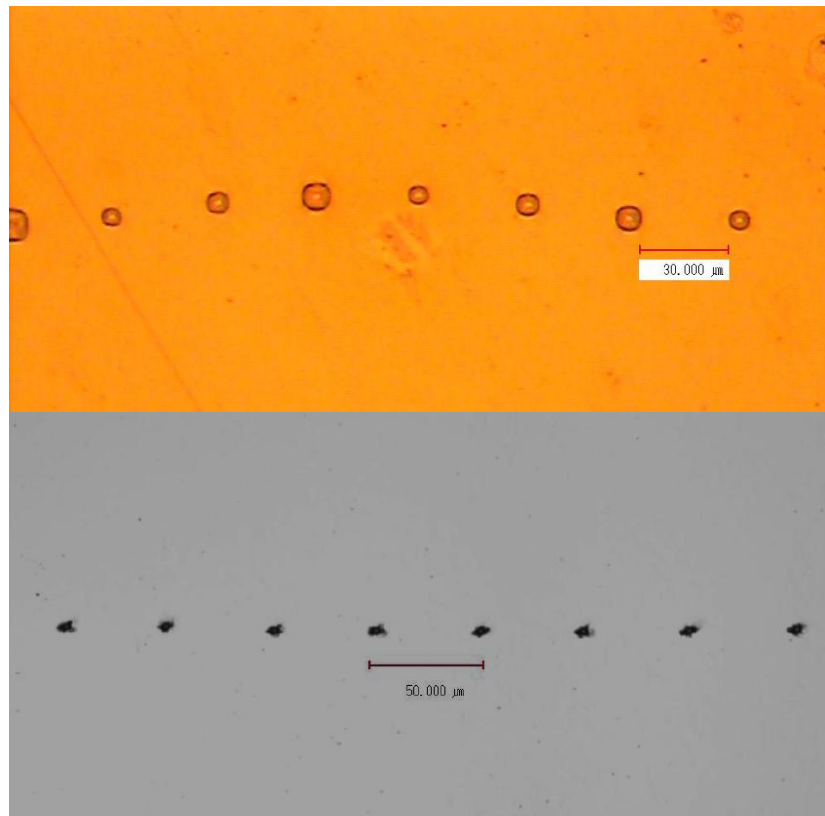
Figure 4.30 The improvement of the indentation pattern before (up) and after (down) implemented the vision-based navigation system

CHAPTER 5. CONCLUSION AND FUTURE WORK

5.1 Conclusion

This thesis presents a microsurface measurement system that is composed of a microrobot and the handmade microindentation mechanism incorporating with the vision-based robot navigation system. It is proposed for investigating the hardness and stiffness of microparts in the special chamber. The small force generator mechanism is simply consisted of a voice coil actuator (VCA) and the tandem leaf spring mechanism. With the help of an image processing technique, a vision-based coordination system with a local close-up view and an overall global view has been developed to identify the locations of the robot and the indenter with high accuracy over the working range. The summarized of this thesis is separated by chapter as follow;

5.1.1 Conclusion of chapter 1

In this chapter, the basic hardness measurement including the basic mechanism of the hardness machine is introduced. Moreover, at the end of this chapter, the research objective is also presented. The hardness test has been widely used for nearly 100 years because indentations are very small and the surface quality of the material is not destroyed. This technique is therefore considered as nondestructive test method. There are three general types of hardness measurements, Scratch hardness, Rebound hardness and Indentation hardness. The research objective is to fabricate a microindentation robot. This unique measurement system with very small body and high mobility can be employed for purposes such as performing an investigation in a special chamber. In cooperate with the vision based coordination system with the local close-up view and the overall global view, the locations of small robot and the indenter can be maneuvered precisely with high accuracy over the working area.

5.1.2 Conclusion of chapter 2

In this chapter, the originally fabricated microindentation mechanism as well as the machine layout and configuration including the basic performance are presented. The microindentation mechanism is composed of the handmade small force generator mechanism, which is simply combination between a voice coil actuator (VCA) and the tandem leaf spring mechanism. It can produce and

verify a small force up to 17mN with good linearity and 50μN resolutions. After attached the microindenter at the pressure plate, this small force generator becomes to microindentation mechanism. The displacement of the indenter head is measured by a linear variable differential transformer (LVDT) which is associated on machine. Thus, this mechanism can generate small force and monitor the depth behavior of the indenter during the indentation test.

5.1.3 Conclusion of chapter 3

In this chapter, the compact size piezo-driven microrobot including the principle and structure design, the control algorithm and the movement performance test are described. The movement test result has shown that, this locomotion movement has step resolution about 1μm per step for forward (FW) direction. It has good repeatability even movement without guidance or feedback control. After that the combination between the microindentation mechanism and the microrobot will be described. And then the indentation experiments on several bio samples; such as human nail, rice grains will be present. At the end of this chapter discussed on the movement problem after an implementation of the microindentation mechanism on a microrobot, leading to the solution that presents in chapter 4.

5.1.4 Conclusion of chapter 4

In this chapter, the vision based navigation system for tracks and controls a microrobot position is discussed. Then the robot position control using the vision based navigation system, including the path control under wide range and microscopic views, respectively are considered. In this chapter, the movement problem of a robot has been eliminated by the navigation system. At the end of this chapter presents the performance of the robot tracking system, including the repeatability experiment results of this navigation system. In the experiment, the artificial unhealthy human tooth with several glue holes was use as a specimen. The tracking experiment results have shown all of the measurement points that are designed inside an enclosure chamber can be reached by a robot. The repeatability experiment results for the camera system are achieved at ±1 pixel for both cameras, i.e., ±2.5μm and ±150μm for the microscopic C_1 camera and the wide-range view C_2 camera, respectively. After the camera tracking system is implemented to control the robot position, accuracy experiment results of the tracking system are achieved at ±3μm and ±1mm for C_1 and C_2, respectively.

The tracking accuracy with ±1mm on the C_2 camera is good enough to maneuver the robot with in a target size of 2.5 × 2mm. Additionally, the accuracy of ±3μm of the C_1 camera is excellent for a measurement part point that is designed within a 100 μm separation. Obviously indicate that this measurement system can identify microsurface stiffness on biosamples, including inside defect identification.

The first prototype of a microindentation robot combined with a vision based navigation system has been constructed and described. At the beginning, the handmade small force generator mechanism can provide a micronewton generated force. And then the microindentation mechanism was constructed by a microforce generator. After that the microindentation robot has been constructed by a combination between a microrobot and a microindentation mechanism. In the experiment several bio materials were investigated by the indentation load-depth characteristics. Finally, the vision based navigation has been implemented to control a robot position inside an enclosure chamber. The movement behavior of a microindentation robot is controlled by the navigation system. The simple image processing technique can provide the benefit of a micropositioning surface scan tasks.

5.2 Future work

The microindentation robot is successfully constructed. And the performance of this tiny mechanism is described by the surface stiffness investigation on several materials including metal and bio materials. The surface stiffness/hardness was successfully checked, and the indentation load-depth characteristics were precisely acquired. With the surface characteristic results of the certified hardness blocks (30HV and 100HV), the degree of stiffness and hardness can be compared. However, because non-standard used of the microindenter as well as the testing cycle and the force applied, the load-depth curve from this machine cannot compare with load-depth curve that come from standard machine. It can be presented only a degree of hardness compared with the load-depth of standard blocks. Moreover, from the experiment results in chapter two the limitation of this micromechanism is discovered. It can only use with the material that softer than 30HV with the maximum testing force at 10mN and 40μm indenter gap. Nevertheless, the performance of the microindentation robot is presented by results of an unhealthy tooth surface investigation. It is shown that simple vision-based navigation controls the position of a small robot precisely. The robot gets all of the measurement points that are designed inside an enclosure chamber. Experimental results indicate that this measurement system can identify microsurface stiffness on bio samples, including inside defect identification.

In the future, the plastic parts of this mechanism should be replaced with the light weight metal material such as aluminium or titanium. Thus the new metal parts can provides more robust structure as well as more generated testing force. And then, to be realised with the worldwide standard hardness tester, previous indenter will be replace with standard indenter. In addition, the automatic elevation angle of the adjustable cantilever will be considered. Moreover, the previous model has a non-symmetric structure as shown in Fig. 5.1 (A), It is caused the limitation of the indentation gap due to the indentation angle. In the near future this old model will be replaced by the new design symmetric structure as shown in Fig 5.1 (B). With this new design, we hopefully that indentation angle problem will be eliminated.
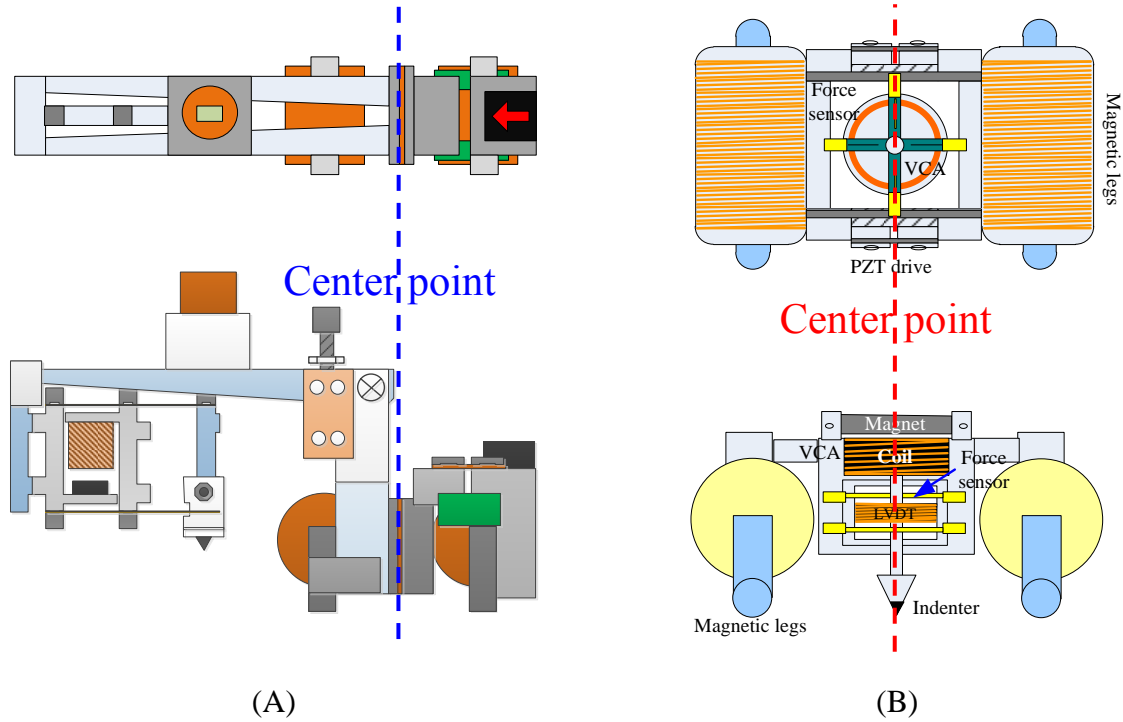
Figure 5.1 The previous model with non-symmetric structure (A) and the new design with symmetric structure (B)

After that, the improvement with the hardness measurement performance of this system will be conducted to verify with hardness standard and well-known commercially available machines. Furthermore the automatic measurement path design by computer and the automatic surface characterization with visual coordinate measuring system will be considered.

References

[1-1]   ISO 18265:2003, "Metallic materials - Conversion of hardness values.", 2003.

[1-2]   [online] available from: <http://www.calce.umd.edu/general/Facilities/ Hardness_ad_.htm#1>.

[1-3]   ASTM G171-03(2009)e2: " Standard test method for scratch hardness of materials using a diamond stylus.", 2009.

[1-4]   [online] available from: <http://www.nanoscan.info>.

[1-5]   [online] available from: <http://www.gardco.com>.

[1-6]   [online] available from: <http:// www.szfable.com >.

[1-7]   M. Kompatscher, " Equotip-rebound hardness testing after D.LEEB.", proceeding of Hardmeko 2004, pp. 1-7, 2004.

[1-8]   ASTM A956-06, "standard test method for Leeb hardness testing of steel products.", 2006.

[1-9]   ISO 6508-1:1999, "Metallic materials – Rockwell hardness test – Part 1: test method.", 1999.

[1-10] ISO 6507-3:1997, "Metallic materials – Vickers hardness test – Part 3: Calibration of reference blocks.", 1997.

[1-11] [online] available from: <http://en.wikipedia.org/wiki/Indentation_hardness#cite_note-0>.

[1-12] [online] available from: <http://en.wikipedia.org/wiki/Knoop_hardness_test#cite_ref-0>.

[1-13] Meyers and Chawla, "Mechanical Behavior of Materials.", Prentice hall, pp. 162–168, 1999.

[1-14] F. Knoop, C.G. Peters and W.B. Emerson, "A Sensitive Pyramidal-Diamond Tool for Indentation Measurements." Journal of research of the national bureau of standards, vol.23, no.1, pp. 39–61, July 1939.

[1-15] [online] "Microhardness Test", Surface engineering forum, available from: <http://www.gordonengland.co.uk/hardness/microhardness.htm>.

[1-16] ASTM E384-11e1, "Standard test method for Knoop and Vickers hardness of materials.", 2006.

[1-17] [online] available from: <http://en.wikipedia.org/wiki/Nanoindentation>.

[1-18] W.C. Oliver and G.M. Pharr, "Measurement of hardness and elastic modulus by instrumented indentation: Advances in understanding and refinements to methodology.", Journal of materials research, vol 19, pp. 3-20, 2004.

[1-19] M.F. Doerner and W.D. Nix, "A method for interpreting the data from depth-sensing indentation instruments.", Journal of materials research, vol. 1, pp. 601-609, 1986.

[1-20] Ian N. Sneddon, "The relation between load and penetration in the axisymmetric boussinesq problem for a punch of arbitrary profile.", International journal of engineering science, vol. 3, pp. 47-57, 1965.

[1-21] A.E.H. Love, "Boussinesq's problem for a rigid cone.", Quarterly journal of mathematics, vol. 10, pp. 161-175, 1939.

[1-22] A.E.H. Love, "The Stress Produced in a Semi-Infinite Solid by Pressure on Part of the Boundary.", Philosophical Transactions of The Royal Society A: Mathematical, Physical and Engineering Sciences, vol. 228, no. 659-669, pp. 377-420, 1929

[1-23] J.W. Harding and I.N. Sneddon, "The elastic stresses produced by the indentation of the plane surface of a semi-infinite elastic solid by a rigid punch.", Mathematical Proceedings of the Cambridge Philosophical Society, vol. 41, pp. 16-26, 1945.

[1-24] Ian N. Sneddon, "Fourier Transforms.", McGraw-Hill, pp. 450–467, 1951.

[1-25] W.C. Oliver and G.M. Pharr. "An improved technique for determining hardness and elastic modulus using load and displacement sensing

indentation experiments.", Journal of materials research, vol. 7, pp. 1564-1583, 1992.

[1-26] A. Bolshakov and G.M. Pharr, "Influences of Pile-up on the Measurement of Mechanical Properties by Load and Depth Sensing Indentation Techniques.", Journal of materials research, vol. 13, pp. 1049-1058, 1998.

[1-27] [online] available from: <http://www.csm-instruments.com>.

[1-28] [online] available from: <http:// www.wilson-hadness.com>.

[1-29] [online] available from:

<http://www.nanoindentation.cornell.edu/Machine/force_machine.htm>.

[1-30] Pethica J B, Hutchings R and Oliver W C, "Hardness measurement at penetration depths as small as 20 nm.", Philosophical Magazine A, vol. 48, pp. 593–606, 1983.

[1-31] [online] available from: <http:// www.agilent.com>.

[1-32] E.T. Lilleodden, W. Bonin, J. Nelson, J.T. Wyrobek and W.W. Gerberich, "In situ imaging of µN load indents into GaAs.", Journal of materials research, Vol. 10, issue 09, pp. 2162-2165, 1995.

[1-33] [online] available from: <http:// www.hysitron.com>.

[1-34] Burnham, N.A. and Colton, R.J., "Measuring the nanomechanical properties and surface forces of materials using an atomic force microscope.", Journal of vacuum science and technology A, Vol. 7, No. 4, pp. 2906-2913, 1989.

[1-35] T. J. Bell, A. Bendeli, J. S. Field, M. V. Swain, and E. G. Thwaite, "The determination of surface plastic and elastic properties by ultra micro-indentation.", Metrologia, vol. 28, no. 6, pp. 463-469, 1992.

[1-36] [online] available from: <http:// www.worldoftest.com>.

[1-37] [online] available from:

< http://www.capacitive-sensing.com/capacitive-sensor-theory.html >.

[1-38] [online] available from:
<http://en.wikipedia.org/wiki/Linear_variable_differential_transformer>.

[1-39] [online] available from: < http://www.macrosensors.com>.

[1-40] [online] available from: < www.powermnc.com >.

[1-41] CSIRO Telecommunication & Industrial Phisics, Lindfield NSW 2070 Australia , "Ultra-micro indentation system(UMIS)", available from: < http://www.tip.csiro.au/>.

[1-42] Hysitron company, "TI-series Tribolndenter", available from: < http://www.hysitron.com/products /ti-series/ti-950-triboindenter> .

[1-43] MTS system corporation.,"Nanoindenter XP", available from: < www.mts.com>.

[1-44] S. Fatikow, T. Wich, H. Hulsen, T. Sievers, and M. Jahnisch, "Microrobot system for automatic nanohandling inside a scaning electron microscope.", International conference on robotic and automation, pp. 1402-1407, 2006.

[1-45] O. Ergeneman, J.J. Abbott, G. Dogangil and B.J. Nelson. "Functionalizing Intraocular Microrobots with Surface coatings.", International conference on Biomedical robotics and Biomechatronics, pp. 232-237, 2008.

[1-46] J. Dong, S. hong, G Hesselgren, "WIP: A Study on Development of Endodontic micro robot.", Proceeding of the 2006 IJME- INTERTECH Conference, pp. 104-110, 2006.

[1-47] Young P.L., Byungkyu K., Moon G.L. and Jong-Oh P., " Locomotive mechanism design and fabrication of biomimetic micro robot using shape memory alloy.", International conference on robotics and automation, pp. 5007-5012, 2004

[2-1]   [online] available from:
         < http://news.calcocutaways.com/2009/04/21/sounds-like-another-
         successful-display/>.

[2-2]   ISO/DIS 14577, "Instrumented indentation test for hardness and materials
         parameters.", 2006.

[2-3]   Alfred R.," Magnetic repulsion: An introductory experiment.", American
         journal of physics, vol. 41, pp. 1332-1336, 1973.

[2-4]   Juan B., Emilia H., Salvador M. and Jose P., "Oscillations of a dipole in a
         magnetic field: An experiment.", American journal of physics, vol. 58, no.
         9,pp.838-843, 1990.

[2-5]   Ramon C., Jose M. M. and Maria J. C. B., "The magnetic dipole
         interaction as measured by spring dynamomoters.", American journal of
         physics, vol. 74, no. 6, pp. 510-513, 2006.

[2-6]   David V., Marco B., Ludek H. and Petr S., "Magnetostatic interactions
         and force between cylindrical permanebt magnets.", Journal of
         magnetism and magnetic materials, vol. 321, pp. 3758-3763, 2009.

[2-7]   S. Defrancesco and V. Zanetti., "Experiments on magnetic repulsion.",
         American journal of physics, vol. 51, no. 11, pp. 1023-1025, 1983.

[2-8]   H. Hertz, "On the contact of elastic solids.", Journal für die reine und
         angewandte Mathematik, vol. 92, pp.156–171, 1981, Translated and
         reprinted in English in Hertz's Miscellaneous Papers, Macmillan & Co.,
         London, Ch. 5, 1896.

[2-9]   H. Hertz, "On hardness.", Verh. Ver. Beförderung Gewerbe Fleisses, vol.
         61, p. 410, 1982, Translated and reprinted in English in Hertz's
         Miscellaneous Papers, Macmillan & Co, London, Ch. 6, 1896.

[2-10]   Y. Pauleau, "Materials surface processing by directed energy techniques.",
         Europiean materials research society, Elsevier 1st edition, July 2006.

[2-11]   Anthony C. Fischer-Cripps, "Introduction to contact mechanics.",
         Springer 2nd edition, 2007.

[2-12] Udo D. Schwarz, Oliver Zworner, Peter Koster and Roland Wiesendanger, "Quantitative analysis of the frictional properties of solid materilas at low loads. I Carbon compounds.", Physical review B, vol. 56, no. 11, pp. 6987-6996, 1997

[2-13] Malgorzata Kopycinska-Muller, Roy H. Geiss, Donna C. Hurley, "Contact mechanics and tip shape in AFM-based nanomechanical measurements.", Elsevier, ultramicroscopy, vol. 106, pp. 466-474, 2006.

[2-14] Huang, Y., Xue, Z., Gao, H., Nix, W.D., Xia, Z.C., "A study of microindentation hardness tests by mechanism-based strain gradient plasticity.", Journal of materials research, vol. 15, pp. 1786–1796, 2000.

[2-15] McElhaney, K.W., Vlasssak, J.J., Nix, W.D., "Determination of indenter tip geometry and indentation contact area for depth-sensing indentation experiments.", Journal of materials research, vol. 13, pp. 1300–1306, 1998.

[2-16] Xue, Z., Huang, Y., Hwang, K.C., Li, M., "The influence of indenter tip radius on the micro-indentation hardness.", J. Eng. Mater. Technol.— Trans. ASME 124, pp. 371–379, 2002.

[2-17] Akihiro Nino, Ayumi Tanaka, Shigeaki Sugiyama and Hitoshi Taimatsu, "Indentation size effect for the hardness of refractory carbides.", Materials transactions, vol. 51, no.9, pp. 1621-1626, 2010

[2-18] N.Chollacoop, M Dao and S.suresh, "Depth-sensing instrumented indentation with dual sharp indenters.", Acta materialia, vol. 51, issue 13, pp. 3713-3729, 2003.

[3-1] Fuchiwaki O and Aoyama H, "Piezo based micro robots for microscope instrument.", Proceedings of the 6th international conference on mechatronics technology, pp. 499–504, 2002.

[3-2] S. Fatikow, T. Wich, H. Hulsen, T. Sievers, and M. Jahnisch, "Microrobot system for automatic nanohandling inside a scanning

electron microscope.", International conference on robotic and automation, pp. 1402-1407, 2006.

[3-3] O. Ergeneman, J. J. Abbott, G. Dogangil, and B. J. Nelson. "Functionalizing Intraocular Microrobots with Surface coatings.", International conference on Biomedical robotics and Biomechatronics, pp. 232-237, 2008.

[3-4] J. Dong, S. hong, and G. Hesselgren, "WIP: A Study on Development of Endodontic micro robot.", Proc. of the 2006 IJME- INTERTECH conference, pp. 104-110, 2006.

[3-5] P. L. Young, K. Byungkyu, G. L. Moon, and P. Jong-Oh, "Locomotion mechanism design and fabrication of biomimetic micro robot using shape memory alloy.", International conference on robotic and automation, pp. 5007-5012, 2004.

[3-6] Manabu Ono, Toshiaki Hamano and Shigeo kato, "Modeling and Fabrication of a mobile inspection microrobot driven by a pneumatic bellows actuator for long pipes.", Journal of robotics and mechatronics, vol. 18, no.1 pp. 11-17, 2006.

[3-7] ASTM D2240-05, "Standard test method for Rubber property—Durometer hardnes.", 2010.

[3-8] Robert Katz, A.B.Cordwell, N.D. Collins, A.D. Hostetter, "A new grain hardness tester.", Cereal Chemistry, vol.36, no.5, pp. 393-401, 1959.

[3-9] [online] available from: <http://en.wikipedia.org/wiki/Barcol_hardness_test>.

[3-10] J.R.K.Robson and H.D.EL-Tahawi, "Hardness of human nail as an index of nutritional status.", British journal of nutrition, vol. 26, issue 02, pp. 233-236, 1971.

[3-11] Nails again, " Basic nail info.", [online] available from: < www.mynailsagain.com>.

[3-12] Norman O, Jules M. and Joseph H. "The effect of aging on the rate of linear nail growth.", The journal of investigative dermatology, vol. 73, pp.126-130, 1979.

[3-13] Agriculture and consumer protection department, "Chapter 3- Grain structure, composition and consumers' criteria for quality.", [online] available from: < www.fao.org>.

[3-14] Encyclopaedia Britannica, Inc., "Rice: layers and structures of rice grain.", [online] available from: <www.britannica.com>.

[3-15] Adyss design, "Human teeth-Types of teeth- Tooth morphology.", [online] available from: <users.forthnet.gr>.

[3-16] James K. Avery, "Oral development and history 3rd ed.", Thieme medical publishers Inc., pp. 72-73, 2002.

[3-17] Indiaaccess.com, UG dental services.com, "Patient education-the tooth.", [online] available from: <www.ugdentalservices.com>.

[3-18] Craig R.G., Peyton F.A., "Microhardness Studies of Intact Surface Enamel.", Journal of dental research, vol. 37, pp. 661- 668, 1958.

[3-19] Caldwell R.C., Muntz M.L., Gilmore R.; Pigman W., "Microhardness Studies of Intact Surface Enamel.", Journal of dental research, vol. 36, pp. 732-737, 1957.

[3-20] Sweeney W.T., "The KNOOP Indentation hardness instrument as a tool in dental research.", Journal of dental research, vol. 21, pp. 303-310, 1942.

[3-21] Victor P. Totah, "Increase in Hardness of Dentin On Drying.", Journal of dental research, vol. 21, pp. 99-104, 1942.

[3-22] F. Taketa, H. S. Perdue, W. F. 0 'Rourke, H. W. Sievert, and P. H. Philips, "An abrasion method for determining the wear resistance of teeth I. Description of apparatus and variables.", Journal of dental research, vol. 36, 1957, pp. 739-742.

[3-23] Meredith N., Sherriff M., Setchell, D.J., Swanson, S.A.V., "Measurement of the microhardness and young's modulus of human enamel and dentine using an indentation technique.", Archs, Oral Biol. vol. 41, pp. 539-545, 1996.

[3-24] Robinson C., Weatherell J.A., Hallsworth A.S., "Distribution of magnesium in mature human enamel.", Caries Res., vol. 15, pp. 70-77, 1981.

[3-25] Kodaka T., Debari K., Yamada M., Kuroiwa M., "Correlation between microhardness and mineral content in sound human enamel.", Caries Res., v. 26, pp. 139-141, 1992.

[3-26] Maria D.P., Gutierrez-Salazar, Jorge R.G., "Microhardness and chemical composition of human tooth.", Materials research, vol. 6, no. 3, pp. 367-373, 2003.

[4-1] [online] Douglas G.Myers, "Image processing.", Electrical Engineering vol. 1, Encyclopedia of life support systems(EOLSS), available from: < http://www.eolss.net/Sample-Chapters/C05/E6-39A-02-04.pdf >.

[4-2] [online] Steven W. Smith, "Chapter 23: Image formation & Display.", The scientist and Engineer's guide to Digital Signal processing, available from: <http://www.dspguide.com/CH23.PDF>.

[4-3] Bernd Jähne, "Digital Image Processing 5th revised and extended edition.", 5th revised and extended edition, Springer, pp. 29-37, 2002.

[4-4] [online] available from: < http://www.vision.ee.ethz.ch/~cvcourse/lectures/5.pdf>.

[4-5] Saeed B. Niku, "Introduction to Robotics Analysis, Systems, Applications", Prentice hall, pp. 262-263, 2001.

[4-6] [online] available from: < http://www.mathworks.co.jp/help/toolbox/images/ref/im2bw.html>.

[4-7]   [online] available from:

<http://www.codersource.net/MicrosoftNet/CImageProcessing/ConversionofaColorImagetoaBinaryImage.aspx>.

[4-8]   [online] available from

<http://homepages.inf.ed.ac.uk/rbf/CVonline/LOCALCOPIES/OWENS/LECT2/node3.html>.

[4-9]   Saeed B. Niku: "Introduction to Robotics Analysis, Systems, Applications", Prentice hall, pp. 268-269, 2001.

[4-10] [online] available from:

<http://cs.haifa.ac.il/hagit/courses/ip/Lectures/Ip12_Segmentation. pdf>

[4-11] R. O. Duda and P. E. Hart, "Pattern Classification and Scene Analysis.", Wiley-Interscience, New York, 1973.

[4-12] W. H. Highleyman, "An Analog Method for Character Recognition.", IRE Trans. Electronic Computers, EC-**10**, no. 3, pp. 502–510, 1961.

[4-13] L. N. Kanal and N. C. Randall, "Recognition System Design by Statistical Analysis.", Proceeding of 19th ACM National Conference, pp. 42.501-42.5020, 1964.

[4-14] J. H. Munson, "Experiments in the Recognition of Hand-Printed Text, I. Character Recognition.", Proceeding of Fall Joint Computer Conference, pp.1125–1138, 1968.

[4-15] William K. Pratt, "Digital Image Processing: PIKS Scientific Inside, Fourth Edition.", John Wiley & Sons, Inc., pp. 623-649, 2007.

[4-16] S. Fatikow, J. Seyfriend, St. Fahlbusch, A. Buerkle and F.Schmoeckel., "Aflexible Microrobot-Base Microassembly Station.", Journal of Intelligent and Robotic Systems., vol. 27, pp. 135-169, 2000.

[4-17] IMAQ Vision concept manual, National Instruments, June 2003.

[4-18] James K. Avery, "Oral development and history 3rd ed.", Thieme medical publishers Inc., pp. 72-73, 2002.

[4-19] Montree PAKKRATOKE, Nguyen N.T., Shinnosuke HIRATA, Chisato KANAMORI and Hisayuki AOYAMA, "Precise navigation based on double vision images for microrobot with surface sensor.", Proc. of the Robotics and mechatronics conference 2012, paper 2P1-R04, May 2012.

[4-20] Montree PAKKRATOKE, Shinosuke HIRATA, Chisato KANAMORI and Hisayuki AOYAMA., "Development of microscopic hardness and stiffness investigation system with microrobot 2nd report, vision based precise navigation.", Journal of Robotics and Mechatronics, vol.25. no.1, pp. 97-105, 2013.

Acronyms

VCA   Voice coil actuator

LVDT   Linear variable differential transformer

HV   Hardness Vickers scale

HB   Hardness Brinell

HK   Hardness Knoop

HR   Hardness Rockwell scale

UTS   Ultimate tensile strength

PZT   Piezoelectric transducer

N   Newton

m   Meter

Mpa   Mega pascal

CCD   Charge-coupled device

2-D   Two dimensions

3-D   Three dimensions

AFM   Atomic force microscopy

Publications

1. Journal papers

(1) Montree PAKKRATOKE, Shinosuke HIRATA, Chisato KANAMORI and Hisayuki AOYAMA., "Development of microscopic hardness and stiffness investigation system with microrobot 2nd report, vision based precise navigation." Journal of Robotics and Mechatronics, vol.25. no.1, pp. 97-105, February 2013.

(2) Montree PAKKRATOKE, Shinosuke HIRATA, Chisato KANAMORI and Hisayuki AOYAMA., "Development of microscopic hardness and stiffness investigation system with microrobot." Journal of Robotics and Mechatronics, vol.24. no.1, pp. 123-132, February 2012.

2. Conference papers

(1) Montree PAKKRATOKE, Nguyen N.T., Shinnosuke HIRATA, Chisato KANAMORI and Hisayuki AOYAMA., "Precise navigation based on double vision images for microrobot with surface sensor.", Proc. of the Robotics and mechatronics conference 2012, paper 2P1-R04, May 2012.

(2) Montree PAKKRATOKE, Nguyen N.T.,Shinnosuke HIRATA,Chisato KANAMORI and Hisayuki AOYAMA., "Micro Diagnostic by Micro Robot with Stiffness Indenter for BIO Materials.", Proc. of 2011 IEEE International Conference on Robotics and Biomimetics (IEEE-ROBIO 2011), pp. 644 – 649, December 2011.

(3) Montree PAKKRATOKE, SMG iroshana, Chisato KANAMORI and Hisayuki AOYAMA., "Development of micro hardness and stiffness testing system by micro robot for biomaterials.", Proc. Of 4th AISM, pp. 206-212, December 2010.

(4) Montree PAKKRATOKE, Natcahpon Luekiatphaisan, Hisayuki AOYAMA and Tassanai saneponpute., "Compact micro force generator with tandem leaf spring and VCA on micro robot for micro hardness and stiffness test.", Proc. of IMEKO 2010 TC5 conference, pp. 355-358, November 2010.

(5) Montree PAKKRATOKE, Natchapon Luekiatphaisan and Hisayuki AOYAMA., "Combination of VCA based Micro Force Generator and

Micro Robot for Micro hardness and stiffness test.", Proc. of SICE annual conference 2010, pp. 3184-3189, August 2010.

(6) Montree PAKKRATKE, Tassanai SANPONPUT, Rugkanawan KONGKAVITUL and Apichaya MEESAPLAK., "Development of Intelligent Hardness Measurement Machine.", 2009 JSME-IIP/ASME-ISPS Joint conference on Micromechatronics for Information and Precision Equipment (MIPE 2009), pp. 49-50, June 2009.

Acknowledgements

Bibliography

Name: Montree PAKKRATOKE

Nationality: Thai

1978 Dec 06:   Was born in Nakhonratchasima,Thailand.

1994 May: Entered the diploma program in Computer technology at Rajamangala Institute of Technology Northeastern campus (Nakhonratchasima, Thailand).

1998 March: Graduated the diploma degree in Computer Technology from Rajamangala Institute of Technology Northeastern campus (Nakhonratchasima, Thailand).

1998 June: Entered the undergraduate program at King Mongkut's institute of technology (North Bangkok).

2001 March: Graduated in the Bachelor of Industrial technology in Electronic technology with First class honors from King Mongkut's institute of technology (North Bangkok).

2001 June: Entered the master of engineer (Industrial metrology) course at King Mongkut's university of technology (Thonburi).

2002 June: Teacher assistant at King Mongkut's university of technology (Thonburi).

2003 April: Research assistant at King Mongkut's institute of technology (Ladkrabang).

2003 October: Graduated in the Master of engineering in Industrial metrology from King Mongkut's university of technology (Thonburi).

2004 May: Joined the National Institute of Metrology (Thailand), metrologist of hardness laboratory.

2008 October: Entered the research student at the department of Mechanical engineering and Intelligent systems, The University of Electro-Communications.

2009 April: Entered the Ph.D. student at the department of Mechanical engineering and Intelligent systems, The University of Electro-Communications.

2013 March: Received Ph.D. in Mechanical Engineering and Intelligent systems from The University of Electro-Communications.